Advanced Powder Bed Fusion-Based Additive Manufacturing with Turbine Engine Hot-Section Alloys through Scanning Laser Epitaxy

Dissertation
Presented to
The Academic Faculty

by

Amrita Basak

In Partial Fulfillment
of the Requirements for the Degree
Doctor of Philosophy in the
George W. Woodruff School of Mechanical Engineering

Georgia Institute of Technology
December 2017

Advanced Powder Bed Fusion-Based Additive Manufacturing with Turbine Engine Hot-Section Alloys through Scanning Laser Epitaxy

Approved by:

Dr. Suman Das, Advisor
George W. Woodruff School of Mechanical Engineering
Georgia Institute of Technology

Dr. Richard Neu
George W. Woodruff School of Mechanical Engineering
Georgia Institute of Technology

Dr. Kyriaki Kalaitzidou, Co-advisor
George W. Woodruff School of Mechanical Engineering
Georgia Institute of Technology

Dr. Hamid Garmestani
School of Materials Science and Engineering
Georgia Institute of Technology

Dr. David McDowell
George W. Woodruff School of Mechanical Engineering
Georgia Institute of Technology

Date Approved: 26th October, 2017

“*You see, one thing is, I can live with doubt, and uncertainty, and not knowing. I think it's much more interesting to live not knowing than to have answers which might be wrong. I have approximate answers and possible beliefs and different degrees of certainty about different things. But I'm not absolutely sure of anything, and there are many things I don't know anything about, such as whether it means anything to ask why we're here, and what the question might mean. I might think about it a little bit; if I can't figure it out, then I go onto something else. But I don't have to know an answer. I don't feel frightened by not knowing things, by being lost in the mysterious universe without having any purpose, which is the way it really is, as far as I can tell - possibly. It doesn't frighten me.*”

– Richard P. Feynman

Dedicated to my dear parents,

Mr. Amaresh Chandra Basak and Mrs. Ujjwala Basak

And my loving brother,

Mr. Arindam Basak

Acknowledgements

I would like to take this opportunity to thank my advisor Dr. Suman Das for his guidance in pursuing the dissertation research at the Direct Digital Manufacturing (DDM) Lab. My progress would not have been possible without his insight, encouragement, objective criticism, and attention to details. Dr. Das offered me to work on this project when I knew nothing about manufacturing or materials science and mentored me to successfully complete a dissertation that has both. It will not be an overstatement to say that my career took a major turn after I joined the DDM lab and I will be forever indebted to Dr. Das for all that he has done for me.

Acknowledgments are in order for my co-advisor, Dr. Kyriaki Kalaitzidou for her help in doing the tensile testing and her support throughout the duration of my research. I would also like to extend my sincere gratitude to Dr. David McDowell, Dr. Richard Neu, and Dr. Hamid Garmestani for serving on my reading committee and providing critical insights on my research. I feel extremely honored and privileged to have such a stellar reading committee and I am going to carry the pride of being a mentee of this wonderful committee all my life.

The research work has been performed through grant N00014-11-1-0670 as part of the Cyber enabled Manufacturing Systems (CeMS) program by Office of Naval Research. In particular, I would like to acknowledge Dr. Richard Fonda, Dr. Khershed Cooper, and Dr. Ralph Wachter for their support. I would like to thank the School of Materials Science and Engineering for providing me with the financial support in performing some of the XRD experiments carried out in this research.

I wish to extend my sincere thanks to Dr. Jeff Jagoda for his help during my transition

from AE to ME and on several occasions during my stay at Georgia Tech. I would also like to thank Dr. Tequila Harris for accepting me as a ME Teaching Practicum mentee. Acknowledgments are in order for Ms. Glenda Johnson and Ms. Camelia Henry from the ME Academic Office for their help on several occasions.

I gratefully acknowledge the help I received from the past members of the DDM lab specially Dr. Ranadip Acharya, Dr. Rohan Bansal, and Shashank H R. I am fortunate to work with Yunpei Yang and Andriy Dotsenko with whom I shared the frustration and happiness of pursuing my graduate research. The XRD work done in this dissertation would not have been possible without the help from David Tavakoli. I would also like to thank Nathan Maudlin from the Montgomery Machining Mall for his help in processing my research samples and P. Debs Kulia for his help in performing the microhardness indentation measurements.

I decided to do a Ph.D. after spending a few years in industry. I would not have attained the required "escape velocity" to leave a nice and comfortable life had I not met Dr. Nayan Patel. Dr. Patel, a Georgia Tech alumni, persuaded me to come to GT, and today in retrospect I feel that coming to Tech was one of the most rewarding and fulfilling decisions I took so far in my life. Special thanks to my roommate, Ms. Sridevi Pogaru for showering me with the love of a sister when I needed it the most. I would also like to acknowledge the support I got from Dr. Parthasarathi Chakraborti, an MSE Ph.D. from Georgia Tech, in pursuing my research. His knowledge and dexterity in materials characterization, willingness to help, and extraordinary patience in dealing with a restless soul like me are lovingly appreciated. Finally, I would like to thank my parents and my younger brother for their constant love, support, and encouragement. They taught me to believe in my dreams and to pursue them against all odds.

Table of contents

List of tables

List of figures

List of equations

List of abbreviations

EQ	Equiaxed
DS	Directionally solidified
SX	Single-crystal
AM	Additive manufacturing
LPBF	Laser powder bed fusion
SLE	Scanning laser epitaxy
UGT	Utility gas turbine
RIT	Rotor inlet temperature
FCC	Face centered cubic
TCP	Topologically closed pack
LCF	Low cycle fatigue
LMP	Larson-Miller parameter
LMC	Liquid metal cooling-assisted casting
HAZ	Heat-affected zone
PWHT	Post-weld heat treatment
GTA	Gas tungsten arc
TIG	Tungsten inert gas
EB	Electron beam
SLS	Selective laser sintering
HIP	Hot isostatic pressing
DMLS	Direct metal laser sintering

SLM	Selective laser melting
LMD	Laser metal deposition
DMD	Direct metal deposition
LENS®	Laser engineered net shaping
ELMF	Epitaxial laser metal forming
EBM	Electron beam melting
SEBM	Selective electron beam melting
BCT	Body centered tetragonal
SMD	Shaped metal deposition
3DMW	Three-dimensional micro welding
PDAS	Primary dendrite arm spacing
CET	Columnar-to-equiaxed transition
OMT	Oriented-to-misoriented transition
SG	Stray grain
FEM	Finite element modeling
CFD	Computational fluid dynamics
CAD	Computer-aided design
DAQ	Data acquisition
CW	Continuous wave
DFM	Dynamic focusing module
API	Application programming interface
XML	eXtensible markup language
DLL	Dynamic-link library

PPM	Parts per million
IR	Infrared
UV	Ultraviolet
VIS	Visible
NIR	Near infrared
PI	Proportional – integral (PI)
OSAAC	One step ahead adaptive control
OM	Optical microscopy
SEM	Scanning electron microscopy
EDS	Energy dispersive spectroscopy
XRD	X-ray diffraction
EBSD	Electron back scattering diffraction
DoE	Design of experiments
Micro-LAAM	Micro-laser aided additive manufacturing
LSW	Lifshitz-Slyozov-Wagner
PSD	Particle size distribution
PDF	Probability distribution function
VH	Vickers hardness
PF	Pole figure
IPF	Inverse pole figure

List of symbols

T_i	Turbine inlet temperature
T_e	Turbine exhaust temperature
η	Efficiency
T	Temperature
t	Time
C_t	Material constant
G	Temperature gradient
V	Solidification velocity
n	Material constant
x, y	Coordinates
X, Y	Coordinates
E	Scan energy density
P	Laser power
V_S	Raster scan speed
N	Number of repeats
r	Volume fraction
ρ_S, ρ_L	Solid and liquid density
r_S, r_L	Solid and liquid volume fraction
h_S, h_L	Solid and liquid phase enthalpy
$\underline{U_S}$, $\underline{U_L}$	Solid and liquid phase velocity
T_S, T_L	Solid and liquid phase temperature

Y_S, Y_L	Solid and liquid mass fraction
t	Time
I	Interphase heat transfer
$\bar{\rho}$	Mixture density
h	Mixture enthalpy
$\underline{U}$	Mixture velocity
$\bar{k}$	Mixture thermal conductivity
S	Source term
S_M	Permeability source term
m_L	Liquid viscosity
K_0	Proportionality constant
C_M	User specified constant
S_{TKE}	Sink term for turbulent kinetic energy
S_ε	Sink term for turbulent eddy dissipation
tke	Turbulence kinetic energy
ε	Turbulence eddy dissipation
ρ	Density
H	Enthalpy
K	Thermal conductivity
S_0	Source/sink term
$I(y_n)$	Intensity at y_n location
P_i	i^{th} Polynomial coefficient
μ_{Laser}, σ_{Laser}	Laser beam parameters

γ	Surface tension coefficient
ψ, θ	Angle
$\hat{n}$	Normal vector to the solid-liquid interface
$\hat{u}$	Direction vector
a, n	Material constant
ϕ	Equiaxed fraction
G_{hkl}	Temperature gradient in hkl direction
V_{hkl}	Dendrite growth velocity in hkl direction
N_0	Nucleation density
ΔT_{tip}	Tip undercooling
ΔT_n	Nucleation undercooling
k	Degree of segregation
SS	Scan spacing
Q	Total repeat scan energy
t_p	Powder thickness
f	Density function
D	Precipitate size
<D>	Average equivalent diameter
A	Area
ϕ	Normalized diameter
λ	Wavelength
d	Lattice spacing
(hkl)	Lattice plane

d_n	Lattice spacing (no stress condition)
σ_y	Yield stress
σ	Standard deviation
k_{DI}	Segregation parameter between the dendritic core and the interdendritic region
k_{EI}	Segregation parameter between the eutectic pools and the interdendritic region
k_{CI}	Segregation parameter between the carbides and the interdendritic region

Summary

Nickel-base superalloys are extensively used in the fabrication of gas turbine hot-section components as this class of alloys offers higher yield strength with increase in operating temperature due to the presence of secondary phase precipitates. Traditionally, hot-section components are manufactured using conventional manufacturing methods such as investment casting. However, a realization of complex designs with functionally graded materials, microstructures or properties are not feasible with the conventional manufacturing methods. Additionally, if the parts suffer material loss due to prolonged service or manufacturing defects, it is impossible to repair the superalloy components using conventional methods as these alloys are extremely difficult to weld.

Additive manufacturing (AM)-based processes offer an alternative as, when properly controlled, they have shown encouraging results in depositing as-desired microstructures through optimization of processing conditions for a range of metallic material systems. However, fundamental research to advance the scientific understanding of the AM-based processing of high-performance structural materials such as nickel-base superalloys is lacking. Furthermore, lack of knowledge on how the material microstructures and properties are affected by the processing parameters significantly hinders the capabilities of the AM-based processes in producing high quality parts in nickel-base superalloys.

The goal of this dissertation research is to advance the scientific understanding of the underlying physics of melting and re-solidification, microstructure, and properties of various nickel-base superalloys deposited using a powder bed fusion (PBF)-based AM process, scanning laser epitaxy (SLE). Multiphysics-based simulation, experimental validation, and

advanced materials characterization techniques are combined to advance the AM-based processing of nickel-base superalloys enabling repair of hot-section components with as-desired microstructure and properties.

Chapter 1: Introduction

Advancements in the design, optimization, and manufacture of turbine engine hot-section components during the past few decades have contributed enormously to the improvement in power-ratings and efficiency levels of gas turbine engines. Modern day turbine engines typically operate under the Brayton cycle in which inlet air is first compressed and then mixed with fuel. The fuel-air mixture is combusted and finally exhausted through an expansion turbine to generate power. The efficiency (η) of the cycle is given by Equation 1:

Equation 1. Efficiency of Brayton cycle.

$$\eta = 1 - \frac{T_e}{T_i}$$

Here, T_e is the exhaust temperature and T_i is the inlet temperature. Since, the exhaust temperature cannot be reduced below the ambient temperature, the design focus has always been on increasing the inlet temperature, which in effect increases the operating temperature of the hot-section components in gas turbine engines. Typically, an increase of 10 ^oC (50 ^oF) in the operating temperature increases the efficiency by 1%. Hence, over the past 30 years, the operating temperature has constantly been increased from about 982 ^oC (1800 ^oF) to about 1427 ^oC (2600 ^oF), posing a serious design challenge for hot-section components. In order to deal with such high temperatures, three complimentary approaches have been adopted. The first approach is to provide thermal protection to the components by coating them with metallic and ceramic materials to improve the oxidation and corrosion resistance. The second approach is to incorporate elaborate and complex film cooling designs to keep the metal temperature within design limits. The third approach is to use high-creep strength and fatigue resistant

materials such as superalloys that enable hot-section components to operate at higher temperatures.

Superalloys are nickel-, iron-nickel-, and cobalt-based alloys that can withstand loading at temperatures close to the melting temperature and are generally used in applications with temperatures exceeding 540 ^{o}C (1000 ^{o}F) [1]. The superalloy components cast with a polycrystalline or equiaxed (EQ) microstructure are susceptible to failure because they contain grain boundaries that are transverse to the loading direction. Voids are likely to form at these transverse grain boundaries [1]. To alleviate this problem, directionally solidified (DS) microstructure is introduced where the resulting oriented grain structure is parallel to the major axis of loading and contains a limited number of transverse grain boundaries. Elimination of the transverse grain boundaries results in additional creep and rupture strength. In addition, alignment of the grain structures provides a favorable modulus of elasticity in the loading direction enhancing the fatigue life. Creep strength and fracture toughness can be further enhanced by casting the blade with a single-crystal (SX) microstructure that contains no grain boundaries at all. The SX microstructure also allows removal of grain boundary strengthening elements such as carbon and boron that are typically responsible for reducing the melting temperature and the fatigue life of the alloy [2].

Superalloys typically derive their strength from the presence of secondary γ' phase that forms an anti-phase boundary and locks the associated dislocation movement [3]. However, the same strengthening mechanism also increases the susceptibility to cracking. The hot-section components such as turbine blades have a limited operating life due to material loss at the blade tip resulting from the abrasion between the blade and the engine shroud. Once a blade has experienced a certain amount of material loss [typically in the range of 0.5 – 1 mm on an

8 cm tall blade as shown Figure 1(a)], it cannot be used any further and has to be scrapped. Additionally, fatigue cracks and other forms of damage limit the life of platform components shown in Figure 1(b). With several hundred such components installed in each gas turbine engine, their total replacement cost at the time of overhaul is upwards of hundreds of thousands or even millions of dollars per engine.

(a) **(b)**

Figure 1. (a) Turbine airfoil with worn out blade tip and (b) cracking in the platform section [4].

Component repair through weld build-up is not possible as the superalloys involved are prone to cracking. Hence, there is a great commercial interest in developing additive manufacturing (AM)-based processes that can restore the worn-out hot-section components while maintaining the parent metallurgical microstructure and geometry at damage locations, allowing for the blades to be reused rather than scrapped and replaced. If successful, the AM-based processes will also be able to fabricate entirely new hot-section parts. Such success will venture into the previously unattainable design territory with gas turbine hot-section components as the designers will be able to incorporate novel design and functional features that are currently not feasible through the conventional manufacturing methods. Overall, the successful demonstration of AM-based processing of nickel-base superalloys has the potential

to revolutionize the gas turbine industry resulting in improved performance and cost savings.

1.1 Research motivation

AM-based processes offer unparalleled opportunities as they enable the realization of complex geometries with functionally improved materials, microstructures, and properties. During the past few decades, a considerable amount of research has been done on AM-based processing of various metallic materials [5]. However, fundamental research to advance the scientific understanding of AM-based processing of high-performance alloy systems is lacking. Additionally, there are a significant number of technical challenges yet to be overcome in order to realize successful processing of exotic material systems such as nickel-base superalloys through AM.

AM-based processing of high-performance alloy systems typically involves a complex interplay between multiple modes of energy and mass transfer, fluid flow, phase change, and microstructural evolution under rapid solidification conditions. Components fabricated using AM processes have structure, properties, and performance that are significantly different from their cast and wrought counterparts due to very high cooling rates (~10^5 – 10^8 K/s). At these cooling rates, several effects can be realized such as suppression of diffusion-controlled solid-state phase transformations, formation of supersaturated solutions and non-equilibrium phases, formation of extremely fine and refined microstructures with little elemental segregation, and formation of very fine second-phase particles such as inclusions and carbides. Because of the rapid cooling rates and directional solidification, significant crystallographic texture can also be expected in components made using AM-based processes (*Source: https://manufacturing.llnl.gov/additive-manufacturing/metal-additive-manufacturing*).

An open problem in the AM-based processing of nickel-base superalloys is associated with processing difficulty of these material systems due to the presence of secondary phase precipitates. The alloys also contain a large number of alloying elements which have significant differences in their thermo-physical properties leading to extremely complex solidification paths. While achieving crack-free superalloy structures may sound extremely difficult, ensuring epitaxial depositions having as-desired microstructures such as EQ, DS or SX is even more challenging. Lack of fundamental knowledge on how the material microstructure and properties are affected by the processing parameters significantly hinders the capabilities of the AM-based processes in producing as-desired epitaxial structures in nickel-base superalloys.

Finally, the composition of various superalloys are different, and thus, they exhibit a wide variation in thermo-physical and rheological properties (i.e., heat capacity, thermal conductivity, liquidus and solidus temperatures, surface tension, and viscosity). Therefore, it is expected, that each superalloy will interact differently with the energy source. Hence, the knowledge gained for a specific superalloy may not be readily applied to another superalloy even if the desired dimensions and the microstructure (EQ, DS or SX) of the final part are exactly the same.

1.2 Research objectives

This doctoral research aims to advance the field of AM-based processing of nickel-base superalloys with an eye towards developing process-structure-property relationships in these material systems. The specific research objectives are:

- Develop a metal powder-bed based AM process to enable fabrication of crack-

free gas turbine hot-section superalloy components *without altering the base alloy chemistry*. In this work, the presence of cracks is investigated by the high-resolution optical microscopy and scanning electron microscopy.

- Obtain scientific insights on understanding the *physics of material consolidation, melting, and re-solidification processes* in AM through an experimentally validated multi-physics-based model.

- Provide a fundamental understanding of the *process-structure-property relationships* through a systematic experimental study combined with advanced microstructure and property characterization techniques for a range of superalloys.

1.3 Outline of the dissertation

Chapter 2 of this dissertation documents the evolution of nickel-base superalloys and the processing difficulties of these materials systems. Prior repair efforts on nickel-base superalloys are also discussed with an emphasis on understanding the process-property relationship and resultant defects associated with AM processing of these alloys. The challenges in modeling the complex physics are also highlighted.

Chapter 3 presents details on the development of a laser powder bed fusion (LPBF)-based AM process, scanning laser epitaxy (SLE). This chapter also documents the experimental setup and materials characterization techniques implemented in this dissertation.

Chapter 4 covers the development of a coupled flow-thermal model in order to predict the flow-thermal-microstructural evolution in SLE. The flow-thermal model is extended to a number of different superalloys.

Chapter 5 focuses on details of a feasibility study of fabricating EQ deposits through SLE. Two high-γ′ alloys namely IN100 and MAR-M247 are investigated. MAR-M247 contains 13.7 wt. % refractory elements while IN100 contains only 3.0 wt. % of such elements. Hence, the results from this chapter are used to qualitatively address the effects of refractory elements on the AM-processed deposit characteristics.

Chapter 6 focuses on details of a feasibility study of fabricating SX deposits through SLE. Two high-γ′ alloys namely CMSX-4® and René N5 are investigated. René N5 contains 0.05 wt. % carbon and 0.004 wt. % boron while CMSX-4® does not contain any such elements. Carbon and boron are carbide/boride formers. Hence, the results from this chapter are used to qualitatively address the effects of carbon and boron on the AM-processed deposit characteristics.

Chapter 7 focuses on details of a feasibility study of fabricating heterogeneous deposits through SLE. The depositions of high-γ′ René 142 on SX René N5 and EQ René 125 are carried out and the resultant microstructures are compared. By comparing the deposit characteristics of SX/DS René 142 on SX René N5 and EQ René 142 on EQ René 125, the results from this chapter are used to qualitatively address the effects of solidification on deposit characteristics.

Chapter 8 provides a summary of the research conducted as part of this dissertation, address the novel contributions, and outline some potential avenues for further research.

Chapter 2: Background

In this section, a background study is presented on nickel-base superalloys. Additionally, previous research attempts on the AM-based processing of superalloys along with the role of simulation in predicting the solidification microstructure in such material systems are also discussed.

2.1 Nickel-base superalloys

Superalloys were introduced in order to deal with the increasing demand for stronger and more corrosion-resistant materials for aircraft engines during World War II. Figure 2(a) shows the increase in efficiency of the utility gas turbine (UGT) sector after the World War II. This increase can be attributed to the increase in rotor inlet temperature (RIT) from 500 ^{o}C to 1600 ^{o}C [6]. The demand for high-temperature systems was met by increasing the use of superalloys in gas turbine components. Figure 2(b) shows the change in relative weight of superalloy components for UGTs. To improve efficiency, weight must be reduced. Hence, high-specific-strength materials that can retain their properties near the melting temperature are required.

Figure 2(c) shows the comparison of specific strength for different superalloys [7]. The set of temperature-dependent specific strength curves take account of the material's density, and indicates that even though nickel-base alloys are denser than titanium-base alloys, it is the only material that retains sufficient integrity at high temperatures. Figure 2(d) shows the progression in turbine operating temperature over the past 70 years as the material microstructure evolved from EQ to DS, and finally to SX [8].

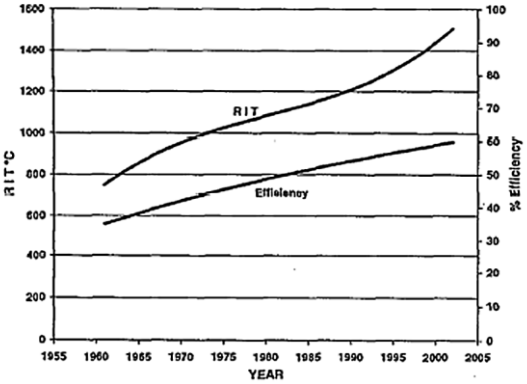

(a)

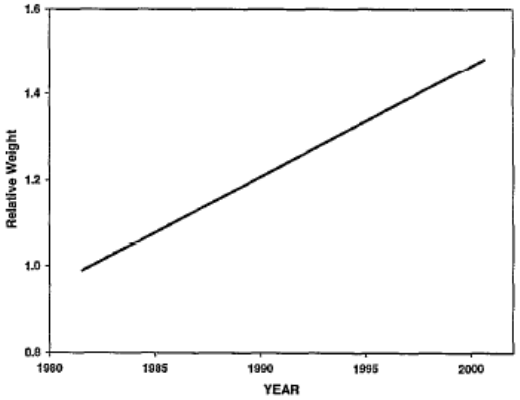

(b)

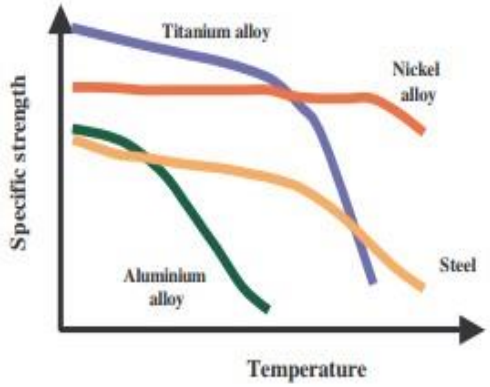

(c)

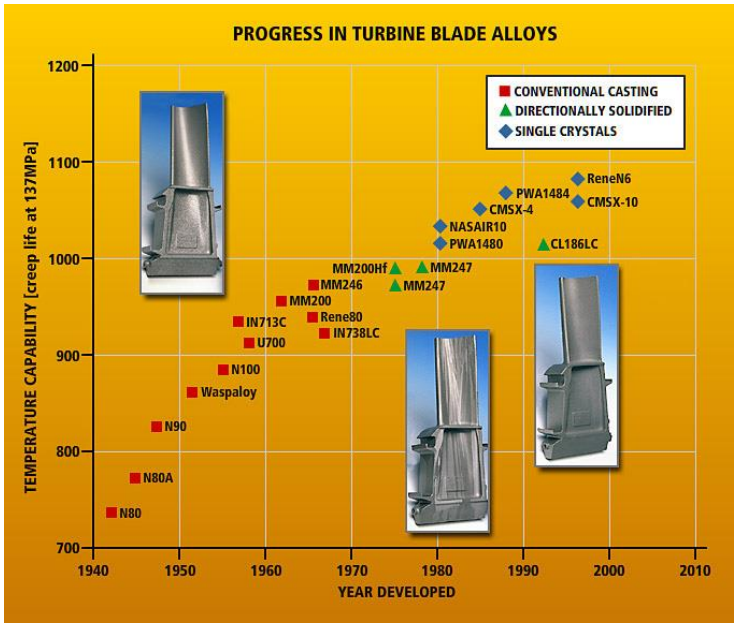

(d)

Figure 2. (a) Improvement in RIT and efficiency (1960 – 2005) [6], (b) increase in relative weight of superalloys in UGT (1980 – 2000), (c) temperature-dependent specific

strength behavior for different superalloys [7], and (d) progress in turbine blade alloys (1940 – 2010) [7]. The temperature capability here corresponds to 1000 hrs. of creep life that results in 1% strain at that temperature.

2.1.1 Microstructure and composition

Superalloys contain a number of different alloying elements to attain the desired property level for hot rupture strength, fatigue resistance, and creep strength. Typically high-gradient casting (investment casting with high and well controlled thermal gradient) is used to develop customized and fine structured superalloys, although some wrought superalloys are also in use. Properties of the superalloys are controlled by the presence of different phases in the microstructures such as the close packed phases (γ', γ'', and η etc.) and the carbides (MC, M_6C, $M_{23}C_6$ where M denotes the metal).

Nickel-base superalloys primarily consist of intermetallic precipitates in a solid solution of face-centered cubic (FCC)-Ni (nickel) matrix or γ matrix. The intermetallic precipitates are known as γ', and a high volume fraction of γ' (up to 70%) is typically added to improve the strength of the γ-matrix. The γ' phase is chemically represented as Ni_3(Al, Ti), with Al (aluminum) and Ti (titanium) replacing the corner Ni atoms in an FCC structure and forming a coherent phase with FCC-L_{12} phase. The secondary phase precipitates retard dislocation motions by forming anti-phase boundaries and locking the dislocations at high temperatures [9, 10]. Figure 3(a) shows the crystal structure and arrangement of γ and γ' phases in nickel-base superalloys.

While Al, Ti, and Ta (tantalum) are used as precipitation-strengthening or γ' forming elements, Cr (chromium) is added to improve the corrosion resistance. Mo (molybdenum) and W (tungsten) are used to increase the melting temperature of the alloy [1]. Al can also build a

protective Al_2O_3 layer and improve the corrosion and oxidation resistance. W, Nb (niobium), Ta, and Mo improve the creep strength of the alloy, as they diffuse slowly because of their higher atomic weight, thus imparting more microstructural stability. Some of these elements partition to the γ matrix while others partition to the γ′ precipitate [11]. Re (Rhenium) is added to retard coarsening of the γ′ precipitate. It generally partitions to the γ matrix. C (carbon) and B (boron) are used as grain boundary strengthening elements for EQ-cast superalloys as they drive precipitation of carbides and borides. However, they also reduce the melting point and high-temperature microstructural stability of the alloy.

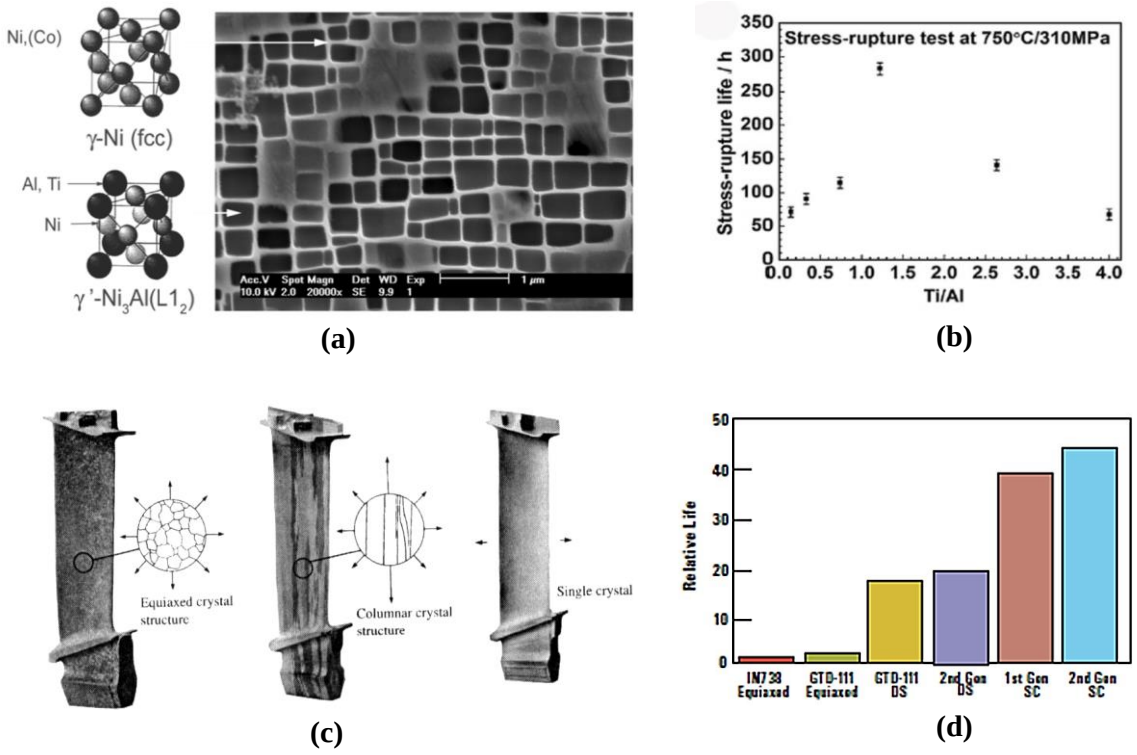

Figure 3. (a) γ matrix and γ′ precipitate in CMSX-4® superalloy [12], (b) variation of stress-rupture life (in hours) as a function of Ti/Al ratio [13], (c) EQ, DS and SX microstructure in turbine blade [14], and (d) increase in bucket life due to change in morphology and Re content.

Careful element addition is necessary in superalloys, since some elements facilitate the

formation of brittle plate-like μ, σ, or Laves phases. The μ phase is typically of rhombohedral crystal structure and is found in alloys with excess percentage of Mo or W. The σ phase is a tetragonal phase that forms after prolonged exposure to a temperature between 540 ^{o}C and 980 ^{o}C. The Laves phase is hexagonal and also forms due to high-temperature exposure. These phases are topologically close-packed (TCP) phases and cause reduction in rupture strength and ductility [1]. Cr is a potential brittle σ phase former. Hence it is increasingly being put in the coating material rather than the superalloy for the blade itself [11]. However, the reduction in Cr wt. % results in the loss of solid-solution-strengthening and oxidation resistance.

Table 1. Role of alloying elements in nickel-base superalloy [11].

Elements	Effect on microstructure and properties
Co, Cr, Fe (iron), Mo, W, Ta, Re	Participate in solid-solution strengthening
Ti, W, Mo, Ta, Nb, Hf, Cr	Form carbides
C, N	Form carbonitrides
Al, Ti	Form γ′ phases
Co	Raises solvus temperature of the γ′ phase
Re	Retards γ′ phase coarsening
Nb, Ta	Form γ′′ phases [Ni_3(Nb, Ta)]
Al, Ti, N	Form hardening precipitates and/or intermetallics
Al, Cr, Y	Increase oxidation resistance
Y (yttrium), La (lanthanum), Ce (cerium)	Increase oxidation resistance
La, Th (thorium)	Improve hot corrosion resistance
Cr, Co, Si (silicon)	Increase sulphidation resistance
B, Ta	Improve rupture strength
B, C, Zr (zirconium), Hf (hafnium)	Refine grain
Hf	Improves ductility at intermediate temperatures

The addition of Mo for solid-solution-strengthening and Al for oxidation resistance initially compensated for the reduced Cr, but it was found that Cr levels around 1.5 wt.% were

needed to avoid the onset of hot corrosion [15]. Mo levels above approximately 3.5 wt.% were also found to be harmful to hot corrosion resistance, leading to the substitution of some amount of Mo by other refractory metals such as W, Ta, or Nb [16]. Grain boundary carbides play a major role in the control of creep and fracture behavior and can be modified by heat treatment and by addition of minor constituents such as B and Zr [6]. Hf is also a strong carbide former and is added to improve grain-boundary ductility [17]. Table 1 shows the role of various elements on the properties of nickel-base superalloys.

2.1.2 Advantages

The Ti/Al ratio has great influence on the high-temperature corrosion resistance and mechanical properties of nickel-base superalloys [13]. The precipitate of β-NiAl in the γ matrix for alloys with low Ti/Al ratios leads to the propagation of cracks in the grain interior. In contrast, a high Ti/Al ratio leads to the precipitation of η-Ni_3Ti at grain boundaries, which weakens the strength of the grain boundaries. The precipitates of both the β-NiAl and the η-Ni_3Ti phases are harmful to the stress-rupture life, and a peak stress-rupture life appears at intermediate values of the Ti/Al ratio, as shown in Figure 3(b). The rupture strength also depends on the heat treatment procedure involved. The goal of the engine manufacturer is to obtain a high longitudinal rupture strength while maintaining an adequate transverse rupture strength. The method of determining the heat treatment cycle to optimize the rupture strength is an essential procedure in the development of superalloys [18].

Despite the superior properties attained by optimizing the alloying elements, nickel-base superalloys are still tested in the extreme performance limit when it comes to gas turbine applications. As mentioned earlier, turbine components cast with an EQ or polycrystalline

microstructures are prone to failure because they contain some grain boundaries that are transverse to the longitudinal direction of the blades or to the main axis of stress when a blade is rotating in an engine. EQ grains are prone to form voids at the grain boundary that are transverse to the longitudinal direction.

Hence to alleviate this problem, DS superalloys were introduced around 1960 [19]. The resultant oriented grain structure runs parallel to the major axis of the part and contains no transverse grain boundaries. The elimination of these transverse grain boundaries imparts additional creep and rupture strength to the alloy by reducing creep void formation, and the orientation of the grain structure provides a favorable modulus of elasticity in the longitudinal direction to enhance fatigue life. By directionally solidifying the alloy GTD-111, an increase of approximately 23 ºC (40 ºF) in creep strength and an increase of approximately 10X in fatigue life was realized [19].

The increase in creep strength and fracture toughness can be further enhanced by casting the blade with SX microstructure that does not contain any grain boundary at all. This SX microstructure also allows removal of C and B that would otherwise reduce the melting temperature and the fatigue life of the alloy. As an example, Rene´N5, a SX-cast alloy, shows an increase of more than 35 ºC (~ 60 ºF) in creep strength and 2X to 3X increase in fatigue life compared to DS GTD-111. Figure 3(c) shows the grain structures of EQ, DS, and SX turbine blades.

SX microstructures can be further improved by adding Re. The "first-generation" SX superalloys (e.g. PWA 1480) do not contain Re and offer 25 – 50 ºC improvement over RIT and 1% improvement in creep life. The "second-generation" SX superalloys (e.g. CMSX-4®)

contain 3% Re and offer 30 – 35 ºC improvement in RIT. The "third-generation" SX superalloys (e.g. CMSX-10®) contain more than 5 wt. % Re. This further enhances the creep-rupture strength and improved the RIT by 30 ºC, enabling use of un-cooled blades at 1200 ºC, thus causing increased efficiency by reducing cold air requirement [19]. Figure 3(d) shows the improvement in the low-cycle- fatigue (LCF) life of the turbine buckets by introducing the SX microstructure and increasing the Re content.

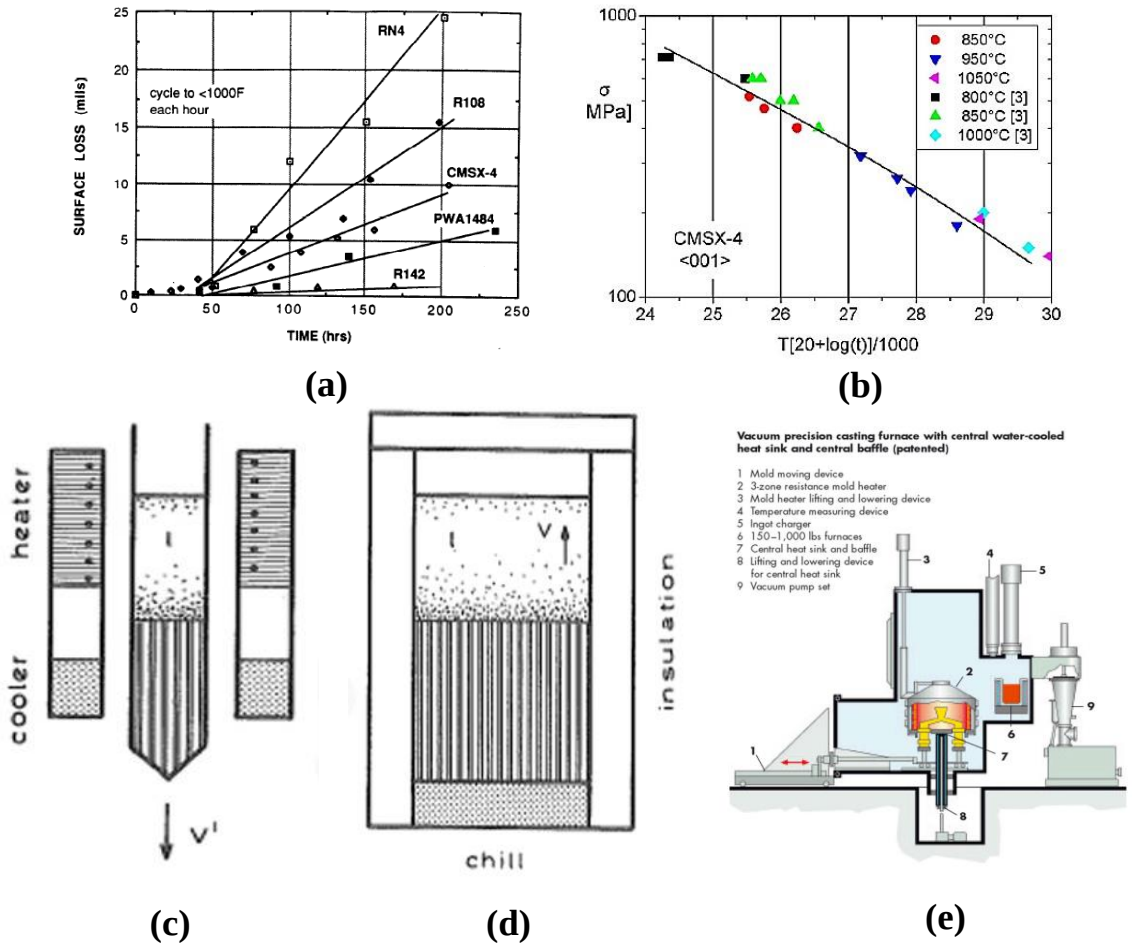

Figure 4. (a) Comparison of oxidation resistance for different superalloys at 2150 ºF and at Mach 1 velocity [18], (b) Larson-Miller plot for CMSX-4® with at different temperatures [20]. Bridgman casting for (c) SX superalloy and (d) DS superalloy [21]. (e) Schematic of the LMC process [22].

High velocity oxidation resistance is a desirable characteristic of the nickel-base

superalloys. Pursuit of this goal has led to the development of DS René 142 from René 150. DS René 142 also contains 3 wt. % Re for solid solution strengthening. The presence of 2.2 wt. % V (vanadium) was the primary reason for poor oxidation resistance in René 150. Optimization of Ti, Al, and Cr content and elimination of V provided the exceptional oxidation resistance in René 142. The oxidation test verified only 1 mil of metal surface loss at 2150 ^{o}F with velocity at Mach 1 [18]. Figure 4(a) compares the oxidation resistance of different superalloys. The surface loss in René 142 is clearly 5 – 25 times smaller than those of different "second-generation" superalloys.

Superalloy components need to endure impact loadings against foreign objects during their service at high temperatures; thus high impact toughness is also required to prevent catastrophic failure. A study of M951 alloy based on Charpy test concluded that MC carbides are the crack initiation sites [23]. The nucleation, growth, and coalescence of dimples formed at the fracture surface are found to be the major fracture feature at elevated temperature. Superalloy components are also subjected to prolonged loading at high temperature. Hence, high creep resistance is a very important criterion for superalloys. Nickel-base superalloys last longer at elevated stress and temperature levels compared to Fe-Ni and Co-base alloys.

The grain structure of the superalloy also contributes to the creep properties. SX microstructures provide higher stress rupture strength. The Larson-Miller parameter predicts the lifetime of material with respect to time and temperature; this is done by using a correlative approach based on the Arrhenius rate equation. The value of the parameter is usually expressed as shown in Equation 2.

Equation 2. Larson-Miller parameter.

$$LMP = T(C_t + \log t)$$

Here, C_t is a material specific constant often approximated as 20, t is the stress-rupture time in hours and T is the temperature in Kelvin [24]. The Garofalo sine–hyperbolic expression suitably correlates stress dependence for the entire stress regime, as it reduces to a power-law relationship at low stresses and becomes exponential at higher stress limits [25]. Scholz et al. studied the creep behavior of SX CMSX-4® in the temperature range 850 ºC to 1050 ºC [20]. Figure 4(b) shows the Larson-Miller plot obtained for [001] crystal growth direction (i.e. growth direction of the primary dendrites) and demonstrates the creep response for CMSX-4®. Egly et al. also investigated the fatigue and lifetime effects for CMSX-4® resulting from thermo-mechanical loadings tests that used different strain paths and different phase shifts between temperature and mechanical strain [26].

2.1.3 Fabrication

Investment casting is the traditional method for creating superalloy components. However, the complexity of the casting process increases as the desired microstructure progresses from EQ to DS and to SX casting. For EQ components, the molten metal is poured into a ceramic mold at a pressure below 10^{-2} torr. The entire process is conducted in vacuum to prevent the highly reactive elements in the superalloys from reacting with oxygen and nitrogen in the air [27]. With proper control of metal and mold thermal conditions, the molten metal solidifies from the surface toward the center of the mold, creating an EQ structure. To prevent the formation of shrinkage pores, care is taken to allow proper feeding of molten metal to the casting while it solidifies.

DS and SX components are typically investment cast using either a Bridgman or Stockbarger technique. In these techniques, the mold is vertically withdrawn at a low speed from a casting furnace or induction heater at a controlled rate (on the order of several centimeters per hour), thus allowing propagation of the solid-liquid interface and elongation of the grains along the direction of withdrawal. Normally, this results in a DS microstructure, but if a seed crystal or seed selector is placed at the bottom of the casting mold, these techniques can produce SX microstructures [14]. Figure 4(c) shows a Bridgman casting process where the crucible is drawn downwards at a uniform rate. The cooling rate is the product of the temperature gradient and the crucible velocity. The other process shown in Figure 4(d) is for DS components, and the microstructure is no longer uniform. Here the growth rate and the temperature gradient decrease as the distance from chill increases.

To improve the productivity of SX casting, liquid metal cooling-assisted casting (LMC) has been adopted [22]. Low thermal gradient, slow growth rate and long solidification time restrict the use of the Bridgman technique in the industrial environment. In LMC, a liquid metal such as Al/Sn (tin) is used as cooling medium. The main advantage of LMC is the increased thermal transfer due to the conductive cooling as compared to the radiative cooling in the Bridgman process. The liquid metal is in equal contact with every individual mold, which enables greater part to part consistency. The increased withdrawal rate due to the higher thermal gradient decreases the time for mold-metal reaction and increases the rate of production. Figure 4(e) shows the details of the LMC process [22].

2.2 Repair techniques

The superalloys that are investigated in this dissertation are all precipitation-hardened

alloys or γ′ formers. These alloys contain significant concentrations of Al and Ti. The improvement in properties comes at the cost of processing difficulty, primarily evidenced by crack formation. Nickel-base superalloys are extremely difficult to weld due to their susceptibility to heat-affected zone (HAZ) and weld metal cracking during fabrication, post-weld heat treatment (PWHT), and subsequent operation [28].

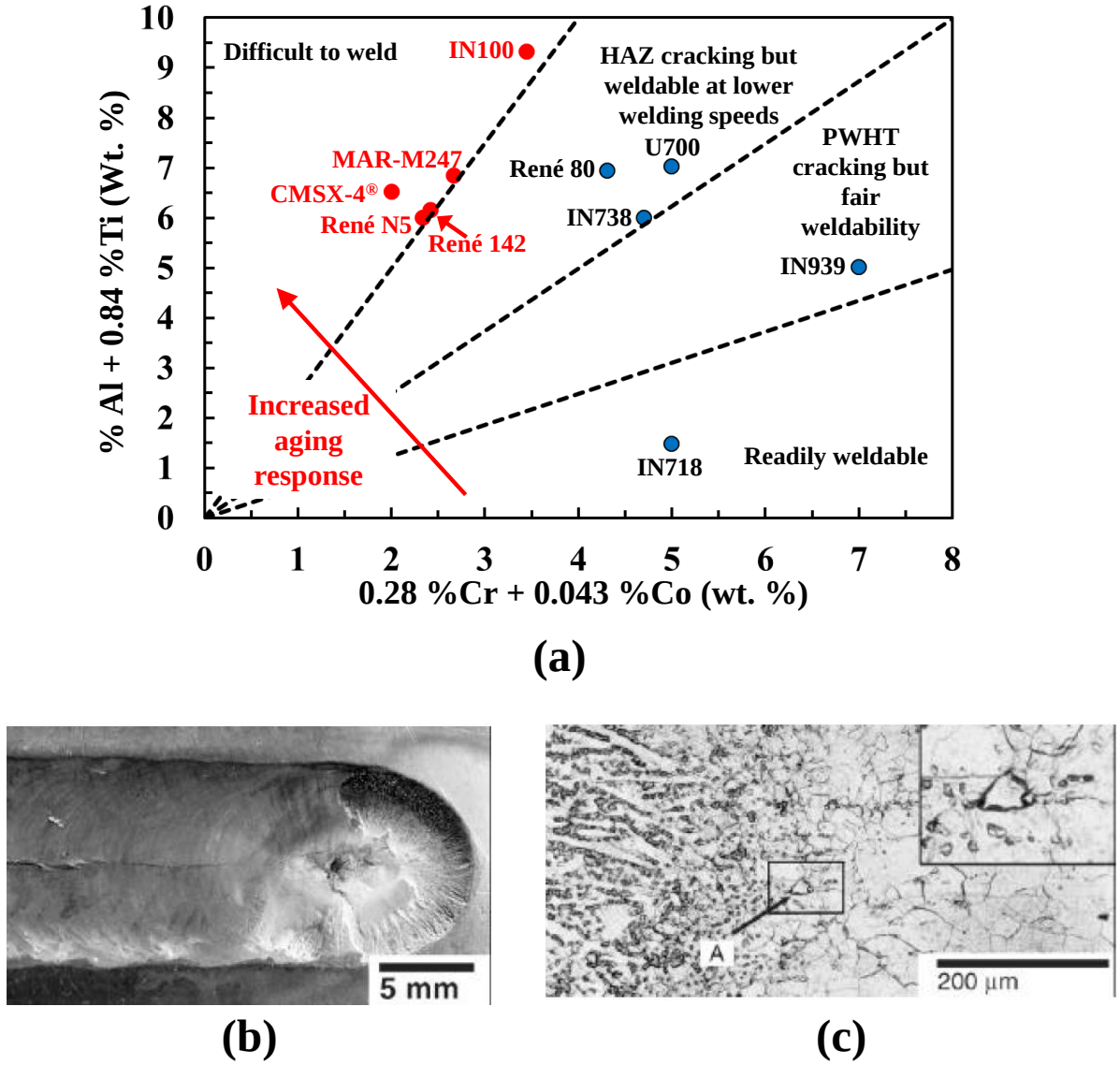

Figure 5. (a) Modified weldability assessment chart after considering the effect of Cr and Co [28]. The alloys that are to be investigated in the proposed research are marked in red. Example of (b) solidification cracking in IN718 during gas tungsten arc

welding (GTAW) and (c) hot tearing in IN718 during GTAW.

The susceptibility to strain-age cracking and the alloy weldabilty are often qualitatively described for nickel-based superalloys by plotting Al vs. Ti content in the alloys [1]. An alloy is considered "difficult to weld" if the total Al + Ti content exceeds 4 wt. % [29]. A more generalized approach for characterizing weldability involves tracking the Cr and Co content in addition to the Ti and Al content in the superalloy [28]. Figure 5(a) shows the weldability assessment of superalloys based upon compositions of %Al + 0.84 %Ti (in wt. %) versus 0.28 %Cr + 0.043 %Co (in wt. %) [3]. The alloys to be investigated in the present research fall in the "difficult-to-weld" category as shown in Figure 5(a). Repair attempts on modern superalloys started in the late sixties. Different welding techniques such as activated diffusion bonding involving vacuum furnace brazing, and diffusion and aging heat treatments were attempted [22]. The state-of-the-art processes for repair of turbine blades are still based either on the welding or the AM-based approaches.

2.2.1 Welding-based methods

The most commonly used welding-based processes are gas tungsten arc (GTA) welding or tungsten inert gas (TIG) welding, electron beam (EB) welding, and laser welding. Each of these processes is typically subjected to the same limitations in producing specified microstructures such as DS or SX and crack formation [29-31]. Stueber et al. tried to minimize the crack formation by heating the weld adjacent zone above the ageing temperature and maintaining it below the incipient melting temperature [32].

United Technologies attempted a two-step process for the welding. The first step deposited filler metal into the repair, and in the second step, a broad and shallow melt pool was

created by using a defocused beam to obtain epitaxial morphology from the substrate to the top of the deposit [33]. Hence, this method is typically suited for local repair on simple contours. Different methods have since then been tried in order to repair components having complex shapes [34-36]. Laser welding and EB welding of superalloys such as CMSX-4® were shown to be less susceptible to cracking and stray grain formation than GTA welding.

2.2.2 AM-based methods

Although various metal AM processes are based upon the same principle of layer-wise material consolidation, each is distinct with regard to, e.g., energy source type, processing techniques, operating conditions, usable materials, and metallurgical consolidation mechanisms [5]. IN625 was processed using selective laser sintering (SLS) and SLS/HIP (hot-isostatic processing) methods to produce a number of cylindrical specimens. Micrographs of SLS-processed and HIP-post processed IN625 demonstrated EQ morphology [5]. The direct SLS process was also used to manufacture MAR-M247/CBN/alumina cermets for a typical high-pressure turbine blade tip sealing system that showed directional epitaxial growth. In addition to SLS, direct metal laser sintering (DMLS) was used to sinter IN625 powders onto a steel substrate, resulting in columnar dendritic microstructure [5].

IN718 was processed by the selective laser melting (SLM) process to produce columnar microstructural morphology composed of primarily [200]-textured γ″ phase precipitate columns. In other uses of IN718 processing, similar epitaxial behavior was obtained [5]. Mumtaz et al. processed Waspaloy® using SLM. However, the deposit was plagued by long and short cracks. SLM was also used to consolidate MAR-M247 powders on IN718 polycrystalline flat sheets, revealing epitaxial growth in the [001] direction from the melted

substrate to approximately half the height of the deposits [5]. Above that height, the [001] dendritic front bowed toward the [100] direction. A dendritic-EQ transition appeared near the free surface of the deposit. SLM was used in the production of columnar dendritic structures along the build direction for the CM247LC alloy system [5].

Various laser metal deposition (LMD) processes were extensively used to process different nickel-base alloy systems [5]. A series of crack- and porosity-free IN625 samples were successfully fabricated using the direct metal deposition (DMD) process; the as-deposited microstructure consisted of columnar dendrites growing epitaxially from the substrate. SX deposits of René N4 and René N5 substrates were produced using the DMD process; the deposits were observed to grow epitaxially from the substrate. IN718 was processed using laser rapid forming (LRF) and consisted of columnar dendrites that grew epitaxially from the substrate parallel to the deposition direction, with a thin layer at the top of the sample where the dendrites grew along the laser scanning direction, referred to as direction-changing dendrites [5]. The LMD process was used to fabricate components made of René 41 having fine DS microstructure. Liu and DuPont processed the IC221W alloy using LENS® and produced deposits consisting of three distinct regions: epitaxial dendritic growth in the [001] direction, epitaxial dendritic growth in the [100] direction (the beam traveling direction), and stray grains (SGs).

Epitaxial laser metal forming (ELMF) was extensively used to process CMSX-4® that showed excellent epitaxial SX growth in the [001] direction with a very thin layer of EQ region near the top [5]. Epitaxial M-Cr-Al-Y growth was obtained on a CMSX-4® substrate by using laser cladding processes. Here M represents Ni, Co, or Ni-Co. Similar results were obtained for Ni-Cr-Al-Y depositions on SRR99 substrates [5]. An LMD-based microlaser-aided AM

process was used to produce crack-free IN100 samples that showed columnar dendrites growing epitaxially from the partially remelted grains of the previously deposited layers. Laser powder buildup welding that uses a combination of the welding and cladding techniques showed epitaxial growth of MAR-M002 on a directionally solidified MAR-M002 substrate [5].

Electron beam melting (EBM) process was used to process IN625 (EQ), IN718 (EQ), and René 142 (DS). Although both IN625 and IN718 exhibited directional precipitate architectures within the EBM melt zones, in the EBM-fabricated IN625, these epitaxial columnar precipitates were γ″ [body-centered-tetragonal (BCT)] Ni_3Nb disk platelets coincident with the Ni-Cr (FCC) [111] planes [5]. In the IN718 deposit, the epitaxial γ″ (BCT) precipitate disk platelets were coincident with the Ni-Cr (FCC) [100] planes. SX CMSX-4® was also processed through EBM, and the resulting microstructure grew epitaxially from the substrate [5]. The arc-based welding process shaped metal deposition (SMD) was used on IN718, in which epitaxial deposition was observed. The 3D micro welding (3DMW) process was used to produce epitaxial multilayer objects from IN600 powder [5].

2.2.2.1 *Effects of processing parameters*

Prior research showed strong influence of process parameters on the mechanical properties and microstructural transitions of the weld bead/deposited superalloy. Rush et al. studied the effect of process parameters on the cracking behavior of René 80 deposit using cold metal transfer with IN625 as filler alloy [37]. Welding power was shown to have high significance on the level of cracking, whereas welding speed had little effect. When laser welding was used, it was shown that the power and spot size were more crucial to the material cracking than the travel speed. It was indicated that the weld bead geometry had high

significance over the occurrence of cracking, with a relationship between welding power, weld bead geometry, and stresses controlling the occurrence and magnitude of cracking.

Lippold et al. studied SX CMSX-4® and analyzed the susceptibility to cracking as a function of process parameters for electron beam welding, and they compared the results with those obtained for GTAW. It was shown that electron beam processes were less prone to cracking [38]. Anderson et al. studied the formation of stray grains for GTAW, laser beam and electron beam welding processes and concluded that with the use of localized heat in the laser beam and in the electron beam processes, stray grain formations are reduced [39].

2.2.2.2 *Defect formation*

Different forms of cracking present challenges in the repair or processing of nickel-base superalloy components. They can be primarily distinguished as solidification cracking, grain boundary liquation cracking/hot tearing, strain-age cracking (cold cracking) and ductility dip cracking. Solidification cracking occurs within the newly formed weld bead when the mushy, two-phase liquid-solid region experiences tensile stresses and the high fraction of solid present (typically solid fraction > 0.9) restricts the flow of liquid metal to backfill the interdendritic regions. The interdendritic regions are torn apart by tensile thermal stresses generated behind the weld bead as it progresses. Formation of solidification cracking is promoted by a wide solidification range for the alloy and low welding traverse speeds. Figure 5(b) shows one example of such cracking along the centerline of a weld bead in IN718. This form of welding defect in nickel-base superalloys can be avoided by optimizing the welding procedures.

Local or partial dissolution of grain boundary phases leads to the formation of low melting point eutectics and melting of grain boundary regions, thus, leading to grain boundary

liquation cracking or hot tearing when the liquid film in HAZ fails under tensile stress. Typically the intermetallic carbide compounds (MC and M_6C) and different secondary phases (Laves- and σ-phases) contribute to partial dissolution, and hence, reduction of the melting point. Different impurities such as sulfur, boron, and phosphorus act to suppress the eutectic melting temperature and consequently increase the HAZ fissuring susceptibility.

A second mechanism known as constitutional liquation particular to precipitation-hardened materials occurs when a constituent particle such as TiC reacts with the surrounding matrix causing localized melting. Creation of smaller grains exposes more boundary area and lowers the strain value, resulting in reduction of hot tearing. It is also verified that welding conditions such as heating rate affect the formation of this kind of cracks. Higher welding power results in more area being liquated increasing the tendency of HAZ cracking. Figure 5(c) shows an example of hot tearing in HAZ.

In traditional casting processes, two different types of porosities are typically observed. During solidification, a third gas phase may form resulting in pores. Such pores are called casting defects. Pores may also be formed due to inadequate supply of liquid to solid and partitioning of solutes such as hydrogen, nitrogen, and oxygen [40]. In laser repair processes, similar types of porosities are observed. The deposit sometimes shows porous structure due to gas entrapment. Because of insufficient supply of liquid due to the resistance in mushy region, pores may be formed in the interdendritic region leading to cracks [41]. In powder-bed AM processes, pores may also be formed if the feedstock powder contains internal porosity [42].

2.2.2.3 *Microstructure transition*

A DS/SX deposit formed through an additive process can be characterized by several

microstructural features such as the primary dendrite arm spacing (PDAS), the columnar-to-equiaxed transition (CET), the oriented-to-misoriented transition (OMT) and the presence of stray grains (SG). An increase in the dendrite arm spacing adversely affects the high-cycle fatigue life. Fatigue cracks were found to originate at shrinkage porosity and the largest pores are correlated with a large PDAS [43].

During solidification, the solidified region acts as a heat sink, and the temperature gradient ahead of the solidification front decreases resulting in a change from the SX microstructure to an EQ microstructure. This change is referred to as CET. CET limits the epitaxial SX growth and makes the deposit near the top surface EQ in nature [44]. A second solidification phenomenon, known as OMT occurs when there is a change in the direction of the temperature gradient in the solidifying metal. This occurs primarily because of the competition between the possible columnar growth directions [45]. Both CET and OMT are critical to the quality of the SX deposit as they limit the SX height. Existing literature reveals that the local inhomogeneity in the temperature gradient and the solidification velocity or the presence of broken dendrite arms and subsequent convection of those broken pieces acts as sources of new nucleation sites that result in the formation of SGs. Due to segregation of γ/γ' eutectics, a liquid film forms around the SG boundary. Such SG formation results in higher grain boundary wetting making the material prone to cracking [46].

2.3 Modeling schemes

The modeling approach involved in solving the laser-material interaction started with the analytical modeling of thermal distribution due to a localized moving heat-source. Recent simulations tried to solve the detailed physics of AM processes numerically. However, to

reduce the computational burden, often, the analysis is restricted to a domain, such as agglomeration of powder, tracking of a melt pool or modeling a single bead scan with constant material properties.

2.3.1 Analytical modeling

Rosenthal first proposed a solution of the temperature field due to a moving point heat source over a solid body [47]. Since the experimentally observed melt pool was ellipsoidal, Christensen et al. tried to improve on it and their results suggested an elliptic melt pool in the beam travel direction and a transverse semi-circular cross-section [48]. Goldak et al. in their research assumed a double-ellipsoid weld pool shape that consisted of the front and rear ellipsoid quadrants [49]. Liu et al. used this approach and formulated the 3D melt pool shape by assuming a non-right angle value of these angles [50].

2.3.2 Numerical modeling

The analytical models cannot take into account the melting and solidification of a complex alloy system such as superalloys. An accurate representation of the heat-source is also difficult with the analytical models. Most of the analytical models cannot incorporate temperature dependent thermo-physical property variation. Hence, significant efforts have been devoted to simulating the flow-thermal-microstructure evolution in AM processes using advanced numerical models.

2.3.2.1 *Fluid dynamics modeling*

Approaches based on finite element methods (FEM) and finite volume methods FVM) were employed for the thermal modeling of the laser-material interactions [51-57]. Investigation of the effect of fluid convection in the laser melt pool started in mid-1950s [58].

A CFD-based model allows modeling of convection inside the melt pool [59, 60]. A coupled flow-thermal model was developed in order to simulate the conditions inside the laser melt pool while considering surface tension driven flow known as Marangoni convection (or Bernard-Marangoni convection). The presence of a gradient in surface tension (due to temperature gradient) causes the liquid to flow away from regions of low surface tension. This extends the melt pool laterally and makes it shallower [61, 62]. Marangoni convection was found to have a major influence on surface rippling [63]. Oreper et al. developed a two-dimensional convection model incorporating buoyancy, electromagnetism, and surface tension driven gradient forces [64]. The surface tension gradient was shown to have the dominant effect on determining the flow pattern. Different flow-zones in a weld pool were identified to characterize the flow vortices and the stagnant region [65].

The characteristics of the flow vortices for different power and welding speed were obtained by Paul et al. [66]. In this study, a portion of the vaporized material was allowed to condense in the interior surface of a hollow quartz tube. The composition of the condensate was used to determine the relative rates of vaporization of the individual elements and the effective weld pool temperature for vaporization. Recently, the shape of the deposited layers was predicted by using a modified immersed boundary method with a finite difference scheme [67]. A level-set method was been attempted to track the free surface motion of the molten pool for multilayer cladding of SX deposits [68].

2.3.2.2 *Microstructure modeling*

The emphasis on the prediction of solidification microstructure started in the seventies [26]. A considerable amount of attention has been given to characterize the solidification microstructure of DS/SX deposits. Microstructure modeling of SX deposits through AM

processes was done comprehensively [69, 70]. However, it has been established that these models cannot provide a precise prediction for PDAS and are only useful in obtaining a qualitative estimate for PDAS [71].

The theoretical basis of the CET was first proposed in the eighties by Hunt by considering the instability criterion of the columnar front [72]. Hunt simplified the solution by assuming a pseudo-binary alloy composition. Later on, the accuracy was improved by taking into account the composition and the associated liquidus temperature profile of the multicomponent dendrites [73, 74]. The Rappaz modification took into account the multi-component dendrites instead of pseudo-binary alloy composition and the dependence on dendrite orientation. This model was applied to predict the CET [75]. Gäumann et al. used a depth-weighted average of G^n/V (where V is the solidification velocity, G is the temperature gradient, and n is a material constant) to characterize a single weld pool [44, 69]. Later, Vitek et al. applied the Rosenthal solution to compute G and the melt pool shape [76]. Recent simulations used a complete CFD-based 3D model for a single-bead scan pattern, allowing the variation of G and V over the melt pool coordinates [51].

The OMT is caused by a change in the direction of the temperature gradient in the solidifying metal deposit. This occurs as the substrate becomes increasingly hot toward the end of the laser scan, resulting in a growth competition between the columnar grains. OMT in a single bead scan was predicted by finding the minimum dendrite growth velocity [45, 50, 77]. This leads to minimum undercooling at the dendrite tip [77]. Hence, this process essentially relies on finding the direction that is most closely aligned to the heat flux direction.

2.4 Summary

This chapter summarizes the background on nickel-base superalloys and their repair technologies along with a focus on predicting solidification characteristics for these material systems obtained through AM-based processing. The existing state-of-the-art repair technologies demonstrate limited capability in restoring superalloy components having high-γ' content. The key conclusions are:

- Nickel-based superalloys are prone to various types of cracking namely solidification cracking and liquation cracking. Hence, it is of immense interest to develop a process that can produce crack-free deposits.

- DS/SX deposits, in particular, suffer from additional defects such as loss of epitaxy due to CET, OMT, and SGs. Without SX morphology, maintaining the creep strength of the original component will not be possible. Hence, a capability in fabricating epitaxial deposits is desired in AM-based processing of nickel-base superalloys.

- Experiments are time-consuming and expensive. Hence, a high-yield predictive model is desired to assess the effects of process parameters on flow-thermal-microstructure evolution. Such models need to be tied up to the experimental optimization process to develop process maps for different superalloys.

- The parts built through AM-based processing often exhibit microstructures and properties that are significantly different from those processed through conventional deformation processing, solidification, powder metallurgy or other approaches. Hence, a thorough investigation is desired using advanced materials characterization techniques in order

to characterize the deposits obtained by AM.

- The superalloys exhibit a multitude of property variation as a function of their composition. However, it is of immense interest to evaluate the effects of elemental composition on the deposit characteristics as obtained through AM-based processing.

Chapter 3: Overview of scanning laser epitaxy (SLE)

Scanning laser epitaxy (SLE) is a direct descendant the selective laser sintering (SLS) process developed in the late 1990s at the University of Texas at Austin [78]. SLS starts with a CAD model of the part to be built. The CAD file is sliced at discrete intervals in the build direction and the resulting cross-sections are stored sequentially in a "build file". Scanning algorithms are devised to control the path of the laser beam. The powder bed is sintered conforming to the geometry requirement for the layer. Next, the power bed is lowered by a distance equal to the layer thickness and a fresh layer of powder is deposited by a roller mechanism. The next cross-section is then laser-sintered to fuse it to the underlying layer and thus, by sintering layer upon layer, the entire part is fabricated. The components created through direct SLS processes are fully dense or nearly fully dense, and can be post-processed through the use of HIP to achieve full density. SLE extends the work on SLS facilitating the direct construction of net-shape engine-ready components without requiring HIP for microstructure densification.

SLE is a LPBF-based AM process that creates nickel-base superalloy structures through controlled melting of alloy powders onto like-chemistry substrates. The goals of SLE process development are: a) the additive repair of damaged turbine engine hot-section components and b) the fabrication of completely new three-dimensional superalloy components with as-desired microstructure. Thus, the SLE process allows for the manufacture and repair of metallic parts with specified microstructure as well as the manufacture and repair of components with

functionally graded microstructures. An overview of the SLE process is shown in Figures 6(a) and 6(b). In SLE, a tightly focused laser beam is guided by high-speed galvanometer scanners allowing for precise control over the amount of energy being applied to the top of the pre-placed powder bed. Under the proper operating conditions and with sufficient amount of substrate melt-back, the melted powder undergoes epitaxial solidification. The solidified microstructure in the new deposit, thus, follows the microstructure of the underlying substrate, allowing for EQ, DS, and even SX growth.

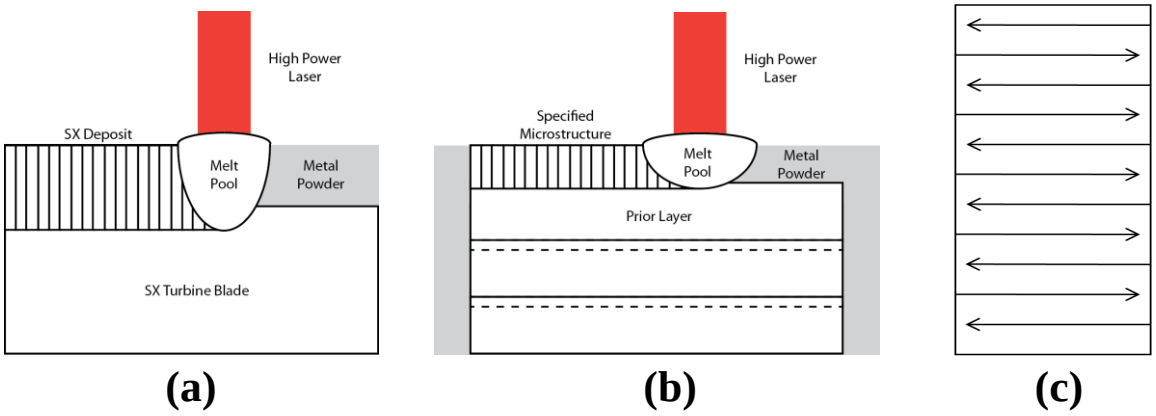

Figure 6. SLE process overview for (a) a single-layer repair process and (b) a multi-layer fabrication process. (c) Schematic of the raster scan pattern adopted in SLE [4, 22].

The raster scan pattern with alternating scan vectors is illustrated in Figure 6(c). In SLE, after each pass the laser moves over by the raster scan step distance and starts to move in the opposite direction. The step distance or the scan spacing is chosen to ensure that there is an optimized amount of overlap between each successive scan pass. Such optimization ensures both pre-heating of the powder to enable complete melting and post-heating of the deposited layer to reduce the thermal stresses and related cracking. The thermal control achieved in the process allows the creation of previously unattainable SX and DS microstructures with AM. With an optimized set of process parameters, fully consolidated and crack-free three-

dimensional parts with region-specific microstructure are achievable.

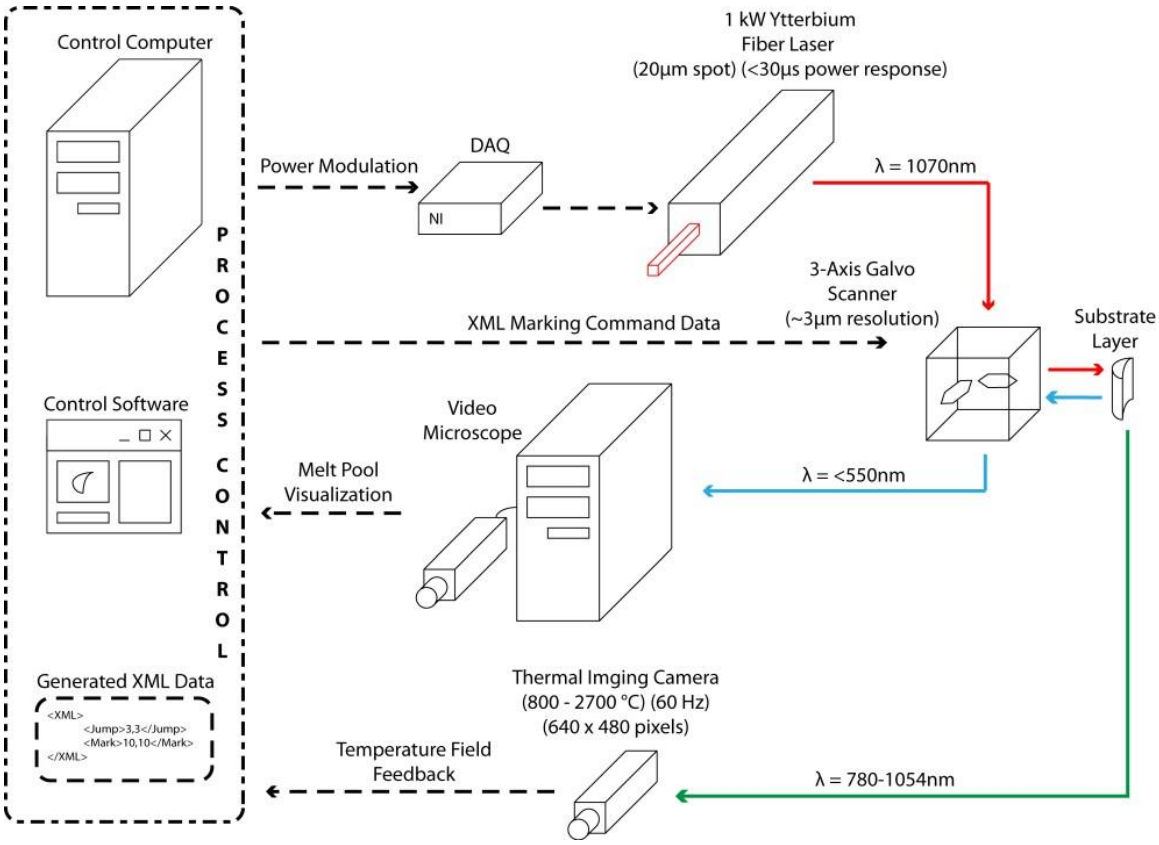

Figure 7. Overview of the SLE process [4].

This chapter provides an overview of the hardware and software implemented for the SLE process to successfully fabricate components. It also describes the experimental procedure followed to verify, validate, and qualify the created components. Instead of using a commercially available machine, a custom designed and built machine is utilized to enable easier access and broader level of control over the process. Figure 7 shows the schematic of the SLE process. A control computer is responsible for the pre-set scan path generation and process parameter input, which is transmitted via a data acquisition (DAQ) card to the laser and scanner. A video microscope enables visualization of the SLE process in real time while

a thermal imaging camera allows determination of the melt pool and records its average temperature. This response signal, when coupled with feedback control allows real-time on-the-fly regulation of the melt pool temperature by computer control of the laser power.

3.1 Experimental setup

The key pieces of hardware involved in the SLE process are a high-power 1kW Ytterbium fiber laser, a 3-axis galvanometer scanning system, a controlled atmosphere processing chamber, a thermal imaging camera, and a melt pool video microscope.

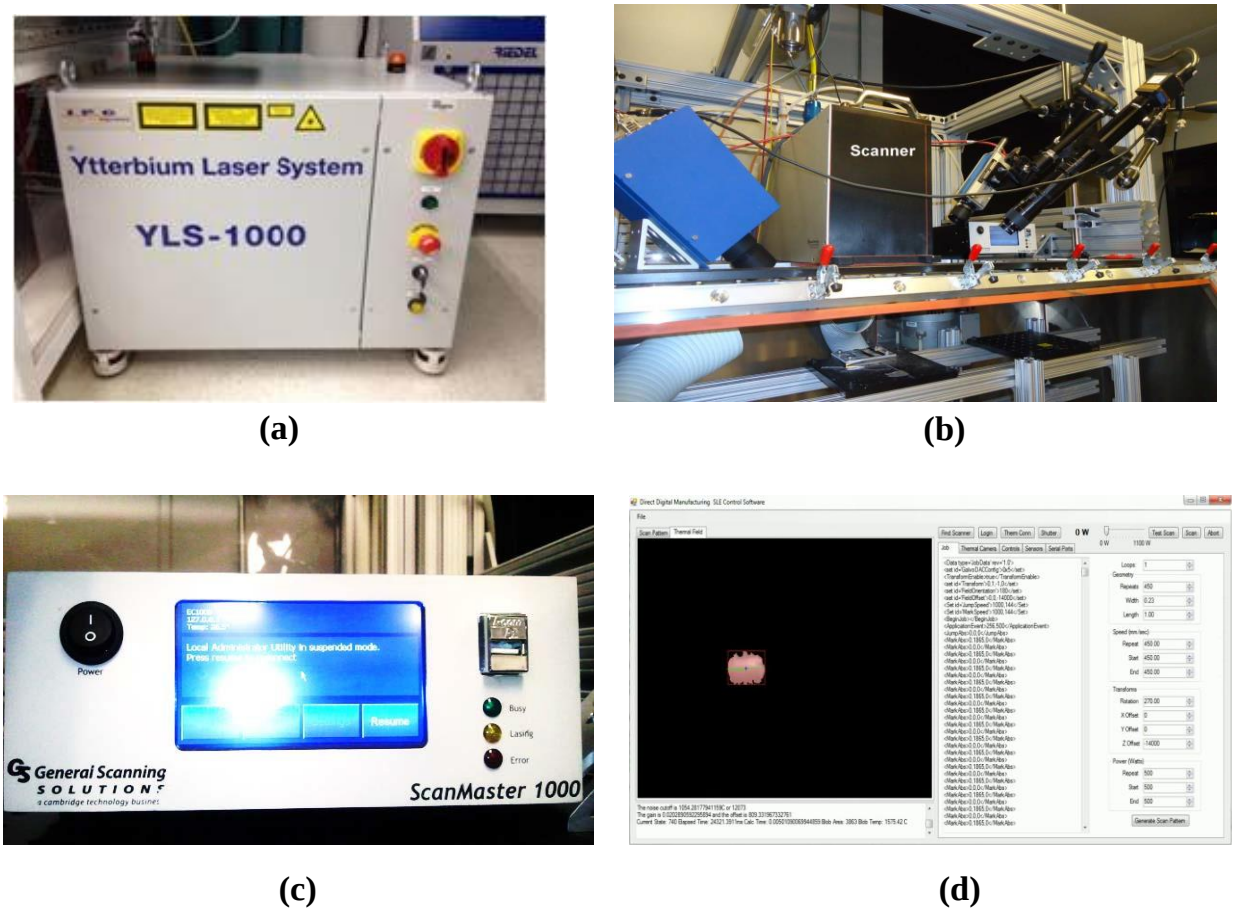

(a) **(b)**

(c) **(d)**

Figure 8. (a) The YLS-1000 fiber laser, (b) scanner arrangement on top of the glovebox, (c) ScanMaster module for scanner control, and (d) overview of the custom C# software to control the SLE process showing job generation and thermal image processing/melt pool detection via thermal imaging camera [4, 22].

3.1.1 YLS-1000 Laser

The laser currently used for the SLE processing is an IPG Photonics YLS-1000 continuous wave (CW) diode-pumped single mode Ytterbium fiber laser with a wavelength of approximately 1075 nm. The 0-10 V analog voltage provided to the YLS-1000 to control the laser power is supplied by a National Instruments PCIe-6321 DAQ card with a maximum modulation rate of 900 kS/s and a 16-bit resolution. The DAQ card converts the computer's digital control signal into the analog voltage required by the laser during open loop as well as closed loop control. The laser power is correlated with the analog input voltage by using the laser power meter built into the YLS-1000. The selected YLS-1000 laser can shutter the laser beam on and off within 100 μs and adjust its power in response to an external analog voltage signal at a rate of 5 kHz, allowing for high bandwidth control of the amount of energy being applied to the substrate. Figure 8(a) shows the fiber laser.

3.1.2 Scanner

The scanner currently used with the YLS-1000 fiber laser is a 3-axis galvanometer scanner (HP/GSS-Frauno, Cambridge Technology, Bedford, MA, USA). The optical head of the laser is connected to the scanner using a custom designed collimator by Cambridge technology. The fiber laser is focused by the scanner to a spot of 40 μm in diameter, enabling both tight control of the local temperature conditions surrounding the melt pool and post-process cleanup operations via laser cutting. The laser scanner has the capability to move the incident laser beam across a 185 mm by 185 mm X-Y scan field at speeds of up to several m/s. Prior to entering the scan head the incoming laser beam is collimated by a 50 mm diameter IPG-1070 collimator with a focal length of 160 mm and an output beam $1/e^2$ value of 16 mm. The optics internal to the Cambridge scanner then focuses this beam down to a minimum spot

size of 40 µm in diameter. The third axis of the scanner, the z-axis, is a prescanning objective dynamic focusing module (DFM) that can adjust the beam focus during the scanning operation. The beam focus adjustment corrects for the focus loss due to changes in working distance as the laser moves across the scan field. Additionally, it can adjust the focus to enable scanning on curved surfaces. Figure 8(b) shows the scanner unit arrangement on top of the controlled atmosphere glovebox.

3.1.3 Scanner controller and software

The 3-axis galvanometer controlled scanner is controlled by a ScanMaster^{TM} (Maker: Cambridge Technology, Bedford, MA, USA) EC1000 unit via a custom code written in visual C#. The scanner controller unit is shown in Figure 8(c). The board-level API for the EC1000 makes extensive use of XML to pass parameters between a client application and the DLLs. The control software enables coupling of all the hardware components, such as the laser, the scanner, the DAQ, and the thermal camera in a customized package specifically written for the SLE process by Bansal [4]. The software is capable of importing XML job data, producing raster scan patterns of specified parameters, streaming marking commands to the scanner on the y, controlling the laser power, and measuring and analyzing the temperature field data acquired by the thermal imaging camera at a rate of 60 Hz. An overview of the C# software is shown in Figure 8(d).

The software allows control over four primary input parameters namely the laser power (P), the raster scan speed (V_S), the number of repeats (N), and the scan path [including scan spacing (SS)]. The scan path depends on the geometry and can be varied. Different geometries are shown in Figure 9(a). During the scan, the leading edge of the substrate coupon with pre-

placed powder on top of it is scanned repeatedly (N times) to initiate a melt pool allowing some pre-heating of the substrate coupon. Once the melt pool is established, smooth propagation of the melt pool is obtained by choosing a proper value of the energy density.

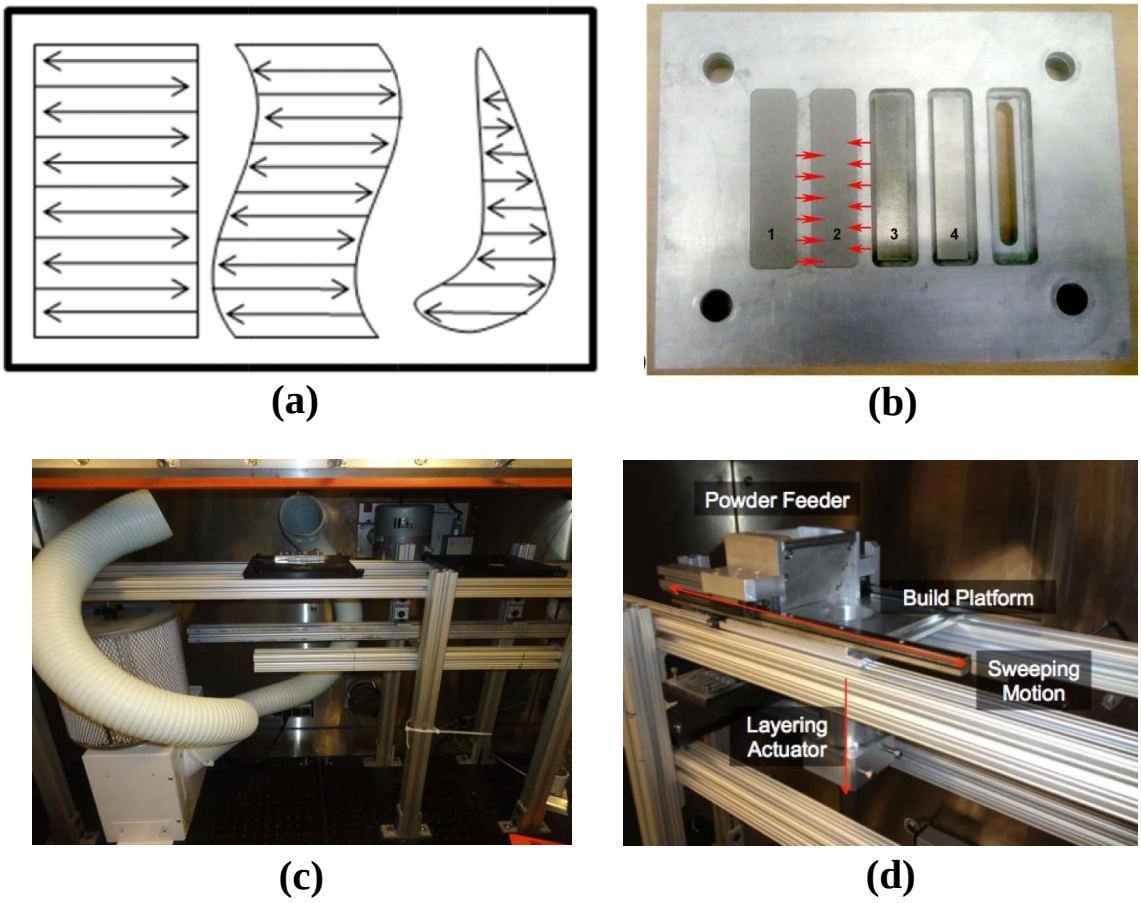

(a) **(b)**

(c) **(d)**

Figure 9. (a) Representative possible scan paths in SLE. (b) Placement of the superalloy coupons in the SLE process. The rightmost position shows the blank base to simulate the cooling holes in the turbine blades. Positions 4 and 3 show bare coupons and positions 1 and 2 show coupons with powder placed on top. The raster movement of the scan is shown for the coupon in position 2. (c) Conveyor belt assembly in glovebox with the fume extractor unit. (d) The proposed multi-layer deposition system [4, 22].

3.1.4 Controlled atmosphere processing unit

The SLE process is carried out inside a controlled-atmosphere customized glove box (Terra Universal, Fullerton, CA, USA). During processing, the chamber is backfilled with

argon until the chamber atmosphere contains less than 10 parts-per-million (PPM) oxygen at atmospheric pressure. The oxygen level is measured by an Ntron Model 3100 oxygen analyzer that has been calibrated at atmospheric and 99.999% pure argon levels. An IN625 plate is used to hold the substrate coupons in place during processing, as shown in Figure 9(b). The plate acts as a heat sink comparable to a turbine blade, and the through holes allow for heat distribution comparable to the tip cap of a turbine blade. The chamber contains a conveyor belt-like assembly that can accommodate up to five carrier plates to hold the substrate coupons with the pre-placed powder samples during laser processing as shown in Figure 9(c). Such arrangement enables high throughput during experimentation. A smoke exhauster unit (Model:S- 981-2B Extract-All, Air Impurities Removal Systems, Wauwatosa, Wisconsin, USA) is installed inside the glovebox to protect the scanner mirrors from the smoke generated during processing. The processing chamber is also equipped with a layering system shown in Figure 9(d) to enable fabrication of components from scratch.

3.1.5 Thermal imaging camera

A Mikron MCS640 thermal imaging camera (shown in Figure 10(a)) is used to capture the temperature field for the entire processing zone at a rate of up to 60 Hz, which is the limiting rate on the real-time control scheme. The thermal imaging camera utilizes a microbolometer array to measure the infrared energy emitted by an object and turn it into an electrical signal. The normal operating frequency range of the camera is 780 nm to 1080 nm, but a notch blocking filter has been added to the camera to additionally block the 1060 nm to 1080 nm range such that reflected energy from the incoming laser beam is rejected. There are a significant number of spectral emission lines within the 780 nm to 1060 nm band for the major alloying elements such as Ni and Cr, and thus, if the emissivity is properly calibrated, the

thermal camera can measure the melt pool temperature [4].

(a)

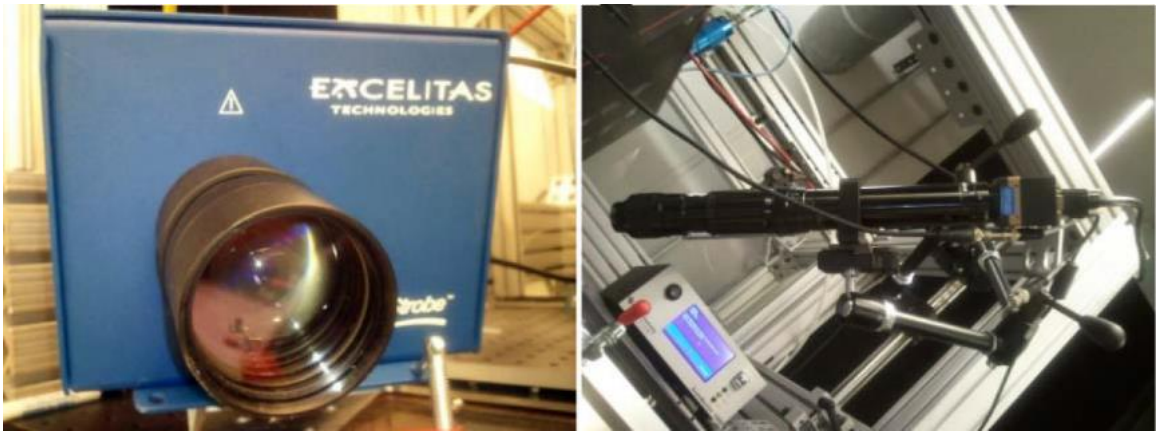

(b) **(c)**

Figure 10. (a) Mikron IR camera mounted on top of glovebox, (b) Xenon strobe, and (c) Pyrocam video recording microscope [4, 22].

An accurate emissivity value is required as an input setting for the thermal camera in order to obtain reliable temperature measurements. The emissivities of different superalloys are measured using a method similar to that described in the work of Ghaemi [79]. In this work, the emissivity is approximated for a temperature between the solidus and liquidus temperatures by defocusing the laser beam and using a low power to slowly heat up and melt a sample of the cast substrate while the thermal camera measures the average temperature of the laser spot location [4]. For instance, the emissivity value for René 80 is found to be 0.52 at

the solidus temperature, which is near the emissivity value of 0.4 – 0.5 reported for partially oxidized molten nickel-base superalloys in the literature [80].

3.1.6 Video microscope

The PyrocamLP video microscope (Control Vision, Inc., Sahuarita, AZ, USA) allows a real-time view of the operation at a maximum frame rate of 60 frames per second. The minimum exposure of the video microscope is 3.3 µs, and it can provide up to 20 µm resolution. The images can be saved as a sequence of images or as a compressed or uncompressed .avi file to enable post-process diagnostics and inspection.

A high-power, pulsed xenon strobe illumination (X-strobe, Model:X-1200, Excelitus technologies, Waltham, MA, USA) synchronized with high-speed shuttering, illuminates the processing zone while suppressing the ambient light associated with the SLE process, allowing the process details to be observed in real time. The xenon strobe produces intense pulses of radiant energy covering the ultraviolet (UV), visible (VIS), and near infrared (NIR). Additionally, an external triggering feature allows the PyroCamLP system to be synchronized with the SLE process, making it possible to view specific events in the process. Figures 10(b) and 10(c) show the strobe and the PyroCam video microscope, respectively.

3.1.7 Arrangement

The arrangement of the hardware and the control computer along with the purging lines is shown in Figure 11. This arrangement allows simultaneous operation of the thermal imaging camera and video microscope while running the SLE process via the control computer that integrates the laser, the scanner controller, and the IR camera.

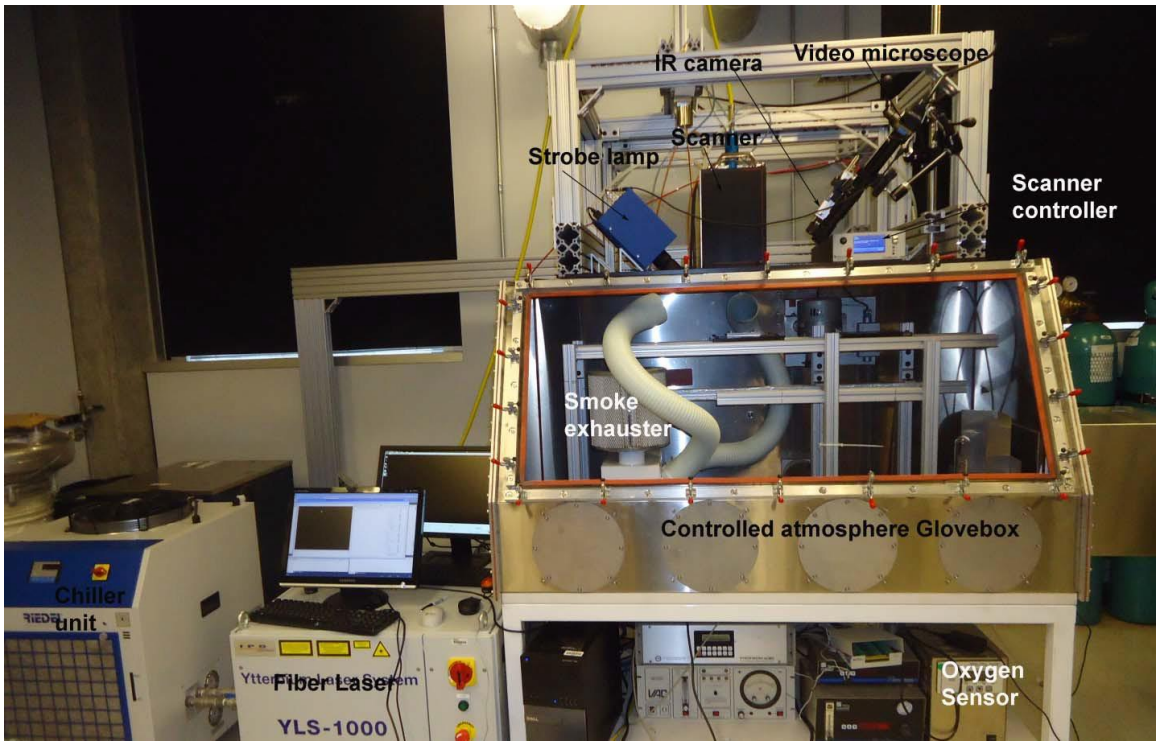

Figure 11. Arrangement of the SLE equipment [4, 22].

SLE allows simultaneous operation of the thermal imaging camera and video microscope during processing via the control computer that integrates the laser, the scanner controller, and the IR camera [4]. Bansal explored real-time feedback for the development of SLE to evaluate the impact of process control on the deposit quality [4]. Though the feedback control results can improve the deposit quality, in this dissertation research, the open loop control is used.

3.2 Materials characterization

Hereafter, the substrate coupon with the pre-placed powder fused to it after SLE processing is referred to as "sample". Each sample is sectioned using an IsoMet 4000 linear precision sectioning saw (Buehler, Lake Bluff, Illinois, USA) along the length and width to allow for views of the microstructure. The saw allows a rotational speed of 3600 rpm and a

feed rate up to 0.25 in/min while sectioning the samples. Cool 2™ (Buehler) coolant is used during the sectioning operation. The samples are first cut lengthwise, and then, sectioned by widthwise cut, as shown in Figure 12(a).

Table 2. Polishing procedure adopted for nickel-base superalloy [81].

Surface	Abrasive/Size	Load(Lb) / Specimen	Platen Speed (rpm)/Direction	Time (minutes)
Carbimet® waterproof discs (psa) water cooled	220-240 (P240-P280) grit SiC	6	240-300/Comp	Until Plane
Ultra-Pol Silk Cloth (psa)	9-µm Metadi® Supreme Diamond Suspension	6	100-150/Comp	5
Trident cloth (psa)	3-µm Metadi® Supreme Diamond Suspension	6	100-150/Comp	4
Trident cloth (psa)	1-µm Metadi® Supreme Diamond Suspension	6	100-150/Comp	3
Microcloth pad (psa)	0.05-µm Masterprep™ alumina slurry	6	80-150/Contra	2

Each section of the sample is mounted in Bakelite using a Buehler SimpliMet 3000 compression mounting press as shown in Figure 12(b). The mounting cycle comprises an automated heating and cooling cycle at 4200 psi. Epomet™ molding compound (Buehler) is

used as the mounting medium. The mounted samples are polished using an EcoMet 250 (Buehler) automated polisher. The polishing unit is illustrated in Figure 12(c). The rough polishing is conducted by 240 grit paper. The samples then undergo a fine polishing operation with diamond solutions. Finally, the samples are polished to a mirror finish using a 0.5 µm colloidal alumina suspension. To remove the trapped alumina particles, the samples are sonicated using a Branson B-200 Jewelry and Optical Ultrasonic Cleaner for 180 s. The detailed procedure is established in the work of VanderVoort et al. and provided in Table 2 [81].

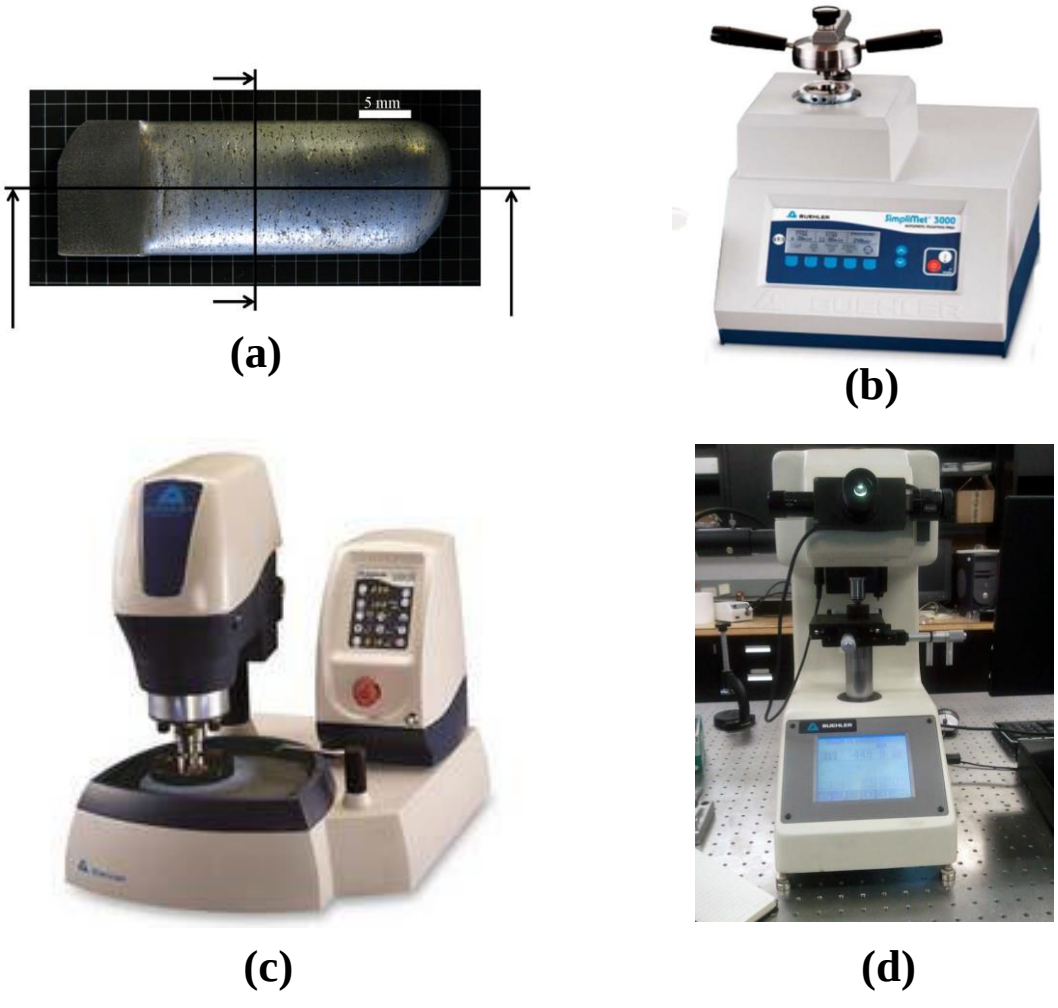

Figure 12. (a) Representative lengthwise and widthwise cuts for the SLE samples.

(b) Buehler SimpliMet 300 mounting press. (c) Buehler Ecomet 250 polisher. (d) Buehler microhardness instrument [4, 22].

The polished samples are exposed to Marble's etchant (50 ml HCl, 50 ml H_2O, and 10.0 gm $CuSO_4$) to eliminate the γ′ phases and reveal the microstructure. Optical microscopy (OM) is conducted using a Leica DM6000 optical microscope. This microscope is capable of stitching images obtained through an X-Y scan and is capable of accounting for surface unevenness using predictive focusing.

SEM investigation is carried out on a Hitachi 8230 SEM. The SEM is equipped with an Oxford Instruments' Aztec Energy EDX system which is used for the elemental analysis. Marble's reagent (50 ml HCl, 50 ml H_2O, and 10.0 gm $CuSO_4$) is again used as this etchant preferentially attacks the γ′ phase leaving the residual γ channels for microstructural inspection. Crystalline phases are analyzed on a PANalytical Empyrean XRD system. EBSD analysis is performed on a Philips XL-30 FEG-SEM equipped with a TSL/EDAX Hikari EBSD camera. The acceleration voltage is 20 kV.

Microhardness measurement is carried out using a microindentation hardness indenter (Wilson TukonTM 1102, Buehler). The Tukon 1102 Tester is equipped with a three position turret which includes one indenter position and two objective lenses having 10x and 50x magnifications. The hardness values are reported in Vicker's microindentation hardness scale (HV). The force is applied smoothly, without impact, and held in contact for 10 to 15 s. The instrument is shown in Figure 12(d). A spacing of 2.5 times the average diagonal of the indentation is maintained between different indentations. This is done to avoid the effect of the strain field from the previous indentation. The indenter employed in the Vickers test is a square-based pyramid whose opposite sides meet at the apex at an angle of 136º [22]. The

tensile properties of the samples are determined according to ASTM D638 using an Instron 33R 4466 equipped with 10 kN load cell.

3.3 Heat treatment

In order to relieve the residual stresses and enable precipitation of the strengthening phases, the SLE-fabricated samples are subjected to commercially available heat treatment procedures. For example, MAR-M247 samples are heated and kept at 1080 ^{o}C (1975 ^{o}F) for an hour. Thereafter, the samples are cooled at 5.6 ^{o}C/minute (10 ^{o}F /minute) or faster to a temperature below 870 ^{o}C (1600 ^{o}F). Samples are then given a typical commercial aging treatment consisting of 12 hours at 870 ^{o}C (1600 ^{o}F), followed by air cooling at a minimum average cooling rate of 5.6 ^{o}C/minute (10 ^{o}F /minute) to 650 ^{o}C (1200 ^{o}F) to fully develop the strengthening phases.

The SLE-deposited CMSX-4® samples are subjected to heat treatment via aging. The samples were heated and kept at 1080 ^{o}C for an hour. Thereafter, the samples are cooled at 5.6 ^{o}C /minute or faster to a temperature below 900 ^{o}C. Samples are then given a typical commercial low-temperature precipitation heat-treat cycle consisting of 4 hours at 900 ^{o}C, followed by air cooling at minimum average cooling rate of 5.6 ^{o}C / minute to 650 ^{o}C to fully develop the strengthening phases.

3.4 Digital metallography

The melt depth, the deposit height, warpage, voids, and cracks are extracted from the microstructural images. Consistent manual calculation of all of these parameters for a larger batch of samples can be very tedious. Thus, an efficient image-analysis code to perform this task automatically and consistently is highly desirable. However, most image analysis software

tools (e.g., Image tools [75]) are semi-quantitative and based on SEM. To address this need, a previously developed customized active contour-based MATLAB^{TM} (Math works, Inc.) image-analysis code is applied to extract necessary information from the digital images using quantitative metallography techniques [82].

3.5 Summary

This chapter explains the fundamental working principles of SLE and elaborates upon the key components involved. A custom-made open architecture LPBF-based AM process is developed in this dissertation research.

- The open architecture AM process integrates several different key components such as laser, scanner, scanner controller, video camera, and thermal imaging camera.

- The custom built process enables complete control over the process parameters such as laser power, scan speed, scan spacing, scan geometry, and powder layer thickness.

- The SLE process can be conducted at an extremely pure environment reducing the possibilities of oxide formation.

- Laser injected into the build envelope during can accumulate on the irradiated particles causing “smoking”. A smoke exhauster strategically placed inside the build chamber eliminates the formation of smoke in SLE.

- The experimental coupon setup, carrier plate design, and the conveyor belt assembly inside the customized build chamber is geared towards developing new alloys through experimentation in short time.

- The modular assembly of the SLE process allows both single pass and multi-layer fabrication using the same setup.

- The laser spot diameter can be tightly controlled enabling precise transfer of energy to the powder bed and the substrate facilitating repair and manufacture of complex geometries.

Chapter 4: Multi-physics modeling

This chapter sheds fundamental insights on the material consolidation, melting, and solidification in SLE as the laser beam performs high-resolution raster scan atop the powder layer. A two-dimensional (2D) transient, multi-domain model with temperature-dependent thermo-physical properties is developed to simulate the flow-thermal-microstructure evolution in SLE [83-85].

4.1 Simulation setup

The 2D model includes two separate domains – (1) the deposit domain consisting of the substrate at the bottom and the powder layer at the top and (2) the IN625 baseplate domain as shown in Figure 13(b). The domain is obtained by taking a section at AA′ as shown in Figure 13(a). The sectioning direction is perpendicular to the plane of the paper. Figure 13(c) shows the geometry and mesh for the 2D configuration. The deposit domain has a finer mesh to accurately capture the 20 μm radius laser heat source. The total node count of the mesh is close to 137k and the skewness is below 0.2. The simulation is performed in ANSYS CFX solver.

4.1.1 Flow-thermal model

The solid and liquid component enthalpy equations, expressed in terms of volume fractions, r, are:

Equation 3. Solid enthalpy equation.

$$\frac{\partial(\rho_s r_s h_s)}{\partial t} + \nabla \bullet (\rho_s r_s \underline{U}_s h_s) = \nabla \bullet (r_s k_s \nabla T_s) + I$$

Equation 4. Liquid enthalpy equation.

$$\frac{\partial(\rho_L r_L h_L)}{\partial t} + \nabla \bullet (\rho_L r_L \underline{U}_L h_L) = \nabla \bullet (r_L k_L \nabla T_L) - I$$

Here, ρ is the density, h is the enthalpy (including the latent heat), T is the temperature, $\underline{U}$ is the velocity, and I is the interphase heat transfer. The subscripts S and L refer to the solid and liquid components respectively. Equations (3) and (4) can also be expressed more compactly as:

Equation 5. Mixture enthalpy equation.

$$\frac{\partial(\bar{\rho} h)}{\partial t} + \nabla \bullet (\bar{\rho} \underline{U} h) = \nabla \bullet (\bar{k} \nabla T) - \nabla \bullet (\bar{\rho} Y_S (\underline{U} - \underline{U}_S)(h_L - h_S)) + S$$

Here $\bar{\rho}$ is mixture density, h is the mixture enthalpy, $\bar{k}$ is mixture conductivity, Y_S is the mass fraction of solid [86]. The final term in Equation (5) represents an additional source due to the difference in velocity between the solid and the liquid components. This term takes a finite value in the mushy region of the flow ($0 < Y_S, Y_L < 1$). In the regions of pure liquid or pure solid, the mixture enthalpy equation reduces to the appropriate component enthalpy equation.

The volume fractions of liquid and solid components are incorporated using tabular data representing the solid and liquid fraction of the superalloys in the melting range. The Boussinesq approximation is implemented to model the effect of variable liquid density. A Darcy like source term is incorporated to model the resistance to flow in the mushy region. The permeability is modeled using Kozeny-Carman equation [87].

Equation 6. Kozeny-Carman equation.

$$S_M = \min\left(C_M, \frac{\mu_L}{K_0}\frac{(1-r_L)^2}{r_L^3}\right)(U - U_S)$$

Here, μ_L is the viscosity and K_0 is a proportionality constant in Kozeny-Carman equation. To prevent division by zero, the term is bounded by a user-specified maximum, C_M.

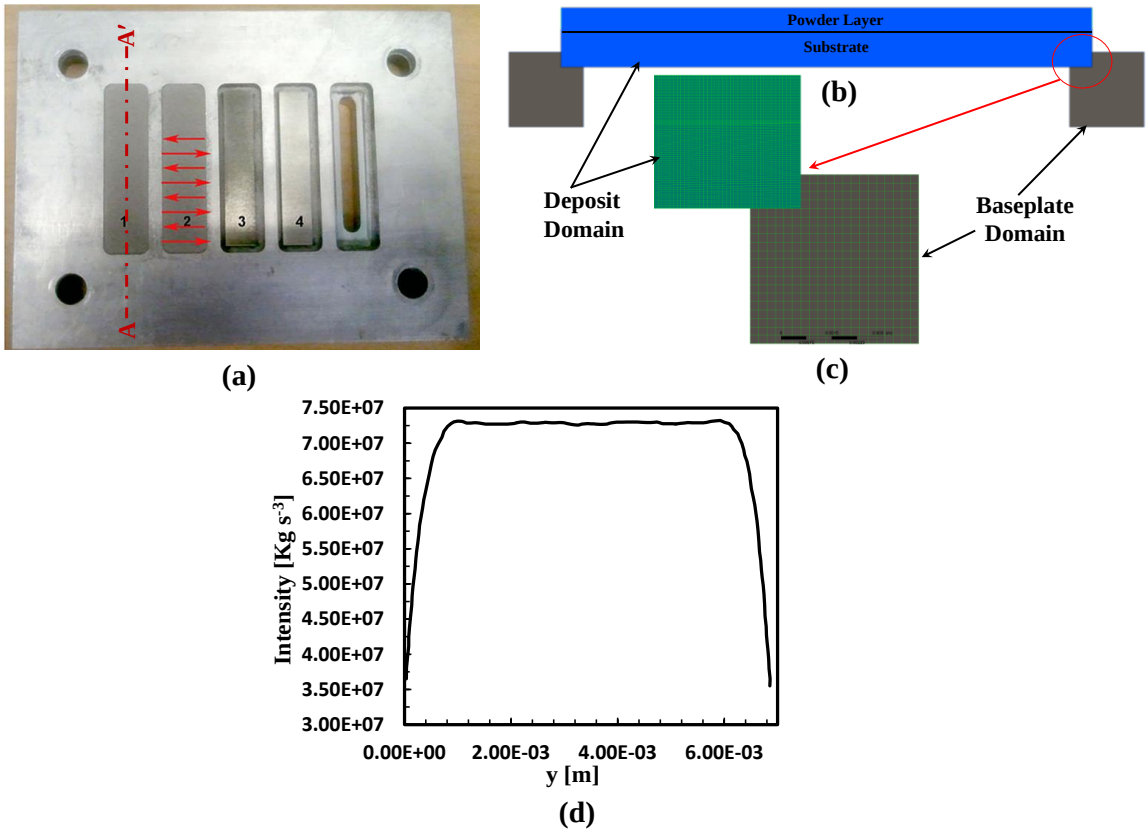

Figure 13. (a) Experimental coupon setup showing the section plane location AA′ that generates the pseudo-CFD domain; ANSYS CFX simulation model showing (b) deposit domain and baseplate domain, and (c) mesh details in the deposit and the baseplate domain. (d) Representative laser heat source intensity variation in the y-direction obtained from the 3D model [22].

In the turbulence equations, sink terms similar to the Darcy term in the momentum equation are applied to damp the turbulence in solid regions [86].

Equation 7. Darcy terms for turbulent kinetic energy and turbulent dissipation.

$$S_{tke} = -\frac{\mu_L}{K_0}\frac{(1-r_L)^2}{r_L^3}tke \quad , \quad S_{\varepsilon} = -\frac{\mu_L}{K_0}\frac{(1-r_L)^2}{r_L^3}\varepsilon$$

Here, tke is the turbulence kinetic energy and ε is the turbulence eddy dissipation. For the base-plate domain, the solid conduction equation is solved.

Equation 8. Conduction equation.

$$\frac{\partial(\rho H)}{\partial t} = \nabla \bullet (K \nabla T) + S_0$$

Here ρ is the density, H is the enthalpy, K is the thermal conductivity, and S_0 is the source/sink term. Since there is no flow into or out of the domain, the chosen model prevents the use of an explicitly varying density for the liquid. Therefore, the volumetric changes are accounted for by using the Boussinesq approximation to artificially include a buoyancy-induced source term.

The laser heat source is modeled as a Gaussian moving heat source in 3D [22]. The spatial profile in the y-direction is averaged over a single scan length over the sample width and fitted with a 10th-degree polynomial. This particular profile is then used as a line source with Gaussian distribution applied in the x-direction. The intensity profile used is,

Equation 9. Laser intensity profile.

$$I(y_n) = \sum_{i=0}^{10} \left(P_i y_n^i\right)$$

With, $y_n = (y - \mu_{Laser})/\sigma_{Laser}$ (μ_{Laser} and σ_{Laser} are laser beam parameters). The coefficients are determined from the simulation of a laser beam rastering in the y-direction and by averaging the power profile in the y-direction. The polynomial used for the laser heat source intensity in the y-direction is found to be flat in the middle region with some reduction of intensity near the edges of the sample as shown in Figure 13(d). This small variation in y-direction is neglected while modelling the problem physics in 2D. This line source represents the term S in Equation (5).

The top surface of the deposit domain is modeled as wall with a specified shear value determined by the Marangoni effect. The effects of Marangoni convection are modeled by imposing a surface tension driven shear force at the free surface.

Equation 10. Surface tension driven shear flow.

$$\mu \frac{\partial U_x}{\partial x} = r_L \frac{\partial \gamma}{\partial T}\frac{\partial T}{\partial x}, \quad \mu \frac{\partial U_y}{\partial y} = r_L \frac{\partial \gamma}{\partial T}\frac{\partial T}{\partial y}$$

Here, $\delta\gamma/\delta T$ represents the temperature coefficient of surface tension and subscripts x and y denote the component values in the x- and the y-direction, respectively. The boundary surfaces of the connected solid domains that are not interfaced with the deposit domain are treated as adiabatic walls. Conservation of thermal energy is ensured at all interfaces. The side surfaces of the deposit domain are modeled as openings which allow both inflow and outflow and provide solver stability. The convection heat loss to the environment is modeled using the Newton's law of cooling through a surface sink term. Radiation loss is also modeled using a sink term.

SLE starts from ambient condition and hence, 300K is used as initial temperature. The transient model is solved using a time step value equal to 0.00215s. The inclusion of convection, phase change model and Darcy sink term together necessitates the use of a lower time step value to ensure solver stability. The imbalance in the system is kept within 1% and the convergence is assured when the residual RMS value goes below $1x10^{-4}$. Once solved, the result is post-processed in CFD-post to analyze the melt pool nature, the melt depth profile, and the temperature distribution.

4.1.2 Microstructure modeling

Modeling of solidification microstructure is carried out to understand the following phenomena of single-crystal superalloys – (a) oriented-to-misoriented-transition (OMT) and (b) columnar-to-equiaxed-transition (CET).

4.1.2.1 *Oriented-to-misoriented-transition (OMT) modeling*

In order to characterize the columnar orientation, the inner product of the normal component of the solid-liquid interface with the (100) and (001) direction vectors is resolved. Here, the direction vectors represent the possible dendrite orientations. The maximum value of the inner product provides the minimum of the cosine component of the inclination angle between the two directions.

Equation 11. Minimum of the cosine component of the inclination angle.

$$\cos \Psi = \max \left(\hat{n}.\hat{u} \right)$$

Here, $\hat{n}$ is the normal vector to the solid-liquid interface and $\hat{u}$ is the direction vector. The orientation vectors for (001) and (100) are assigned values of 1 and 100 respectively.

4.1.2.2 *Columnar-to-equiaxed-transition (CET) Modeling*

The temperature gradient at the solid–liquid interface (G) is computed from the ANSYS CFD model. The solid-liquid interface orientation (θ_i) is calculated from the following expression:

Equation 12. Solid-liquid interface orientation.

$$\theta_i = \cos^{-1}(G_i/G) \text{ (For } i = x, y, z)$$

The growth rate of the solid–liquid interface is given by $V = V_S \cos\theta$ (V_S = Scan speed). The angle ψ refers to the angle between the normal vector and the possible dendrite growth orientation at the solid–liquid interface, and is evaluated in CFX-Post. The temperature gradient parallel to the dendrite growth direction is calculated using the equation, $G_{hkl} = G/\cos\psi$. The dendrite growth velocity, V_{hkl}, is calculated using the equation $V_{hkl} = V_S \cos\theta / \cos\psi$. The Rappaz modification is applied to predict the CET as follows [75]:

Equation 13. Rappaz modification criteria.

$$G_{hkl}^{n} / V_{hkl} \geq a \left[\left(\frac{-4\pi}{3\ln(1-\varphi)} \right)^{1/3} \sqrt{\frac{N_0}{n+1}} \left(1 - \frac{\Delta T_n^{n+1}}{\Delta T_{tip}^{n+1}}\right) \right]^n$$

Here a, n = material constants, φ = equiaxed fraction (critical value = 0.066 %), N_0 = nucleation density, ΔT_{tip} = tip undercooling, and ΔT_n = nucleation undercooling [75].

4.2 Material properties

Thermo-physical properties for IN100, René 80, CMSX-4®, and René N5 are accurately

modeled [88-90]. The properties for IN625 are also modeled using tabular data [91]. The absorptance of laser energy is modeled using the Hagen-Rubens relationship [91]. Since this relationship does not account for the powder phase, a discrepancy is expected during the repeat scan period as the laser beam directly interacts with the powder. However, repeat scans in SLE ensures the formation of a continuous melt pool at the leading edge of the substrate. Hence, the Hagen-Ruben relationship can provide a reasonable estimation of the absorptivity [92]. Figure 14(a) and 14(b) describe the variation of absorptance for IN100 and CMSX-4® as a function of temperature, respectively. The temperature-dependent values marked by round bullets are used as tabular data in CFX to perform the simulation.

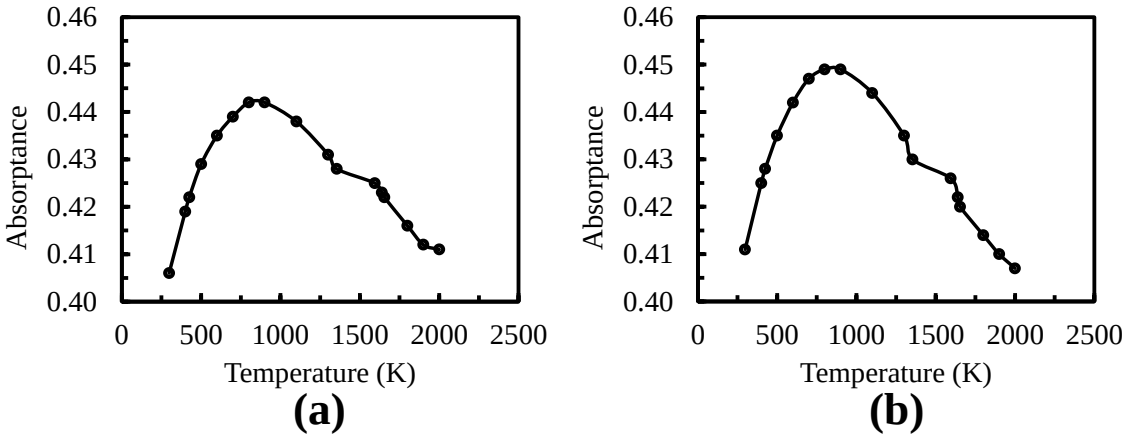

Figure 14. Variation of absorptance as function of temperature for (a) IN100 and (b) CMSX-4®.

4.3 Process parameters

Table 3 lists the process parameter ranges used for CMSX-4® and IN100 respectively for 2D domain simulations. The scan spacing of 25.4 μm required a very fine mesh to be generated for all the simulation. For René 80 and René N5, single simulations are performed mainly for the verification and validation purposes.

Table 3. Process parameter ranges used for IN100 and CMSX-4®.

Process parameter	IN100	CMSX-4®
Powder thickness (mm)	1.4	1.4
Laser power (W)	300 – 500	400 – 700
Scan speed (mm/s)	300 – 600	400 – 750
# of repeat scans	100 – 200	300 – 500
Scan spacing (μm)	25.4	25.4

4.4 Experimental validation

Flow-thermal simulation results are primarily validated with the experimental melt depth data. Additionally, the IR camera allows in-line temperature monitoring and the 'blob' detection algorithm provides the average melt pool temperature in real time. The proposed 2D model can, therefore, be validated using the average melt pool temperature obtained from the IR camera. The current methodology relies on matching only the maximum temperature.

4.5 Results and discussion

This section provides flow-thermal results for two EQ deposits namely IN100 and René 80 and two SX deposits namely CMSX-4® and René N5. For SX deposits, microstructure modeling results are also presented.

4.5.1 Results on EQ deposits

Computational simulation of the SLE process sheds light on the flow-thermal field generated by the moving heat source as it traverses across the substrate. The flow field affects

the melt pool formation and the temperature distribution within the melt pool. Figures 15(a) and 15(b) show the velocity and temperature distribution inside the melt pool for IN100 respectively. The melt pool is identified in the regions with liquid IN100 mass fraction of 0.99 or more.

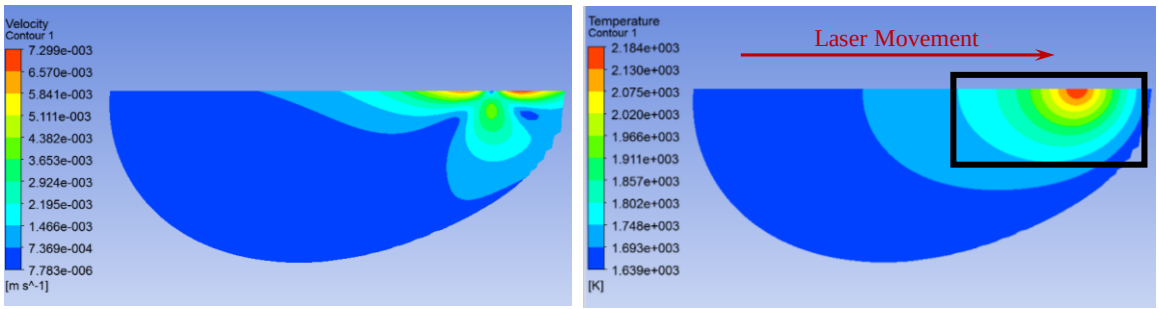

Figure 15. Contour of (a) velocity and (b) temperature inside the melt pool for IN100.

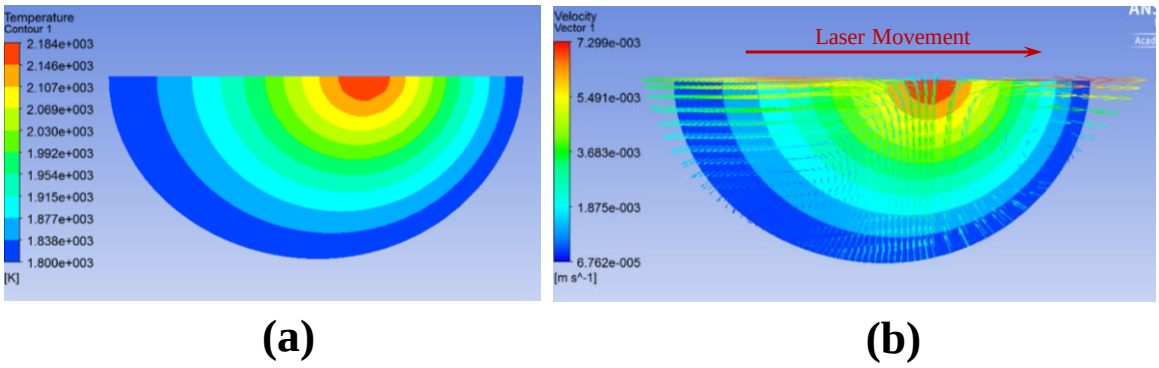

Figure 16. Zoomed view [marked by the black box in Figure 15(b)] of the (a) contour of temperature and (b) velocity vector overlaid on the contour of temperature inside the melt pool for IN100.

This calculation is validated by the fact that inside the melt pool, the temperature is greater than 1639 K, the liquidus temperature of IN100. The maximum velocity reaches a value of 7.3 mm/s at the top of the melt pool while the bottom of the melt pool showed a velocity of 0.78 mm/s. Figures 16(a) and 16(b) show the zoomed view of the temperature contour near

the laser source with and without velocity streamlines superimposed.

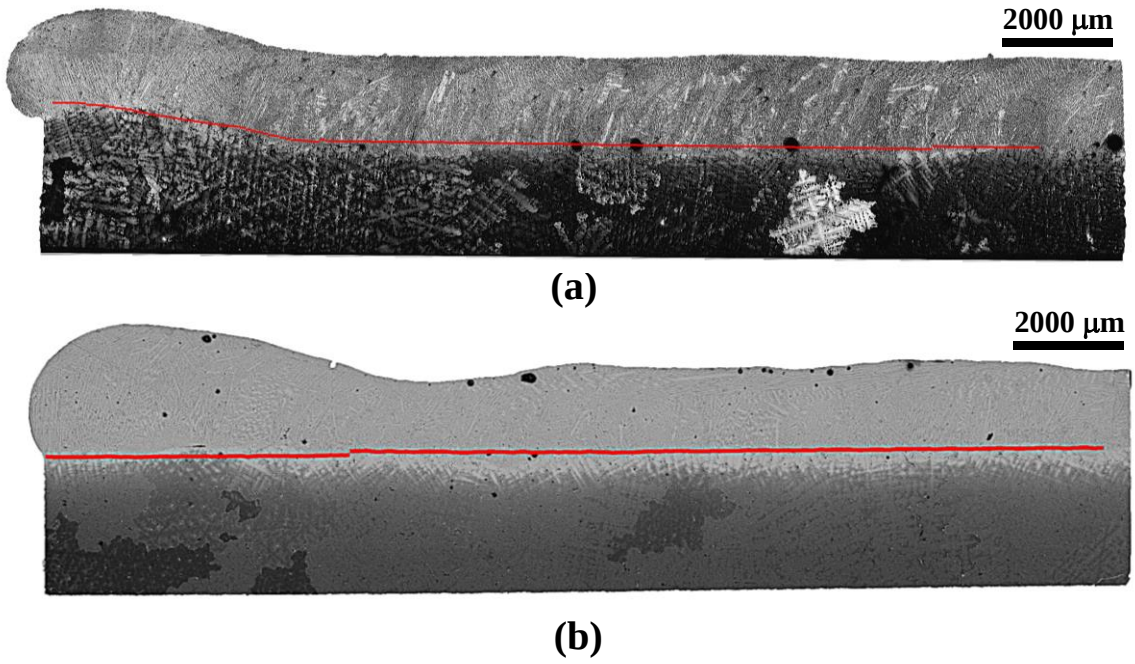

Figure 17. Comparison of the simulated melt depth (red line) with actual micrograph for (a) IN100 and (b) René 80.

The melt pool consists of two counter rotating vortices with their center located approximately at the location of the laser heat source. The flow field draws loose powder at the top and feeds the melt pool as it expands. The melt depth profile is of particular interest for the present application and hence compared with the actual cross-sectional optical micrographs. Figures 17(a) and 17(b) demonstrates the melt depth comparison between simulation and experimental results for IN100 and René 80, respectively. Good agreement is obtained between the simulation and the experimental results for these two superalloys.

Characterizing the effect of SLE processing parameters on the melt pool depth is critical for understanding and control of the process. The effect of these parameters on the CFD-simulated average melt depth is analyzed and presented in Figure 18. The blue dotted lines

represent the 95% confidence intervals for the experimental data [42], black circles represent the CFD simulated data points, and the black line denotes the best-fit line generated from the CFD simulated data points. The nominal SLE run is performed with number of repeat scans of 100, scan speed of 400 mm/s and laser power of 400 W. The experimental and the CFD data points for the melt pool depth are normalized by the nominal SLE run. The prediction shows excellent agreement with the experimental data across the entire range of the experimental data points.

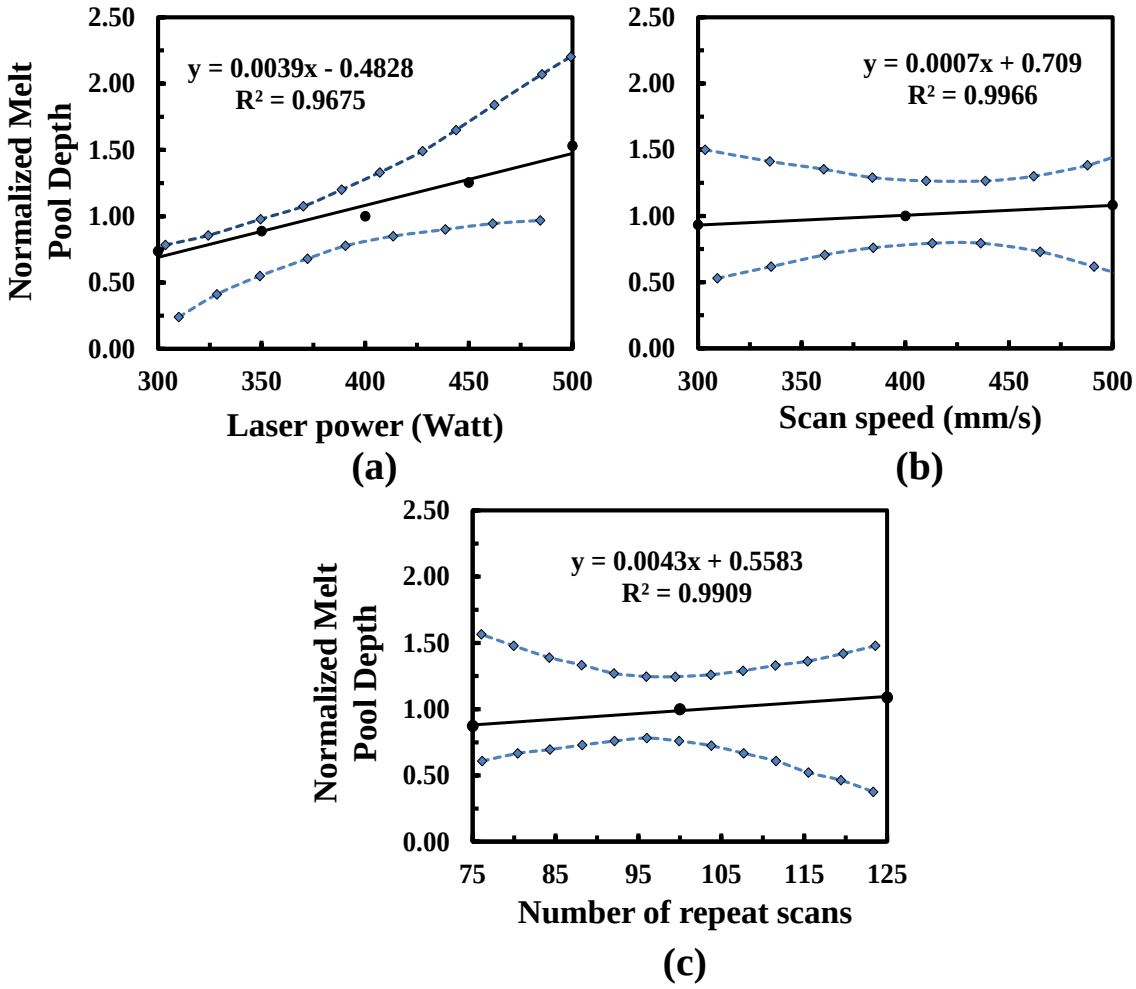

Figure 18. Effect of process parameters on SLE deposit characteristics – (a) laser power, (b) scan speed, and (c) of number of repeat scans for IN100.

It can be seen from Figure 18(a) that laser power impacts the melt pool depth significantly. With increasing laser power, the melt pool extends laterally and transversely, thereby increasing the melt depth. Increasing the scan speed and the number of repeat scans does not show any significant effect on the melt depth [Figures 18(b) and 18(c)] for this material system.

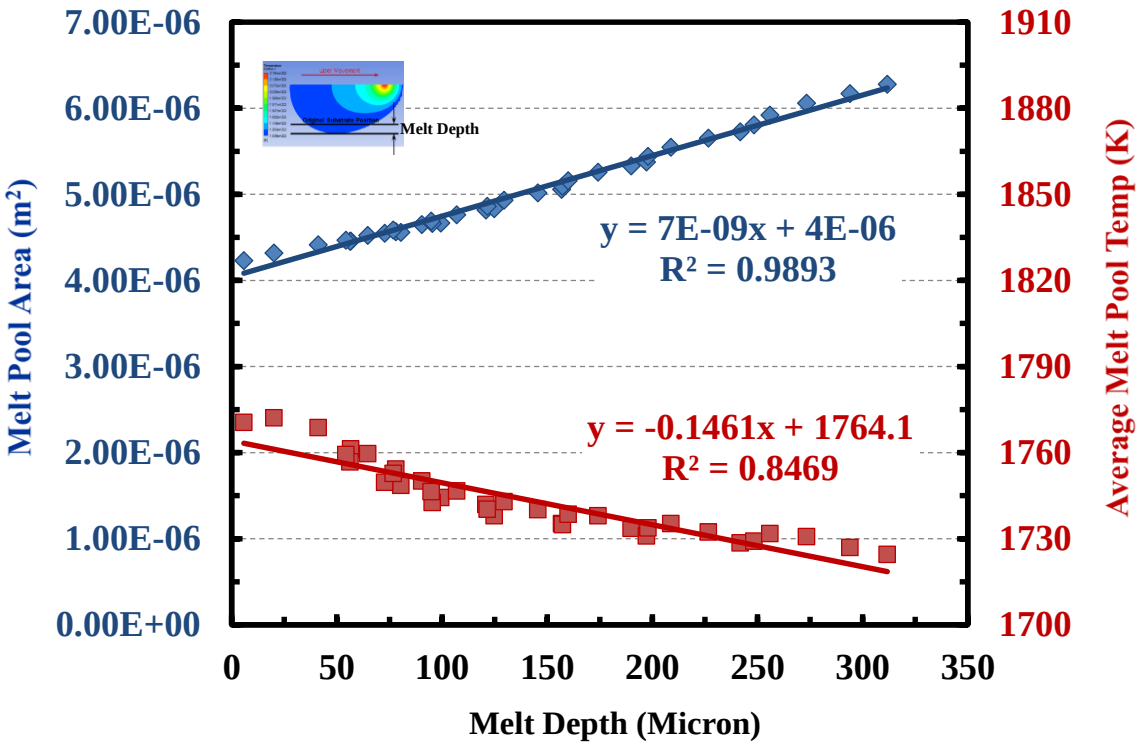

Figure 19. Variations of the melt pool area and average melt pool temperature with the melt depth for IN100.

The laser heat source performs a raster scan and traverses across the substrate increasing the temperature of the substrate significantly as the scan progresses. Figure 19 shows the relation between the melt pool area and the melt pool depth for a complete scan of a representative IN100 sample. Since the dominant thermal gradient is along the vertical direction, an increase in the melt pool area is expected to increase the melt depth. The linear

relation in Figure 19 reveals that if the melt pool area is kept constant at a desired value, a uniform melt depth can be achieved. The plot also shows the relation between the average melt pool temperature and the melt pool depth for the same sample. Again, the linear relation reveals that if the average melt pool temperature is kept constant at a desired value, a uniform melt depth can possibly be achieved.

4.5.2 Results on SX deposits

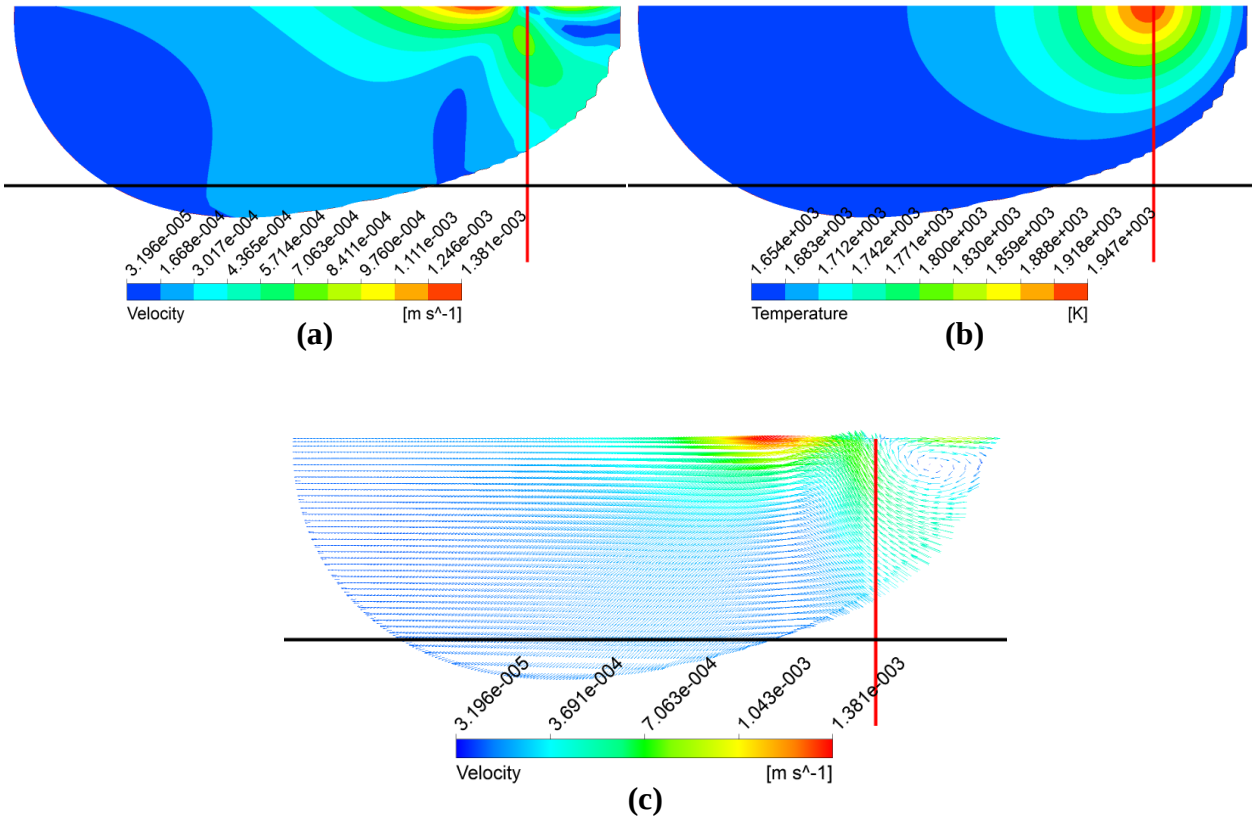

Figure 20. Representative contours of (a) temperature, (b) velocity and (c) velocity vectors due to the moving heat source for CMSX-4® inside the melt pool. The yellow line indicates original substrate position before laser processing and the red line indicates the instantaneous position of the laser. Laser movement is from the left to the right.

Computational simulation of the SLE process sheds light on the nature of the flow-thermal field generated by the moving heat source as it travels along the length of the substrate.

The flow field affects the melt pool formation and the temperature distribution within the melt pool. Figures 20(a) and 20(b) show the temperature distribution and the velocity vectors superimposed on the temperature field inside the CMSX-4® melt pool. The melt pool is identified in the regions with liquid CMSX-4® mass fraction of 0.99 or more.

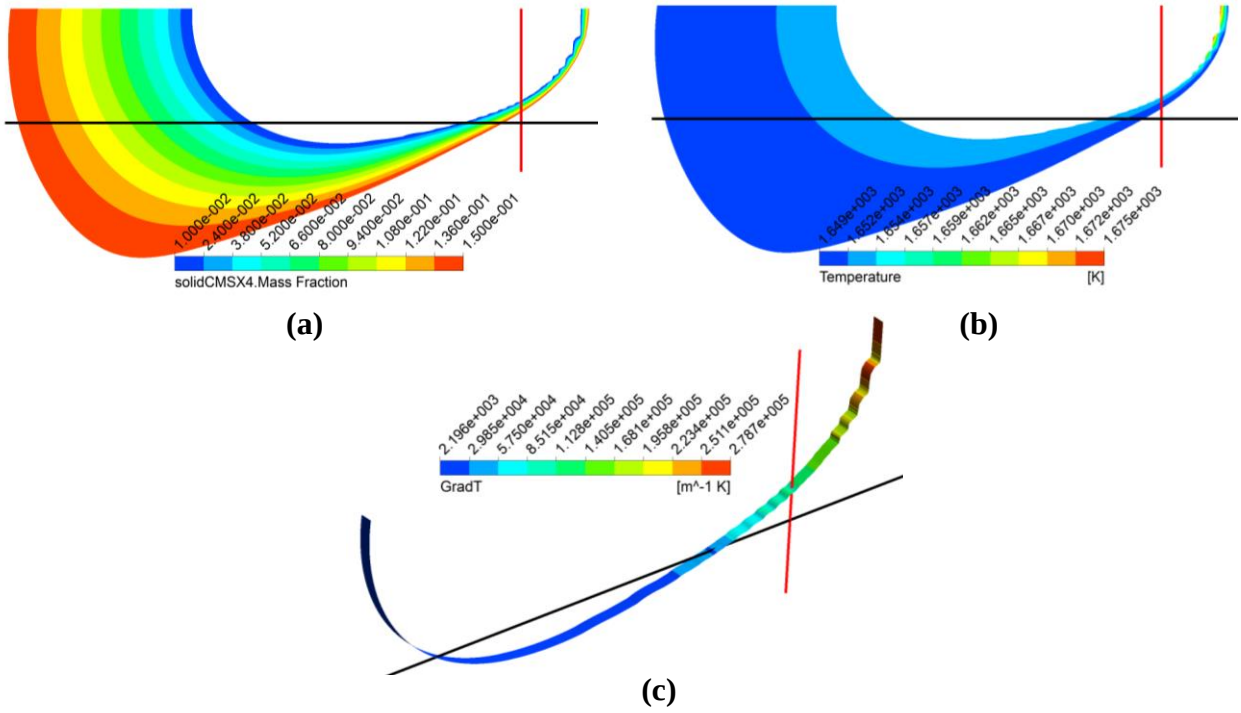

Figure 21. (a) Identification of the mushy region, (b) contours of temperature in the mushy region due to the moving heat source in CMSX-4® melt pool, and (c) representative contour of the temperature gradient in the CMSX-4® melt pool. The yellow line indicates original substrate position before laser processing, and the red line indicates the instantaneous position of the laser. Laser movement is from the left to the right.

This calculation is validated by the fact that inside the melt pool, the temperature is greater than 1654 K, the liquidus temperature of CMSX-4®. The melt pool consists of two counter rotating vortices with their center located approximately at the location of the laser heat source. The maximum velocity reaches a value of 1.38 mm/s at the top of the melt pool while the bottom of the melt pool showed a velocity of 0.32 mm/s. The higher viscosity of

CMSX-4® resulted in higher shear stress and forced the trailing edge vortex to follow the surface velocity pattern as shown in Figure 20(c). This shows up in the velocity vector plot inside the melt pool where the vortices were partially developed for CMSX-4® as opposed to IN100 which has lower liquid viscosity and thus shows fully developed vortices. Figures 21(a) and 21(b) show the mushy zone and its temperature contour. The mushy zone showed temperature ranging from 1649 K to 1675 K (1375.85 °C to 1401.85 °C) in the representative scenario. Figure 21(c) shows the temperature gradient at the solid–liquid interface. The temperature gradient again reduces to 2.2×10^3 K/m at the trailing edge as compared to a value of 2.8×10^5 K/m at the leading edge.

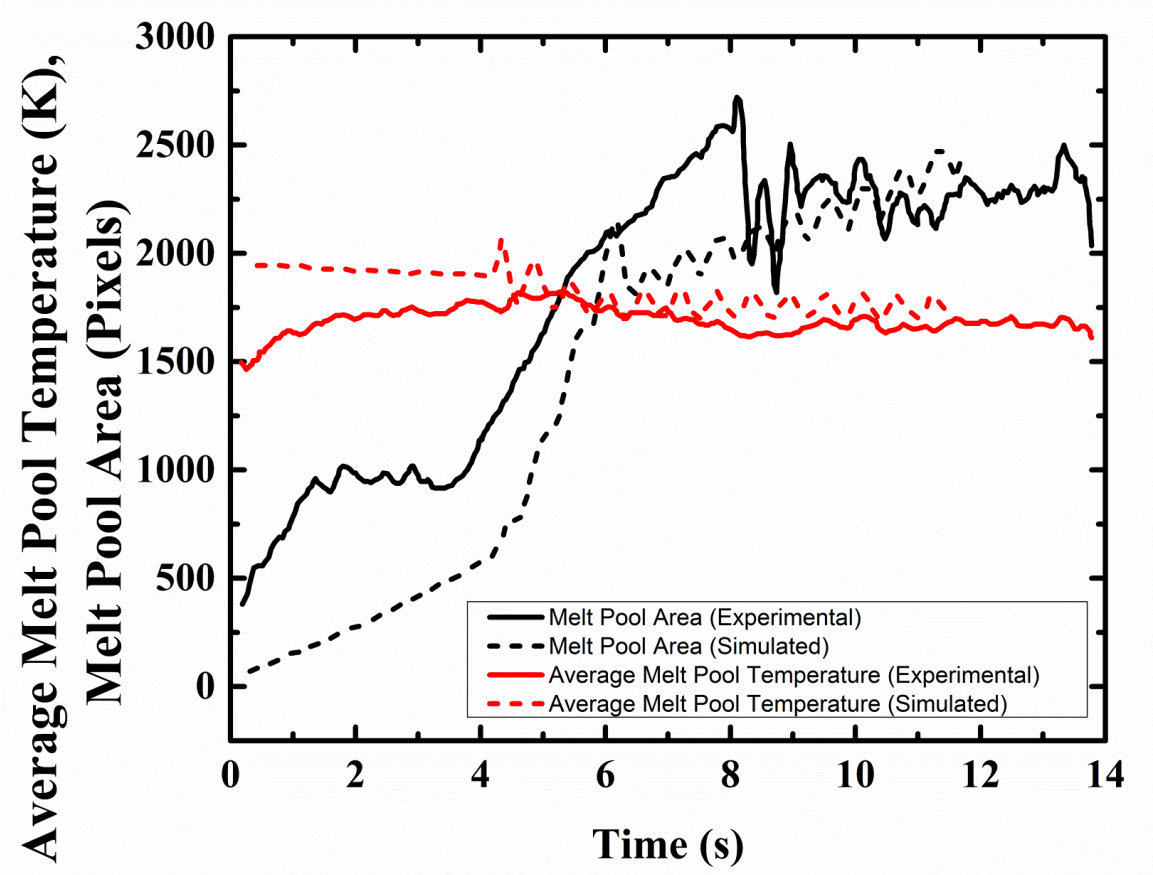

Figure 22. Comparisons of the simulated and experimentally obtained melt pool size and average melt pool temperature variation with time for the processing of CMSX-4® when observed from the top surface.

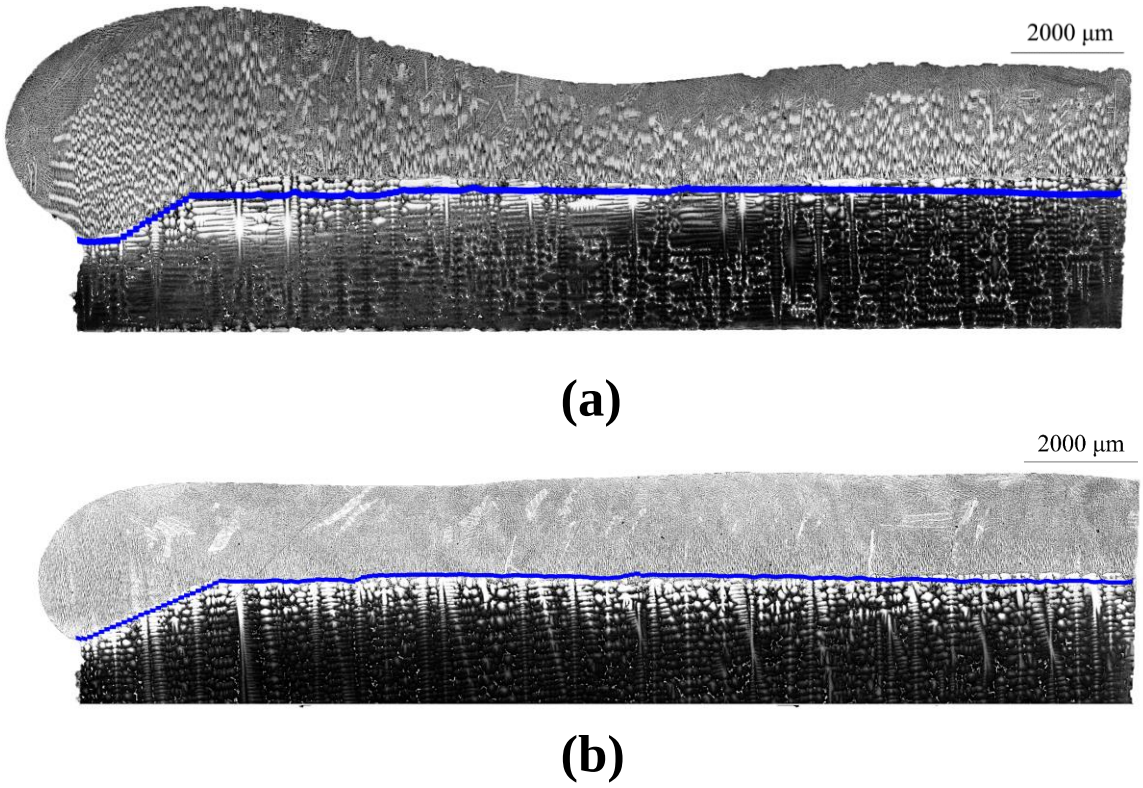

Figure 23. Comparison of the simulated melt depth (blue line) with actual micrograph for CMSX-4® (a) Sample 1 and (b) Sample 2.

Figure 22 shows the comparison of the experimentally obtained profile of the melt pool size and the average temperature with the simulated results for one particular CMSX-4® trial. The simulated melt pool size in the x-direction is multiplied with the sample width (70 pixels) to compute the melt pool size at the top surface. The IR camera also fixes the bounding box of the melt pool to 70 pixels. The melt pool extent in the x-direction obtained by simulation is lower at the beginning and of the order of 0.7 mm or 7 pixels, while the experimental value is close to 1.4 mm or 15 pixels. However, these two values gradually converge as the scan progresses. In the steady state, the value is close to 32 pixels or 3 mm in the x-direction.

The simulation identifies the melt pool if the liquid mass fraction is above 0.99. It may be possible that the molten powder and the mushy region ahead of the actual melt pool are

detected by the IR camera. During the repeat scans, the anomaly is higher, since in reality the extension of the melt pool might not be gradual, and it could occur in discrete steps. The simulation predicts an average temperature in the range of 1900 K to 1800 K (1626.85 °C to 1526.85 °C), whereas the IR camera records an average temperature ranging from 1500 K to 1750 K (1226.85 °C to 1476.85 °C). Since the molten powders and mushy region are detected as melt pool by the IR camera, the average temperature value is reduced as shown in Figure 22.

The melt depth profile is of particular importance for the present study, and hence, it is compared with the actual cross-sectional optical micrographs. Figures 23 and 24 illustrate the melt depth comparison between simulation and experimental results for CMSX-4® and René N5, respectively showing excellent agreement.

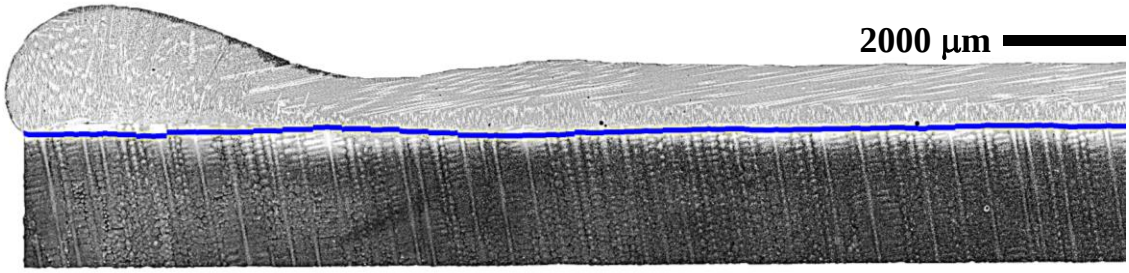

Figure 24. Comparisons of the simulated melt depth (blue line) with actual micrograph for René N5 sample.

The plot of the orientation vector is shown in Figures 25(a) and 25(b) for CMSX-4® Sample 1 and Sample 2 for a given position of the laser heat-source. The flip in direction from (001) to (100) is suggested in the plot as evidenced in the lengthwise metallographic images of the samples. The two-dimensional simulation cannot capture the flip along the y-direction (010). The trailing edge flip location is calculated for Sample 1 and Sample 2; and is indicated by the yellow line. The melt-back depth is indicated by the green line while the instantaneous

laser heat-source is denoted by the purple plane. The flip height for Sample 1 is higher compared to Sample 2 that can be seen in the lengthwise metallographic images of the samples [Figures 23(a) and 23(b), respectively].

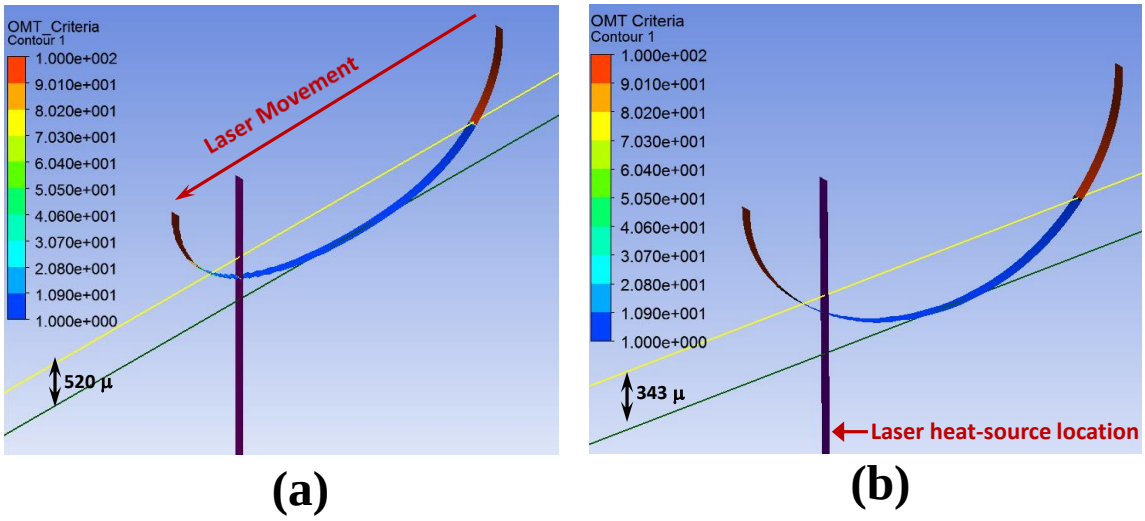

Figure 25. Orientation vector plot showing OMT for CMSX-4® (a) Sample 1 and (b) Sample 2 on the solid-liquid interface. The purple surface shows the instantaneous laser heat-source position.

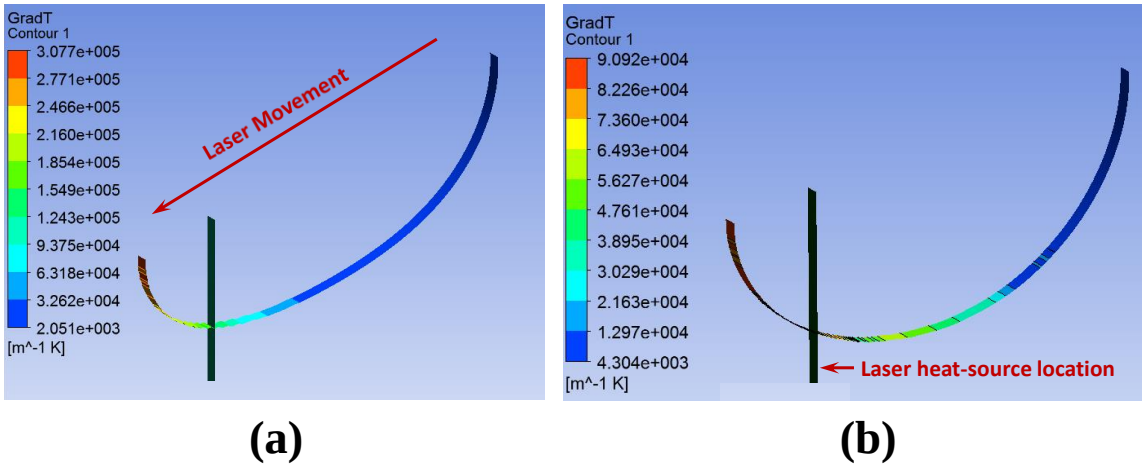

Figure 26. Temperature gradient at the solid-liquid interface for CMSX-4® (a) Sample 1 and (b) Sample 2. The green surface shows the instantaneous laser heat-source position.

Figures 26(a) and 26(b) show the temperature gradient contour for CMSX-4® Sample 1 and Sample 2 for a given position of the laser heat-source denoted by the green surface. The laser heat-source movement direction is marked by the red arrow in Figure 26(a). The leading edge shows a temperature gradient that is much higher compared to the trailing edge (Approximately 150 times higher).

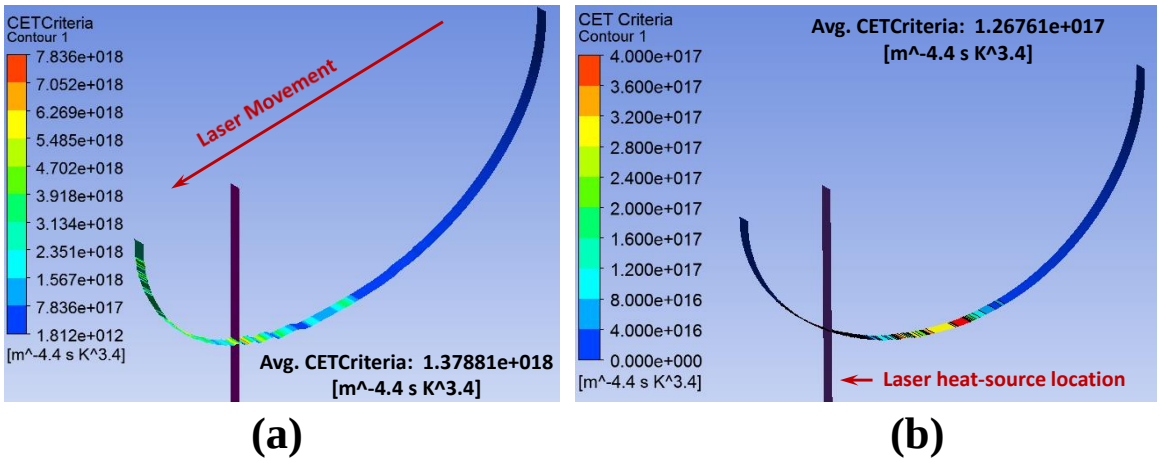

Figure 27. CET criterion plot for CMSX-4® (a) Sample 1 and (b) Sample 2 at a representative laser heat-source position. The green surface shows the instantaneous laser heat-source position.

This elevated temperature gradient at the leading edge reduces the surface tension coefficient significantly. Any change in temperature at the leading edge may affect the way loose powder is drawn towards the melt pool resulting in waviness in the deposit height. Figures 27(a) and 27(b) show the plot of the G^{n}_{hkl}/V_{hkl} ratio for CMSX-4® Sample 1 and Sample 2 at the same laser-heat source position. Figure 27(b) shows a lower value of G^{n}_{hkl}/V_{hkl} ratio. Hence, the model suggests a lower columnar height in Figure 27(b) that can be verified from the metallographic images as observed in Figures 28(a) and 28(b).

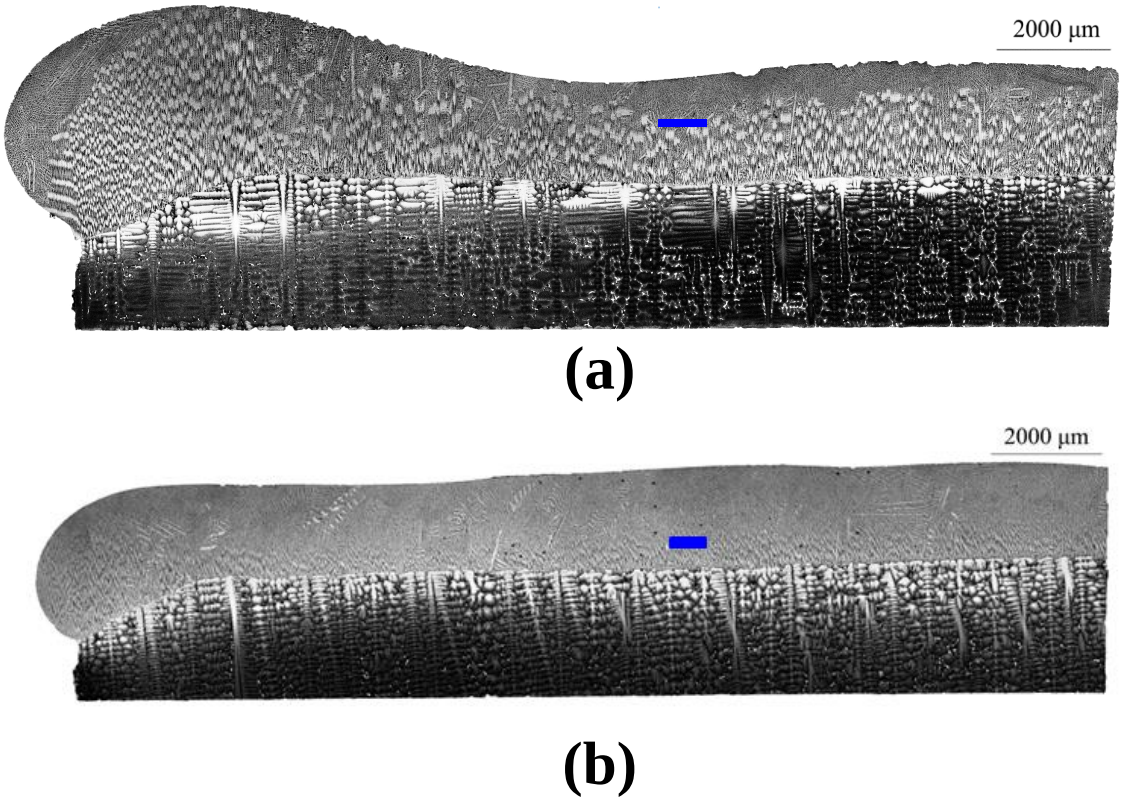

Figure 28. Experimental micrograph showing CET (indicated by blue line) for CMSX-4® (a) Sample 1 and (b) Sample 2 at laser heat-source position of 10.00 mm.

4.6 Summary

This chapter studies the fundamentals of SLE process to shed insights into the flow-thermal-microstructure-warpage evolution in SLE. The findings of this chapter can be used to in the future to improve the predictive capability in order to obtain user-specified microstructure and deposit properties. A CFD-based modeling scheme is developed to accurately capture the flow-physics in SLE. The model can predict the temperature distribution and melt pool behavior. The simulation platform also allows prediction of the CET by modeling the solidification microstructure.

The model is validated using the melt pool data obtained from the thermal imaging

camera as well as the experimentally obtained melt depth profile. The average melt pool temperature profile and melt pool size agree well with the simulated profile for EQ as well as SX deposits. Due to differences in the thermo-physical properties, the melt pool dynamics vary for different alloys. However, the leading and trailing edge temperature gradients, the formation of two rotational vortices, and the presence of higher velocity at the top surface are found for both EQ and SX deposits. This 2D simplification of the domain does not necessarily reduce accuracy. Hence, the 2D model facilitates assessment of the processing parameters using shorter computation time. Some of the key conclusions from this study are:

- The current work investigates the SLE process for two EQ deposits and two SX deposits. This methodology proved to be applicable to other alloys if reliable thermo-physical properties are available.

- The melt pool shows a range of velocities and temperature for different superalloys. The vortices also show different characteristics based on the thermo-physical properties. Such difference in vortices structure can significantly alter the way the loose powder is drawn inside the melt pool. Hence, it is concluded from the present research that the knowledge gained for one material through an AM system may not be readily applicable to other material systems.

- The CET and OMT phenomenon are investigated. The results show that time tracking of the solidification history is critical in predicting CET. An alternate approach to predict the OMT phenomenon, based on the temperature gradient, is presented here. The competition of differently oriented dendrites in the raster scan pattern, and the subsequent flip in the direction of the columnar orientation, occurs over a range of the ratio of the temperature

gradient in the [100] to the [001] directions.

- With knowledge of alloy-specific properties, the CET and OMT criterion can be developed to predict microstructural transitions in SLE of DS/SX alloys as functions of SLE processing parameters. This predictive capability enables control of the solidification microstructure in laser-based AM of DS/SX superalloys.

Chapter 5: SLE process development for EQ deposits

This chapter studies the feasibility of fabricating EQ or polycrystalline deposits by SLE. Two high-γ′ "non-weldable" alloys that are traditionally cast with EQ/DS microstructures namely IN100 and MAR-M247 are selected for investigations. MAR-M247 contains 13.7 wt. % refractory elements such as W, Ta, and Mo while IN100 contains only 3.0 wt. % of such elements. Hence, a comparison between the deposit characteristics of these two alloys fabricated using the SLE process sheds insights on the role of refractory elements in laser deposition of high-γ′ superalloys.

5.1 Study on IN100

IN100 is a nickel-base precipitation hardened, vacuum cast alloy that has a rupture strength through 1038 ^{o}C (1900 ^{o}F) [93]. Higher content of lighter elements such as Al and Ti and lower content of heavier elements such as refractory metals make IN100 particularly attractive on the basis of strength to density ratio. The alloy has been extensively used in the fabrication of turbine blades, vanes, and nozzles in the gas turbine engines. IN100 has a nominal density of 7750 kg/m^3 with melting range of 1260 – 1335 ^{o}C. The alloy exhibits excellent performance during cyclic testing and after 200 hours with 16 hours of heating and 8 hour of cooling cycle, the alloy showed 0.8% change in the weight [93].

The total Al + Ti content for IN100 is 11.0 wt. %. Hence, it is considered to be one of the most "difficult-to-weld" alloys. Due to the "non-weldability" of this alloy, a limited

research results are available on this alloy system [5]. The micro-laser aided additive manufacturing (micro-LAAM) process showed successful depositions of IN100 on cast IN100 substrates [94]. However, this process showed limitation with regards to the deposit thickness due to low laser power.

5.1.1 Materials

The SLE process is carried out on rectangular EQ cast IN100 substrate coupons with dimensions of 35.56 mm x 6.86 mm x 2.54 mm. Argon gas-atomized IN100 powder produced by Pratt & Whitney – HMI Metal Powders (Clayville, NY) is used in this study. The powder composition is given in Table 4.

Table 4. Composition of the IN100 powder (wt. %).

	Cr	Co	Mo	Al	Ti	B	C	Zr	Ni
IN100	10	15	3	4.7	5.5	0.014	0.18	0.06	Bal

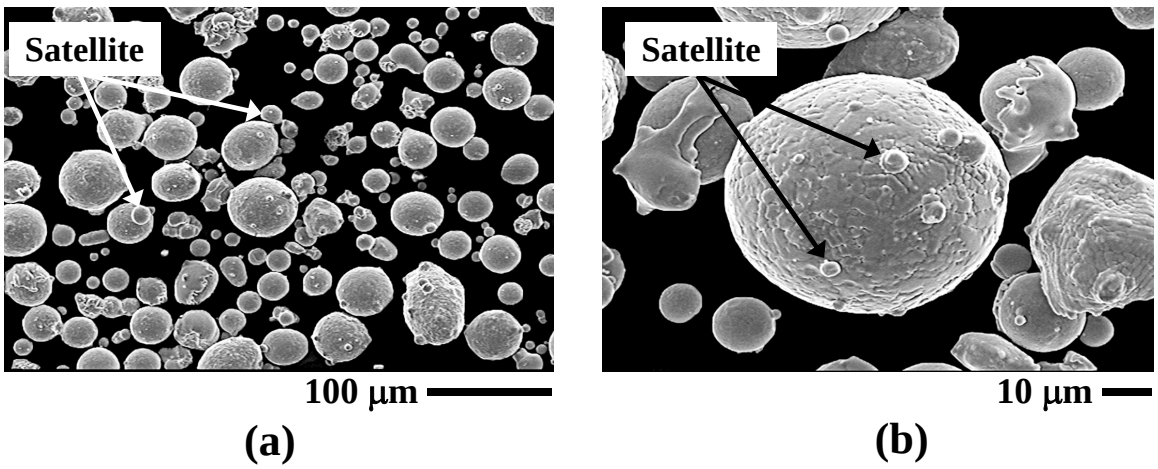

Figure 29. SEM image of the (a) IN100 powder and (b) IN100 powder particle showing the surface dendritic microstructure.

The IN100 powder particles are mostly spherical with particle diameter varying from 20 to 60 μm as shown in Figure 29(a). Figure 29(b) illustrates the morphology of a single powder particle showing dendritic microstructure on the particle surface. A few powder particles show secondary satellites. The powder is mounted in Bakelite and polished to a mirror finish. The cross-section is analyzed under an optical microscope for the inspection of internal porosity, revealing that the powder contains a significant number of pores [42].

5.1.2 Deposit characteristics

The longitudinal cross-sections of two representative SLE-processed IN100 samples are shown in Figures 30(a) and 30(b) [95]. As illustrated, the crack-free and dense deposit is continuously bonded to the substrate along the entire length of the substrate without any interface fusion defects. The melt pool is found to be stable and non-oscillating during the laser processing as shown in Figures 30(a) and 30(b). The samples do not show any warpage during the laser processing. Overall, SLE is able to deposit more than 1000 μm thick IN100 in a single pass.

The microstructures of the as-deposited IN100 reveal the presence of columnar and equiaxed dendrites as shown in Figure 30(c). The deposit region shows a finer microstructure compared to the substrate region as shown in Figure 30(d). The microstructural refinement may be attributed to the localized heating and rapid cooling due to the high-speed heat source. The microstructure of the deposited region reveals dendrite segregation patterns as shown in Figure 30(d). As shown in Figures 30(a) and 30(b), an insignificant number of pores are observed in the deposit region. A design-of-experiments (DoE)-based optimization study demonstrates that the pore count may be reduced by increasing the volumetric energy density

by means of reducing the scan spacing, increasing the power or reducing the scan speed [42]. An increase in the volumetric energy density expands the melt pool allowing it to overlap with the solidified region deposited in the previous pass. Thus, the pores formed in the previous pass are re-melted, and thereafter, when re-solidification takes place, there are less chances for the formation of pores again.

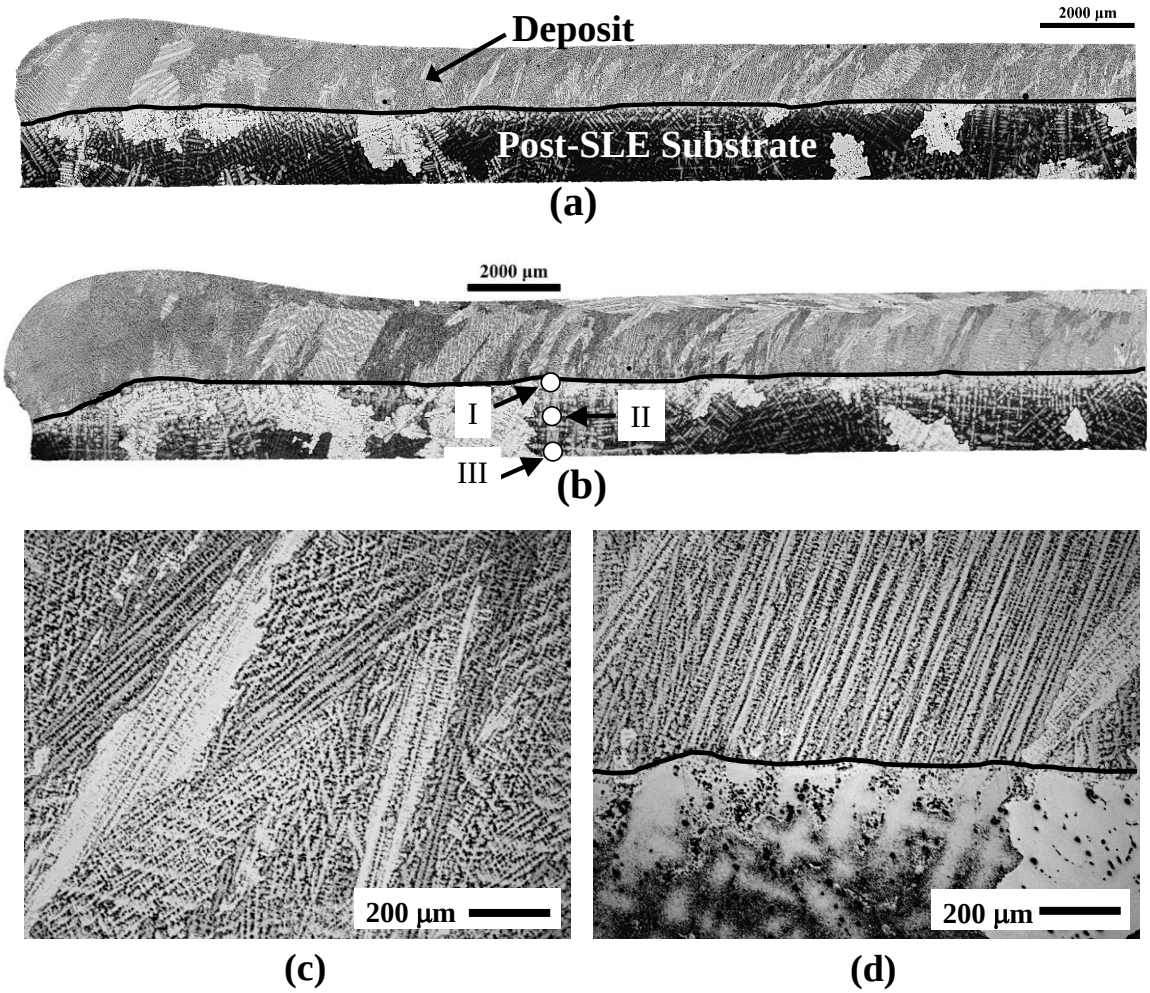

Figure 30. OM image showing (a) – (b) longitudinal cross-sections of the SLE deposited IN100 on IN100 substrate, (c) the IN100 microstructure in the deposit region, and (d) the metallurgical bond between the substrate and the deposit. The black line in (a), (b), and (d) represents the substrate-deposit interface.

Figures 31(a) and 31(b) compare the XRD profiles for the pre-alloyed IN100 powder

with the IN100 deposit. The XRD spectra for the IN100 powder is coincident with solid solution γ-FCC NiCr (a = 0.359 nm) and exhibits a prominent (111) peak as shown in Figure 31(a). The diffraction peaks occurred at 2θ = 44° and 51 indicating the diffraction of (111) and (200) planes of the γ matrix. Both γ and γ′ phases have cubic structures with less than 0.5% difference in lattice parameters for most commercial nickel-base superalloys, and are therefore, hard to differentiate [94]. A major peak at around 51° indicates a strong presence of a preferred crystal growth along the build direction in the as-deposited IN100 as shown in Figure 31(b).

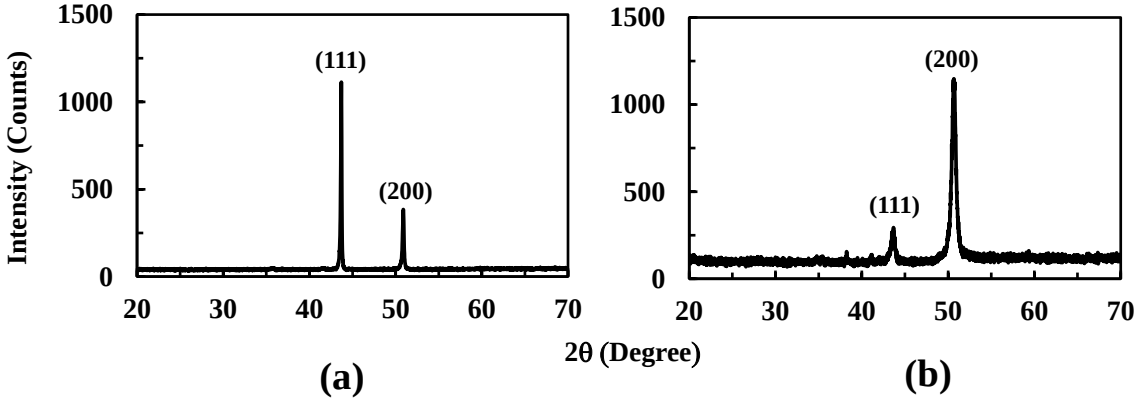

Figure 31. XRD profile of the (a) pre-alloyed IN100 powder and (b) SLE deposited IN100.

5.1.3 Microstructures

The major constituents of the microstructure of the SLE deposited IN100 are the γ matrix, the γ′ precipitates in the γ matrix, the eutectics, and the carbide precipitates. Figures 32(a) and 32(d) illustrate SEM images showing the major constituents in the substrate and deposit regions, respectively. In the deposit region, in addition to discrete carbide precipitates, a few residual carbide precipitates embedded in the eutectic pools are found as shown in Figure 32(d). The carbide precipitates are of order 50 – 200 nm in the deposit region whereas in the

substrate, they are of order 1 – 5 μm.

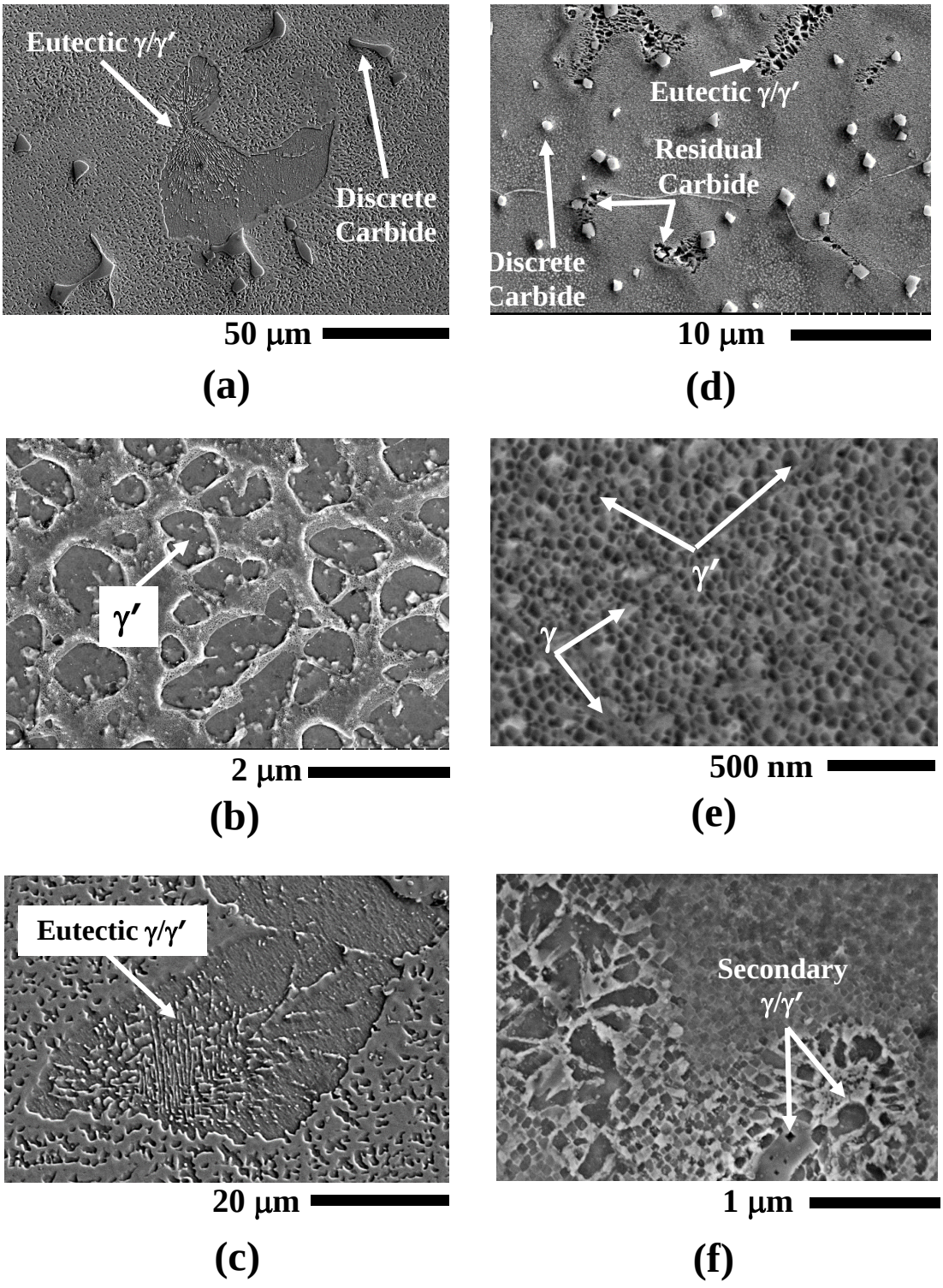

Figure 32. SEM image showing (a) the major constituents, (b) the γ/γ′ structure, and (c) the eutectic region in the substrate. SEM image showing (d) the major constituents,

(e) the γ/γ′ structure, and (f) the eutectic region in the deposit.

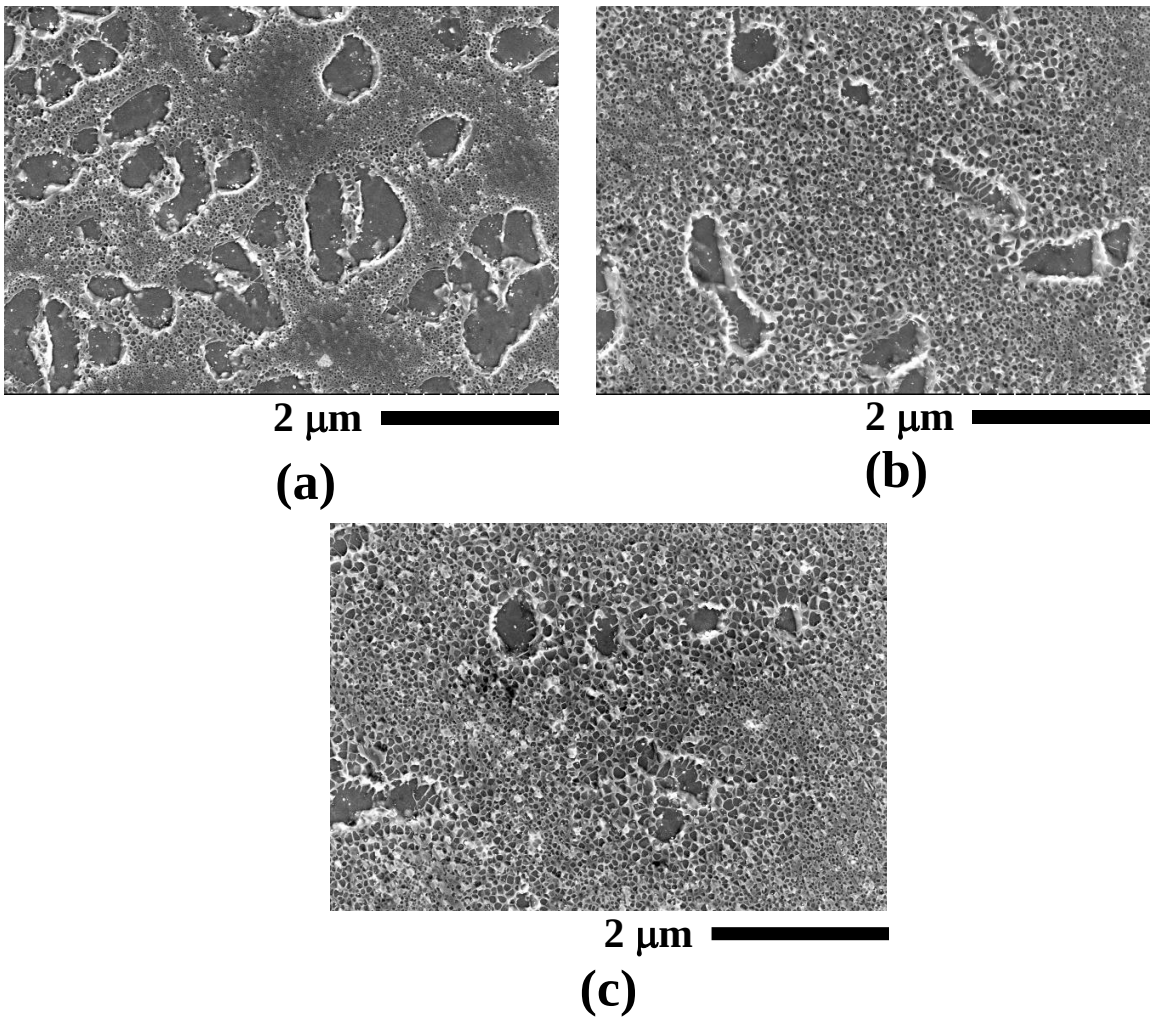

Figure 33. SEM image showing the γ/γ′ structure in the post-SLE substrate at (a) Location III, (b) Location II, and (c) Location I of Figure 30(b).

As shown in Figure 32(b), the primary γ′ precipitates show a characteristic dimension in the range of 1 – 2 μm in the substrate region whereas, in the deposit region, the γ′ precipitates are in the range of 50 nm, as shown in Figure 32(e). Overall, the deposit region shows approximately 95% reduction in the γ′ size. Figures 32(c) and 32(f) illustrate the γ/γ′ morphology in the eutectic regions of the substrate and the deposit, respectively. The microstructures in Figure 32(c) illustrate the irregular shaped γ/γ′ precipitates in the substrate

eutectic region. The size of the eutectic regions is of order 25 – 75 μm in the substrate, as shown in Figure 32(c). The finer cubic γ/γ′ precipitates are of order 50 – 100 nm near the eutectic region in the deposit, as shown in Figure 32(f). The larger γ/γ′ precipitates in the deposit eutectic region are of order 200 – 400 nm, as shown in Figure 32(f). The eutectic region in the deposits also shows secondary γ/γ′ microstructure with the γ′ size in the range of 10 – 20 nm [Figure 32(f)].

The microstructure of the substrate region showed significant changes after the SLE process was conducted. Figures 33(a), 33(b), and 33(c) show the γ′ structure in the post-SLE substrate at different locations [marked in Figure 30(b)] along the direction of dominant thermal gradient i.e. [001]. At Location III, the γ′ structure in the post-SLE substrate shows similar size and shape compared to the substrate as shown in Figures 33(a) and 32(b), respectively. Here, the substrate and the post-SLE substrate show a bimodal γ′ distribution with the primary γ′ precipitates showing a characteristic dimension of order 1.5 μm and the secondary γ′ precipitates showing a characteristic dimension of order 100 nm. However, at Locations II and I, the post-SLE substrate shows the collapse of larger γ′ precipitates and moves from a bimodal distribution to a single mode distribution due to the heat effect during the SLE process.

5.1.4 Elemental segregation

Figures 34(a) and 34(b) illustrate EDS maps of a representative region in the IN100 substrate and the deposit region, respectively. Note that the eutectic region, the discrete carbide precipitates, and the residual carbide precipitates are marked by E, DC, and RC, respectively. In the substrate, Ni, Al, and Ti show strong segregation to the eutectics. Co, Cr, and Mo show

strong segregation to the core (Figure 34(a)). Ti, Mo, Zr, B, and C segregate to the carbides whereas Ni, Al, and Co are present in the carbide precipitates in trace amounts (Figure 34(a)).

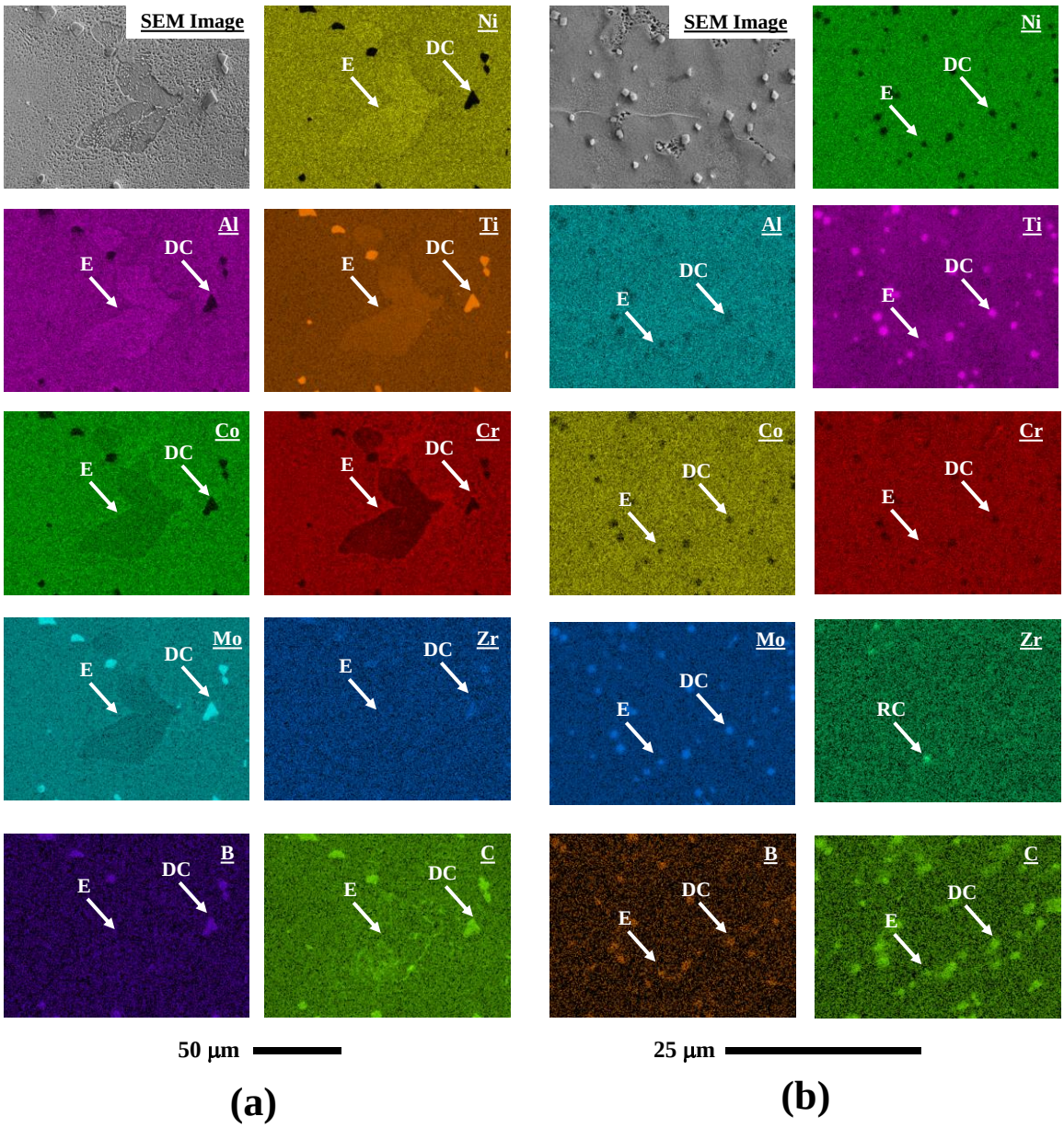

Figure 34. SEM-EDS elemental maps of a representative region in the (a) substrate and (b) deposit region.

In the deposit region, however, no elements show strong segregation to the eutectics as shown in Figure 34(b). The elements show similar segregation behavior to the carbide

precipitates in the substrate and the deposit. The only noticeable difference is with Zr that shows segregation to the residual carbide precipitates in the deposit region as shown in Figure 34(b).

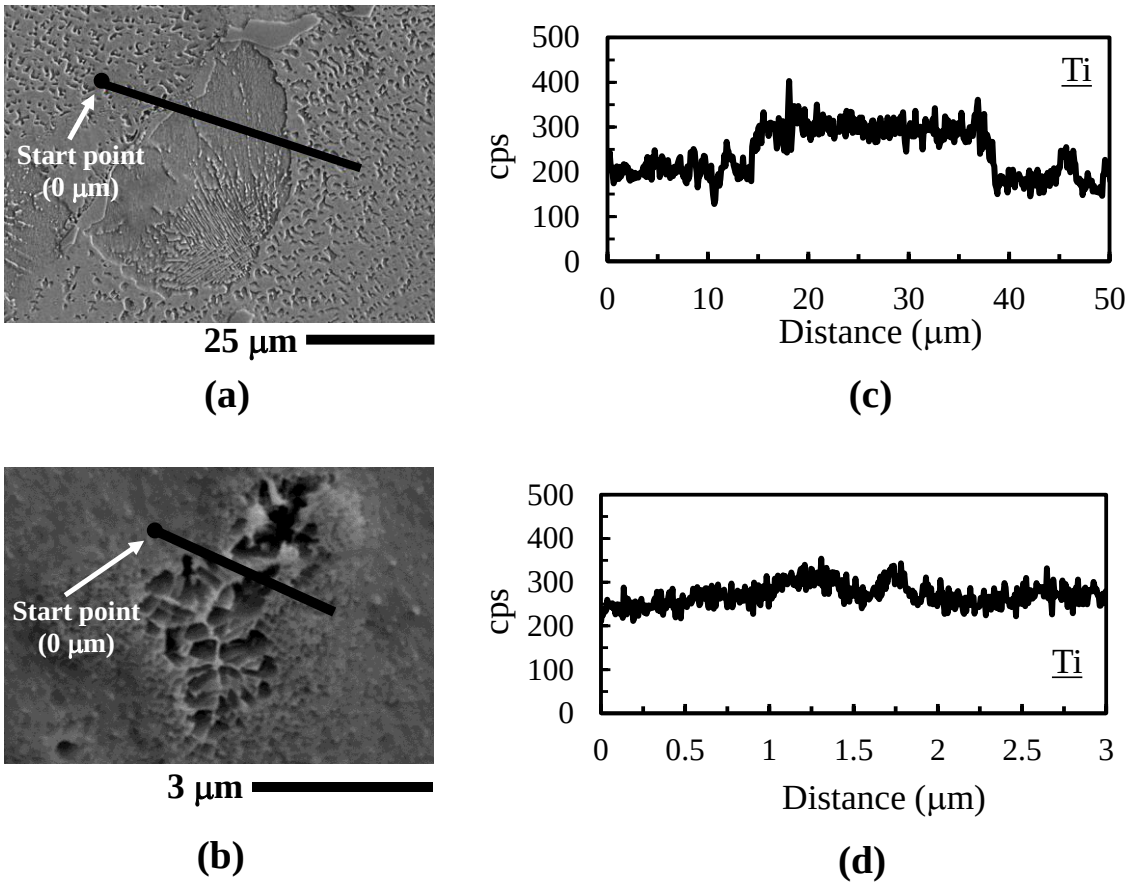

Figure 35. SEM image of a representative line scan domain in the eutectic region of (a) substrate and (b) deposit. EDS line profile of Ti across a representative eutectic region in the (c) substrate and (d) deposit.

In order to quantitatively characterize the elemental segregation in the eutectic regions, EDS line scans are performed across representative eutectic regions in the substrate and deposit, respectively (Figures 35(a) and 35(b)). The line profiles of a representative element (Ti) across a eutectic region in the substrate and the deposit are shown in Figures 35(c) and 35(d), respectively.

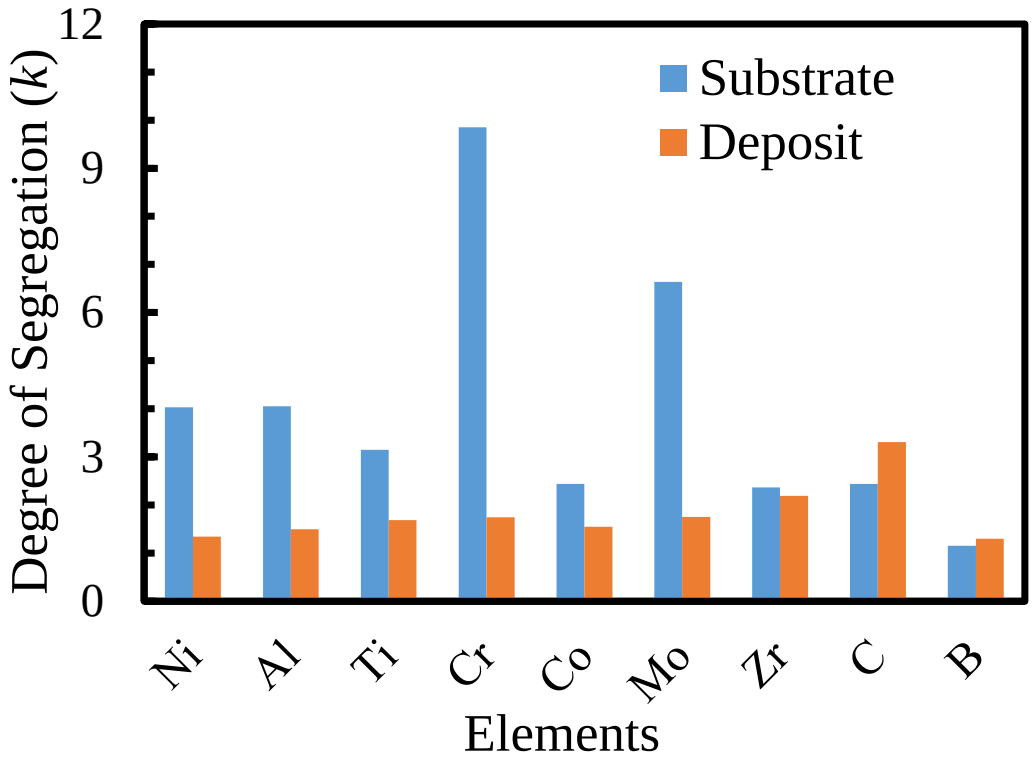

Figure 36. Degree of segregation (k) of various alloying elements across representative eutectic pools in the substrate and the deposit.

From the elemental line profiles, the maximum and the minimum counts are extracted and a segregation parameter is defined as degree of segregation (k) = maximum cps/minimum cps (where cps denotes counts per second). The k values for various elements are plotted in Figure 36 for the substrate and the deposit region. In comparison to the bulk alloy composition, the γ/γ′ eutectic phase shows strong elemental segregation for the substrate. In the deposit region, the degree of segregation is considerably lower.

IN100 contains about 0.18 wt. % C and 0.014 wt. % B resulting in the formation of carbide and boride precipitates in the deposit region. The blocky type of carbide precipitates are predominantly observed in the deposit region. The deposit region also shows a few residual carbide precipitates that are embedded in the eutectic pools as shown in Figure 37(a). Figure

37(b) illustrates the composition of 4 different carbide precipitates in the deposit region. The carbides are found to be rich in Ti, Ni, Mo, and Co; however, trace amounts of Cr and Al are also present. Zr only shows up in the residual carbide precipitates as shown in Figure 35(b).

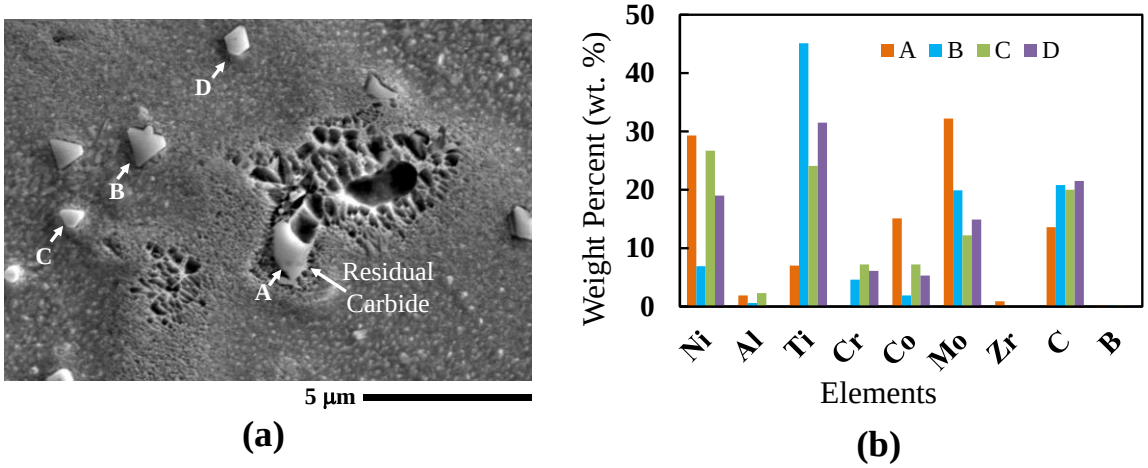

Figure 37. (a) SEM image of the carbide precipitates in the deposit region. (b) Composition of the carbide precipitates (in wt. %).

5.1.5 Vickers microhardness

The microhardness of an alloy is a strong function of the γ′ size, distribution, and volume fraction and the residual stresses generated during the laser processing. In the present study, microhardness results indicate higher hardness values in the deposit region than in the substrate. Figure 38(a) shows three different representative indentation marks in the deposit region and interface region, respectively. Figure 38(b) reports the average hardness values in the deposit, substrate, and interface regions of a representative IN100 sample. The average hardness value of the cast substrate is of order 390±7 HV. The hardness increases to about 405±11 HV near the interface region. The deposit region shows hardness values of order 430 HV±16.

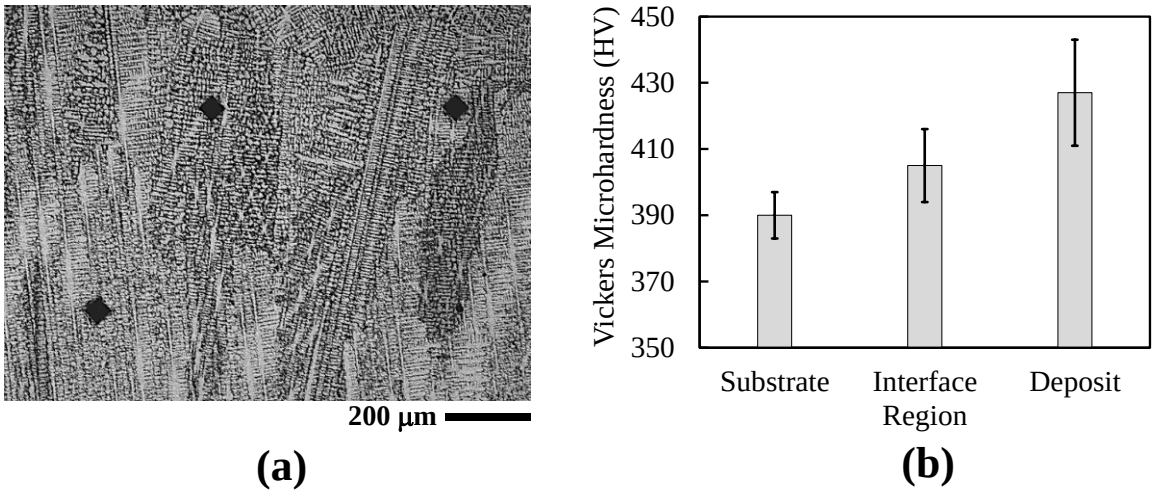

Figure 38. (a) Representative indentation marks in the IN100 deposit and (b) Variation of microhardness.

5.1.6 Conclusions on IN100

The SLE process is found to be capable of producing deposits of IN100 without any indications of cracking. The deposit region consists of the γ matrix, the secondary γ′ phase precipitates in the γ matrix, the eutectics, and the carbides. The deposit region shows a finer γ/γ′ microstructure compared to the substrate. Microhardness measurements demonstrate that the deposit region has approximately 10% higher HV values compared to the substrate. The deposit region also shows higher microstructural uniformity compared to the substrate. The degree of elemental segregation is considerably lower compared to the cast substrate.

5.2 Study on MAR-M247

MAR-M247 is nickel-base superalloy developed at the Martin Marietta Company in the 1970s [96]. Over the past several decades, this alloy has been extensively used in the production of several gas turbine hot-section components such as high-pressure turbine blades

and blade rings because of its excellent thermo-mechanical properties [97]. The alloy demonstrates high creep strength and good castability along with excellent oxidation and corrosion resistance at elevated temperatures [96]. It is a vacuum melted, cast superalloy with a high γ′ [Ni_3 (Al, Ti)] content (62 vol. %). The alloy contains a significant amount (13.7 wt. %) of refractory elements such as Ta, W, and Mo. The semi-coherent γ′ phase is the main strengthening phase, which precipitates in the nickel-rich γ matrix. The γ′ phase is solid-solution-strengthened by Co, Mo, W, and Cr. C, B, Zr, and Hf precipitate at the grain boundaries primarily in the form of carbides and borides contributing to improved creep performance. The presence of refractory elements (Ta + W + Mo), the addition of Hf, and the elemental segregation during solidification cause the formation of γ/γ′ eutectics and carbides in the interdendritic regions [98-100].

The total Al + Ti content for MAR-M247 is 7.0 wt. %, thus making it a "non-weldable" alloy. Limited literature is available on the AM-based processing of MAR-M247 primarily due to the "non-weldability" of this alloy. MAR-M247 was processed by the SLS process, and the results showed a directional epitaxial growth at the mold surface [78, 101]. Deposits of MAR-M247 were also obtained using the SLM process [102]. More recently, MAR-M247 was processed by the high-temperature SLM (HT-SLM) process through which crack-free deposits were obtained once the powder bed was preheated up to about 1200 ^{o}C [103]. The low carbon derivative of MAR-M247, CM247LC was processed by several researchers using the SLM process [104, 105]. However, the deposits were plagued with long and short cracks.

5.2.1 Material

The SLE process is carried out on rectangular EQ cast MAR-M247 substrate coupons

having dimensions of 31.50 mm x 5.84 mm x 2.54 mm. The MAR-M247 powder used in this study is an argon gas-atomized product made by the Praxair Surface Technologies. The morphology, size distribution, and cross-sections of the powder are analyzed using OM and SEM. The MAR-M247 powder particles are mostly spherical as shown in Figure 39(a). The powder is mounted in Bakelite and polished to a mirror finish.

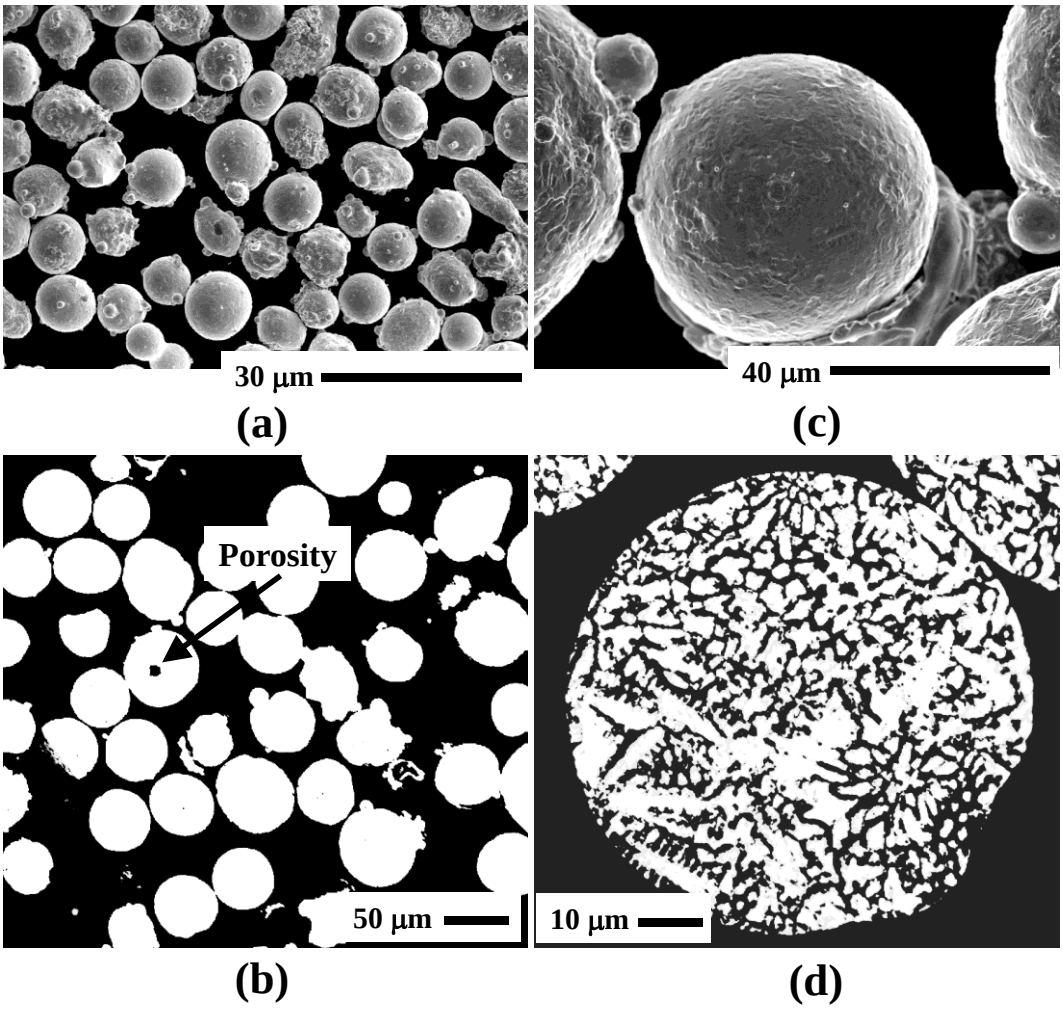

Figure 39. (a) SEM image of the MAR-M247 powder, (b) OM image of the MAR-M247 powder cross-section after polishing, (c) SEM image of a powder particle, and (d) OM image showing etched internal microstructure of a MAR-M247 powder particle.

The cross-section is analyzed under an optical microscope for the inspection of internal

porosity, and limited porosity is detected as shown in Figure 39(b). Figure 39(c) illustrates the morphology of a single powder particle showing the surface texture. The polished cross-section is etched to investigate the internal microstructure. Figure 39(d) illustrates the internal micro-dendritic structure of a MAR-M247 powder particle. The composition of the powder is reported in Table 5.

Table 5. Chemical composition of the MAR-M247 powder (wt. %).

MAR-M247	Cr	Co	Mo	W	Al	Ti
	8	10	0.7	10	6	1
	Ta	Hf	B	C	Zr	Ni
	3	1	0.015	0.15	0.05	Bal

5.2.2 Deposit characteristics

Figure 40(a) shows a representative longitudinal cross-section of an as-deposited MAR-M247 sample [106, 107]. The deposit is crack-free and dense in nature with an average deposit thickness of more than 1500 μm. Very few pores are observed and there is an excellent metallurgical bond between the substrate and the deposit regions as shown in Figure 40(a). The average depth of the melt-back region is of order 75 – 175 μm for all the SLE processed MAR-M247 samples. A shallow melt-back depth of approximately 100 μm ensures that the heat input to the substrate is minimal. Such shallow melt-back depth is beneficial in reducing the thermal stress accumulated within the melt-back region to avoid any crack formation. The absence of cracks in the current study vouches for the reduced thermal stress accumulation in the SLE deposited MAR-M247 samples.

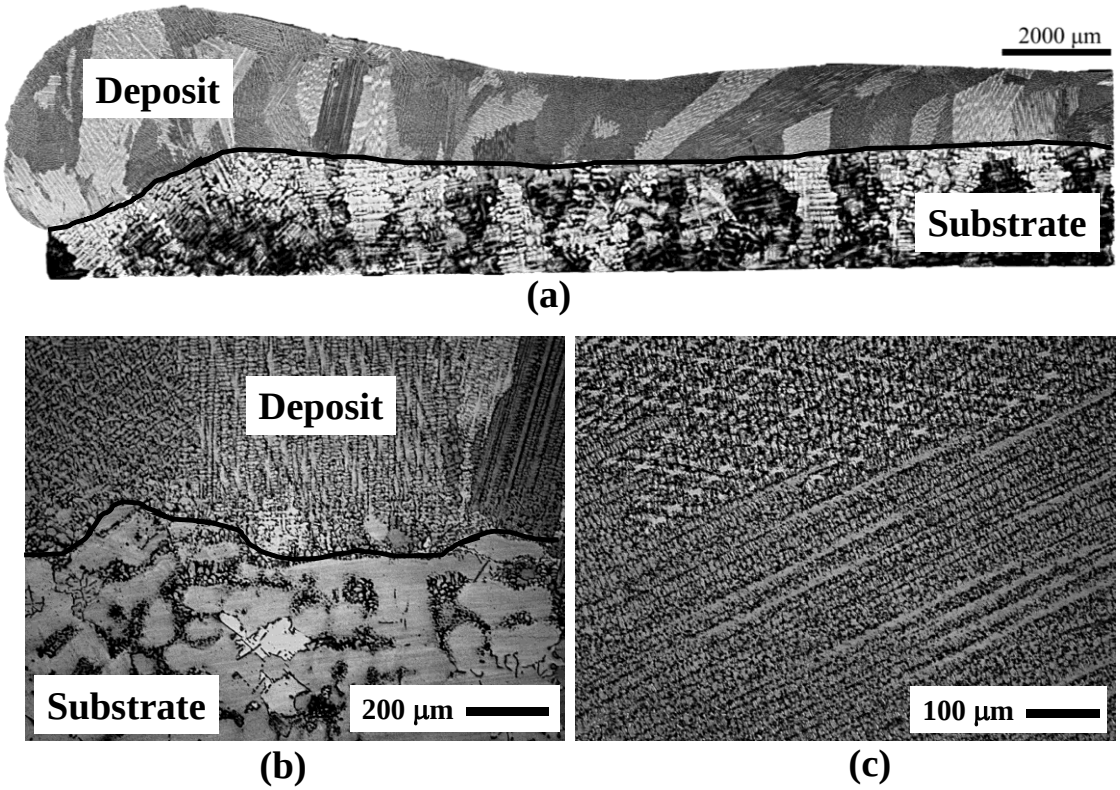

Figure 40. OM image of an as-deposited MAR-M247 sample showing (a) crack-free and dense deposit, (b) metallurgical bond between the substrate and the deposit, and (c) dendrite segregation pattern in the deposit region. The black like denotes the substrate-deposit interface.

The microstructure of the as-deposited MAR-M247 reveals the presence of columnar and equiaxed dendrites as shown in Figure 40(c). However, the microstructures within the melt-back region are different from other regions as shown in Figure 40(b). The deposit region shows a finer microstructure compared to the substrate region as shown in Figure 40(b). The microstructural refinement may be attributed to the localized heating and fast cooling due to the high-speed heat source. The microstructure of the deposited region reveals dendrite segregation patterns as shown in Figure 40(c). Due to the segregation of heavier elements such as W and Mo at the dendrite core and enrichment of the lighter elements such as Al and Ti in the interdendritic region, the dendrite region appears bright after etching as illustrated in Figure 40(c).

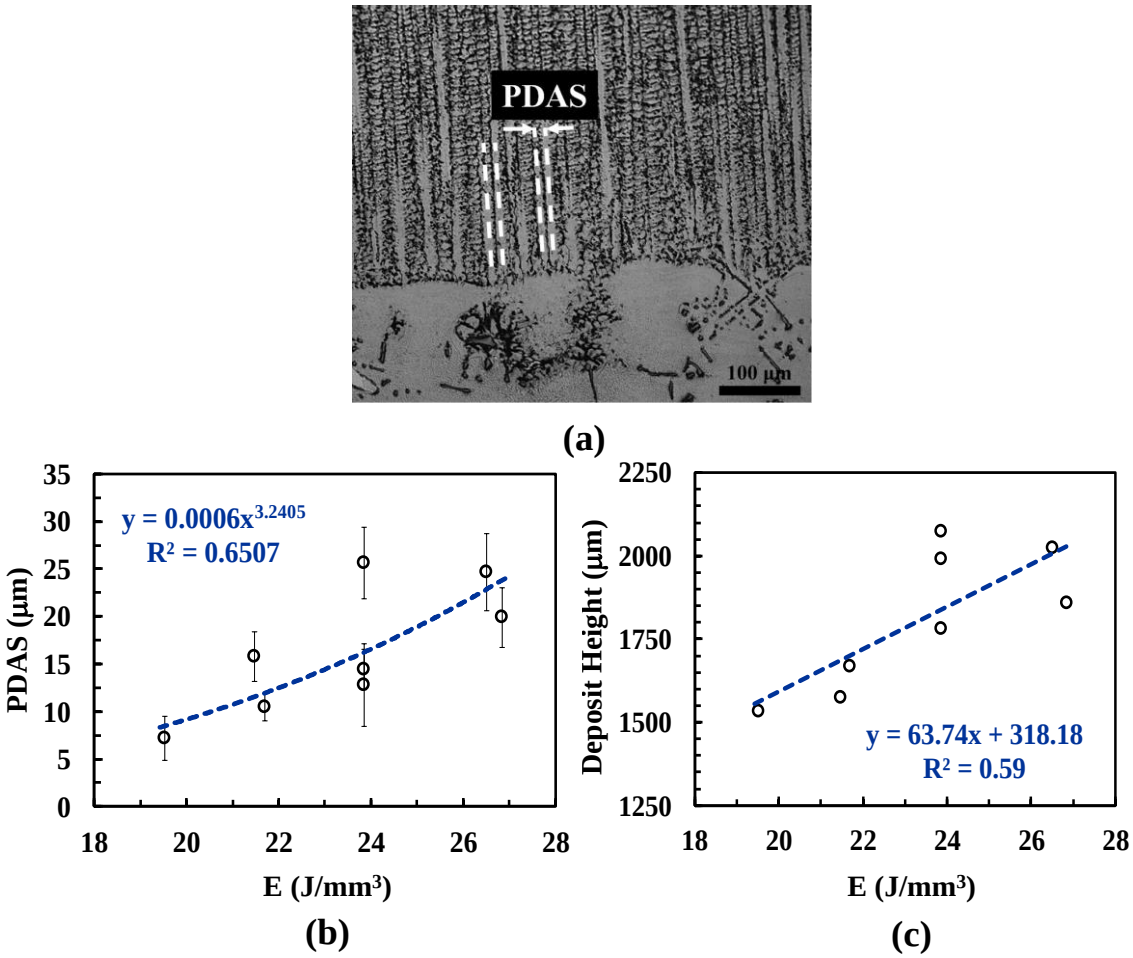

Figure 41. (a) OM image showing two representative measurement locations for PDAS. Effect of E on the (b) PDAS and (c) average deposit height.

The laser power (P) and the scan speed (V_S) are varied in the present study. All samples are run with a scan spacing (SS) of 25.4 µm to account for the smaller beam diameter of the fiber laser [108]. The powder layer thickness (t_p) is kept as 1650 mm. A new measure is defined based upon the SLE processing parameters – the scan energy density, $E = \frac{P}{SS \times V_S \times t_p}$.

Figure 41(a) illustrates a representative microstructure of the SLE deposited MAR-M247 showing columnar dendrites. The columnar dendrites grow in the [001] direction and undergo change to EQ near the top surface.

The statistical analysis on the PDAS of the columnar dendrites is investigated for each sample in the longitudinal sections. A representative measurement is shown in Figure 41(a). For each sample, 20 measurements are performed and the average PDAS values are calculated. Figure 41(b) shows the effect of E on the PDAS. For the SLE deposited MAR-M247, the PDAS increases with E following a power-law relationship as shown in Figure 41(b). Figure 41(c) shows the effect E on the average deposit height. With an increase in E, the melt pool extends laterally and transversely allowing more powder to fall inside the melt pool, and thereby, increasing the deposit height.

Figure 42 shows the longitudinal cross-section of a heat-treated MAR-M247 sample [109]. Very few pores are observed and the sample does not show any evidence of cracking after the heat treatment. The zoomed view of the substrate-deposit interface region is shown in Figures 43(a) and 43(b) for the as-deposited and the heat-treated samples, respectively. Figure 43(a) shows an epitaxial morphology where the columnar dendrites grow in the [001] direction.

The static recrystallization temperature of nickel-base alloys is in the range of 1000 – 1100 °C indicating that if a sample is exposed to a temperature over 1000 °C for sufficient time, recrystallization will take place and the deformed and elongated grains will be transformed into finer equiaxed grains [110]. In the present experiment, the recrystallization of the SLE fabricated MAR-M247 occurs as the heat treatment temperature is higher than 1000 °C. No grain boundary or grain interior incipient melting is observed here. It is maybe due to the finer substructure and the absence of low melting point precipitates such as eutectics at grain boundaries and grain interiors.

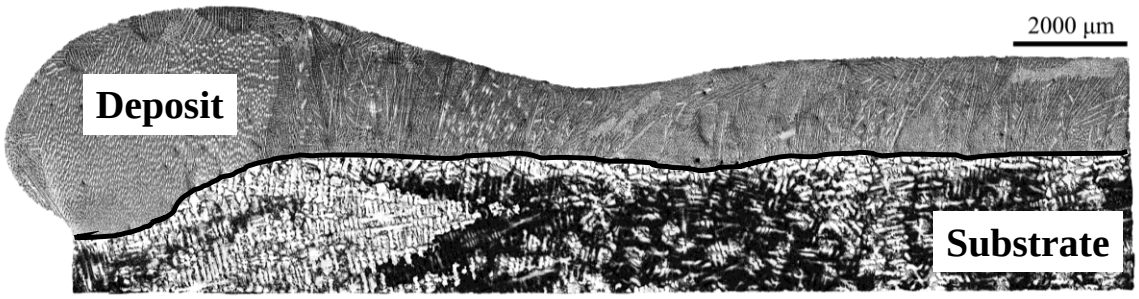

Figure 42. OM image of a heat-treated MAR-M247 sample showing crack-free and dense deposit. The black line denotes the substrate-deposit interface.

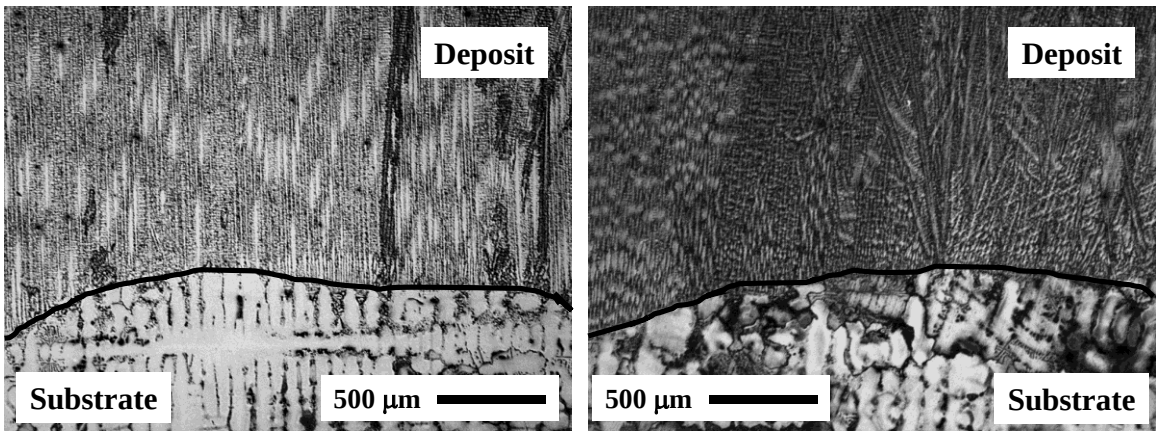

Figure 43. OM image showing the interface microstructure (a) for the as-deposited sample, and (b) for the heat-treated sample. The black line denotes the substrate-deposit interface.

5.2.3 Microstructure

The major constituents of the SLE-processed microstructure of MAR-M247 are the γ matrix, the γ′ precipitates in the γ matrix, the eutectics, and the carbides. Figure 44(a) illustrates an SEM image of the deposit region showing the major constituents in an as-deposited sample. Figure 44(b) illustrates the major constituents in the SLE deposited MAR-M247 after heat treatment. The eutectic volume fraction is visibly reduced after the heat treatment process as shown in Figure 44(b).

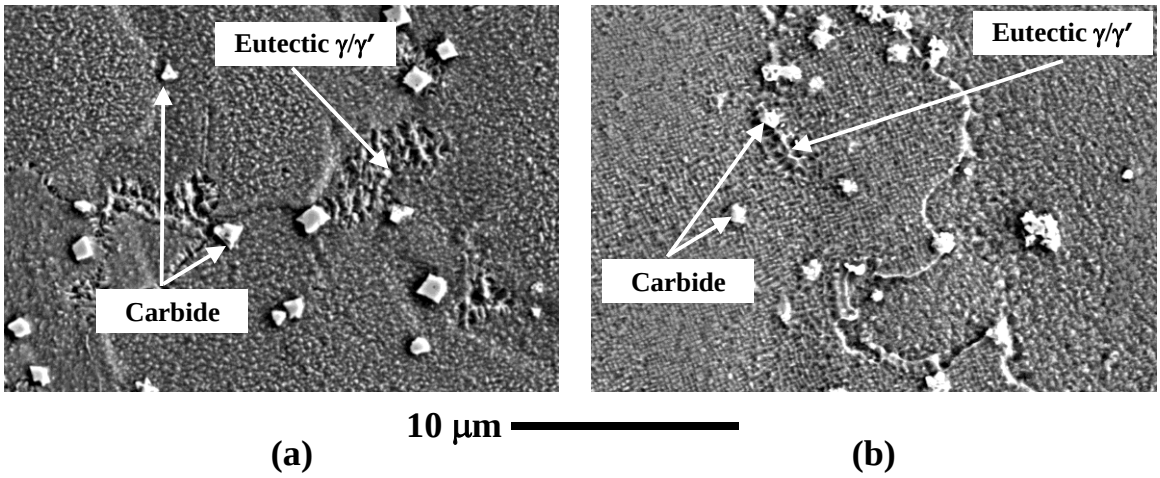

Figure 44. SEM image showing morphologies of various constituents of the SLE processed MAR-M247 samples in the deposit region – (a) as-deposited sample and (b) heat-treated sample.

The volume fraction of the eutectics in the SLE processed deposit is calculated using stereological techniques and is found to be ~ 4±1% for the as-deposited samples [111]. For the heat-treated samples, the eutectic volume fraction is less than 0.5%. The standardized heat treatment procedure originally developed for investment-cast MAR-M247 components proves to be beneficial for the AM fabricated MAR-M247 samples as well. Microstructural uniformity is achieved as the heat treatment that typically involves holding the alloy at sub-solvus temperatures for a prolonged period of time is able to precipitate fine and uniform γ′ phases within the γ matrix.

In the substrate region, the primary γ′ precipitates show a characteristic dimension in the range of 2 μm as shown in Figure 45(a), whereas in the deposit region, the γ′ precipitates are in the range of 50 nm as shown in Figure 45(b). Figure 45(c) illustrates the γ′ size distribution in the heat-treated sample. The primary γ′ size is of order 100 nm in the heat-treated samples. Microstructural refinement in the deposit region is visible from Figures 45(a) and 45(b). The

deposit region shows approximately 40x reduction in the γ′ size for the as-deposited sample compared to the cast substrate.

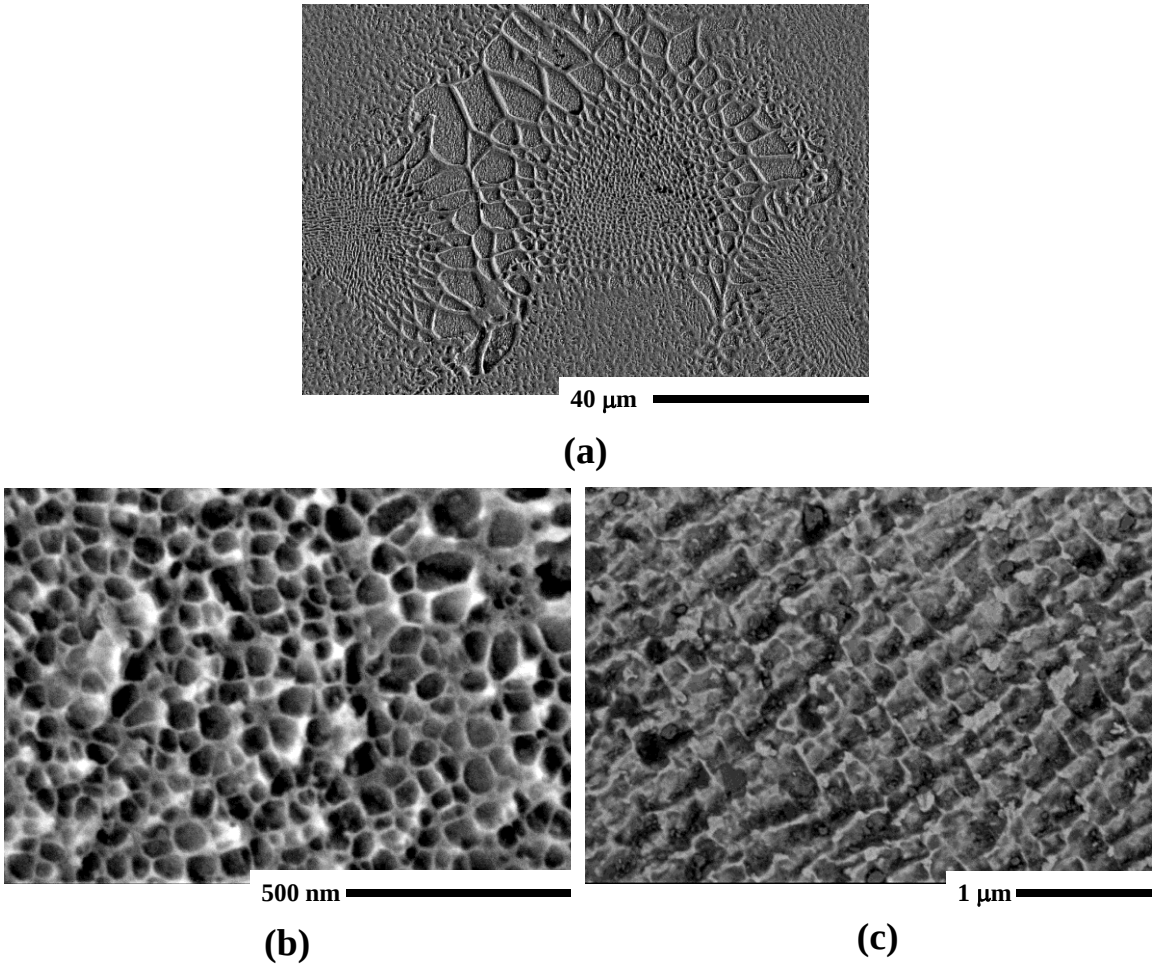

Figure 45. SEM image showing the γ/γ′ morphology in the (a) substrate region, (b) deposit region of an as-deposited sample, and (c) deposit region of a heat-treated sample.

The performance of a material system directly depends on the microstructure. The presence of γ′ precipitates is critical for superalloy performance as they help withstand high-temperature exposure by retaining the desired microstructure for a prolonged period of operation. The lattice mismatch is an important factor that determines the morphology of the γ′ precipitates [112]. A higher lattice mismatch and a higher interfacial area between the γ/γ′

phases improves the material properties of the microstructure [112]. The SLE-deposited MAR-M247 shows mostly polygonal precipitates similar to the cast substrate. However, there is an increase in the interfacial area between the γ and γ′ phases in the SLE deposited MAR-M247 samples indicating that the SLE-processed samples may possess superior mechanical properties compared to the cast substrate.

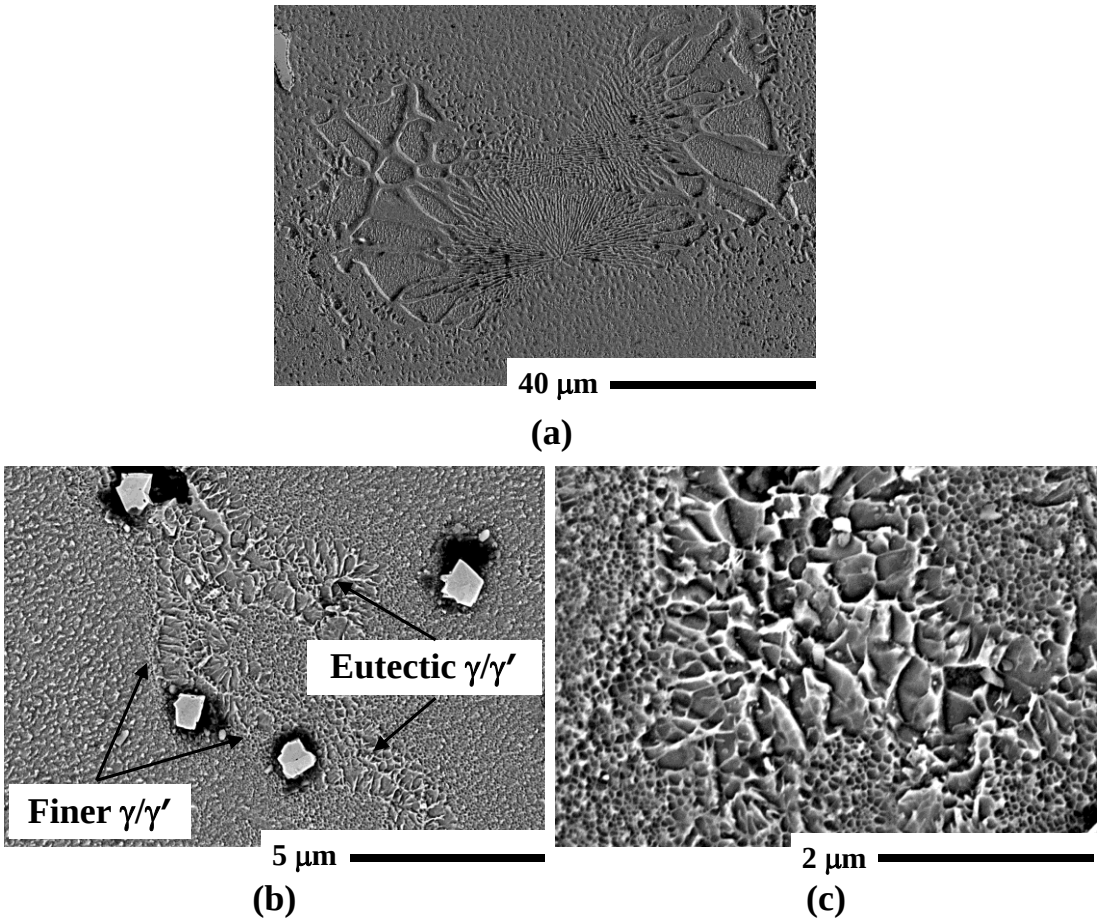

Figure 46. SEM image showing (a) morphology of the γ/γ′ phases in the eutectic regions in the substrate region, (b) morphology of the eutectic γ/γ′ in the deposit region of an as-deposited sample, and (b) zoomed view of the γ/γ′ phases in the eutectic region of an as-deposited sample.

The γ/γ′ precipitates in the eutectic regions of the substrate are of order 4 – 10 μm as shown in Figure 46(a). Typically, the γ′ forming elements i.e. Al and Ta enrich in the melt,

while the elements W and Cr enrich in the dendrites. Thus, as solidification progresses towards the final stage, large γ′ precipitates begin to form in the interdendritic regions. These are commonly called eutectic islands or eutectics. The larger γ/γ′ precipitates are of order 200 – 400 nm in the as-deposited samples as shown in Figure 46(b). Figure 46(c) illustrates the zoomed view of a eutectic region. The finer cubic γ/γ′ precipitates are of order 50 – 100 nm near the eutectic region as shown in Figure 46(c).

Modeling the evolution of the size distribution of a dispersed secondary phase precipitate during heat treatment is of immense scientific and commercial interest. One of the most significant contributions to the field of coarsening was made jointly by Lifshitz and Slyozov and by Wagner [113, 114]. It was shown theoretically that the distribution of precipitate size (D) reaches a steady state and follows the Lifshitz–Slyozov–Wagner (LSW) distribution. The LSW density function (f) is written as:

Equation 14. LSW distribution function.

$$f\left(\frac{D}{<D>}\right)=\frac{4}{9}\left(\frac{D}{<D>}\right)^{2}\left(\frac{3}{3+\frac{D}{<D>}}\right)^{\frac{7}{3}}\left(\frac{1.5}{1.5-\frac{D}{<D>}}\right)^{\frac{11}{3}}\exp\left(\frac{\frac{D}{<D>}}{\frac{D}{<D>}-1.5}\right),\ 0<\frac{D}{<D>}<1.5$$

$$\text{where } f\left(\frac{D}{<D>}\right)=0,\ \ \left(\frac{D}{<D>}\right)>0$$

The probability density function is for the normalized particle size, i.e., D/<D>, and <D>, the population average, is the only parameter to be estimated or calculated. In the current study, to compare the size of the primary γ′ precipitates, their equivalent diameters are calculated. The equivalent diameter, in this study, is defined as $D = (A/\pi)^{0.5}$, where A is the area of a γ′

precipitate determined by measuring the perpendicular sides of an individual precipitate.

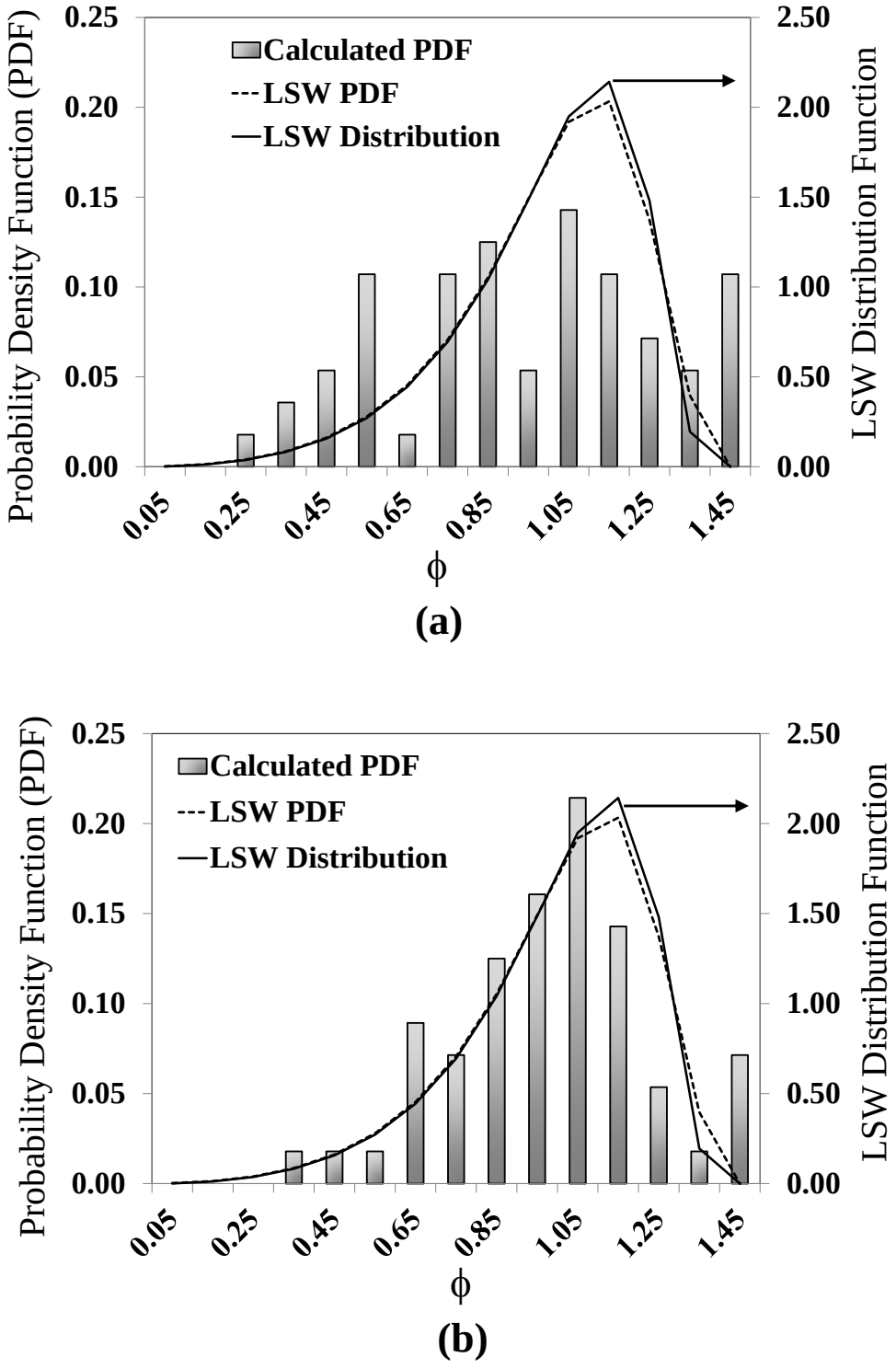

Figure 47. Particle size distribution (PSD) for the γ′ precipitates in the deposit region – (a) as-deposited MAR-M247 sample and (b) heat-treated MAR-M247 sample.

The average equivalent diameter, <D>, is obtained by calculating the mean of ~100 γ′ precipitates. The normalized diameter, ϕ, is defined as D/<D>.Figure 47(a) compares the γ′ particle size distribution (PSD) for the as-deposited MAR-M247 sample with the theoretical LSW distribution. The SLE processed PSD of the γ′ precipitate differs considerably from the theoretical LSW distribution. This may be due to the fact that the size of the γ′ precipitates in the interdendritic regions is found to be larger than those present within the dendrite regions due to the elemental segregation. Note that while performing this calculation, the γ/γ′ precipitates in the eutectic pools are not considered. Figure 47(b) illustrates the γ′ PSD for the heat-treated sample. The γ′ size shows a closer match to the theoretical PSD for the heat-treated sample.

During laser processing, precipitation of the γ′ phases occurs by the nucleation and growth from a supersaturated solution. In the end, a dispersion of the γ′ precipitates embedded in the γ matrix is obtained. Thermodynamically, this state does not satisfy the minimum energy requirement because of the excess surface energy represented by the γ matrix/γ′ precipitate ensemble due to the fast heating and cooling inherent in any AM-based processing. In a favorable environment, the system, therefore, continues to evolve to the state where the surface energy is lowered as much as possible. In general, the Ostwald ripening or the secondary precipitate coarsening is a diffusion-controlled process, and therefore, slow. During heat treatment, the sample is held at a sub-solvus temperature for a prolonged period. Thus, heat treatment provides an avenue for the system to lower the surface energy, and therefore, after the heat treatment, the PSD of the γ′ precipitates follows the theoretical LSW distribution closely.

5.2.4 Elemental segregation

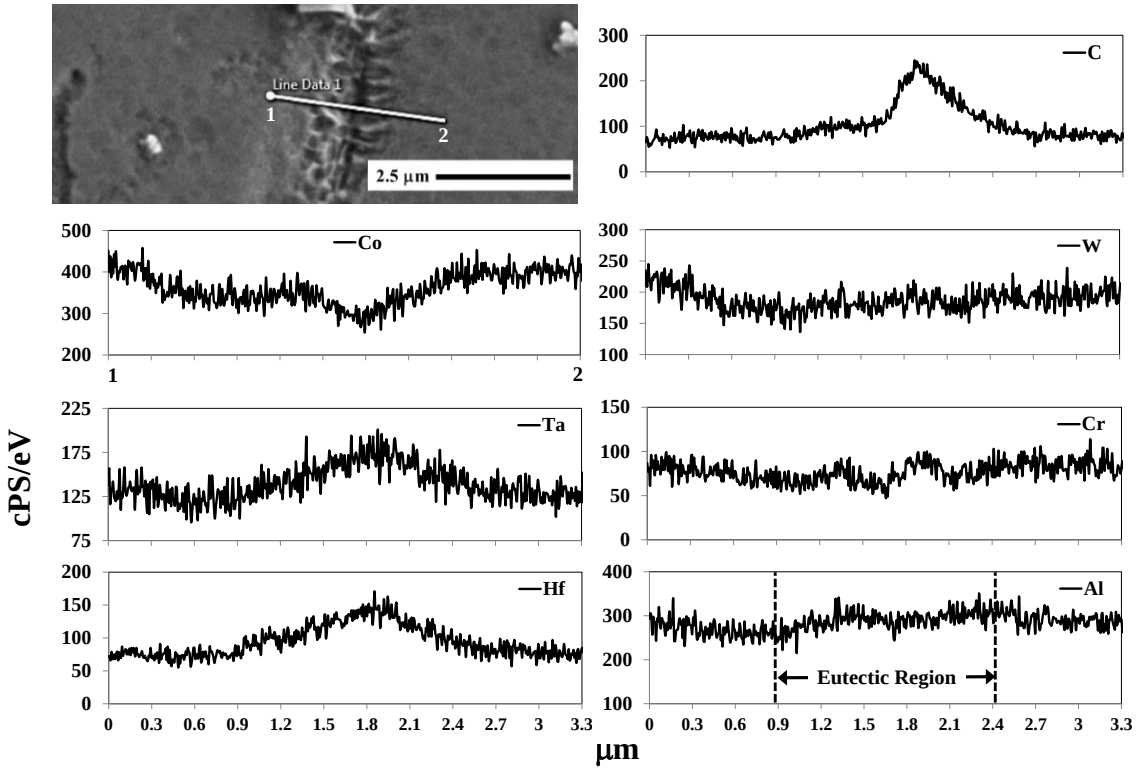

Figure 48. EDS line scan profiles across a eutectic region showing elemental segregation.

EDS line scans are performed across a typical eutectic region in the as-deposited sample. The line scan profiles are shown in Figure 48. Hf, Ta, and C are found to segregate to the liquid while Co segregates to the solid. W, Al, and Cr show extremely weak segregation behavior. Ni and Mo do not segregate consistently to one phase as shown in Figure 48. The results presented here are consistent with an earlier study performed on directionally cast MAR-M247 [100]. EDS scan is also performed across a typical eutectic region in the heat-treated samples. The elements do not segregate consistently to one phase for the heat-treated samples indicating greater level of homogenization.

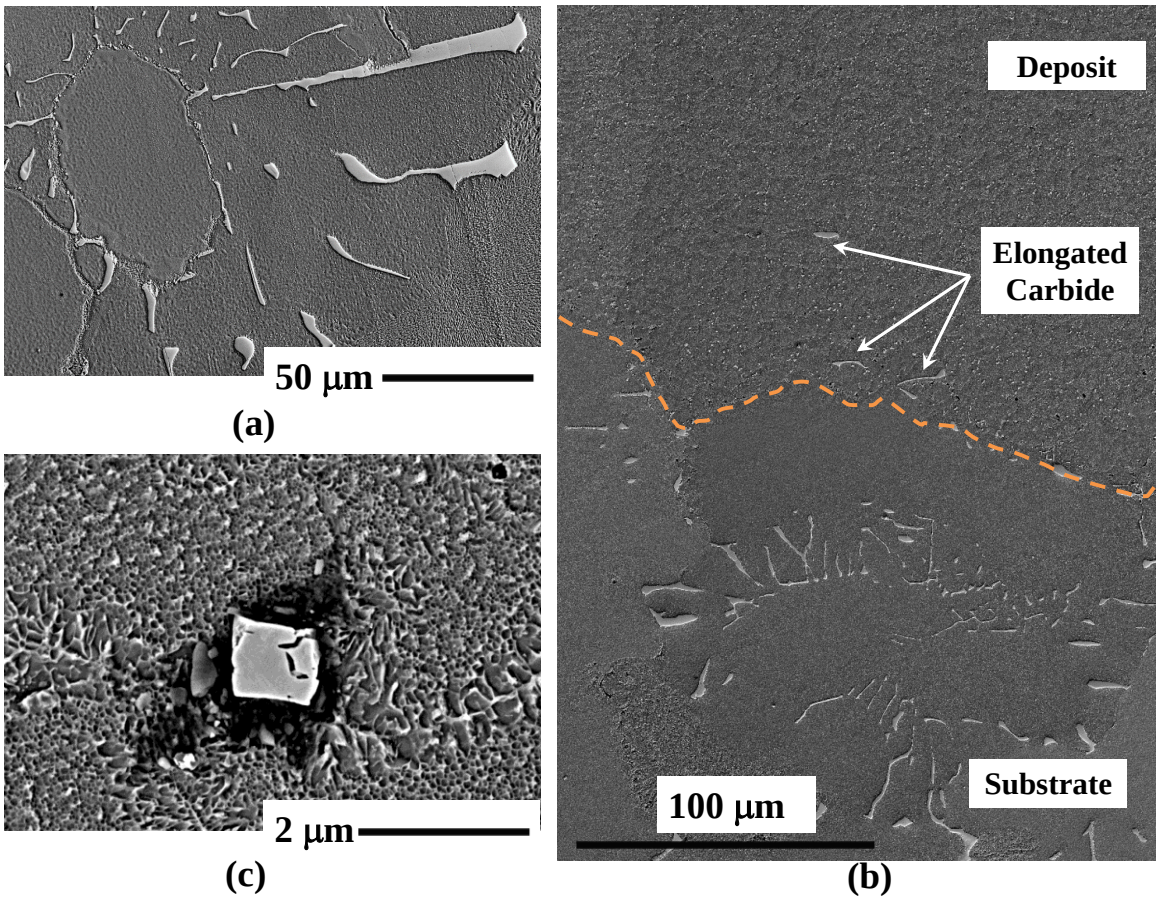

Figure 49. Morphology of the carbide precipitates in the (a) substrate region, and (b) interface region (the orange line represents the substrate-deposit interface), and (c) deposit region of an as-deposited MAR-M247 sample.

MAR-M247 contains about 0.15 wt. % C and 0.015 wt. % B resulting in the formation of carbide and boride precipitates in the deposit region. Blocky and elongated carbide precipitates are found in the deposit region [115]. Figures 49(a), 49(b), and 49(c) illustrate the morphology of typical carbide precipitates in the substrate, the interface, and the deposit region of the as-deposited sample, respectively. The substrate region is abundant in Chinese-script, blocky, and elongated carbide precipitates. However, in the deposit region, blocky carbides are predominantly observed. A few elongated carbides are found near the interface as shown in Figure 49(b).

This may be due to the fact that during laser processing, a thin layer of the substrate material containing a portion of Chinese-script carbides is melted. During combined solidification of the partially-melted substrate and the fully-melted powder, the existing carbide particles are trapped. Another possible explanation could be convection of the broken Chinese-script carbide arms during laser processing and subsequent solidification of those arms in the deposit region. The size of the carbide precipitates in the substrate is of order 1 – 100 μm, while in the deposit the size of the blocky carbides is of order 200 – 400 nm.

The blocky carbides in the deposit region of an as-deposited sample (Figure 49(c)) are found to be rich in Ta, W, Ti, Hf, and C; however, trace amounts of Ni, Cr, Mo, Co, Al, and Cr are also present. The blocky carbides in the deposit region of a heat-treated sample are found to be rich in Ta, W, Ti, Hf, and C; however, trace amounts of Mo, Zr, and B are also found to be present. The deposit region of a heat-treated sample also shows plate-like carbides that are found to be rich in Cr. The plate-like carbides are typically found to form a discontinuous film-like network at the grain boundaries as shown in Figure 50.

Blocky carbides are usually formed during solidification as discrete particles in the interdendritic regions due to the strong segregation of C in the liquid. Although such carbides are very stable at low temperatures, they degenerate into secondary carbides at higher temperatures after the heat treatment. Plate-like carbides are usually found to precipitate at the grain boundaries in Cr-rich alloys as irregular and discontinuous particles [112]. However, long exposure times at high temperatures result in the formation of continuous carbide films along the grain boundaries. These continuous films are shown to negatively affect the ductility and rupture life of the material [112]. In the SLE fabricated MAR-M247, only irregular and discontinuous Cr-rich plate-like carbides are observed after heat treatment.

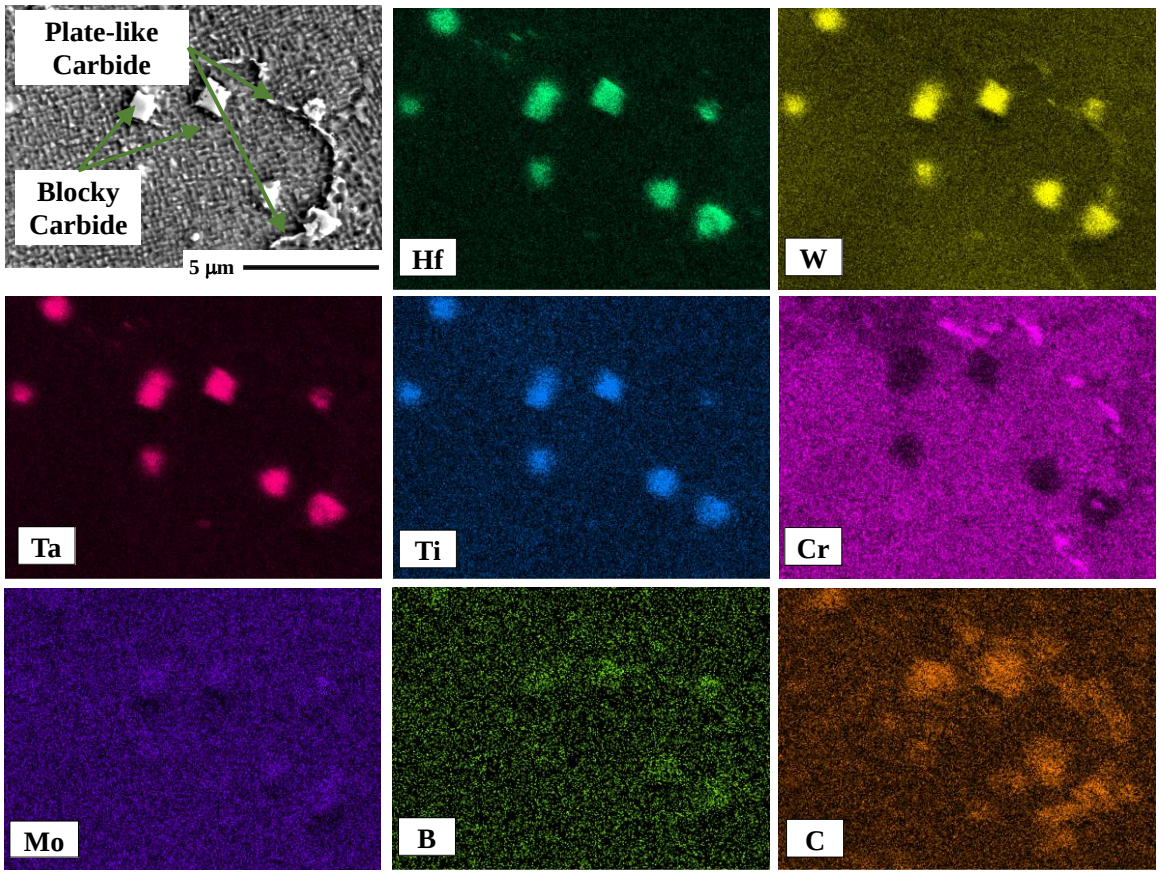

Figure 50. EDS map of carbides in the deposit region of a heat-treated sample.

5.2.5 Crystalline phases

Figure 51 compares the XRD profiles for the pre-alloyed MAR-M247 powder with the as-deposited and the heat-treated deposits. The XRD spectra for the MAR-M247 powder is coincident with solid solution γ-FCC NiCr (a = 0.359 nm) and exhibits a prominent (111) peak. The diffraction peaks occur at 2θ = 44°, 51°, 75°, 91°, 96°, and 119° indicating the diffraction of (111), (200), (220), (311), (222), and (400) planes of the γ matrix.

Two major peaks at around 44° and 51° indicate a strong presence of γ solid solution and/or γ′ phase in the as-deposited sample as shown in Figure 51. The XRD profile for the as-

deposited MAR-M247 also exhibits weak peaks at 91° and 119° indicating the presence of (311) and (400) planes. The strong (200) in the SLE deposited MAR-M247 parallel to the build direction represents a unidirectional solidification and growth texture. Several other weak peaks were also observed indicating the presence of MC-type carbides in the deposit region as shown in Figure 51 [116].

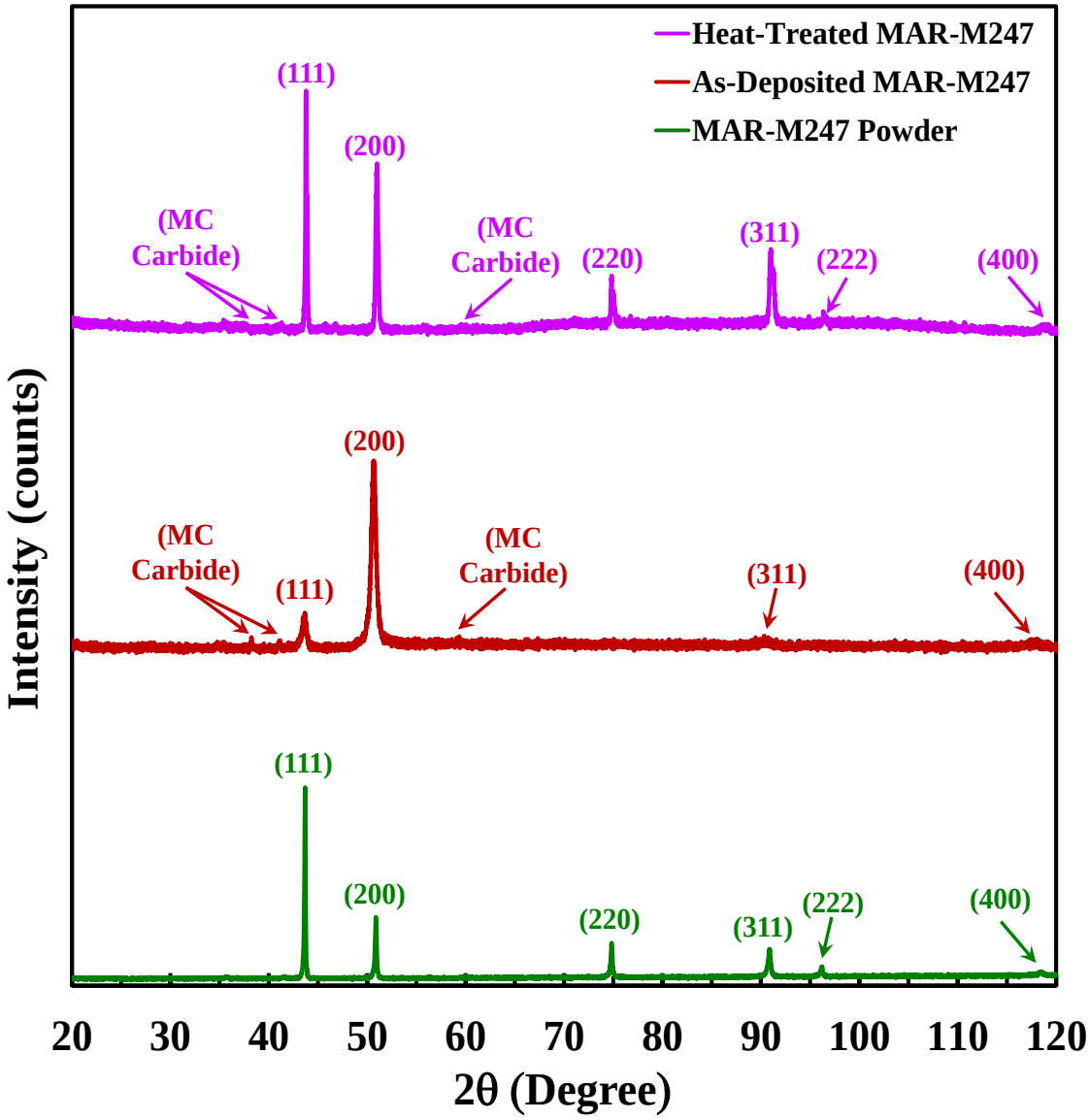

Figure 51. XRD profiles of the pre-alloyed MAR-M247 powder, the as-deposited MAR-M247 sample, and the heat-treated MAR-M247 sample.

Contrary to the as-deposited sample, the heat-treated sample exhibits mixed peaks at 44°, 51°, 75°, and 91° with the 44° degree peak being the strongest as shown in Figure 51. The strong (200) growth is disrupted after the heat-treatment leading to loss of directional growth due to recrystallization [110]. Several other weak peaks are also observed indicating the presence of MC-type carbides in the deposit region as shown in Figure 51.

XRD measures lattice spacing based on Bragg's law: $\lambda=2d\sin\theta$. Here θ is the angle between the incident beam and the (hkl) lattice plane, d is the lattice spacing of the (hkl) plane of interest, and λ is the incident x-ray wavelength. It has been shown that there is a clear relationship between the diffraction pattern that is observed when x-rays are diffracted through crystal lattices and the distance between atomic planes (the inter-planar spacing) within the material. By altering the inter-planar spacing different diffraction patterns will be obtained. The inter-planar spacing of a material that is free from strain will produce a characteristic diffraction pattern for that material. When a material is strained, elongations and contractions are produced within the crystal lattice, which change the inter-planar spacing of the (hkl) lattice planes.

This induced change in d will cause a shift in the diffraction pattern. By precise measurement of this shift, the change in the inter-planar spacing can be evaluated and thus the strain within the material deduced. The most commonly used method for stress determination is the $\sin^2\psi$ method. A number of XRD measurements are made at different ψ tilts for the samples shown in Figures 52(a) and 53 on the plane of the paper in the deposit region. The inter-planar spacing, or 2θ peak position, is measured and plotted. The stress can then be calculated from such a plot by calculating the gradient of the line and with basic knowledge of the elastic properties of the material. This assumes a zero stress at $d = d_n$, where d is the

intercept on the y-axis when $\sin^2\psi = 0$. More complex solutions exist for non-ideal situations where, for example, ψ splitting occurs (caused by the presence of shear stresses) or there is an inhomogeneous stress state within the material [117]. Details on the stress measurements using XRD may be found elsewhere [117].

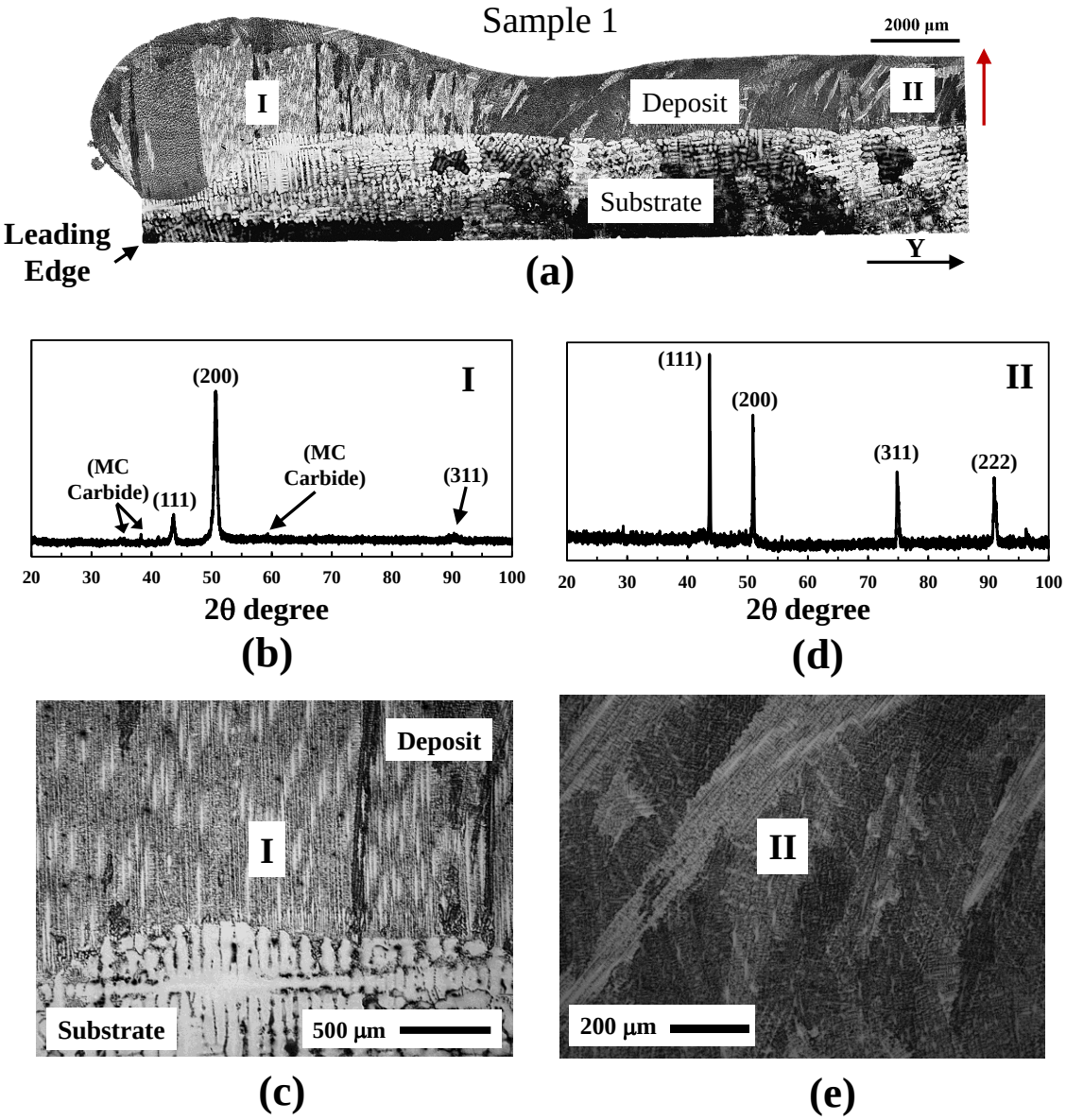

Figure 52. (a) Representative OM images of as-deposited MAR-M247 samples showing crack-free and dense deposit. The red arrow represents the build direction. XRD profiles at (b) location I and (d) location II in (a). OM images showing MAR-M247 microstructure at (c) location I and (e) location II.

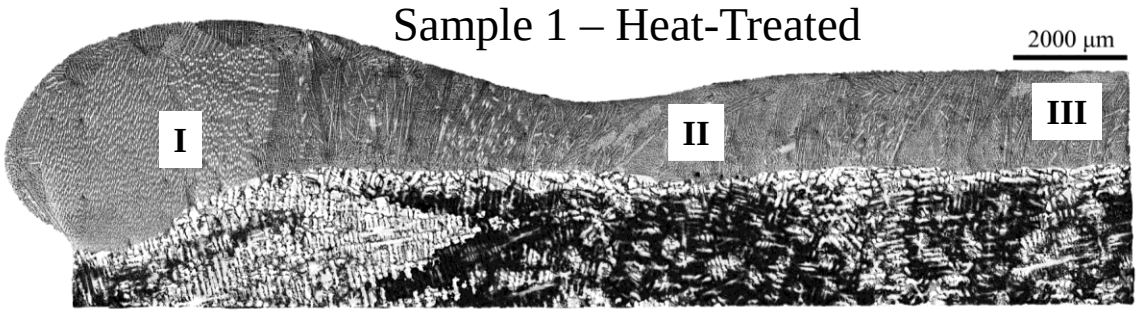

Figure 53. Representative OM image of a heat-treated MAR-M247 sample.

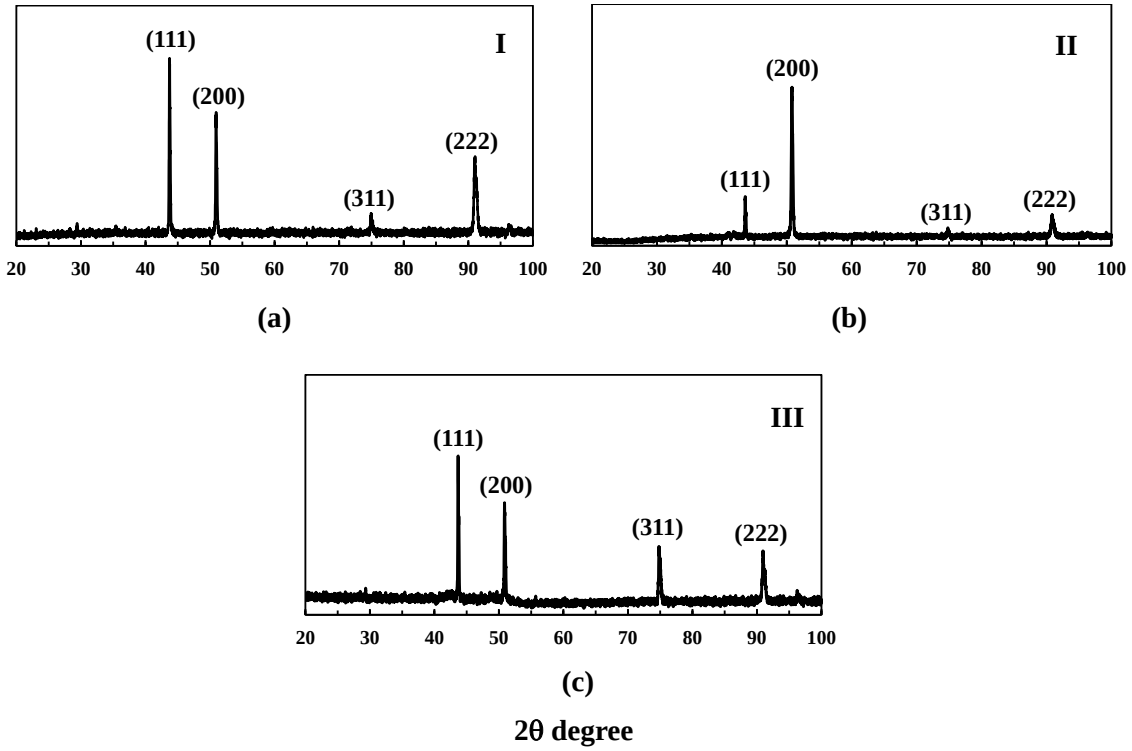

Figure 54. XRD profiles at (b) location I, (c) location II, and (s) location III in Figure 53.

Figure 52(b) shows the XRD profile at Location I of Figure 52(a) in the deposit region. Figure 52(c) illustrates the OM image of Location I showing a columnar growth in the deposit region. Figure 52(d) shows the XRD profile at Location II in Figure 52(a). The strong peak at (200) is not present and the deposit region shows a prominent (111) peak. The OM image of Location II is shown in Figure 52(e). Overall, different regions of the deposit show different

XRD peaks for MAR-M247 samples. Figure 53 shows the locations of stress measurements while Figures 54(a) through 54(c) show the XRD profiles at locations I, II, and III in Figure 53 in the deposit region showing the variation in crystal orientation in the deposit region of a representative heat-treated MAR-M247 sample.

The average stress is of order 257.5±63.3 MPa for the as-deposited sample while it is of order 179.2±33.3 MPa for the heat-treated sample. While heat treatments modify the microstructure and precipitation characteristics, such treatments are effective in relieving the stresses built within the SLE fabricated MAR-M247 deposit. The stresses in the deposit region for the heat-treated sample at locations I and III in Figure 53 are 188±26.2 MPa and 170.3±40.4 MPa, respectively.

5.2.6 Vickers microhardness measurement

The substrate region shows a hardness values in the range of 400 – 415 HV for the as-deposited. However, the hardness increases significantly near the interface region showing values of order 430 – 450 HV. The deposit region shows hardness values ranging from 450 HV to 500 HV. Figure 55 reports the average hardness values in the deposit, substrate, and interface regions of the as-deposited and the heat-treated MAR-M247 samples.

The measurements show an increase of more than 10% in the hardness values over the hardness data reported in the literature [98]. Heat-treated MAR-M247 shows 5 – 10% increase in the hardness values as shown in Figure 55. This increase may be attributed to the uniform γ/γ' distribution obtained after the heat treatment. The yield stress is approximated as, $\sigma_y \sim$ HV/3 (HV measured in GPa) [42]. Table 6 shows the calculated yield stress for the as-deposited and the heat-treated MAR-M247 samples [42].

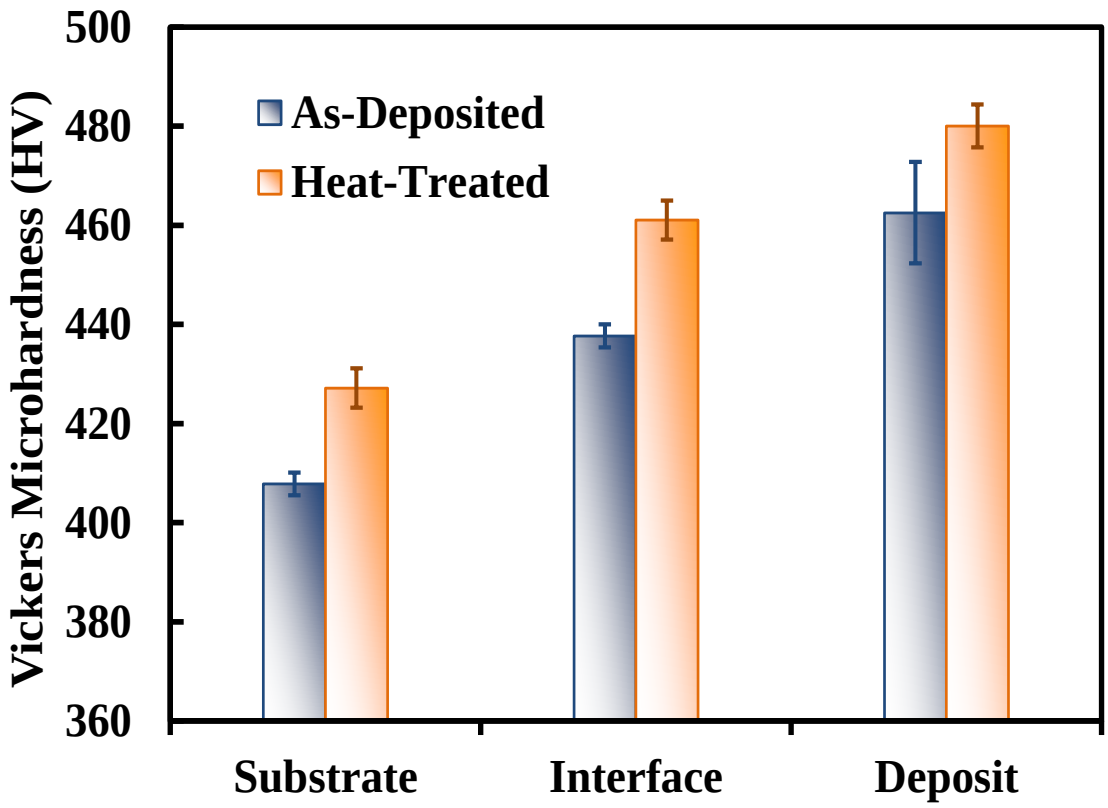

Figure 55. Variation of microhardness with heat-treatment for MAR-M247 samples.

Table 6. Summary of Vickers microhardness results for MAR-M247.

Sample Type	Region	HV_{2000}	HV (GPa)	σ_y (GPa)
As-Deposited MAR-M247	Substrate	407.8	4.0	1.3
	Interface	437.7	4.3	1.4
	Deposit	462.5	4.5	1.5
Heat-Treated MAR-M247	Substrate	427.2	4.2	1.4
	Interface	461.1	4.5	1.5
	Deposit	480.1	4.7	1.6

Variations in hardness value are observed in different regions of the deposit. The

measurements are performed at 5 and 10 different locations along the Y direction and the X direction, respectively. Figures 56(a) and 56(b) show the measurement grid points and two different representative indentation marks in the deposit region, respectively. The measurement pattern is chosen to accurately reflect the variation of hardness along the build direction and the laser movement direction.

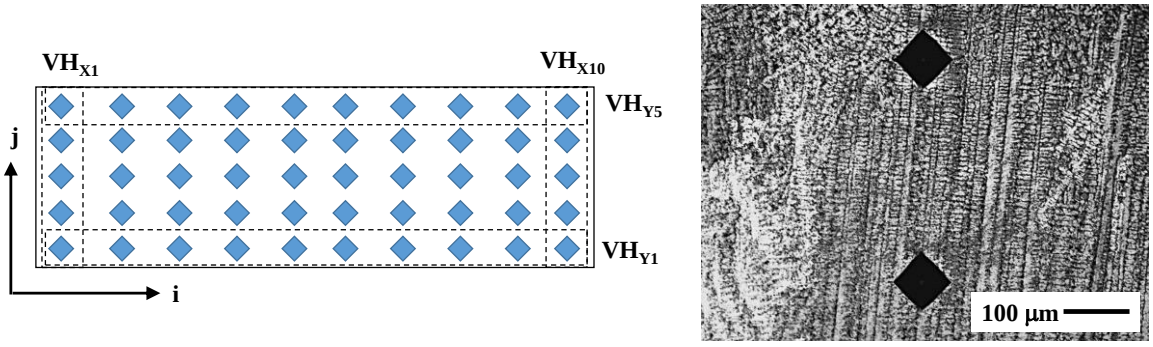

Figure 56. (a) Schematic of the measurement locations in the deposit and (b) representative indentation marks in the MAR-M247 deposit region.

The average values of the hardness parameters are calculated as follows:

Equation 15. Average value of Vickers hardness.

$$VH_{Average} = \left(\sum_{i=1}^{10} \sum_{j=1}^{5} VH \right) /50$$

Equation 16. Average value of Vickers hardness in the X direction.

$$\left(VH_{X}\right)_{i=1,2,3,.....,10} = \left(\left[\sum_{j=1}^{5} VH \right] / 5 \right)_{i=1,\ 2,\ 3,\ ....,10}$$

Equation 17. Average value of Vickers hardness in the Y direction.

$$\left(VH_{Y}\right)_{j=1,\ 2,\ 3,\ ....,\ 5} = \left(\left[\sum_{i=1}^{10} VH \right] / 10 \right)_{j=1,\ 2,\ 3,\ ....,5}$$

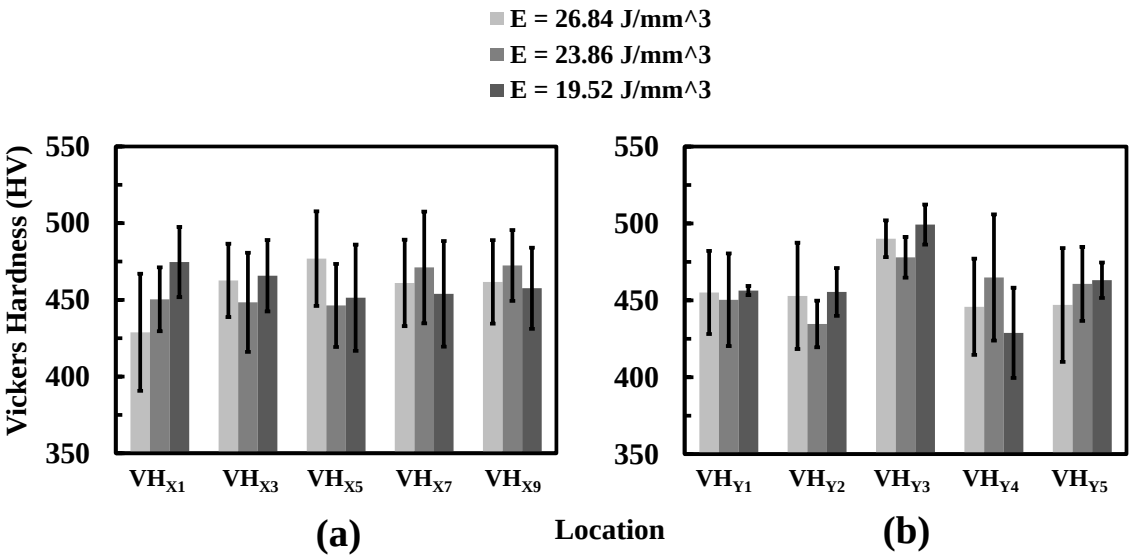

Figure 57. Variation of Vickers microhardness along the (a) build direction and (b) the laser movement direction for different values of E for as-deposited samples.

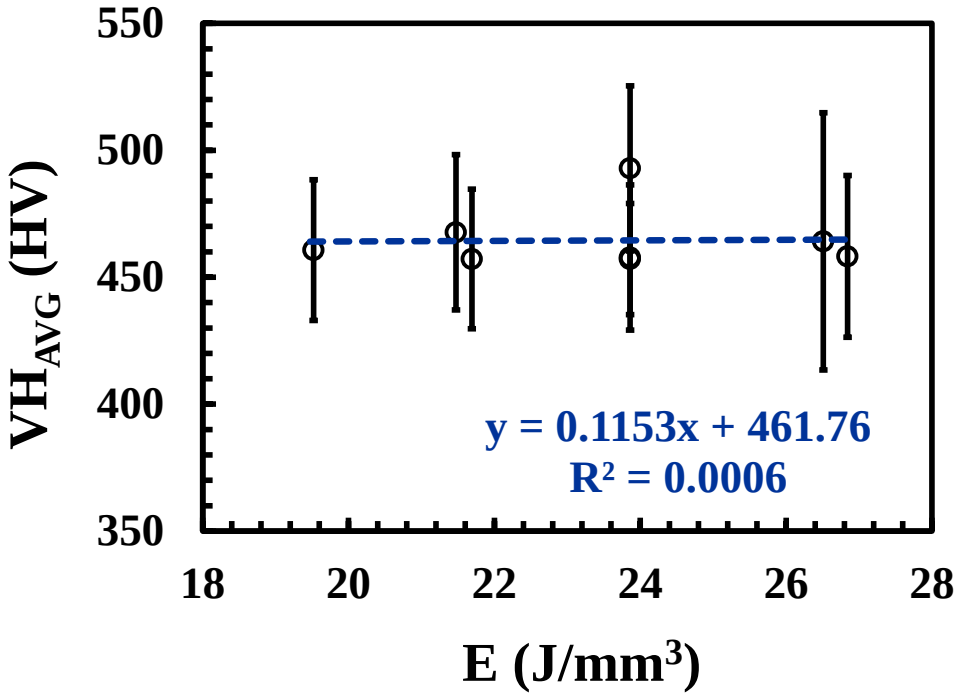

Figure 58. Effects of E on the average Vickers hardness in the deposit region for as-

deposited samples.

The average value of the Vickers hardness for all MAR-M247 samples is of the order of 460-490 HV for as-deposited samples and the variation is of order $\pm 2\sigma$ along the build direction and the laser movement direction as shown in Figures 57(a) and 57(b), respectively. With change in E, no significant changes are observed in the average hardness values as shown in Figure 58. These results are encouraging as it signifies that changing the SLE processing parameters will have a minimal impact on the hardness distribution in the deposit region with most of the variation originating due to the variations in the local microstructure.

5.2.7 Conclusions on MAR-M247

The difficulties associated with welding of high γ' nickel-base superalloys such as MAR-M247 are well established. However, the current study shows encouraging results for MAR-M247 using an LPBF-based AM process. Multiple MAR-M247 samples are produced by altering the SLE processing parameters. The processing parameters are conveniently combined to define the scan energy density (E). The average deposit height is found to increase with E. However, no such relationship is observed for the average hardness values. The hardness values show variations of order $\pm 2\sigma$ along the build and the laser movement directions. The microstructures of MAR-M247 exhibit recrystallization after the heat-treatment. However, the microstructures become uniform after the heat treatment.

The microstructure of the as-deposited MAR-M247 typically consists of columnar and equiaxed grains which grow from the partially re-melted grains of the investment cast substrate. The SLE deposited MAR-M247 also shows 40x reduction in the size of the primary γ' precipitates compared to the cast substrate. Microhardness measurements show an increase

in the hardness in the deposit region by 10% or more when compared with the cast substrate. Blocky carbides are predominantly observed at the grain boundaries while a few elongated carbides are seen near the substrate-deposit interface. The carbides are found to be rich in Ta and Hf. Commercial heat treatment is found to be beneficial in reducing the volume fraction of the low melting point eutectics in the deposit region. Cr is found to segregate at the grain boundaries after the heat treatment forming plate-like carbides.

5.3 Summary

This chapter discusses the SLE development for polycrystalline or EQ deposits. Some of the key conclusions from this study are:

- This is a first-of-its-kind demonstration of deposition of IN100 and MAR-M247 having thickness exceeding 1000 μm, widths exceeding 5000 μm, and lengths exceeding 35,000 μm in a single pass using an LPBF-based AM process.

- Dense deposits are obtained for two high-γ′ nickel-base superalloys such as IN100 and MAR-M247 for a range of operating conditions without preheating the powder bed.

- The SLE process can be accurately controlled in order to achieve a shallow melt back depth. A shallow melt-back depth ensures that the energy input to the substrate is minimal reducing the thermal stress accumulated within the melt-back region and avoiding any crack formation. The absence of cracks in the current study vouches for the reduced thermal stress accumulation in the SLE-deposited EQ samples.

- The deposit region shows finer microstructure compared to the substrate region. The deposit region also shows dendritic segregation. The SLE-deposited microstructures also

show finer γ′ features compared to the substrate. Such finer microstructures improve the microhardness in the deposit region by approximately 10% compared to the substrate. The hardness values are unevenly distributed in the deposit region, however, they show variations within ±2σ along the build and the laser movement directions.

- The deposit region shows three different microstructural features such as the γ′ precipitates, the γ matrix, the eutectics, and the carbides. The γ′ precipitates are polygonal shaped while the carbides are typically blocky shaped.

- The comparison between the SLE-deposited IN100 and MAR-M247 microstructures reveals the following:

    - Dense and crack-free deposits of IN100 with no interface fusion defects can be obtained with E values of 18.75 – 35.79 J/mm^3. For MAR-M247, only a handful of experimental runs are performed and the results show that E values between 19.52 – 26.84 J/mm^3 give deposit formations without interface fusion defects.

    - The carbides in the IN100 deposits are rich in Ti while the carbides in MAR-M247 are rich in Ta. Both of these material systems show residual carbide formation, however, IN100 contains Zr that shows up only in residual carbide precipitates in IN100 deposit.

    - Microhardness of IN100 deposit is in the range of 430 HV while MAR-M247 deposits show hardness values in the range of 462 HV. This suggests that MAR-M247 may have higher yield stress compared to IN100.

Chapter 6: SLE process development for SX deposits

This chapter studies the feasibility of fabricating SX deposits by SLE. Two "second-generation" alloys that are typically cast with SX microstructures namely CMSX-4® and René N5 are chosen. René N5 contains 0.05 wt. % C and 0.004 wt. % B while CMSX-4® does not contain any such elements. C and B drive precipitation of carbides/borides at the interdendritic region. Hence, a comparison between the deposit properties of these two alloys fabricated using the SLE process sheds insights on the role of C and B in laser deposition of high-γ′ superalloys.

6.1 Study on CMSX-4®

CMSX-4® has been extensively used in the manufacture of the turbine blades because of its good yield, creep, and fatigue strength and excellent oxidation and corrosion resistance in aggressive loading scenarios. Numerous SX turbine airfoil castings ranging from 0.25 mm (0.010 in.) thick Lamilloy® crystalfoils, hybrid CastCool® blades and vanes, to large shrouded turbine blades up to 160 mm (6.3 in.) in length for the 80,000 lb. thrust commercial turbofan engines were produced using CMSX-4® over the past few decades. The casting processes had high process yields along with low levels of grain defects [118].

CMSX-4® is a "second-generation" ultrahigh-strength SX-cast superalloy developed using a multidimensional approach over a ten year period through the joint efforts of Canon-Muskegon and Allison at the beginning of the 1990s [119]. The alloy demonstrates a

significant improvement of 35 ^{o}C in the turbine airfoil temperature capability compared to the "first-generation" SX-cast superalloys such as CMSX-2® and CMSX-3® [120]. CMSX-4® is derived from CMSX-2® and enjoys the strengthening effects of Re (3 wt. %) like other "second-generation" SX-cast superalloys. Re partially segregates to the γ matrix, and thereby, delays coarsening of the γ′ phase [121]. CMSX-4® is strengthened by the solid-solution-strengthening effects of Cr, W, and Ta and the precipitation-hardening effects of Al and Ti that form the γ′ phase [119]. To date, other than SLE, only a handful of AM processes such as epitaxial laser metal forming (ELMF) and selective electron beam melting (SEBM) have been successful in processing CMSX-4® [69, 122].

6.1.1 Materials

Commercially available CMSX-4® powder is used in this study. The powder is produced by Praxair Surface Technologies using argon gas atomization. The powder composition is given in Table 7.

Table 7. Composition of the CMSX-4® powder (wt. %).

	Cr	Co	Mo	Re	W	Al	Ti	Ta	Ni
CMSX-4®	6.5	9.7	0.4	3.0	6.4	5.6	1.0	6.5	Bal

The powder is analyzed using OM and SEM. OM reveal that the CMSX-4® powder particles are mostly spherical with particle diameter varying from 90 to 150 μm as shown in Figure 59(a). After polishing the powder to a mirror finish, OM is performed and the results show that the powder particles have limited porosity as shown in Figure 59(b). Figure 59(c) illustrates the morphology of a single powder particle showing dendritic microstructure on the

particle surface. Figure 59(d) illustrates the internal micro-dendritic structure of an etched CMSX-4® powder particle.

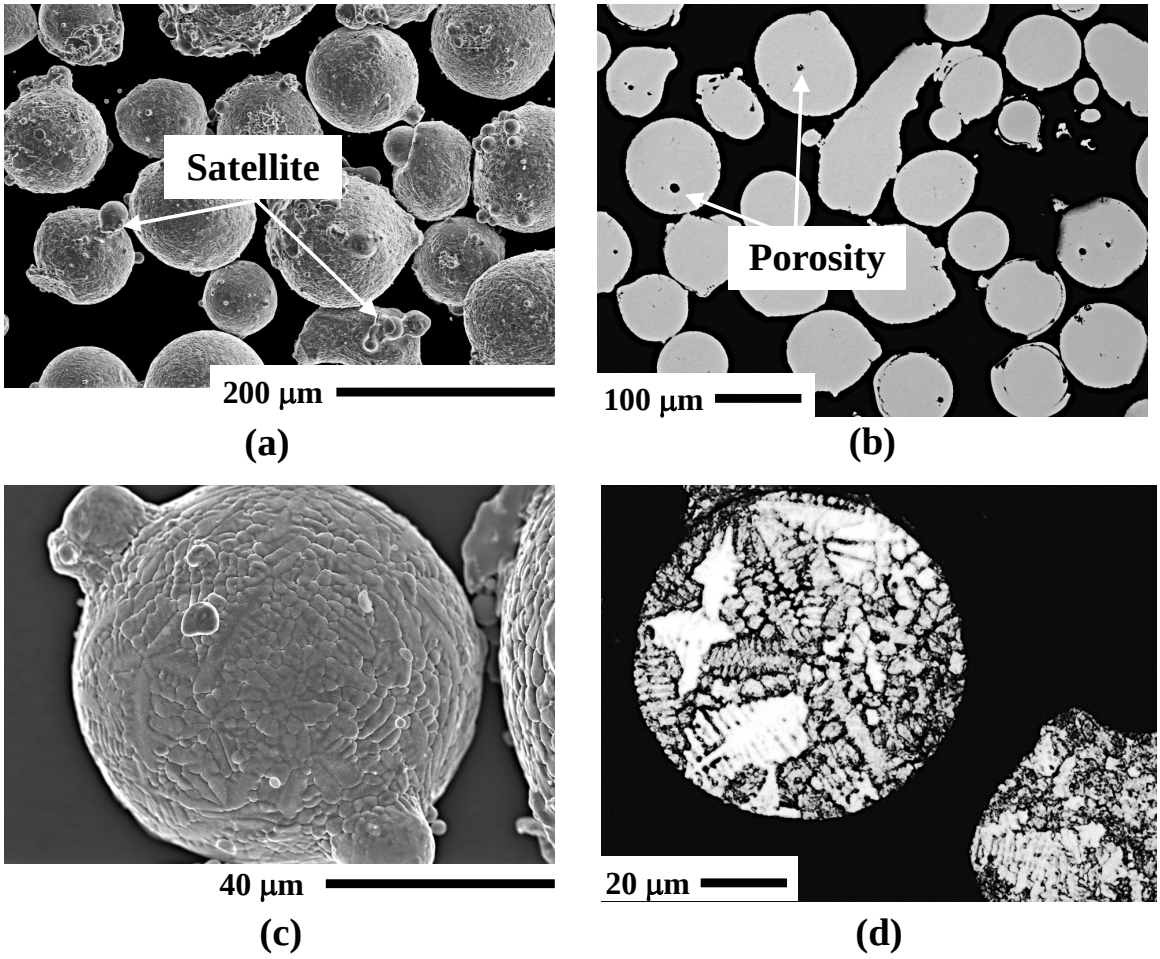

Figure 59. (a) SEM image of the CMSX-4® powder, (b) OM image of the CMSX-4® powder cross-section after polishing, (c) SEM image of a single powder particle, (d) OM image of a CMSX-4® powder particle cross-section after etching showing the internal dendritic microstructure.

The SLE process is conducted on two different rectangular SX cast CMSX-4® substrates with dimensions of 35.56 mm × 6.86 mm × 2.54 mm and 38.10 mm × 11.85 mm × 2.54 mm. Both type of substrates have [001] crystal growth direction [123]. Hereafter, the substrate coupon having dimensions of 35.56 mm × 6.86 mm × 2.54 mm is referred to as “Substrate 1”.

The substrate coupon having dimensions of 38.10 mm × 11.85 mm × 2.54 mm is referred to as "Substrate 2" [124]. The experimental optimization is performed on the CMSX-4® deposited on Substrate 1. The results are then applied to deposit CMSX-4® on Substrate 2.

6.1.2 Results on Substrate 1

In this section, results on Substrate 1 are reported. The deposit characteristics are discussed followed by experimental optimization [123] and mechanical testing results [125].

6.1.2.1 *Deposit characteristics*

The SLE-deposited CMSX-4® on Substrate 1 is analyzed using optical microscopy to investigate the overall deposition characteristics. Figure 60(a) shows the transverse microstructure of a typical SLE-processed CMSX-4® sample demonstrating an excellent metallurgical bond between the substrate and the deposit region. The SLE-processed CMSX-4® deposit is demonstrated to be crack-free and dense as shown in Figures 60(a) through 60(d).

The processing parameters have immense effects on the deposit characteristics. Lack of a sufficient number of repeat scans results in discontinuous substrate-powder metallurgical bond (Figure 60(b)); however, too many repeat scans cause excessive melt back near the starting edge as shown in Figure 60(c). Similarly, if the scan speed is too high, there is a thermal lag in the substrate region, resulting in deformation or warping of the sample as shown in Figure 60(c). Lower scan spacing results in a higher scan energy density, and therefore, expands the melt pool and reduces the vertical or [001] temperature gradient. This can expedite EQ grain formation, lowering the SX height as demonstrated in Figure 60(d). It is, therefore, critical to investigate and determine the optimum parameter sets that would result in acceptable deposit characteristics.

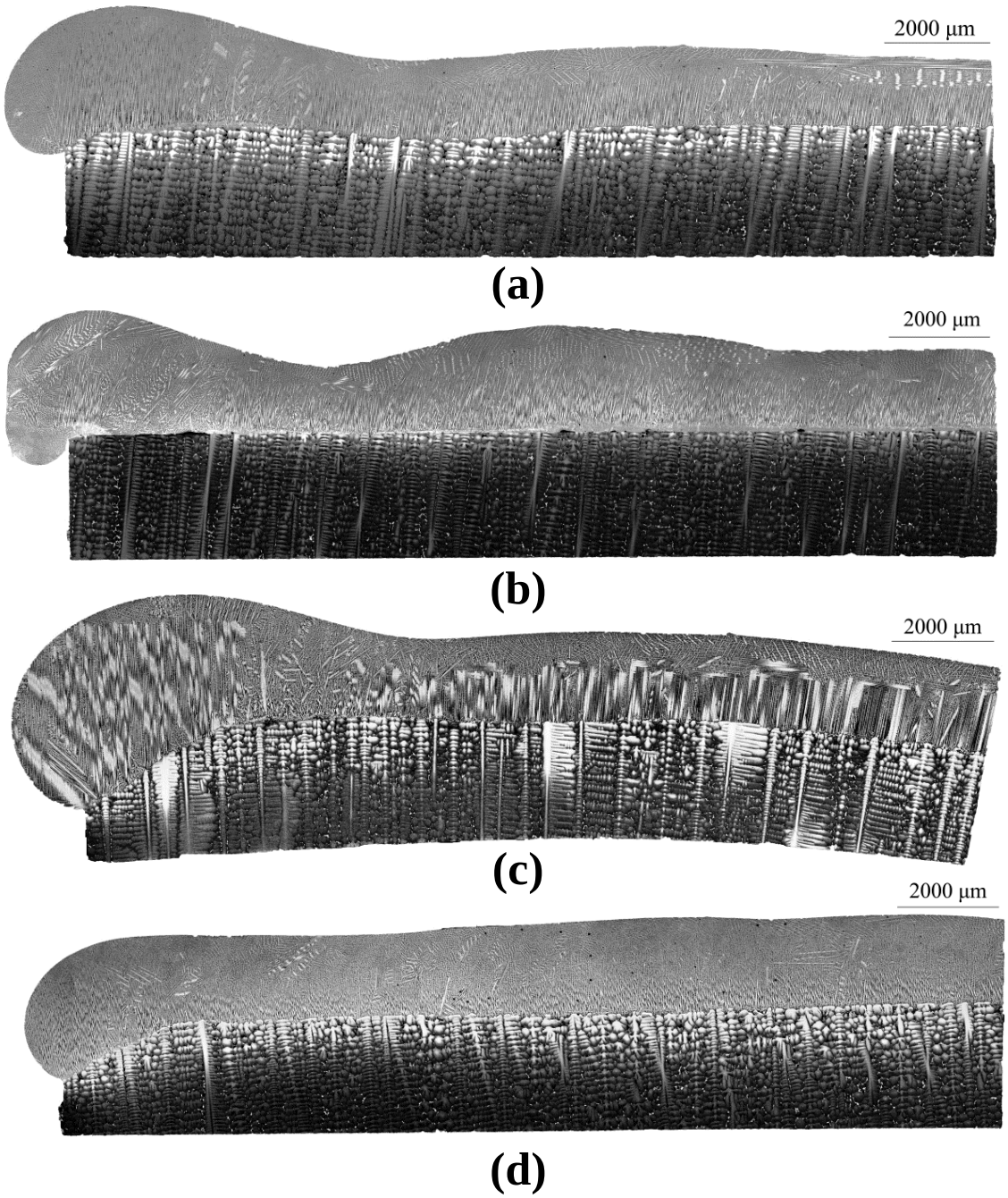

Figure 60. Representative transverse optical micrograph of CMSX-4® deposit showing (a) crack-free and dense deposit, (b) lack of fusion due to reduced number of repeat scans, (c) deformation/warping due to higher scan speed, and (d) lower single-crystal height due to lower scan spacing.

Figure 61(a) provides a detailed view of two different microstructural transitions. The first transition is known as the oriented-to-misoriented transition or OMT. The columnar

dendrites change the growth direction from [001] to [100] due to the change in the direction of the dominant temperature gradient as the substrate and the powder become increasingly hot toward the end of the scan [45].

The second transition is known as the columnar-to-equiaxed/polycrystalline transition or CET. CET occurs due to an increase in isotherm velocity near the surface and a decrease in the temperature gradient resulting in the formation of a constitutionally undercooled zone [44]. Despite this loss of epitaxy due to CET and OMT, all SLE-processed samples show SX deposit height of at least 500 μm. By optimizing the process parameters, the SX height can be further increased to 1000 μm in a single pass as shown in Figure 60(a). Inhomogeneity in the local flow field due to excessive raster scan speed or lower power can promote stray grain formation thwarting epitaxial growth (Figure 61(b)).

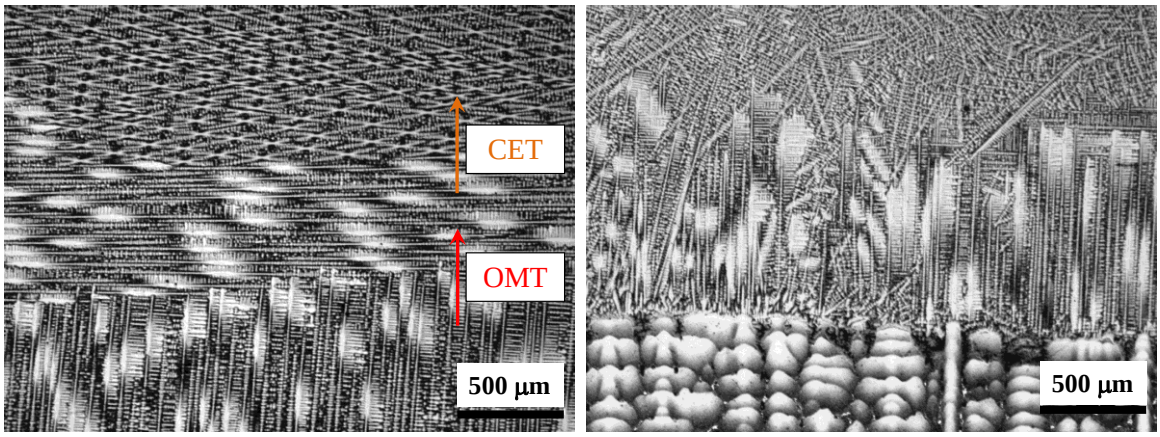

Figure 61. Representative transverse optical micrograph of CMSX-4® sample showing (a) oriented-to-misoriented transition (OMT) and columnar-to-equiaxed transition (CET), and (b) stray grain (SG) morphology.

6.1.2.2 *Experimental optimization*

In SLE, a melt pool is initiated by the raster scan pattern across the width of the sample.

The melt pool propagates linearly along the length of the substrate fusing powder to the substrate. The number of repeat scans, the laser power, the scan speed and the scan spacing are varied in SLE. The number of repeat scans is defined as the number of raster movements that the laser performed at the leading edge of the sample without moving in the forward direction during the start of the scan process. The laser power and scan speed determine the amount of energy being applied while the number of repeat scans affects the formation of a melt pool at the leading edge of the substrate. Sufficient number of repeat scans is required to pre-heat the underlying substrate, establish a stable melt pool, and ensure a continuous metallurgical bond across the entire length and width of the substrate.

The SLE process parameters are combined into two different measures - the total repeat scan energy (Q) and the scan energy density (E). The total repeat scan energy is of immense interest as it determines whether or not a good metallurgical bond is formed between the deposit and the substrate from the beginning of the scan, whereas the scan energy density plays a critical role in maintaining the deposit quality along the entire length of the substrate. The total repeat scan energy is calculated as,

Equation 18. Total repeat scan energy.

$$Q = \frac{P \times N}{V_S}$$

Similarly, the scan energy density is defined as:

Equation 19. Scan energy density.

$$E = \frac{P}{SS \times V_S \times t_p}$$

Here P is the laser power, N is the number of repeat scans, V_S is the raster scan speed, SS is the raster scan spacing, and t_p is the powder thickness.

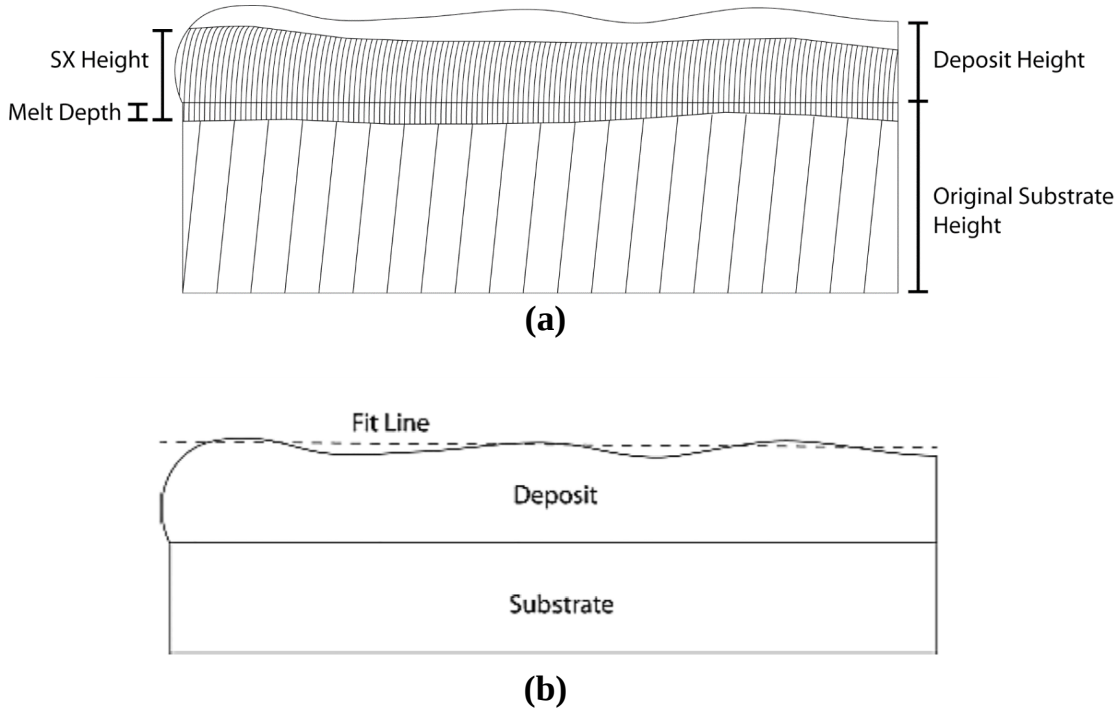

Figure 62. (a) Schematic representation of various deposit characteristics and (b) calculation of the deposit uniformity parameter.

The effects of various processing parameters on metrics such as the SX ratio, the average deposit height, the deposit height uniformity, the number of stray grains, the melt back depth, and the lack of deformation are assessed. These parameters are schematically shown in Figure 62(a). The "lack of deformation" is calculated by developing a linear fit for the bottom edge of the substrate and then calculating the average R^2 or goodness of fit between the initial horizontal line and the linear fit. The higher the R^2 value, the less deformed is the substrate, and hence, this parameter was termed "lack of deformation." The deposit uniformity is also calculated following the aforementioned procedure as shown in Figure 62(b).

The 2D model developed in Chapter 4 is used to come up with an initial set of parameters for experimental optimization runs. Multiple CFD simulations are performed to narrow down the SLE processing parameters to achieve the average melt depth of more than 75 μm but less than 175 μm. The desired average melt depth is of order 100 μm. However, in the present study, a broader parameter range is explored to accurately characterize the effects of SLE processing parameters on the deposit. Higher values of E and Q increase the average melt depth, while lower values of E and Q result in interface fusion error between the substrate and the deposit region. Using the results from the 2D CFD model, the optimization runs are conducted with E in the 15 to 70 J/mm^3 range and Q in the 250 to 700 J/mm range.

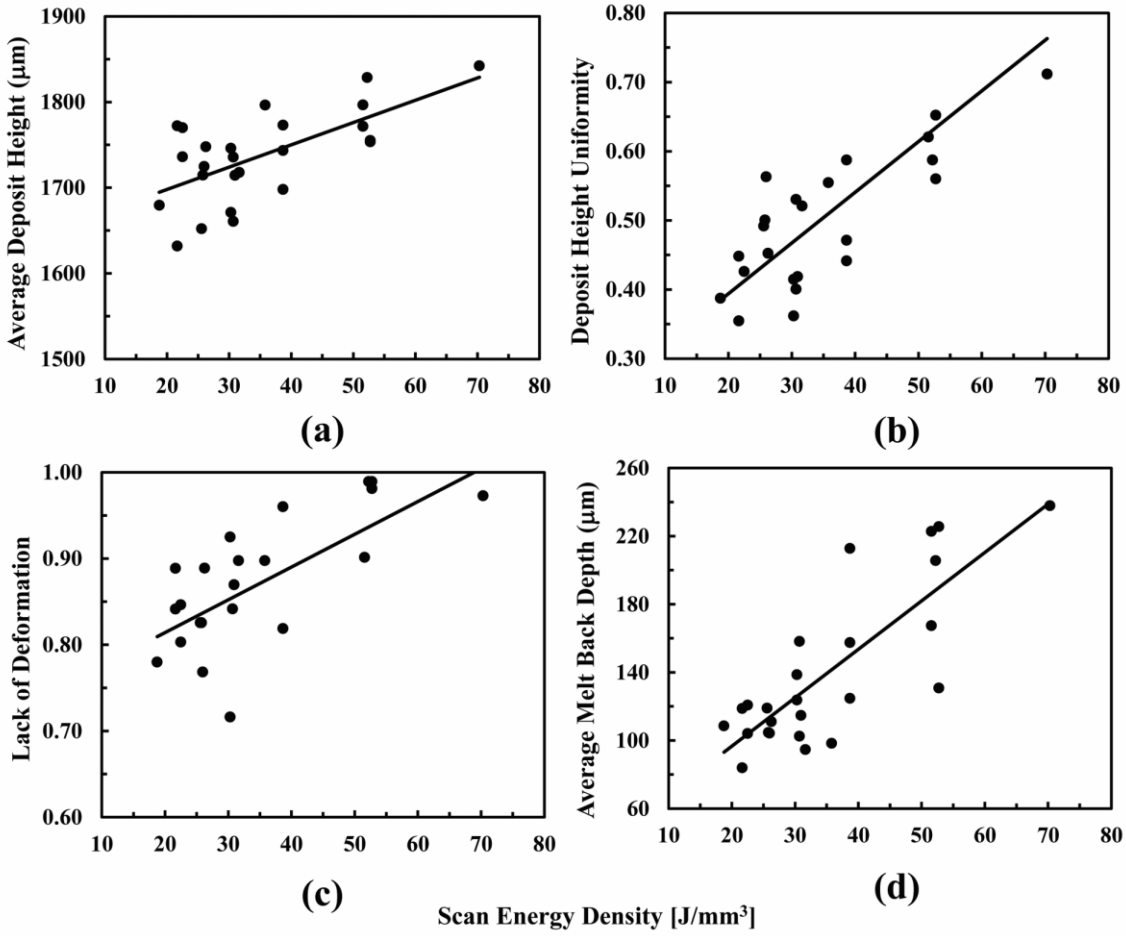

Figure 63. Effect of scan energy density (E) on (a) average deposit height, (b) deposit

height uniformity, (c) "lack of deformation," and (d) average melt back depth for CMSX-4®.

Figure 63(a) shows the effect of E on the average deposit height. Higher values of E cause the melt pool to expand drawing more powder inside the melt pool which increases the average deposit height. Figure 63(b) shows the effect of E on the deposit height uniformity. Higher values of E are associated with higher power and/or lower scan speed. Together, they cause a smoother flow of powder particles into the melt pool, thus removing surface instabilities. Figure 63(c) shows the effect of E on the "lack of deformation." The higher the value of the "lack of deformation" parameter, the lower is the deformation amount. Higher values of E associated with lower scan speeds result in lower thermal lag, whereas lower values of E associated with higher scan speeds promote thermal lag between the melt pool and the bulk substrate. Thus, lower values of E cause more deformation and consequently lower value of the "lack of deformation" parameter in the substrate region. The average melt depth increases with an increase in E (Figure 63(d)) as more energy is being provided to the substrate in this case.

It is also observed that the number of stray grains decreases for higher values of E. The lower scan speeds and higher laser powers cause smoother flow of powder and lower the Marangoni velocity at the top surface of the melt pool, thus decreasing the convection of broken dendrites. This reduces stray grain formation as shown in Figure 64(a). However, the SX ratio decreases significantly for higher values of E as shown in Figure 64(b). The higher laser powers and lower scan speeds expand the melt pool, thus reducing the temperature gradient in the vertical direction. This causes nucleation of new grains due to constitutional undercooling resulting in lower SX ratios at higher values of E.

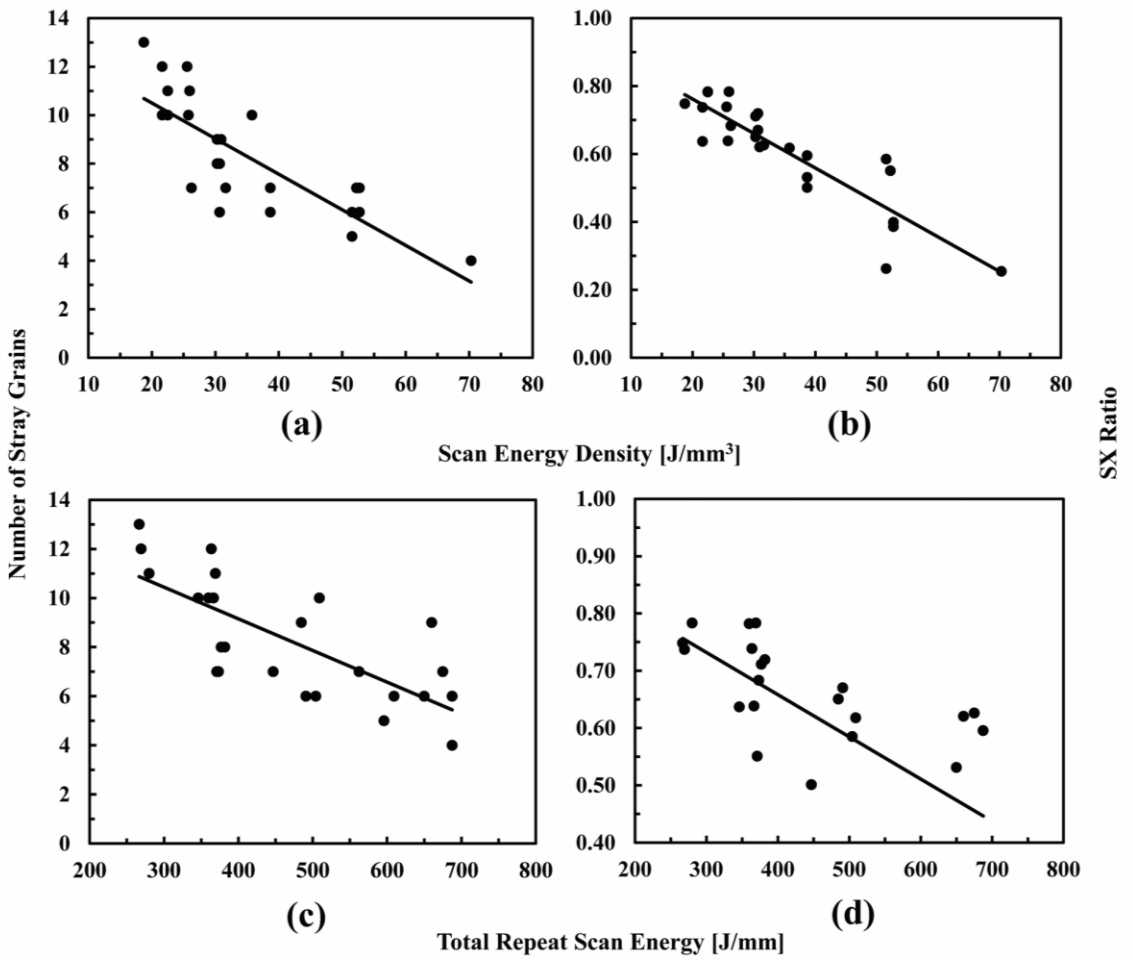

Figure 64. Effect of scan energy density (E) on (a) number of stray grains, and (b) SX ratio for CMSX-4®. Effect of total repeat scan energy (Q) on (c) number of stray grains and (d) SX ratio for CMSX-4®.

Figure 64(c) shows the effect of Q on the number of stray grains. Higher values of Q decrease the number of stray grains as this ensures expansion of the melt pool causing a smoother flow of the powder toward the melt pool. The SX ratio also decreases as Q is increased as shown in Figure 64(d). An increase in Q increases the average substrate temperature and decreases the vertical temperature gradient, thus lowering the SX height. SX ratios exceeding 0.5 and number of stray grains of less than 8 can thus be obtained simultaneously with E in the 35 to 50 J/mm^3 range and Q in the 400 to 500 J/mm range.

6.1.2.3 *Mechanical testing*

The longitudinal sections of two different SLE-processed CMSX-4® samples are shown in Figures 65(a) and 65(b). The characteristics of the samples illustrated in Figures 65(a) and 65(b) are reported in Table 8. Sample 1 is processed with E of 52.73 J/mm^3 while Sample 2 is processed with E of 18.75 J/mm^3. Figure 66 shows the load vs. displacement curves for Sample 1 and Sample 2. Sample 2 shows higher values of modulus, lower values of elongation, and higher yield strength as compared to Sample 1 as illustrated in Figure 66.

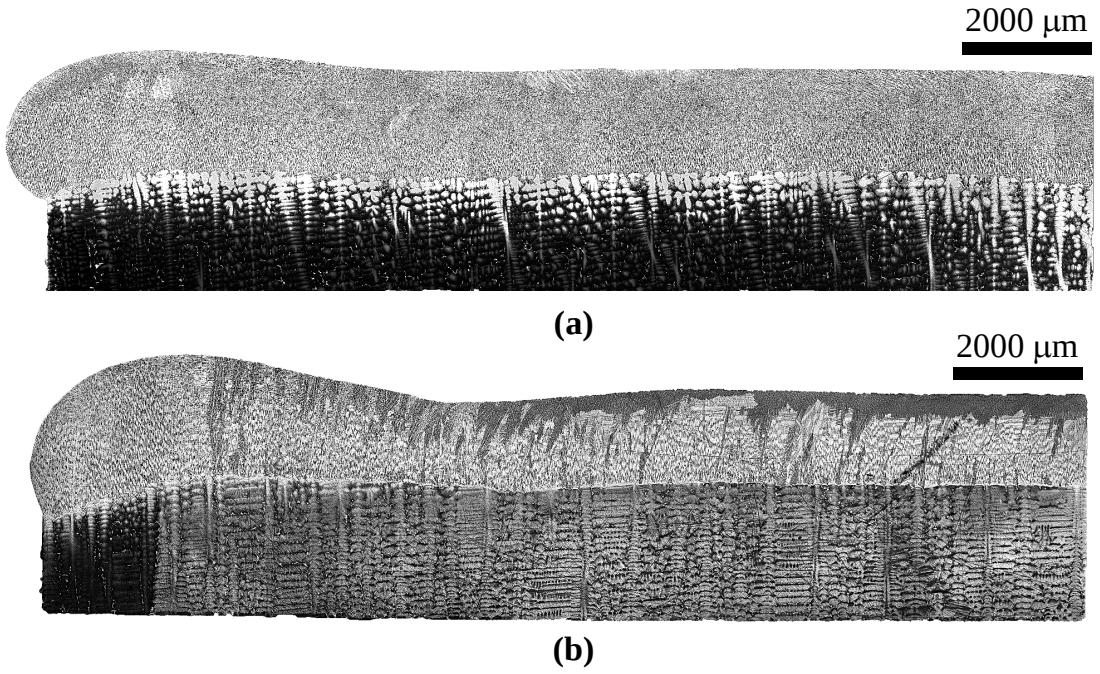

Figure 65. Representative longitudinal cross-section of the as-deposited (a) Sample 1 and (b) Sample 2. Sample 1 is processed at E = 52.73 J/mm^3 and Sample 2 is processed at E = 18.75 J/mm^3.

This difference is due to the fact that Sample 2 has higher SX ratio compared to Sample 1 and therefore, it has higher microhardness. It is noted that the results are presented as load-displacement instead of stress-strain as the cross-section (thickness of the samples is different

for the two samples and is varying along the length within the same sample). That is the reason that no absolute values of the modulus or strength are mentioned.

Table 8. Characteristics of Sample 1 and Sample 2.

Sample #	# of Repeats	Power (W)	Scan Speed (mm/s)	Scan Spacing (μm)	Powder Thickness (mm)	Energy Density (J/mm^3)	SX Ratio
1	600	750	800	12.7	1.4	52.73	0.39
2	400	500	750	25.4	1.4	18.75	0.75

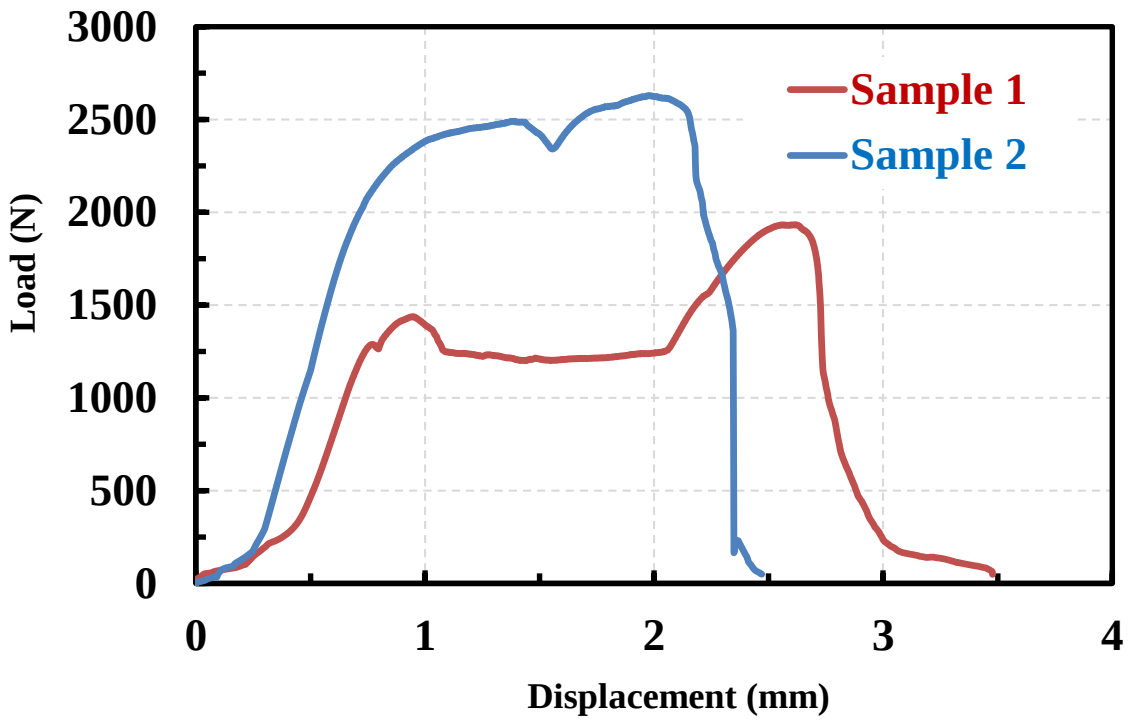

Figure 66. Load vs displacement curves for samples 1 and 2 based on tensile testing.

6.1.3 Results on Substrate 2

In this section, results on Substrate 2 are reported. The deposit characteristic are reported followed by microstructure characterization. The elemental segregation is evaluated and the

effects of heat treatment on the microstructure and microhardness are assessed.

6.1.3.1 *Deposit characteristics*

Using the results from the optimization runs, CMSX-4® is deposited on Substrate 2 with E of 21.38 J/mm^3. The longitudinal cross-section is shown in Figure 67(a). As illustrated in Figure 67(a), the deposit is crack-free and dense in nature. The melt pool is found to be stable during the laser processing. The average columnar height obtained is of order 1000 μm while the average total height obtained is of order 1700 μm in a single-pass.

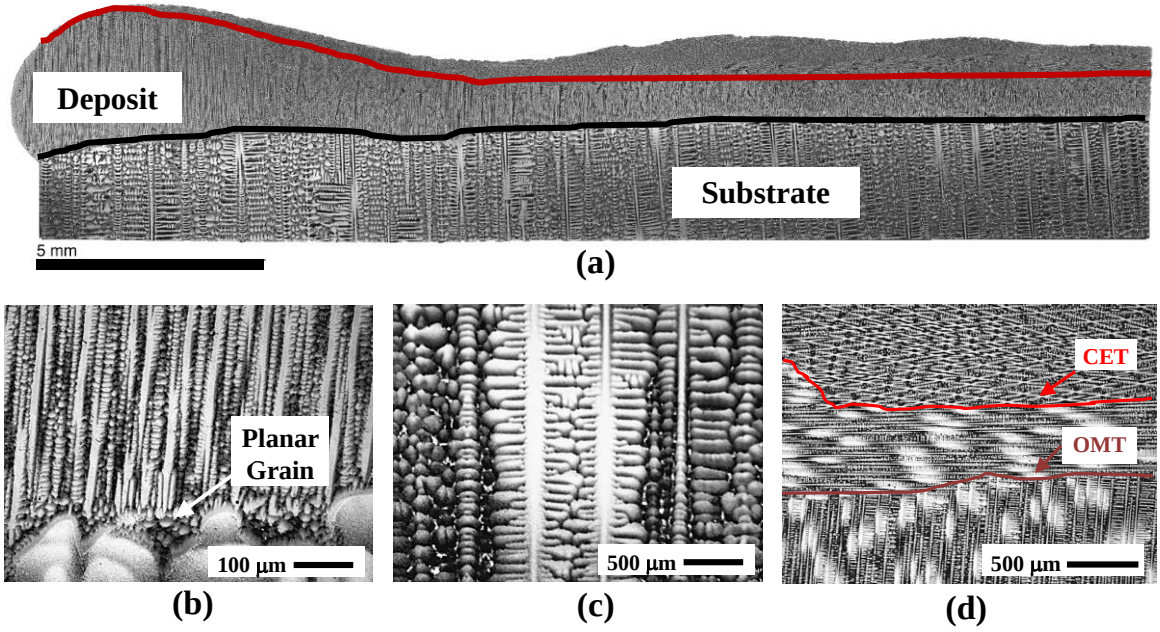

Figure 67. (a) Length-wise cross-section of the CMSX-4® deposit on the CMSX-4® substrate. The black line and the red line represent the substrate-deposit interface and the columnar region in the deposit, respectively. (b) The dendritic structure in the deposit region and planar grain formation at the bottom of the melt pool near the interface, (c) the dendritic structure in the substrate region, and (d) the columnar-to-equiaxed transition (CET) and the oriented-to-misoriented transition (OMT) in the deposit region.

The deposit is continuously bonded to the substrate along the entire length of the substrate without any interface fusion defects. Although the CMSX-4® powder used in the

present study contains some internal porosity as shown in Figure 59(b), an insignificant number of pores is observed in the deposit region as shown in Figure 67(a). The SX ratio for this particular sample is 0.6 which is in line with the optimization results as shown in Figure 64(b).

The microstructure of the SLE-deposited CMSX-4® shows dendrite segregation patterns as shown in Figure 67(b). A columnar grain structure along the [001] direction with epitaxial growth is visible. Figure 67(c) presents a zoomed view of a typical cross-section of the substrate, whereas Figure 67(b) presents a cross-section of the deposit. The primary dendritic arm spacing (PDAS) is a critical parameter that characterizes a SX/DS deposit. Increase in PDAS adversely affects the high-cycle fatigue life [123]. The average PDAS is of order 10 μm in the deposit region while in the substrate the average PDAS is of order 500 μm. Therefore, the microstructure obtained by SLE is about 50 times finer than the as-cast structure.

During laser processing, a portion of the substrate is melted that results in epitaxial growth. Planar grains are observed at the bottom of the melt pool [126]. These grains form at the beginning of the solidification process and were of order 5 – 10 μm as shown in Figure 67(b). Figure 67(d) provides a detailed view of the columnar growth transition from the [001] to the [100] direction and [100] to EQ known as the oriented-to-misoriented transition (OMT) and the columnar-to-equiaxed transition (CET), respectively.

Figures 68(a), 68(b), and 68(c) compare the XRD profiles for the pre-alloyed CMSX-4® powder with the CMSX-4® substrate and the CMSX-4® deposit, respectively. The XRD spectra for the CMSX-4® powder shows a prominent (111) peak as shown in Figure 68(a).

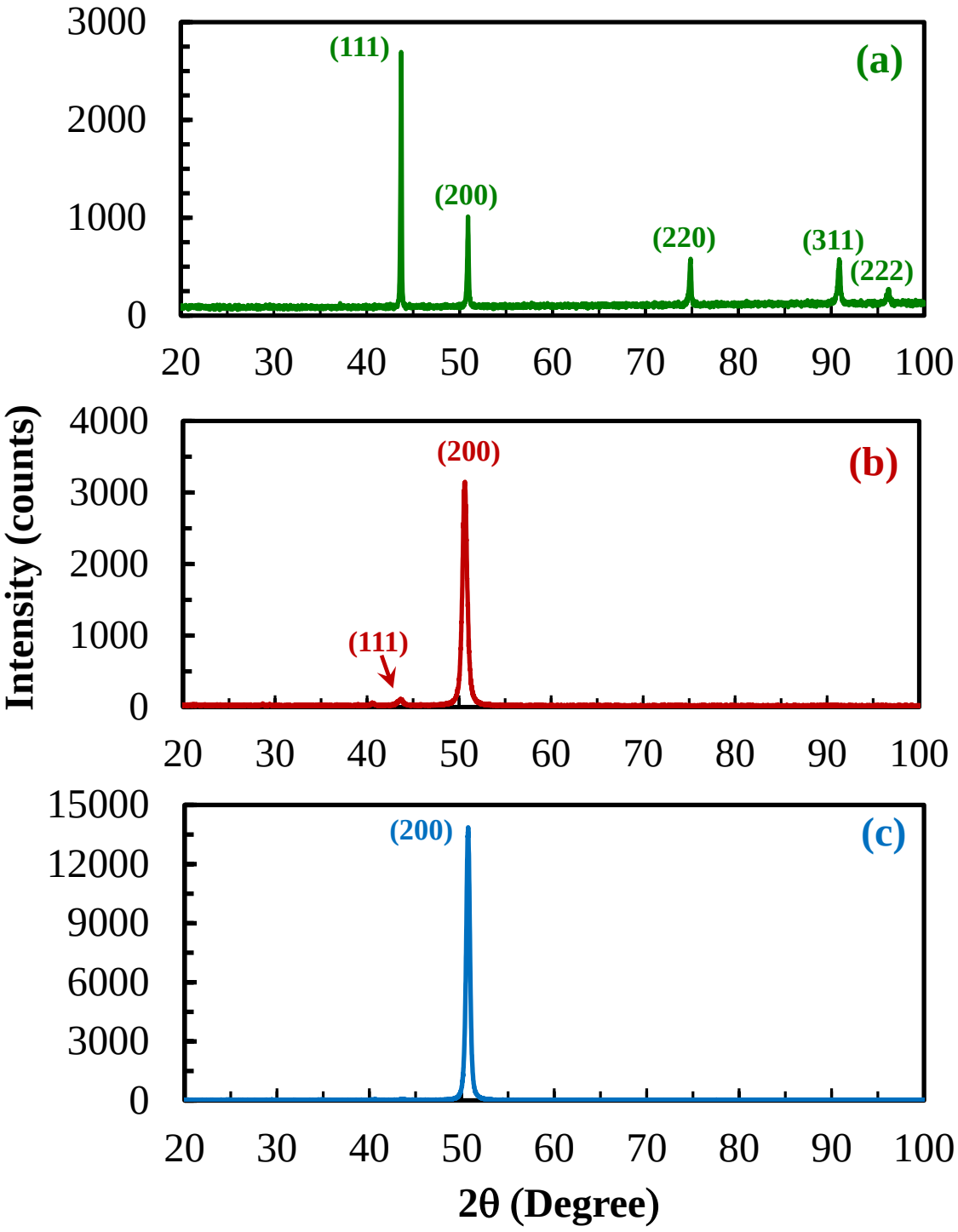

Figure 68. XRD profile of the (a) pre-alloyed CMSX-4® powder, (b) CMSX-4® substrate, and (c) CMSX-4® deposit.

The diffraction peaks occurred at 2θ = 44°, 51°, 75°, 91°, and 96° indicating the

diffraction of (111), (200), (220), (311), and (222) planes of the γ matrix. The strong (200) peak in the SLE deposited CMSX-4® represents unidirectional solidification and SX growth texture as shown in Figure 68(c).

6.1.3.2 *Microstructures*

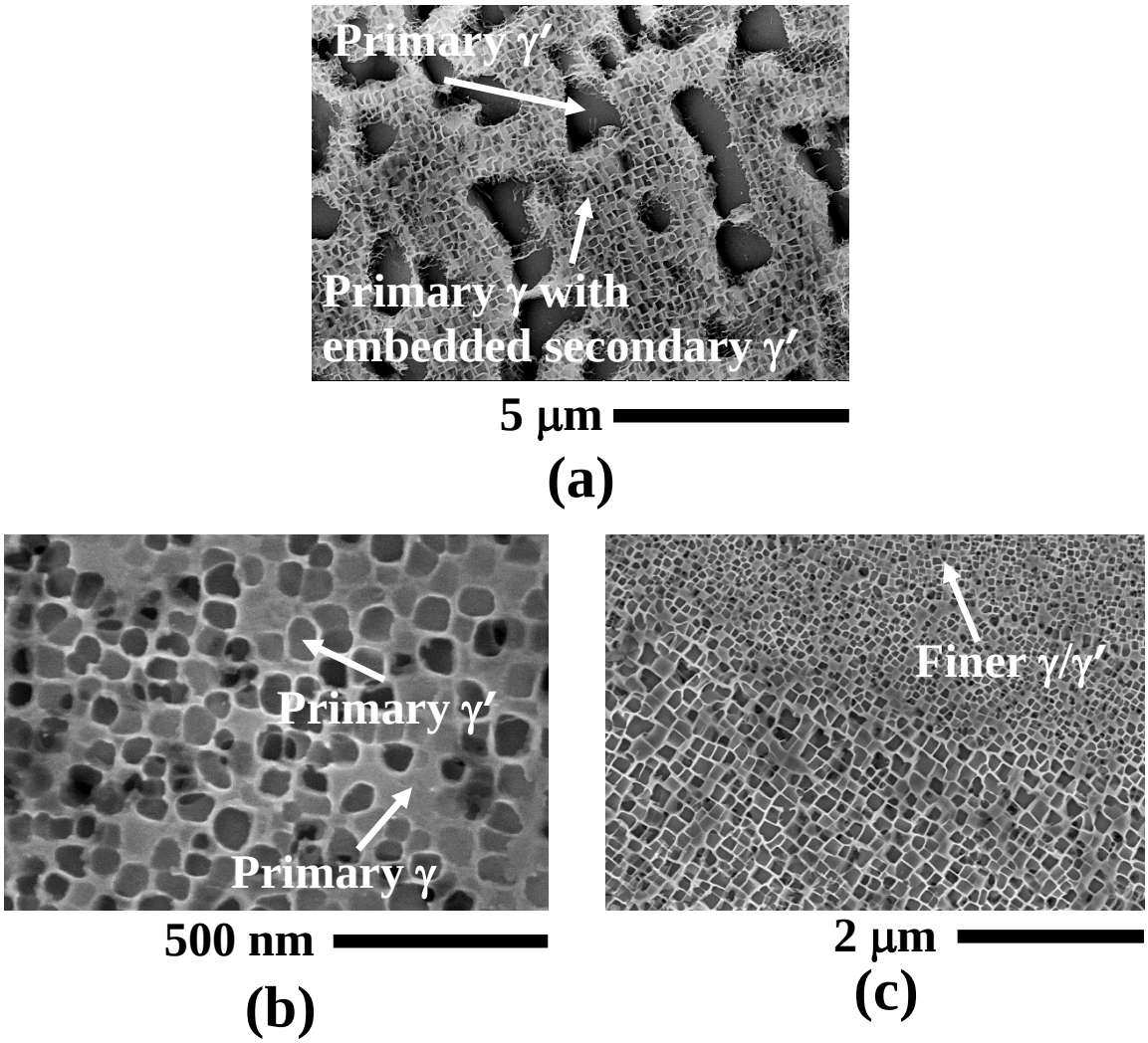

Figure 69. The γ/γ′ structure in the (a) substrate region showing primary and secondary γ/γ′ microstructure. The γ/γ′ structure in the (b-c) deposit region showing variation in the γ/γ′ size depending on the location.

The deposit region shows finer γ/γ′ microstructure compared to the substrate region. In

the substrate region, the primary γ′ precipitates show a characteristic dimension in the range of 2 μm as shown in Figure 69(a), whereas in the deposit region, the γ′ precipitates are in the range of 50 nm as shown in Figure 69(b). The deposit region shows approximately 40x reduction in the γ′ size for the as-deposited sample compared to the cast substrate. The deposit region, however, shows a variation in the γ′ size based on location with the size being finer at the dendrite core as shown in Figure 69(c).

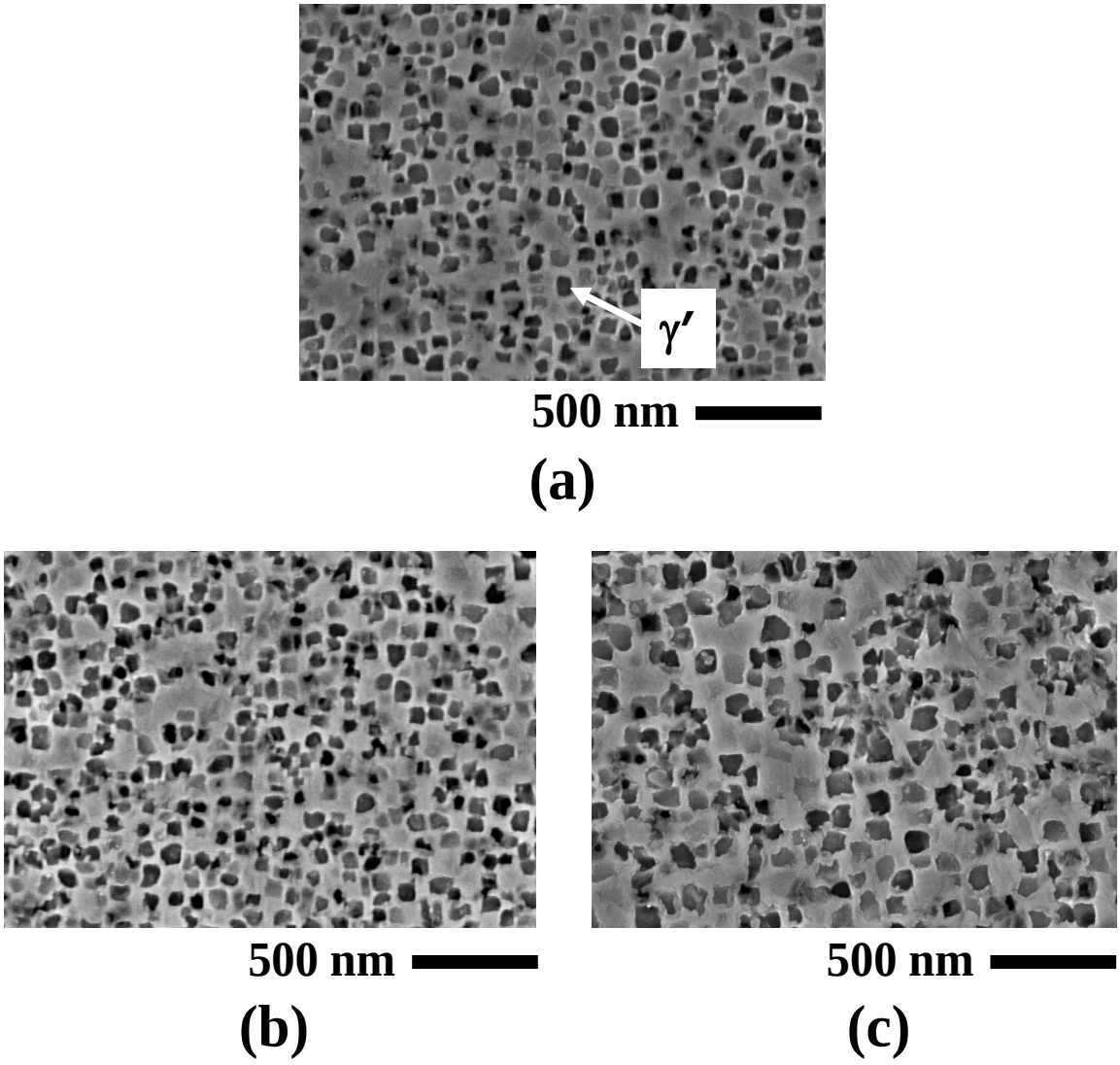

Figure 70. (a-c) The γ/γ′ structure at different locations along the build direction.

(a), (b), and (c) are taken at 500 μm, 750 μm, and 1000 μm distance from the substrate-deposit interface for the sample shown in Figure 67(a).

Figures 70(a) through 70(c) show the γ/γ′ microstructure at different locations in the deposit along the build direction. Note, the γ/γ′ microstructure in Figures 70(a) through 70(c) are obtained at the dendritic core region. The core region shows similar γ′ size of order 50 – 100 nm at different locations in the deposit region along the build direction.

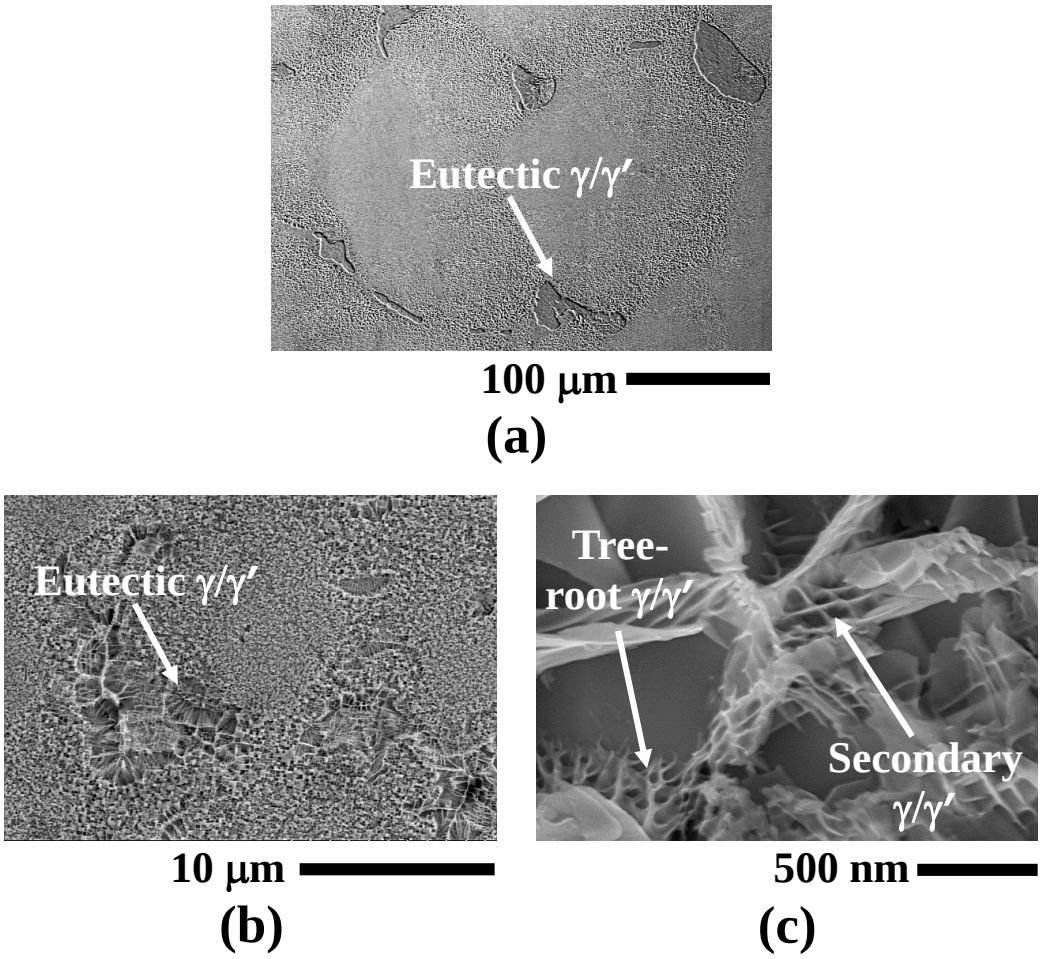

Figure 71. The major constituents in the (a) substrate region and (b) deposit region. (c) A zoomed view of the eutectic γ/γ′ structure in the deposit region.

The constituents of the deposit and the substrate are the γ matrix, the γ′ precipitates, and

the eutectics as shown in Figures 71(a) and 71(b), respectively. However, the eutectic size is finer in the deposit region compared to the substrate. Figure 71(c) illustrates the eutectic γ/γ′ morphology in the deposit region showing the cubic and the channel shaped γ/γ′ precipitates in the deposit. The channel length is from 1 – 2 μm while the channel width is of order 200 – 400 nm. The cubic γ/γ′ precipitates are of order 50 – 100 nm in the eutectic region. The eutectic region shows secondary complex tree-root like microstructure and secondary γ/γ′ precipitates with size of order 100 – 200 nm and 5 – 10 nm, respectively as shown in Figure 71(c).

Contrary to the other researchers who have claimed that epitaxial loss in the deposit region is attributed to the segregation in the substrate region [127], no such evidences are found in the current study. Figures 72(a) and 72(b) show the substrate-deposit interface region. In Figure 72(a), the substrate eutectic region gives rise to SG in the deposit region. However, in Figure 72(b), the deposit region shows epitaxial dendrites forming on a substrate eutectic region.

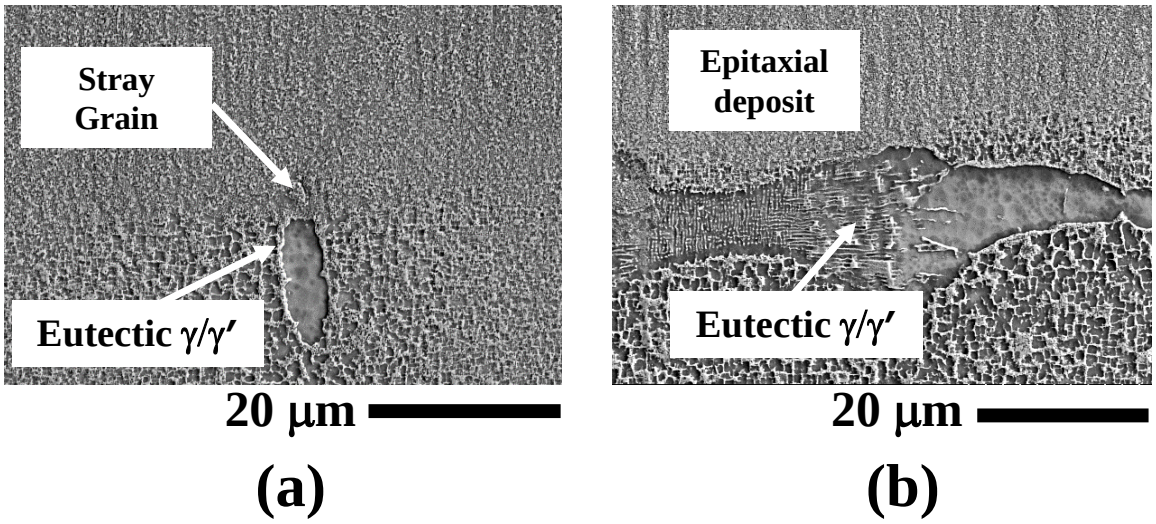

Figure 72. SG formation on top of a substrate eutectic region and (b) epitaxial dendrites on top of a substrate eutectic.

6.1.3.3 *Elemental segregation*

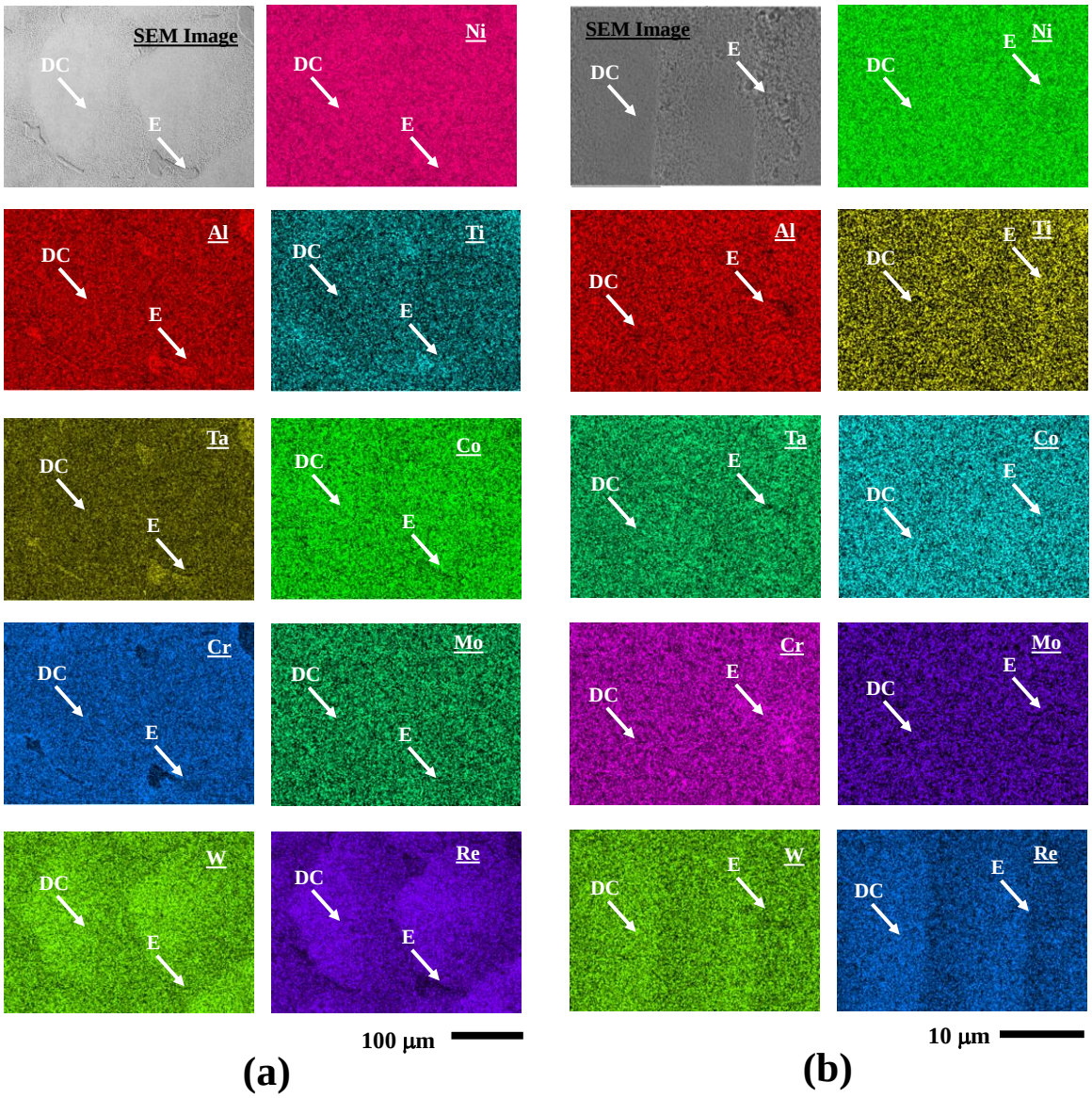

Figure 73. SEM-EDS elemental maps of a representative region in the (a) substrate and (b) deposit region.

Figures 73(a) and 73(b) illustrate EDS maps of representative regions in the CMSX-4® substrate and deposit, respectively. Note that the dendritic core and the eutectic regions are marked by DC and E, respectively. In the substrate, Al, Ti, and Ta show strong segregation to

the eutectics. W and Re show strong segregation to the core (Figure 73(a)). In the deposit region, W and Re show segregation behavior like the substrate, and segregate to the dendritic core region. However, Al shows segregation behavior opposite to the substrate, and segregates to the core. Other elements do not show any strong segregation behavior as illustrated in Figure 73(b).

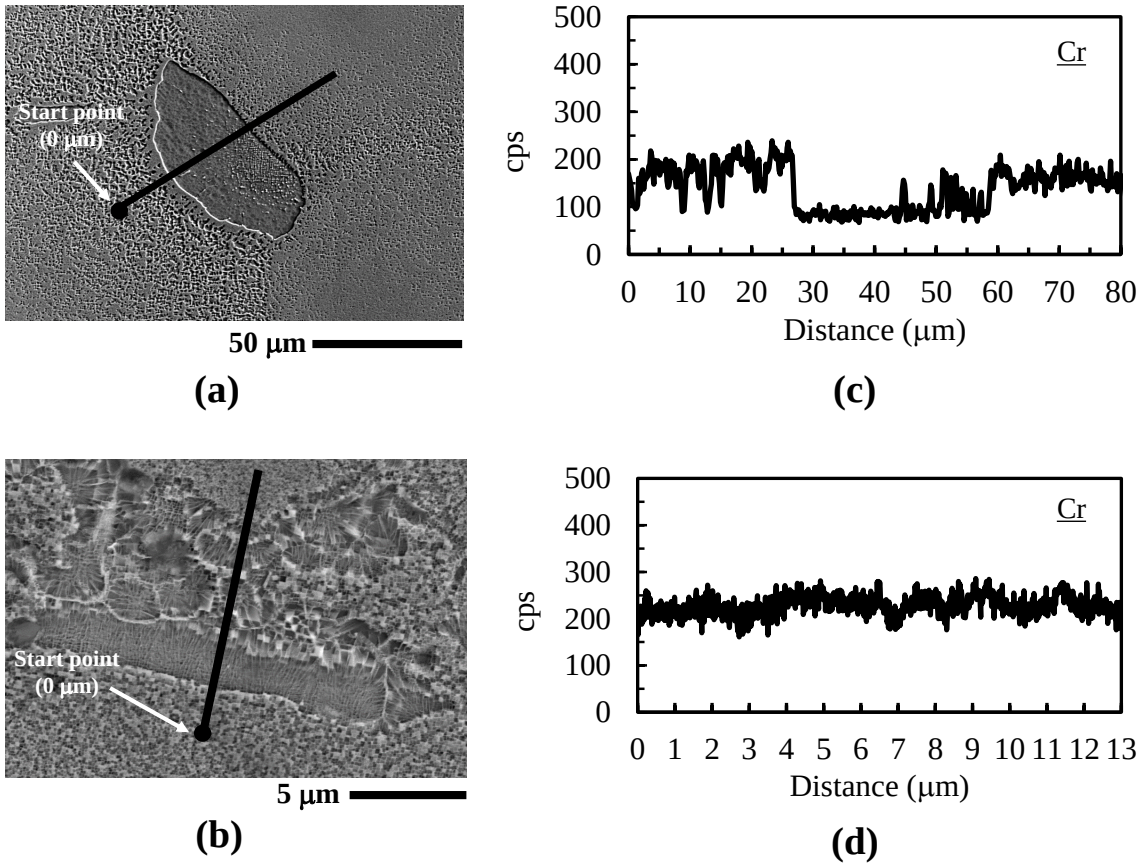

Figure 74. SEM image of a representative line scan domain in the eutectic region of (a) substrate and (b) deposit. EDS line profile of Cr across a representative eutectic region in the (c) substrate and (d) deposit.

In order to quantitatively characterize the elemental segregation in the eutectic regions, EDS line scans are performed across representative eutectic regions in the substrate and deposit, respectively (Figures 74(a) and 74(b)). The line profiles of a representative element

(Cr) across a eutectic region in the substrate and the deposit are shown in Figures 74(c) and 74(d), respectively. From the elemental line profiles, the maximum and the minimum counts are extracted and a segregation parameter is defined as degree of segregation (k) = maximum cps/minimum cps (where cps denotes counts per second). The k values for various elements are plotted in Figure 75 for the substrate and the deposit region. As can be seen, in comparison to the bulk alloy composition, the γ/γ′ eutectic phase shows strong elemental segregation in the substrate. The degree of segregation is considerably lower in the deposit region.

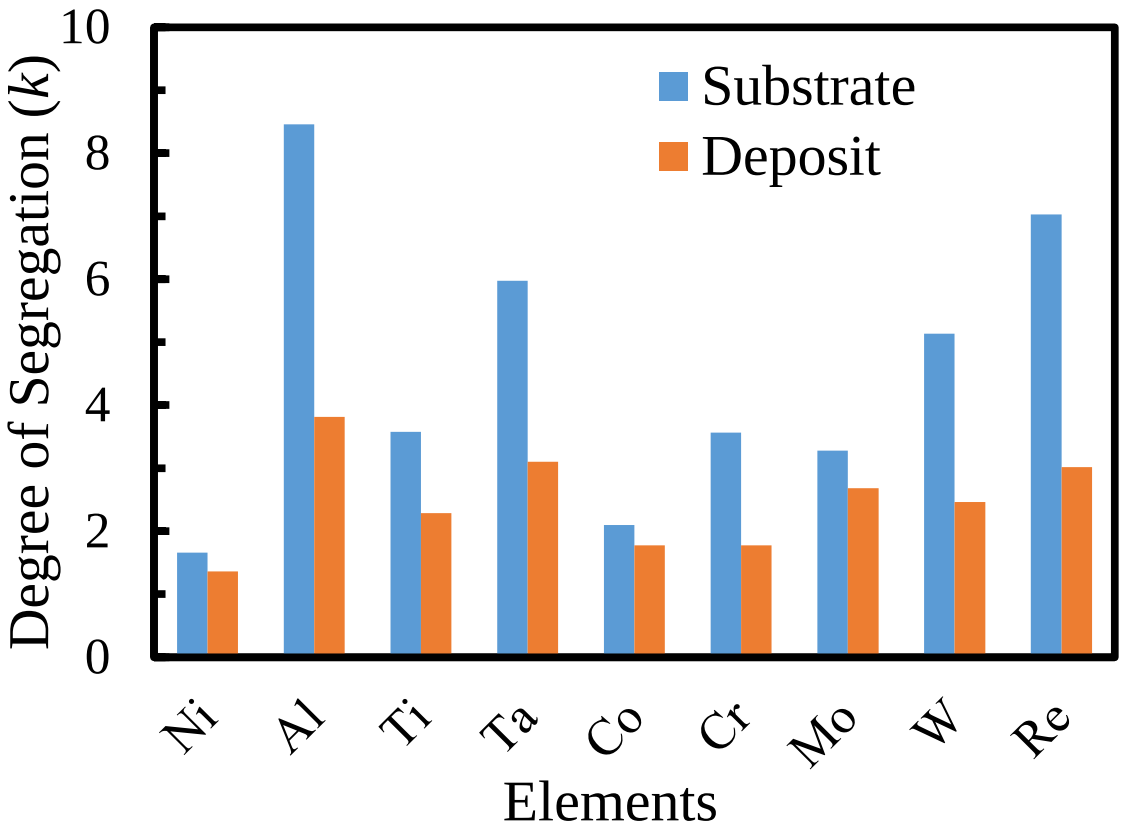

Figure 75. Degree of segregation (k) of various alloying elements across representative eutectic pools in the substrate and the deposit.

6.1.3.4 *Microhardness properties*

In the present study, microhardness results indicate higher hardness values in the deposit

region than in the substrate. Figure 76(a) shows two representative micro indentation marks near the interface and in the columnar region. The [001] columnar region typically shows higher hardness than either the [100] columnar zone or the EQ region. The substrate region shows an average hardness value of 400 HV. Table 9 summarizes the hardness and yield stress results for the substrate and the different regions in the deposit.

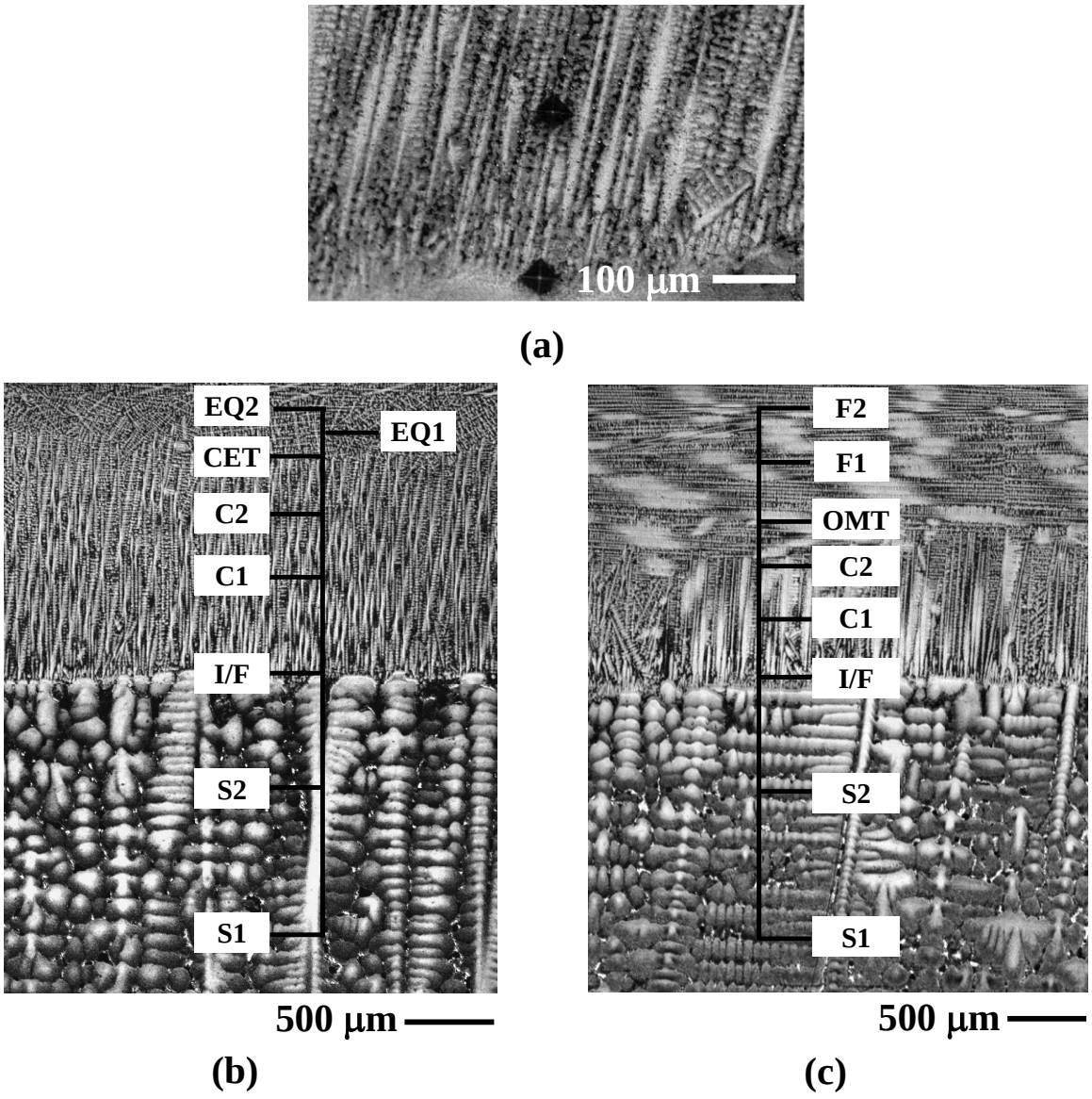

Figure 76. (a) Representative indentation marks in the CMSX-4® sample. Schematic of indentation locations at different region of the CMSX-4® sample to obtain line profiling of HV for (b) deposit with EQ region and (c) deposit with OMT region.

Variations in microhardness values are observed in different regions of the deposit. Figures 76(b) and 76(c) show line profiling of the micro indentation hardness at different regions of the CMSX-4® deposit. The indentations are made near the bottom edge of the substrate, (S1) and then the indenter progressively moved upwards to S2, followed by interface (I/F), columnar region (C1, C2), transition region (CET or OMT), and finally misoriented (F1, F2) or EQ region (EQ1, EQ2). Table 10 describes two typical sets of line profile data obtained for a representative CMSX-4® sample.

Table 9. Summary of microhardness results for CMSX-4®.

Region	HV	GPa	σ_y (GPa)
Columnar	465	4.56	1.52
Equiaxed	430	4.22	1.40
Substrate	400	3.92	1.31

Table 10. Representative Line profile data for a CMSX-4® sample.

Line profile with EQ region		Line profile with misoriented region	
Location	**HV**	**Location**	**HV**
S1	398	S1	363
S2	406	S2	373
I/F	425	I/F	465
C1	449	C1	477
C2	447	C2	482
CET	437	OMT	428
EQ1	418	F1	425
EQ2	449	F2	445

6.1.3.1 *Effect of heat treatment*

The zoomed view of the substrate-deposit interface region is shown in Figures 77(a) and 77(b) for the as-deposited and the heat-treated samples. The heat treatment cycle details are provided in Chapter 3. No significant difference in the interface is observed near the interface

region as shown in Figures 77(a) and 77(b). The microstructure of the deposited CMSX-4® retains the columnar structure after the heat treatment as shown in Figure 77(b) [128].

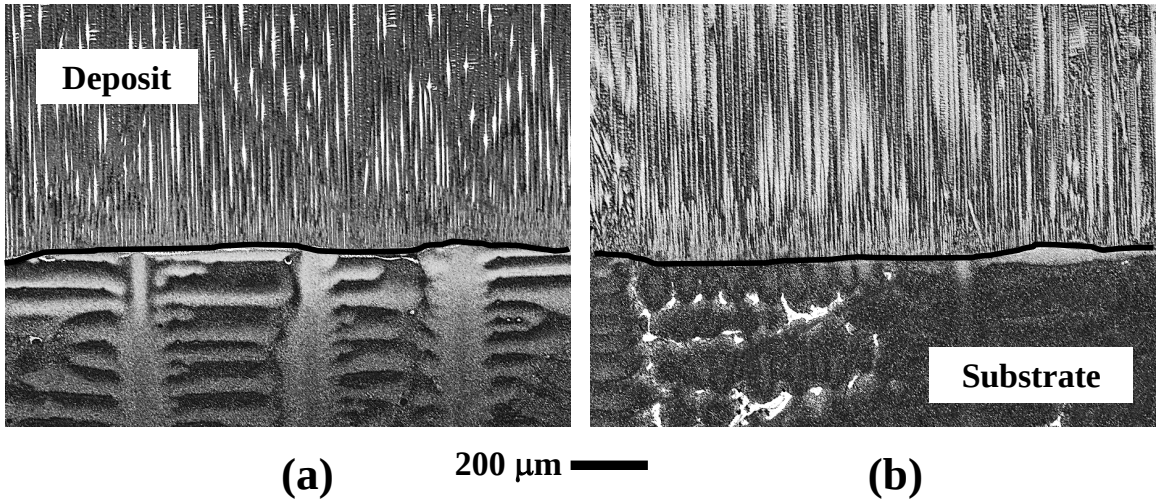

Figure 77. OM image showing interface microstructure (a) of the as-deposited sample, and (b) the heat-treated sample. The black line represents the substrate-deposit interface.

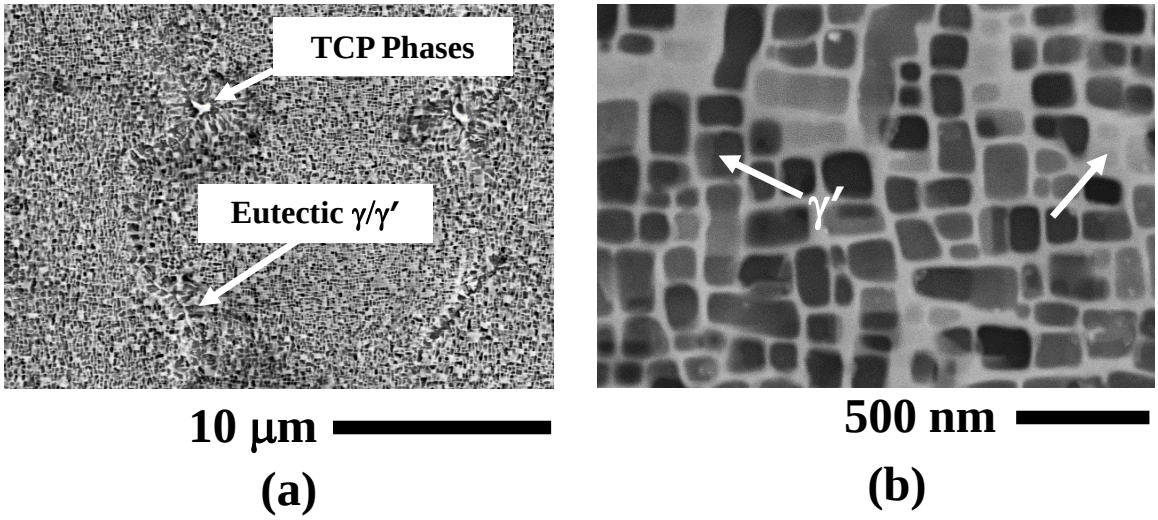

Figure 78. (a) SEM image showing morphologies of various constituents of the SLE processed CMSX-4® deposit after the heat treatment. (b) Representative SEM image showing γ/γ′ morphology in deposit region after the heat treatment.

As mentioned earlier, the major constituents of the SLE processed microstructure of

CMSX-4® are the γ matrix, the γ′ precipitates in the γ matrix, and the eutectics. Figure 78(a) illustrates the major constituents in the SLE deposited CMSX-4® after heat treatment. The eutectic volume fraction is visibly reduced after the heat treatment process as shown in Figures 71(b) and 78(a). Figure 78(b) illustrates the γ′ size distribution in the heat-treated sample. The primary γ′ size is of order 100 nm in the heat-treated samples. The heat-treated CMSX-4® shows predominantly cuboidal precipitates as compared to polygonal shaped precipitates in the as-deposited sample as shown in Figure 69(b).

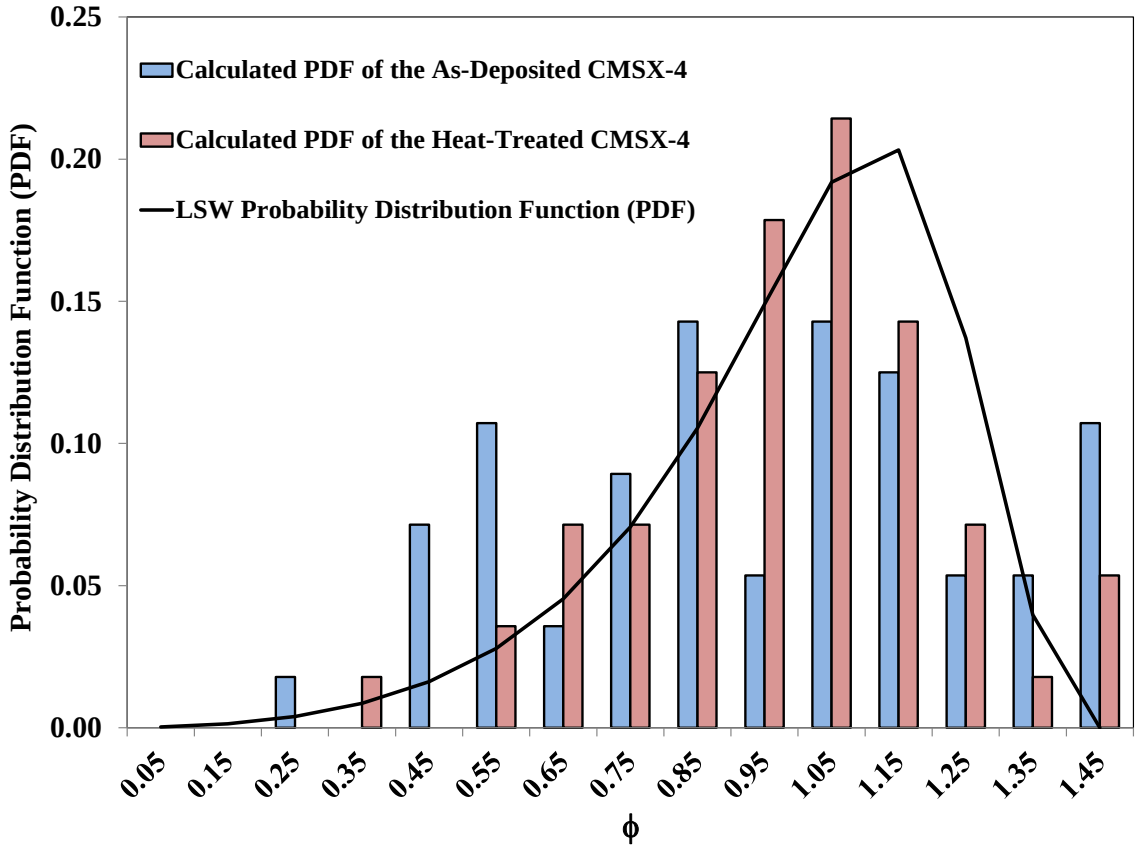

Figure 79. Particle size distribution (PSD) of the γ′ precipitates – as-deposited and heat-treated sample.

To compare the size of the primary γ′ precipitates, their equivalent diameters are calculated. The equivalent diameter is defined as $D = (A/\pi)^{0.5}$, where A is the area of a

γ′ precipitate determined by measuring the perpendicular sides of an individual precipitate. The average equivalent diameter, <D>, is calculated by the mean of ~100 γ′ precipitates. Figure 79 illustrates the γ′ particle size distribution (PSD) with the theoretical Lifshitz-Slyozov-Wagner (LSW) [113, 114] distribution superimposed for the as-deposited and heat-treated CMSX-4® samples. The normalized diameter ϕ is defined as D/<D>.

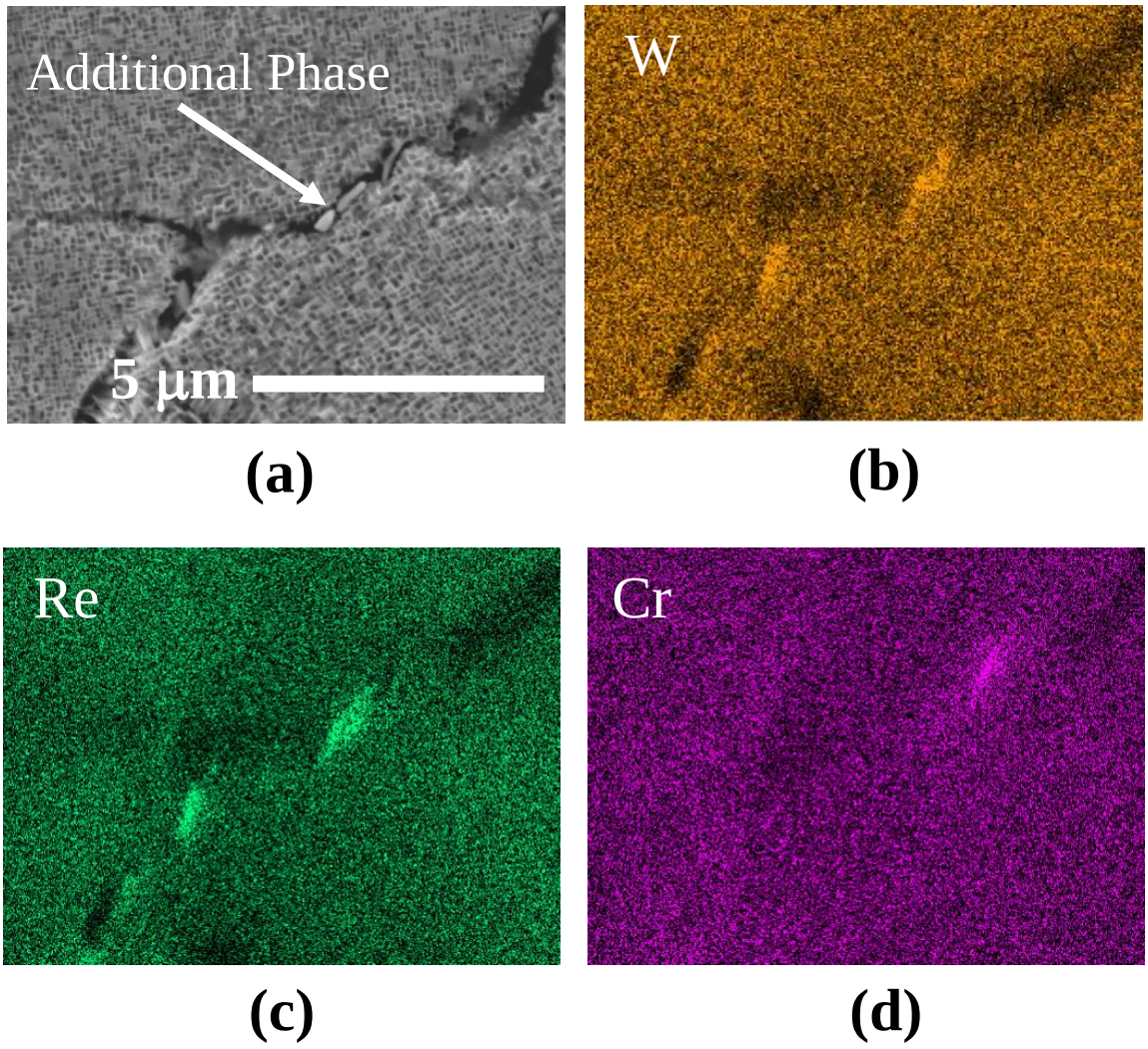

Figure 80. (a) Representative SEM image showing morphology of the secondary phase precipitate in the CMSX-4® deposit after the heat treatment. (b)- (d) EDS Map of the precipitate.

The SLE processed PSD of the γ′ precipitate differs considerably from the theoretical LSW distribution. This may be due to the fact that the size of the γ′ precipitates in the interdendritic regions is found to be larger than those present within the dendrite region. Note that while performing this calculation, the γ/γ′ precipitates in the eutectic pools are not considered. The γ′ size shows a closer match to the theoretical PSD in the heat-treated sample.

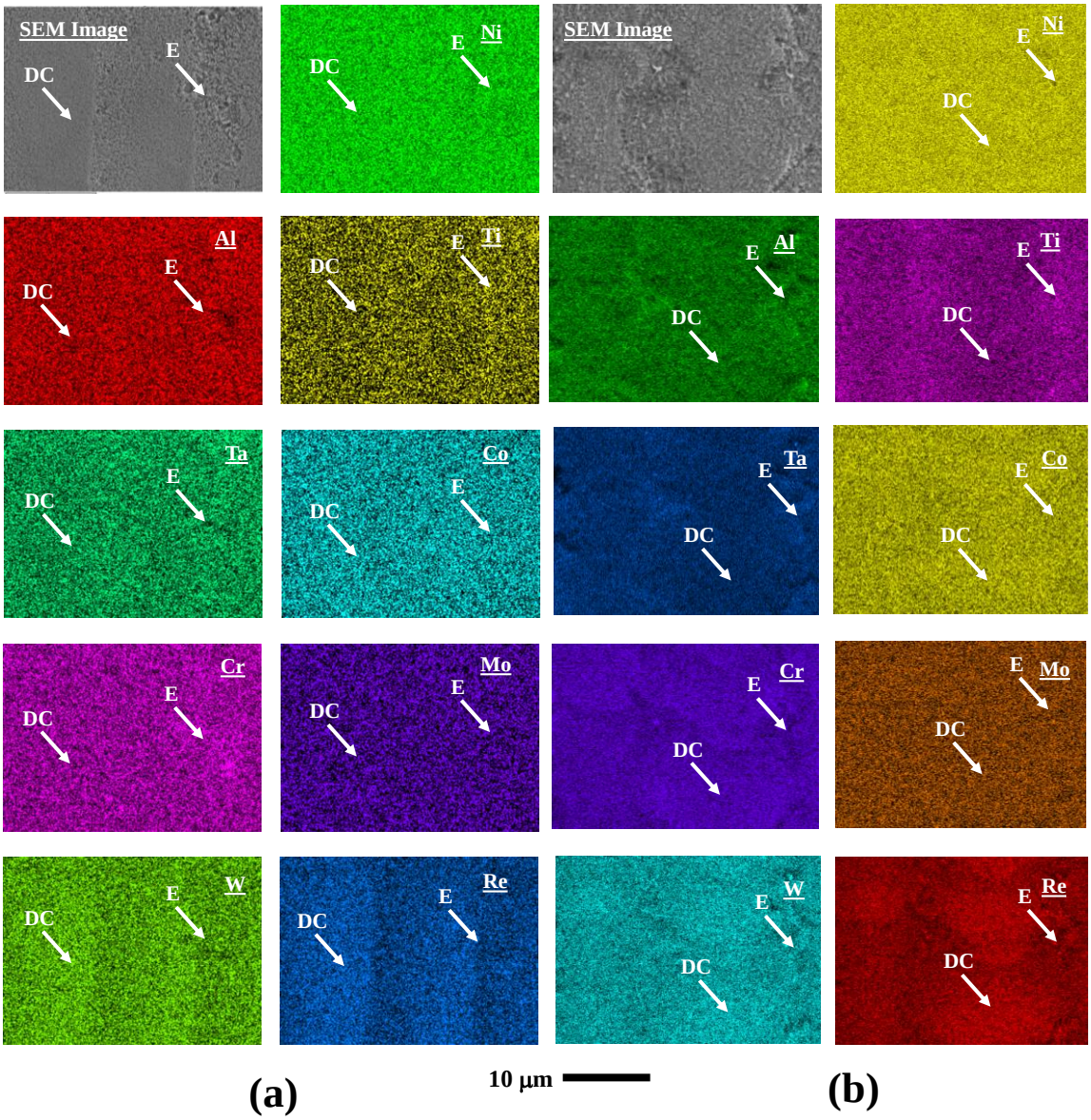

Figure 81. SEM-EDS map of a representative region in the CMSX-4® deposit – (a) as-deposited sample and (b) heat-treated sample.

Figure 80(a) shows SEM images of secondary phase precipitates that are formed after the heat treatment. These precipitates are identified as topologically-closed-pack (TCP) phases. The size of these precipitates are of order 500 nm. These precipitates are observed to line up along the grain boundary surrounded by the γ′ phase. The elemental EDS maps of these particles are shown in Figures 80(b) through 80(d). The precipitates are found to be rich in W, Re, and Cr. The results obtained here are similar to EBM-processed CMSX-4® [129].

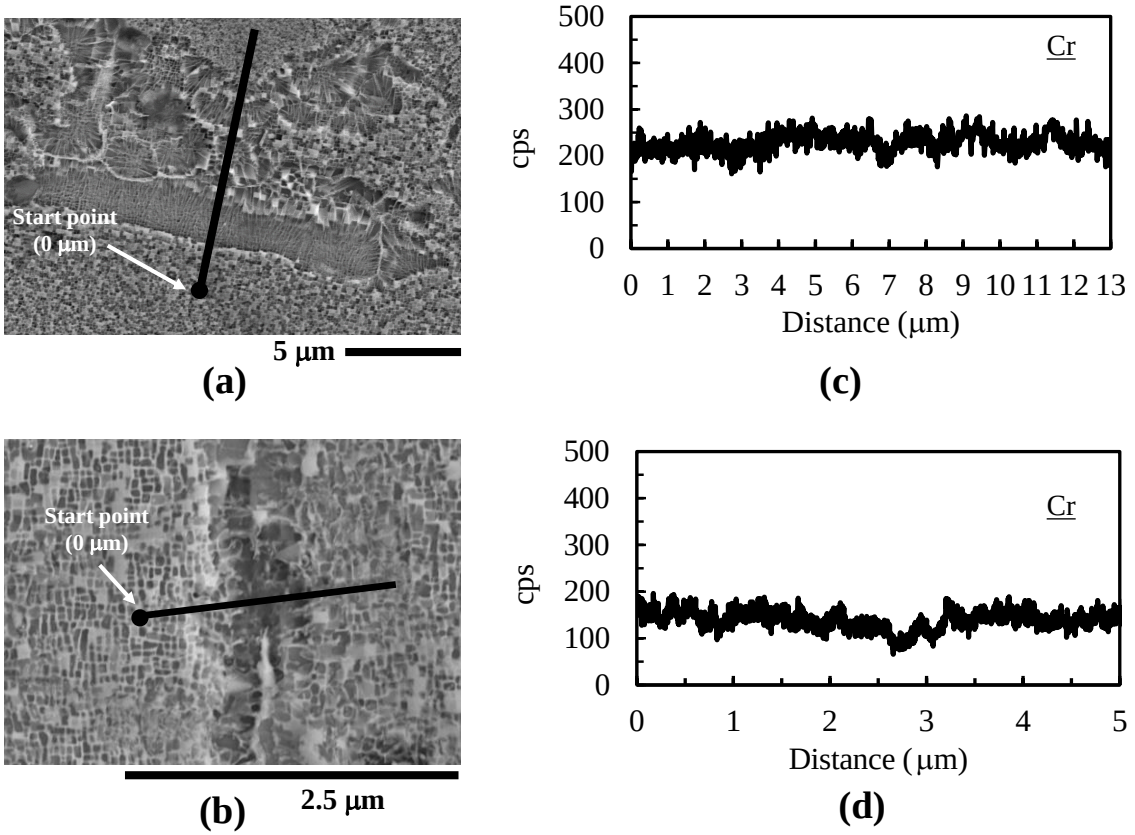

Figure 82. SEM image of a representative line scan domain in the eutectic region of CMSX-4® deposit - (a) as-deposited and (b) heat-treated. EDS line profile of Cr across a representative eutectic region in the (c) as-deposited and (d) heat-treated CMSX-4® deposit.

Figures 81(a) and 81(b) illustrate EDS maps of a representative region in the CMSX-4® deposit before and after the heat treatment, respectively. Note that the dendritic core and the

eutectic regions are marked by DC and E, respectively. Ti and Ta show segregation to the eutectics. W, Al, and Re show segregation to the core (Figures 81(a) and 81(b)). Other elements do not show any strong segregation behavior as shown in Figures 81(a) and 81(b).

In order to quantify the elemental segregation, EDS line scans are performed across representative eutectic regions in the deposit region before and after the heat treatment, respectively (Figures 82(a) and 82(b)). The line profiles of a representative element (Cr) across a eutectic region in the deposit before and after the heat treatment are shown in Figures 82(c) and 82(d), respectively. From the elemental line profiles, the maximum and the minimum counts are extracted and a segregation parameter is define as degree of segregation (k) = maximum cps/minimum cps (where cps denotes counts per second).

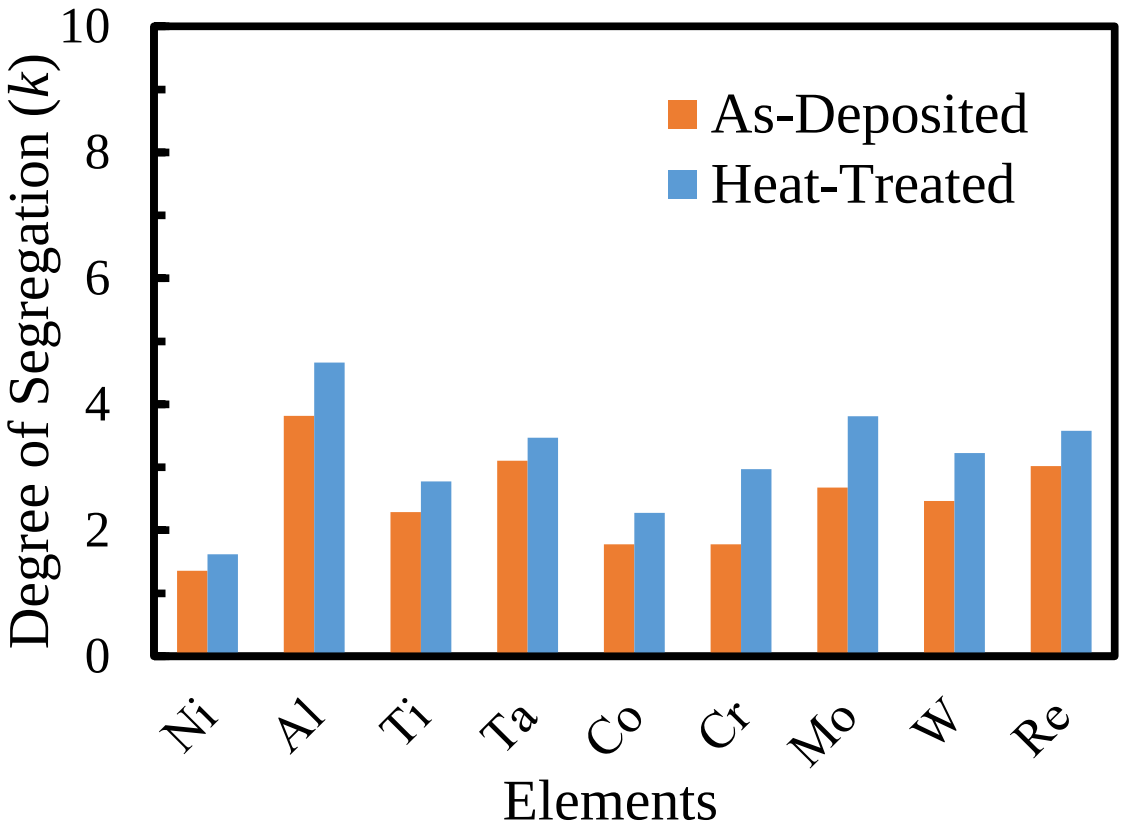

Figure 83. Degree of segregation (k) of various alloying elements across representative eutectic pools in the as-deposited and heat-treated CMSX-4® sample.

The k values for various elements are plotted in Figure 83 for the deposit region before and after the heat treatment. Although, in comparison to the as-deposited sample, the γ/γ′ eutectic phase shows increased elemental segregation for the heat-treated CMSX-4®, the dimension of the eutectic pools is significantly smaller in the heat-treated sample.

Table 11 Summary of microhardness results for CMSX-4®.

Sample Type	Region	HV_{2000}	HV (GPa)	σ_y (GPa)
As-Deposited CMSX-4®	Deposit	464	4.55	1.51
	Interface	423	4.15	1.38
	Substrate	400	3.92	1.31
Heat-Treated CMSX-4®	Deposit	492	4.83	1.61
	Interface	446	4.37	1.46
	Substrate	405	3.97	1.32

In the present study, the heat-treated CMSX-4® shows 10% increase in the hardness values as reported in Table 11. This increase may be attributed to the uniform γ′ distribution obtained after the heat treatment. Table 11 also shows the calculated yield stress for the as-deposited and the heat-treated CMSX-4® samples.

6.1.4 Conclusions on CMSX-4®

The SLE process is shown to successfully deposit CMSX-4® on CMSX-4® substrates. The SLE-deposited CMSX-4® shows columnar growth in the [001] direction with more than 1000 μm of columnar height. The columnar dendrites grow epitaxially from the partially remelted CMSX-4® substrate. After traversing some distance, these [001] dendrites either flip their direction or transition to EQ morphologies leading to loss of epitaxy. Overall, three different types of grain morphologies are observed namely [001] columnar grains, [100] columnar grains, and EQ grains. Microhardness measurements demonstrate that the deposit

region had higher HV values compared to the substrate. Such increase in the hardness values may be attributed to the higher cooling rate in the LPBF processes resulting in a finer microstructure.

The deposit region typically consists of the γ matrix, the secondary γ′ phase precipitates, and the eutectics. The deposit region shows a finer γ/γ′ microstructure compared to the substrate. The deposit region also shows higher microstructural uniformity compared to the substrate. The degree of elemental segregation is lower compared to the cast substrate. The microhardness results obtained in the present study for CMSX-4® are significantly higher than the values obtained from existing literature.

Aluru et al. conducted a study on CMSX-4® processed through transient liquid phase bonding with other EQ superalloys and obtained a hardness value of 420 HV [130]. Lapin et al. investigated the microhardness as a function of γ′ volume fraction and primary γ′ precipitate size in Bridgman casting [131]. It was shown that the hardness value increased with increasing γ′ volume fraction and decreased with increasing size of primary γ′ precipitate. The maximum hardness value obtained for 70 vol. % and 147 nm size of primary γ′ precipitate was close to 430 HV, which is still lower than the hardness obtained for [001] region in the present study.

Commercial heat treatment suited for CMSX-4® is performed. A detailed study is conducted to characterize the microstructural changes due to the heat treatment. The size of the γ′ precipitates increase due to coarsening. However, the microstructures of CMSX-4® become uniform after the heat treatment with significant reductions in the eutectic volume fraction. Hence, the microhardness values increase in the deposit region after the heat treatment.

6.2 Study on René N5

René N5 is a Re containing "second-generation" SX superalloy developed at General Electric. The presence of Re delays coarsening of the γ′ phase, and increases γ/γ′ misfit [121]. René N5 is also strengthened by the solid-solution-strengthening effects of Cr, Ta, and W. Al and Ti provide additional strength due to the precipitation-hardening effects of the γ′ phase [91]. The total Al+Ti content in René N5 is 6.2 wt. %, thus making it a "non-weldable" alloy.

6.2.1 Materials

The René N5 powder used in this study is an argon gas-atomized product made by Praxair Surface Technologies. The composition of the powder is reported in Table 12. Hf (0.15 wt. %), C (0.05 wt. %), and B (0.004 wt. %) are also found in trace quantities. The morphology, size distribution, and cross-section of the powder are analyzed using OM and SEM.

Table 12. Composition of the René N5 powder (wt. %).

	Cr	Co	Mo	Re	W	Al	Ta	Ni
René N5	7.1	8.0	2.0	3.0	5.0	6.0	7.0	Bal

René N5 powder particles are mostly spherical with particle diameters varying from 40 to 100 μm as shown in Figure 84(a). The powder is mounted in Bakelite and polished to a mirror finish. The cross-section is analyzed under an optical microscope for the inspection of internal porosity, and limited internal porosity is detected as shown in Figure 84(b). Figure 84(c) illustrates the morphology of a single powder particle showing dendritic microstructure on the particle surface and Figure 84(d) illustrates the internal micro-dendritic structure of a few René N5 powder particles. The SLE process is carried out on two types of rectangular SX

cast René N5 substrates having dimensions of 35.56 mm x 6.86 mm x 2.54 mm, with [100] and [001] crystal growth directions.

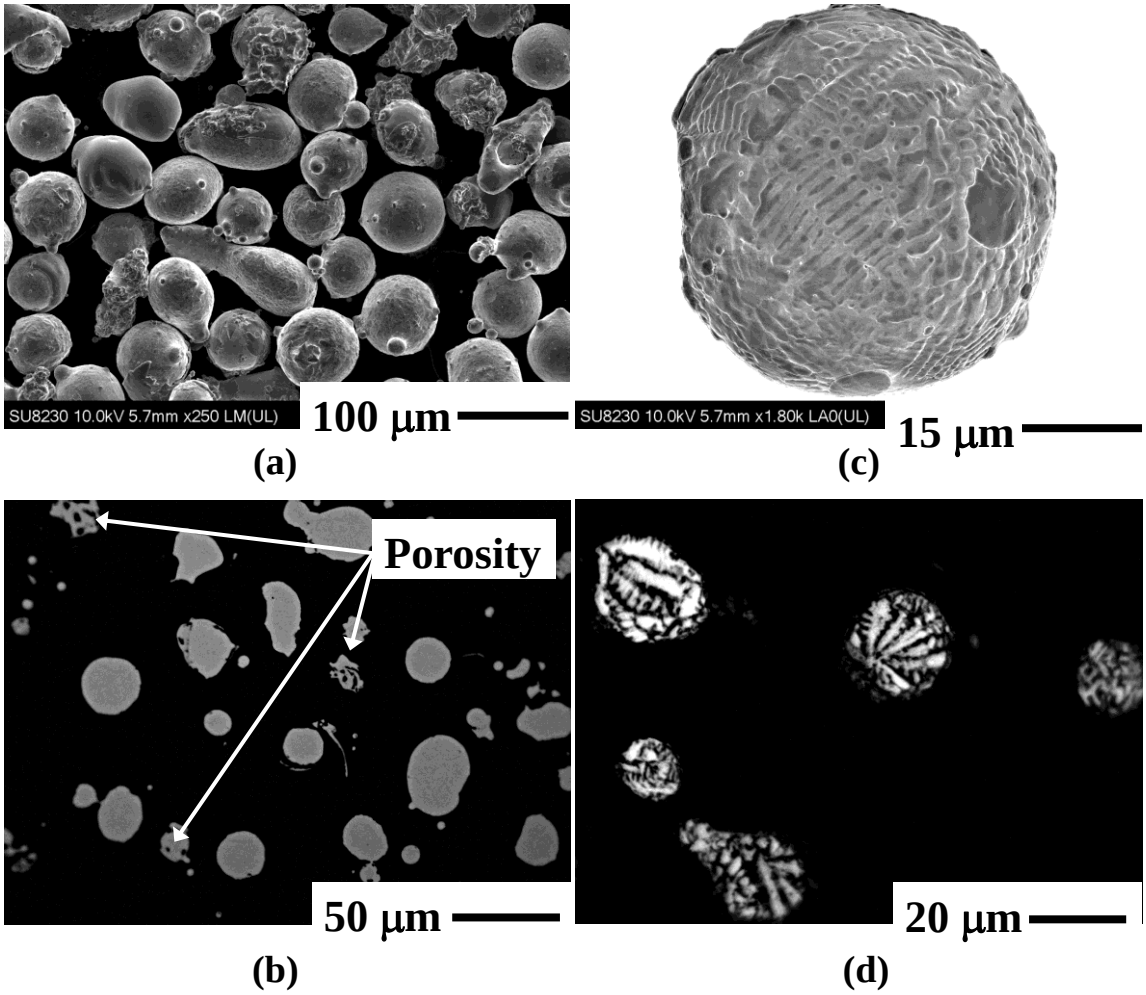

Figure 84. (a) SEM image of the René N5 powder, (b) OM image of the René N5 powder cross-section after polishing, (c) SEM image of a powder particle, and (d) OM image showing the internal dendritic microstructures of etched René N5 powder particles.

6.2.2 Deposit characteristics

Figures 85(a) and 85(b) show longitudinal cross-sections of the SLE deposited René N5 on René N5 substrates with [100] and [001] crystal growth direction, respectively. Both samples are produced under identical SLE processing conditions. The dominant thermal

gradient (in the [001] direction) is perpendicular to the primary dendritic orientation for the [100] substrate. This necessitates more energy to achieve the same melt-back in comparison with the [001] substrate. Hence, the average melt-back depths are 90 μm and 130 μm for the [100] and [001] substrates, respectively. The average melt-back depth is of order 100 μm for all the SLE processed René N5 samples. The relatively shallow melt-back depth ensures that the heat input to the substrate is minimal reducing the possibility of thermal stress accumulation, and therefore, crack formation in the SLE-processed samples. As shown in Figures 85(a) and 85(b), very few pores are observed in the SLE deposited René N5 [132, 133].

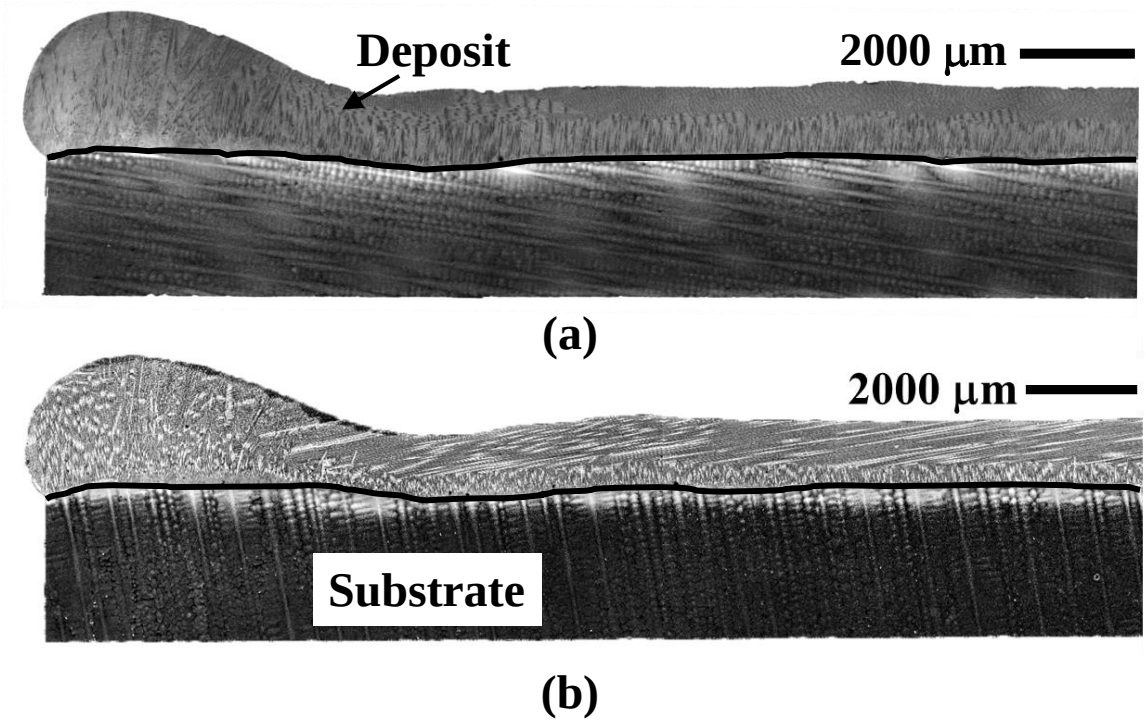

Figure 85. OM images showing longitudinal cross-sections of the SLE deposited René N5 on René N5 substrates with (a) [100] and (b) [001] crystal growth direction. These samples were run with a fixed scan spacing of 25.4 μm and scan speed of 350 mm/s.

As shown in Figures 85(a) and 85(b), the SLE-deposited René N5 thickness is found to

be more than 1000 μm. The deposit is dense and metallurgically bonded to the substrate along the entire length of the substrate. Three types of dendritic structures are observed in the SLE-fabricated René N5 deposits: a columnar dendritic region in the direction of the dominant thermal gradient ([001]), a columnar dendritic region in the direction of the laser beam movement ([100]), and a fine equiaxed region. The columnar dendrites grow epitaxially along the direction of the dominant thermal gradient in the [001] direction from the partially re-melted grains of the substrate that serve as nuclei for directional crystal growth. Cooling of the melt pool via the substrate and the adjacent solidified deposited layer also contributes to an increase in the thermal gradient.

Figures 86(a) and 86(b) illustrate transverse cross-sections of the SLE deposited René N5 on René N5 substrates with [100] and [001] crystal growth direction, respectively showing columnar dendritic growth in the [001] direction. The PDAS was in the range of 15 – 30 μm in the deposit region and 100 – 250 μm in the substrate region, respectively. Therefore, the microstructure obtained by SLE is about 10 times finer than the as-cast structure. All samples fabricated through SLE exhibit microstructural refinement as shown in Figures 86(a) and 86(b).

The substrate crystal growth direction of [100] does not affect columnar dendritic growth in the [001] direction in the deposit region. The maximum height of the [001] columnar region is approximately 150 μm higher for the [100] substrate compared to the [001] substrate. However, the total deposit height is similar. While the total deposit height is related to the powder bed thickness and the processing conditions, the [001] columnar height depends on the local solidification conditions. By evaluating the transient flow-thermal conditions prevailing

in the melt pool, a qualitative prediction of the deposit structure (columnar or EQ) may be obtained.

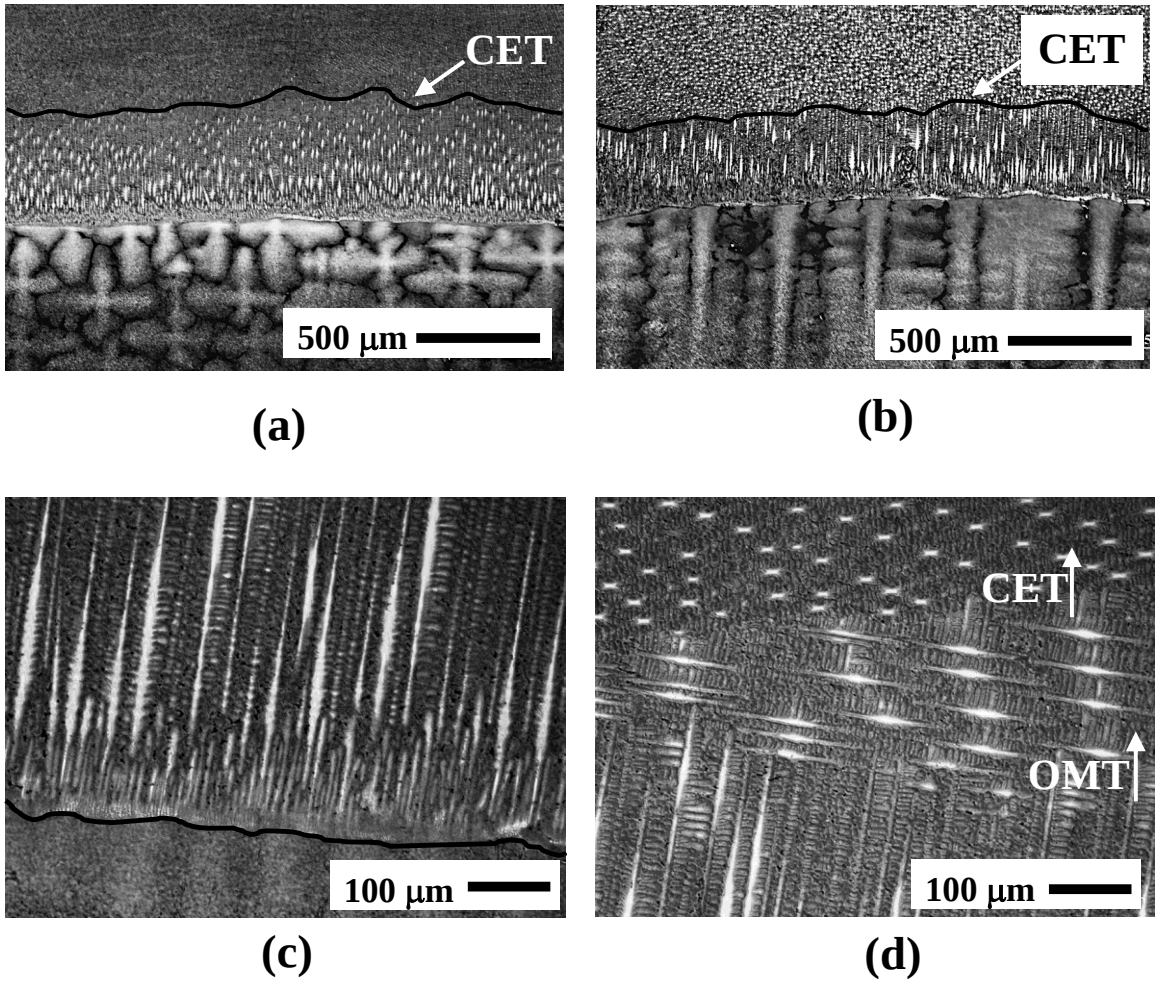

Figure 86. OM images showing transverse cross-sections of the SLE deposited René N5 on René N5 substrates with (a) [100] and (b) [001] crystal growth direction. OM image showing longitudinal cross-sections of the (c) the metallurgical bond between the substrate and the deposit (the black line represents the substrate-deposit interface) and (d) the oriented-to-misoriented transition (OMT) and the columnar-to-equiaxed transition (CET). Figure 4(d) is taken at a location 10 mm from the leading edge in the deposit region of René N5 on René N5 substrate with [100] crystal growth direction.

The G/V ratio governs the columnar height in the deposit. The solidification velocity, V is similar as both samples are produced under identical processing conditions. However, during solidification, the solidified front and the substrate can act as heat-sinks. The directional

growth of the dendritic trunks along preferred directions ([100] and [001] in the present study) can change the conductive heat transfer rates in the substrate region resulting in a change in G [134]. Such a change in G affects the [001] columnar growth in the deposit region as shown in the present study.

Figure 86(c) illustrates the metallurgical bond at the interface between the substrate and the deposit. The interface is nearly flat implying that the melt pool is stable and non-oscillating during the laser processing. Figure 86(d) provides a detailed view of the dendritic growth transition from the [001] to the [100] direction, known as the oriented-to-misoriented transition (OMT). Figure 86(d) also provides a detailed view of the transition from the columnar to the equiaxed microstructure, known as the CET. The CET and the OMT limit the columnar height and, therefore, need to be avoided or minimized.

The microstructures of the deposited region shows prominent dendritic segregation patterns as illustrated in Figure 86(c). The heavier elements such as W, Mo, Re, and Ta do not diffuse rapidly in the solid resulting in elemental segregation at the core of the dendrites. The lighter elements such as Ti and Al are enriched within the inter-dendritic and the eutectic regions. Etching makes the dendritic region bright and the interdendritic region gray.

6.2.3 Microstructures

The major constituents of the SLE deposited microstructure of René N5 are the γ matrix, the γ′ precipitates in the γ matrix, the eutectics, and the carbide precipitates as shown in Figure 87(a). Fine homogeneous γ/γ′ microstructures are observed within the dendrite core as shown in Figure 87(b). Here the γ′ phase precipitates coherently from the γ phase when the deposit is cooled below the γ′-solvus. The cuboidal γ′ precipitates follow variations in size depending on

location as shown in Figure 87(c). The finer precipitates are seen to be of order 50 nm while the coarser precipitates are of order 100 nm. The carbide precipitates are mostly elongated, blocky, and Chinese-script shaped with sizes ranging from 1 – 5 μm as shown in Figure 87(d). The Chinese-script carbides are typically seen to be formed in the inter-dendritic regions.

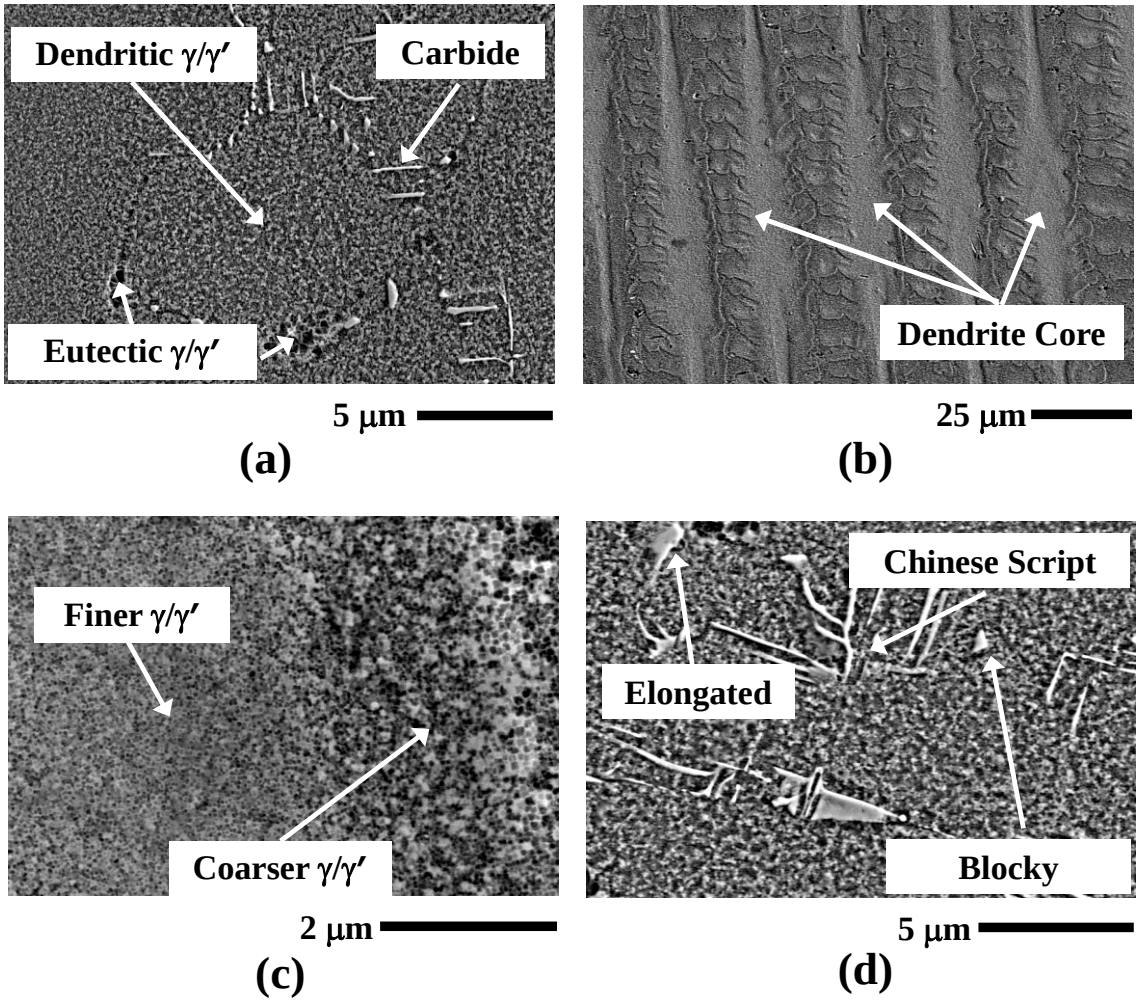

Figure 87. SEM image showing (a) the γ matrix, the γ′ precipitates in the γ matrix, the eutectics, and the carbides, (b) the dendritic structure, (c) finer and coarser γ/γ′ precipitates, (d) the carbide precipitates in the deposit region.

Figure 88(a) shows the cubic and the channel shaped γ/γ′ precipitates in the eutectic region. The channel length is from 0.5 – 1 μm while the channel width is of order 200 – 400

nm. The cubic γ/γ′ precipitates are of order 200 – 400 nm in the eutectic region. The secondary γ/γ′ is in the range of 20 – 50 nm as shown in Figure 88(a). Some of the eutectic regions are found to contain residual carbide precipitates as shown in Figure 88(b).

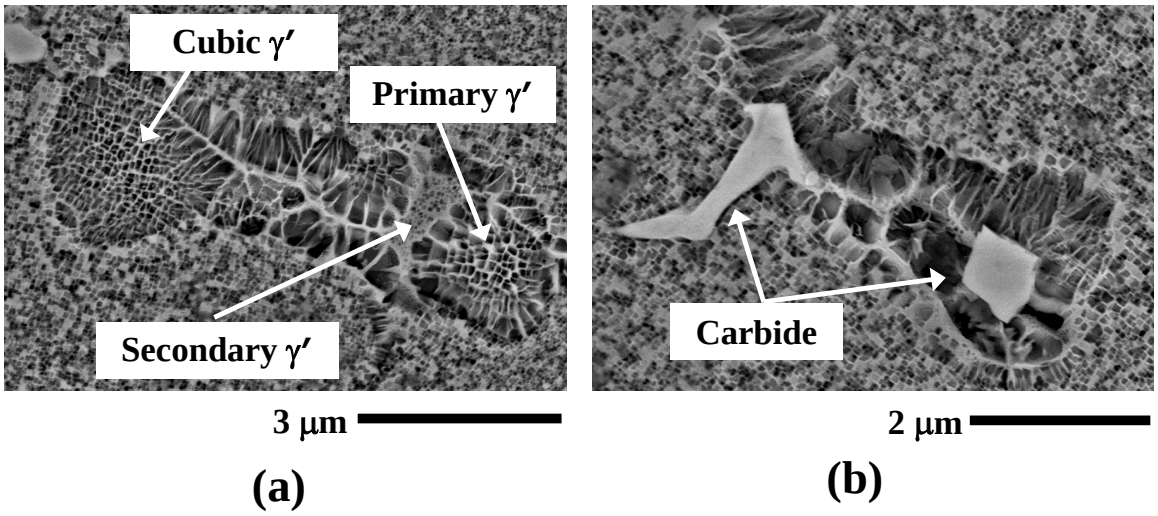

Figure 88. (a-b) the γ/γ′ phases in the eutectic regions.

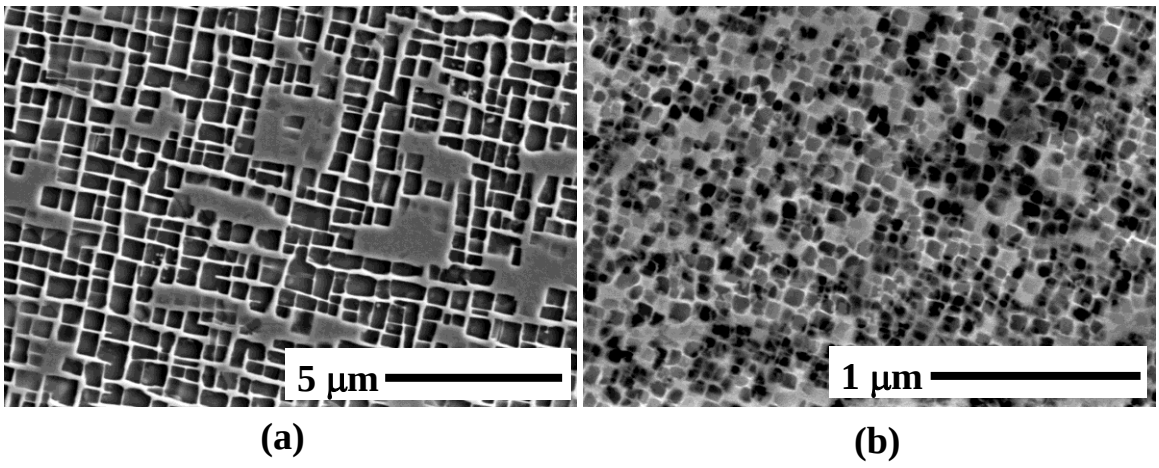

Figure 89. SEM image showing γ/γ′ structure in the (a) substrate region and (b) deposit region.

Figures 89(a) and 89(b) show SEM images of the etched René N5 microstructure in the substrate and deposit regions, respectively. The primary γ′ is of order 0.5 – 1 μm and the

secondary γ′ is of order 50 nm in the substrate region. Microstructural refinement in the deposit region is observed as the primary γ′ here is of order 50 – 100 nm as shown in Figure 89(b). Therefore, the microstructure obtained by SLE is about 10 times finer than the as-cast structure implying that the interface areas between the γ and γ′ structures are higher for the SLE deposited René N5 compared to the cast substrate.

6.2.4 Elemental segregation

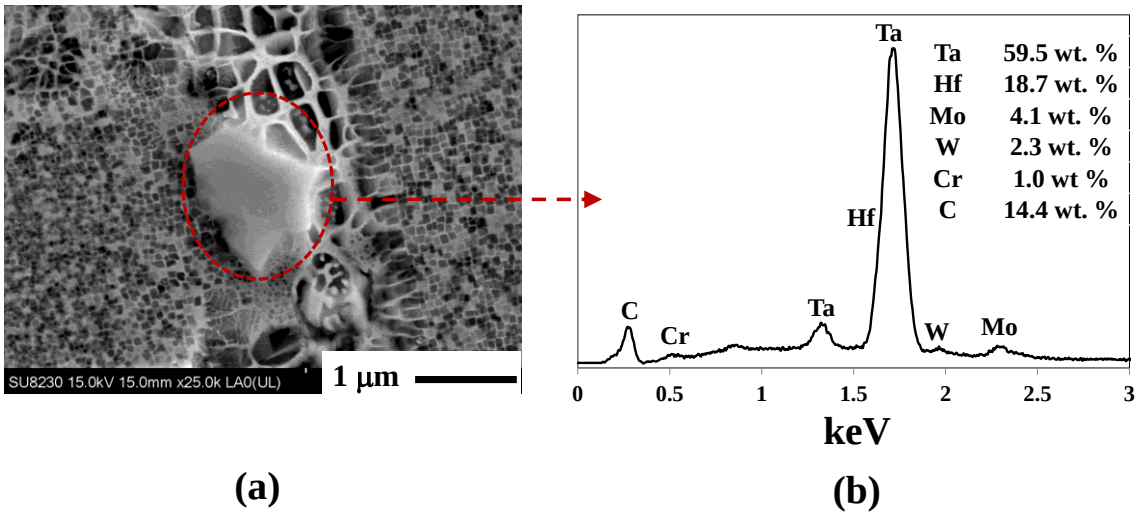

Figure 90. SEM image showing (a) the morphology of a carbide precipitate in the deposit region and (b) EDS profile of a typical carbide precipitate.

René N5 contains about 0.05 wt. % C and 0.004 wt. % B which result in the formation of carbide and boride precipitates in the deposit region. Blocky, elongated, and Chinese-script carbide precipitates are found in the deposit region. Figure 90(a) illustrates the morphology of a typical blocky carbide in the deposit region. Figure 90(b) shows a typical EDS profile. These carbides are found to be rich in Ta and Hf; however trace amounts of Mo, W, and Cr are also present. Trace amounts of boron (0.5 wt. % or less) are found in a few carbide precipitates [135].

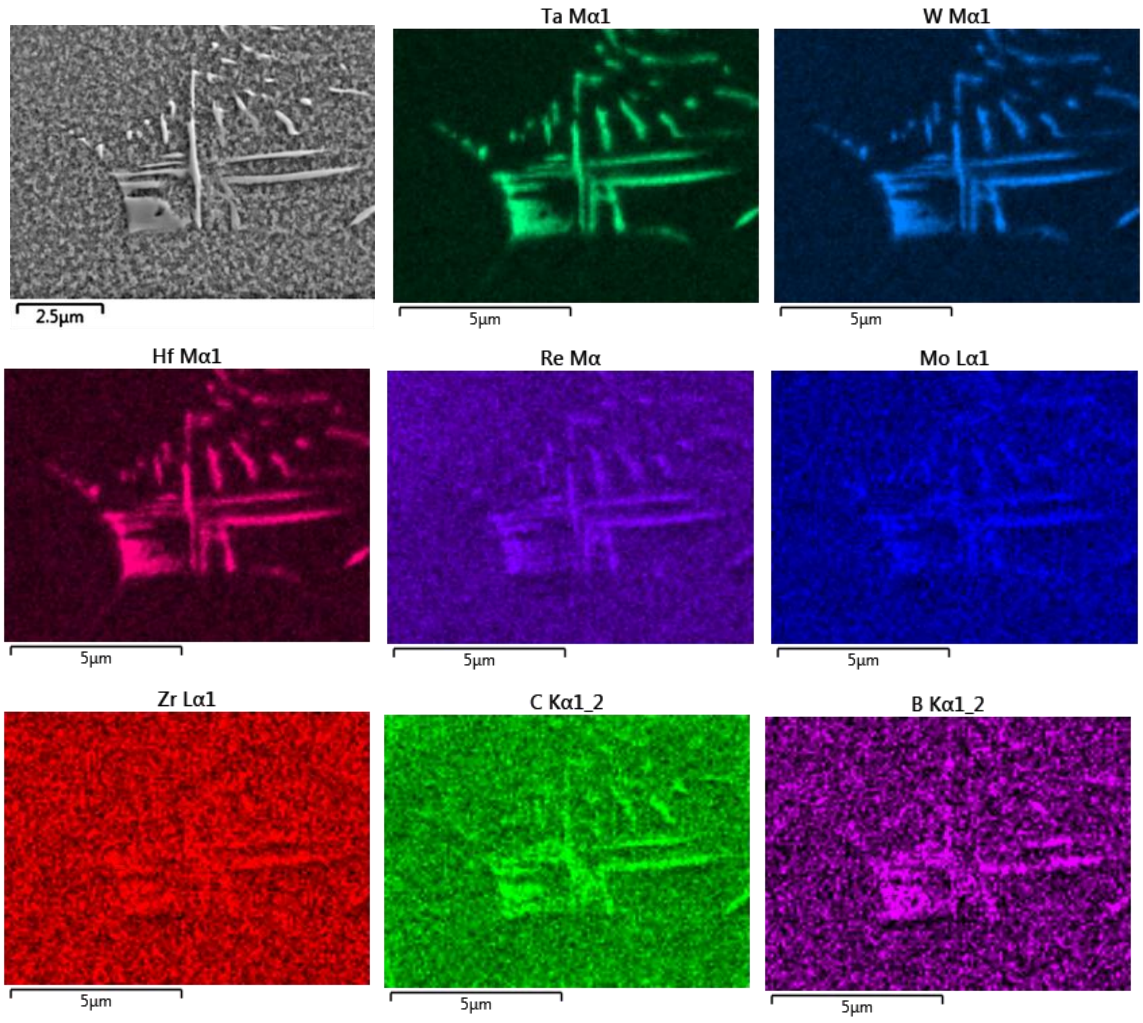

Figure 91. SEM-EDS elemental maps of a typical Chinese-script carbide network in the SLE deposited René N5 deposit.

Script-like networks of carbides consisting of connected rods and plates are formed in the inter-dendritic regions, as shown in Figure 91. These carbides are likely formed due to the presence of C and B in the alloy. These observations are consistent with the results reported in a study that was conducted on C + B modified CMSX-4® [136]. Cores of the carbide networks are observed to be between the primary dendrite arms. The carbides analyzed are found to be rich in Ta, Hf, and W. The EDS elemental maps for various alloying elements are shown in Figure 91. In the current study, a trace amount of Re is also found in the Chinese-script

carbides but is not observed in any of the blocky or elongated carbides. A previous study showed the formation of rhenium carbide using reactive pulsed laser deposition method [137].

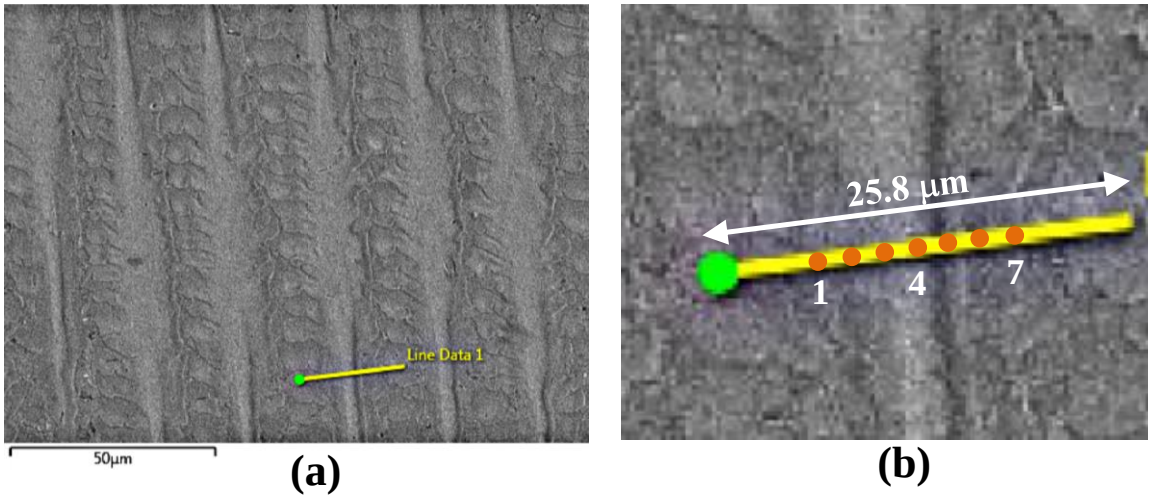

Figure 92. SEM image showing the location of EDS line scan, and (b) zoomed view of the line scan domain illustrating the locations in Figures 93(a) through 93(i).

However, no such formation is reported for laser processing of nickel-base superalloys. The depth of the mushy zone and the time for solidification are expected to be relatively small in AM due to high-temperature gradients and fast cooling rates. As the matrix of γ and γ′ starts to form within the dendrites, C and Ta are rejected to the liquid and enriched in the liquid. The nucleation of the carbide precipitates occurs after the unidirectional dendrites start to grow. Depending on the local thermal gradient and solidification conditions, a coupled growth between the γ matrix and the carbide precipitates may occur leading to the formation of complex Chinese script-type carbides. Towards the end of solidification, the eutectics start to form in the interdendritic regions enriched in Ta. Carbides from the eutectics, thus, grow from the eutectic melt and are enriched in Ta.

In order to quantify the elemental segregation, EDS line scan measurements are

performed across a representative dendrite core as shown in Figure 92(a) [138]. The line data is analyzed and the values are extracted at locations 1 through 7 as shown in Figure 92(b). The EDS concentration (in cps) profiles are shown in Figures 93(a) through 93(i). The refractory elements (Re, W) are present in higher quantities in the dendrite cores than in the interdendritic regions as shown in Figures 93(a) and 93(b), respectively.

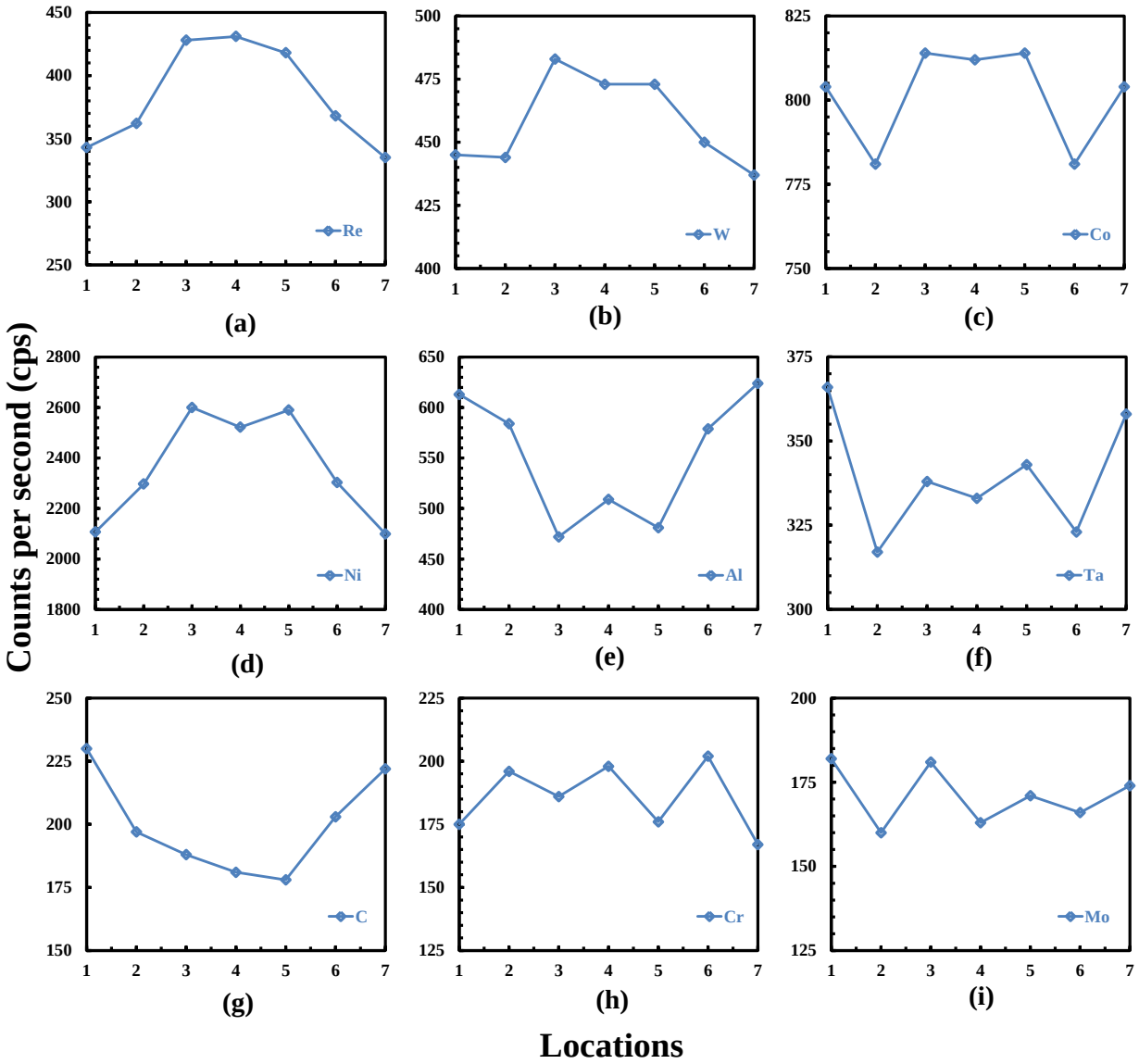

Figure 93. SEM-EDS concentration profiles for various elements in the dendritic core of the SLE deposited René N5.

The γ forming elements, Ni, and Co exhibit higher concentrations in the dendritic region by preferentially partitioning to the γ matrix as shown in Figures 93(c) and 93(d) respectively. However, the γ′ forming elements (Al, Ta) exhibit an opposite behavior, showing higher concentrations in the interdendritic regions as shown in Figures 93(e) and 93(f). EDS scan results also reveal that C strongly segregates in the interdendritic region as shown in Figure 93(g). The higher concentration of C and refractory elements in the interdendritic region form various grain boundary precipitates such as carbides resulting in an improvement in grain boundary ductility and cohesion. Cr and Mo do not show any segregation behavior as shown in Figures 93(h) and 93(i).

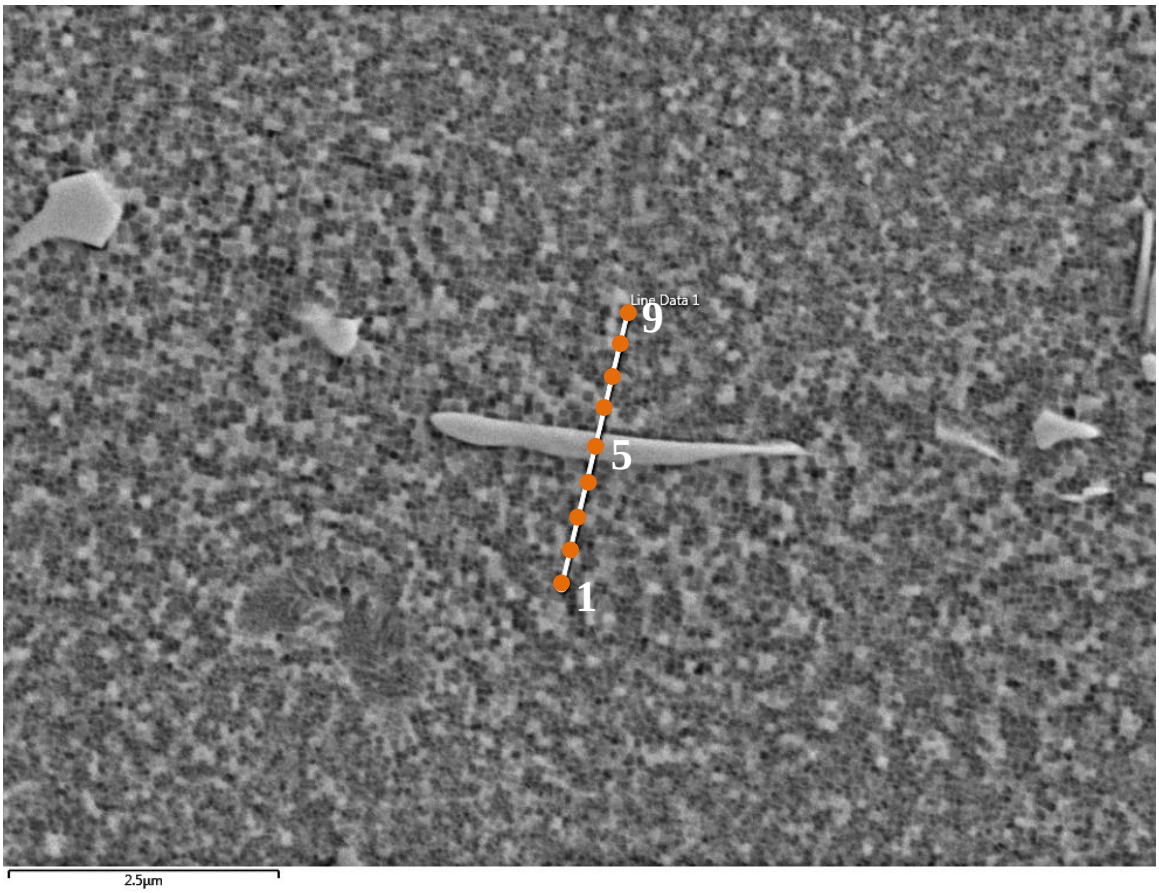

Figure 94. SEM image illustrating the EDS line scan showing the locations in Figures 95(a) through 95(i).

EDS line scan measurements are performed across a representative carbide precipitate as shown in Figure 94. The line data is analyzed and the values are extracted at locations 1 through 9 as shown in Figure 94. Figures 95(a) through 95(i) illustrate the EDS line scan results for a carbide precipitate. The refractory elements (Ta, W) are present in higher quantities in the carbides than in the interdendritic regions as shown in Figures 95(a) and 95(b). Other refractory elements such as Re and Hf are also present in significant quantities in the carbides as shown in Figures 95(c) and 95(d) respectively.

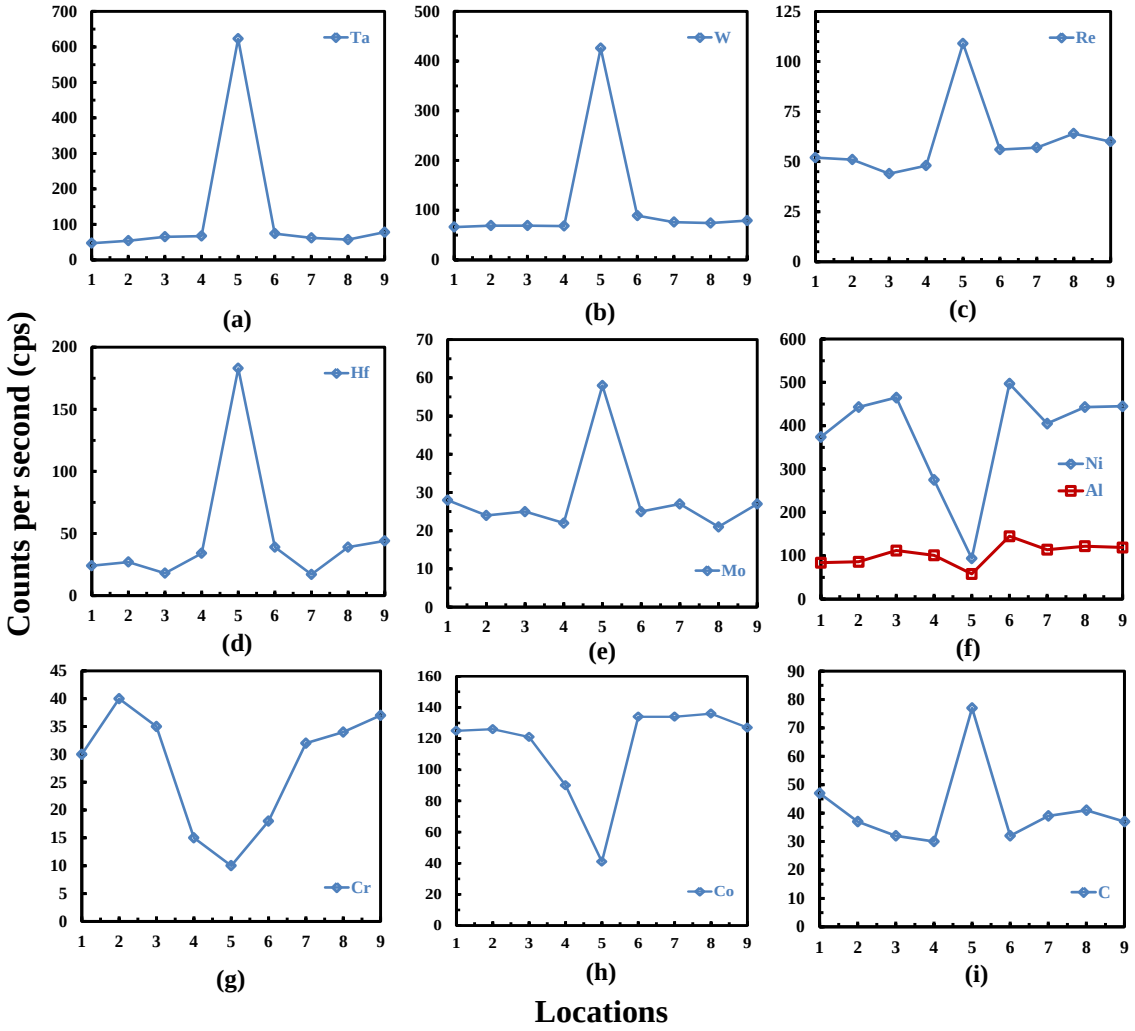

Figure 95. SEM-EDS concentration profiles in the carbide precipitates for various elements in the SLE deposited René N5.

Mo shows weak partition behavior in the carbides as shown in Figure 95(e). The γ/γ′ forming elements such as Ni, Al, Cr, and Co exhibit an opposite behavior, showing higher concentrations in the interdendritic regions as shown in Figures 95(f) through 95(h). C, as expected, shows higher concentrations in the carbide precipitates (Figure 95(i)). René N5 contains about 0.004 wt. % of B. Line scan measurements show an insignificant partitioning behavior for this element between the interdendritic region and the carbide precipitates. Figure 96 illustrate a typical eutectic region across which an EDS line scan measurement was performed. The line data is analyzed and the values are extracted at locations 1 through 6 as shown in Figure 96. The eutectic γ/γ′ is surrounded by the coarse γ/γ′ microstructure. A thick γ boundary is found to separate the eutectic γ/γ′ and the coarse γ/γ′ as shown in Figure 96.

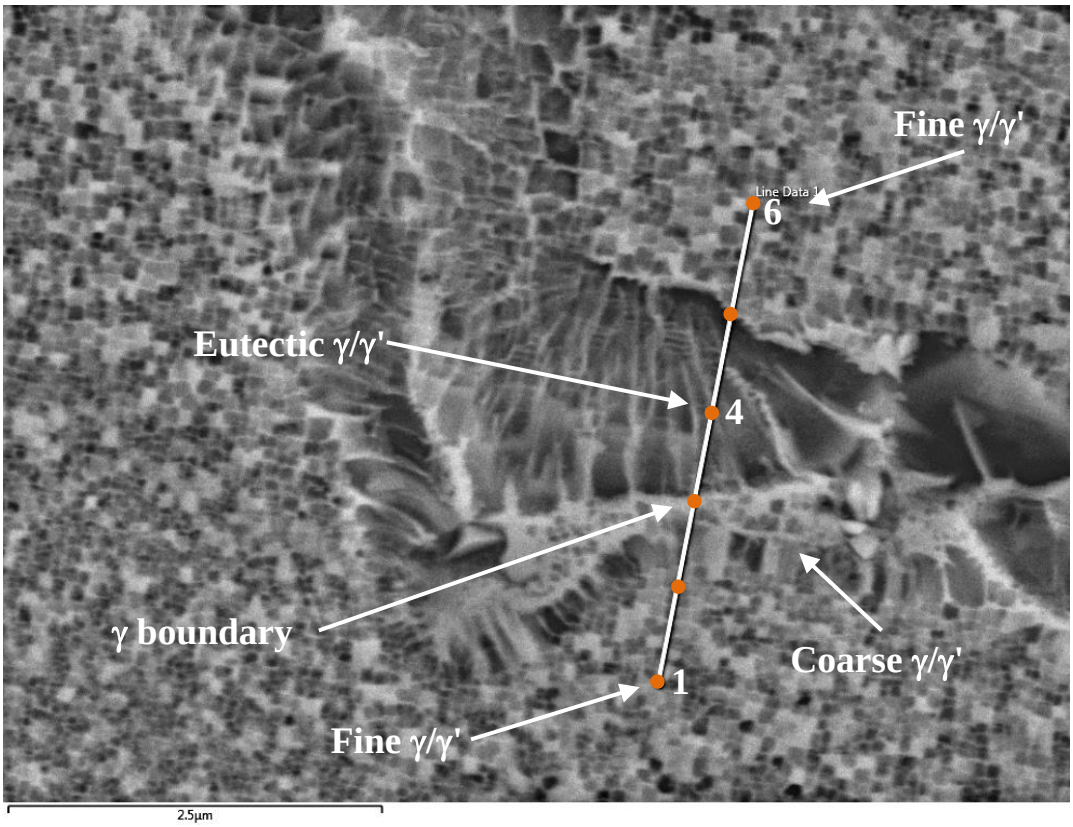

Figure 96. SEM image illustrating the EDS line scan showing the locations in Figures 97(a) through 97(i).

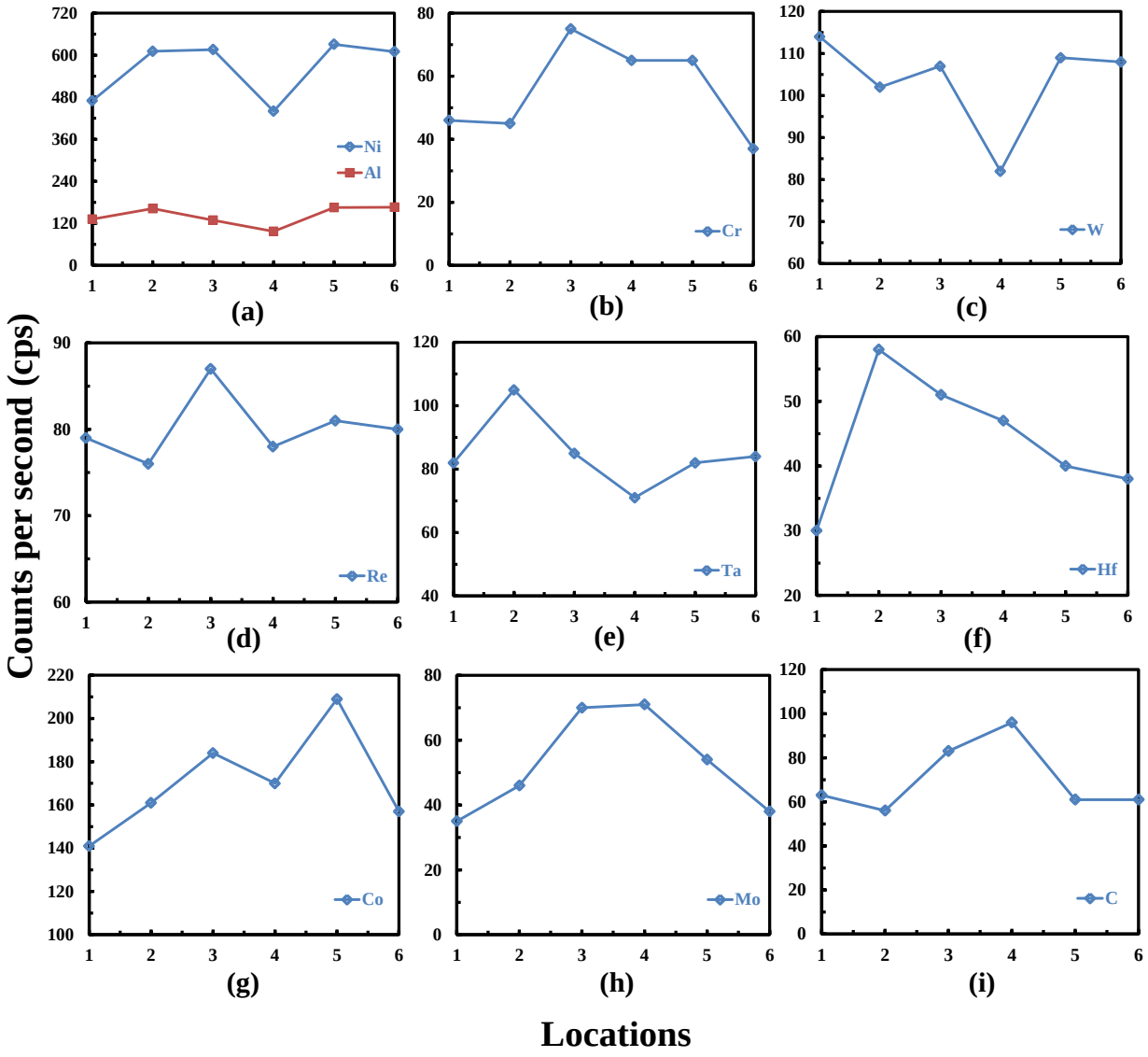

Figure 97. SEM-EDS concentration profiles in the eutectic pools for various elements in the SLE deposited René N5.

As shown in Figure 97(a), Ni and Al are depleted in the eutectic pools (location 4 in Figure 96) compared to the interdendritic region. Cr shows the highest concentration in the γ layer (location 3 in Figure 96) around the eutectic. Because the eutectic pools are depleted in Cr, the enrichment of the surrounding layer can occur only if, in the final stages, the interdendritic region solidifies first and rejects Cr into the last fraction of liquid. W, Re, Ta,

and Hf are also depleted in the eutectic pools as shown in Figures 97(c) through 97(f). W and Re show highest concentration in the γ layer (location 3 in Figure 96) around the eutectic. C strongly segregates to the eutectic as shown in Figure 97(g). Mo and Co are also found to segregate to the eutectic pool (Figures 97(h) and 97(i)).

Table 13. Calculated Partition Coefficients from EDS Results for René N5.

	Al	Ni	C	Cr	Co	Mo	W	Ta	Hf	Re
k_{DI}	0.83	1.20	0.79	1.13	1.01	0.90	1.06	0.91	-	1.26
k_{EI}	0.73	0.94	1.52	1.41	1.21	2.03	0.72	0.87	1.57	0.99
k_{CI}	0.25	0.69	1.64	0.33	0.33	2.07	6.45	13.26	7.63	2.10

The degree of segregation parameter for various elements are calculated. Three different segregation parameters are defined to accurately measure the level of elemental segregation. These are between the dendrite core and the interdendritic region (k_{DI}), between the eutectic pools and the interdendritic region (k_{EI}), and between the carbides and the interdendritic region (k_{CI}). Table 13 summarizes the various partition coefficients. The results show a strong segregation tendency of heavy elements (Re, W) to the dendrite core. Ta, W, Re, Hf, Mo, and C exhibit strong segregation to the carbides. Other elements (Ni, Mo, Co, and Cr) exhibit a moderate tendency to partition either to the dendrites or to the interdendritic areas.

6.2.5 Crystalline phases

Figure 98 compares the XRD profiles for the pre-alloyed René N5 powder against the SLE deposited René N5 on René N5 substrates with [100] and [001] crystal growth direction, respectively. The XRD profile for the René N5 powder is coincident with solid solution γ-FCC NiCr (a = 0.359 nm) and exhibits a prominent (111) peak as shown in Figure 98.

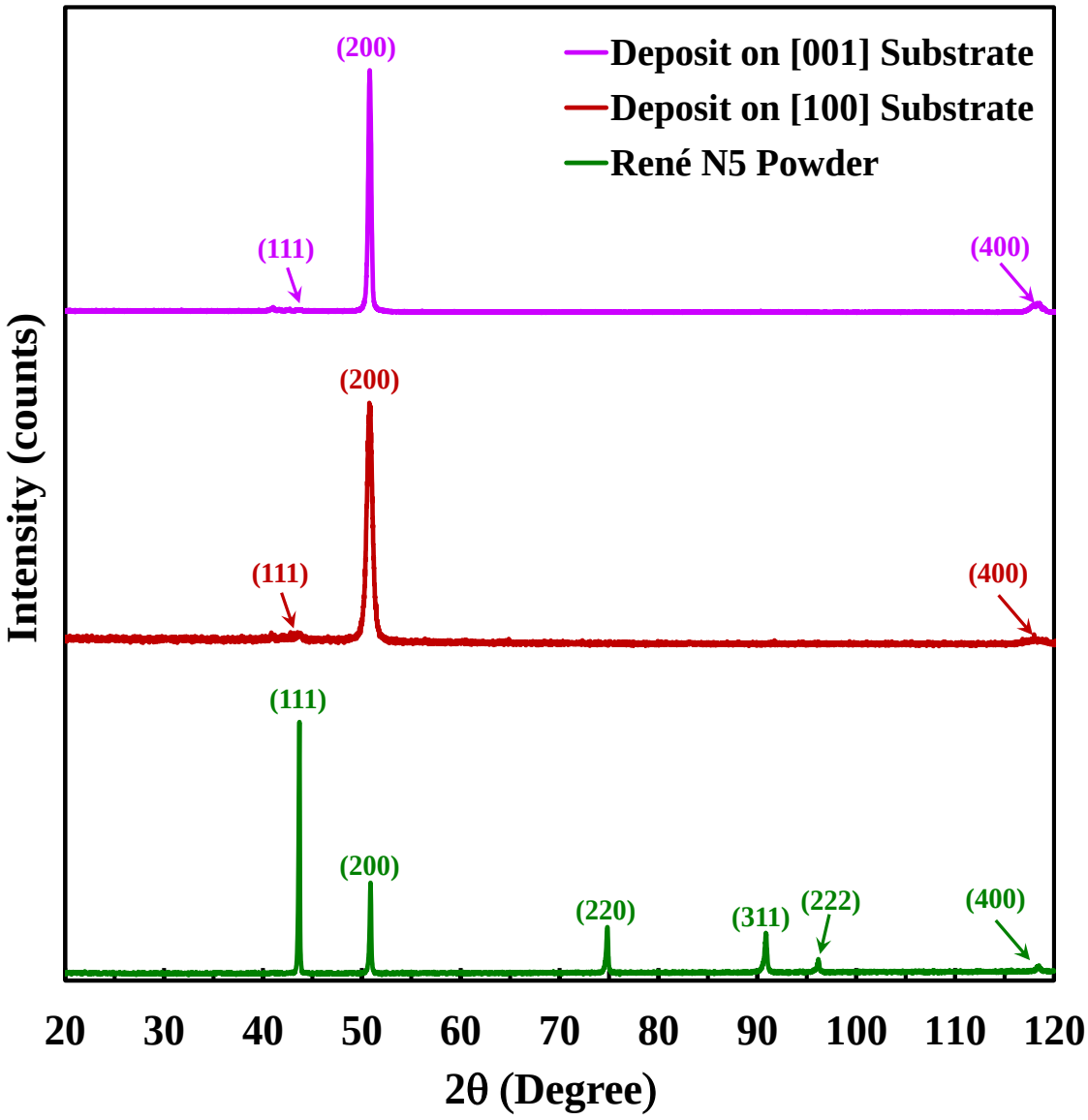

Figure 98. XRD profile of the pre-alloyed René N5 powder and the SLE deposited René N5 on René N5 substrates with [100] and [001] crystal growth direction.

The diffraction peaks occur at 2θ = 44°, 51°, 75°, 91°, 96°, and 119° indicating the diffraction of (111), (200), (220), (311), (222), and (400) planes of the γ matrix. A major peak at around 51° indicates a strong presence of γ solid solution and/or γ' phase in the SLE deposited René N5. These two phases are typically difficult to differentiate because both γ and γ' phases have cubic structures with less than 0.5% difference in lattice parameters for most

commercial nickel-base superalloys .The strong (200) peak is present in both SLE deposited René N5 samples with [100] and [001] substrate crystal growth direction indicating that it does not affect the unidirectional growth.

6.2.6 Texture analysis

EBSD analysis is carried out to characterize the grain orientation and crystallographic texture of two representative René N5 samples with [100] and [001] substrate crystal growth direction, respectively. As illustrated in Figures 99(a) and 99(b), apart from a few stray grains at the leading edge and an equiaxed region at the top, most of the deposit region appears to be a single grain.

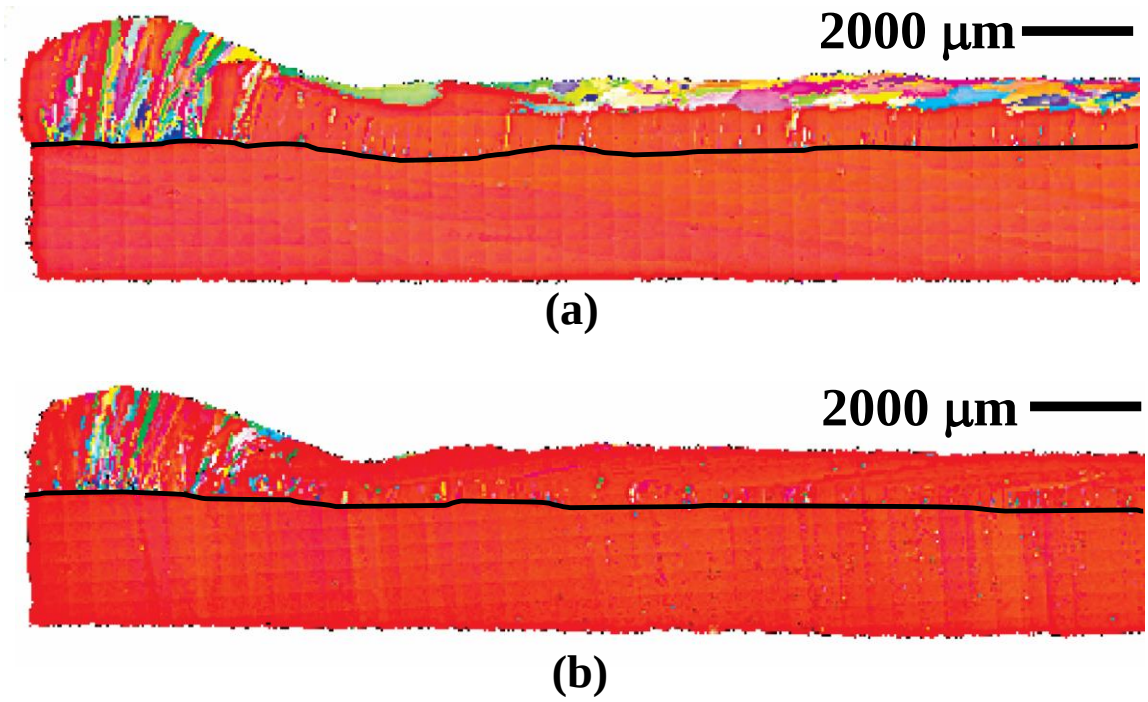

Figure 99. Large area orientation map obtained by EBSD for René N5 deposit on René N5 substrates with (a) [100] and (b) [001] crystal growth direction. The black line denotes the substrate-deposit interface.

Figure 100 shows the grain size distribution as estimated from the EBSD analysis for the

entire deposit region (the region indicated above the black line in Figures 99(a) and 99(b)). Most of the deposit region is a single grain with an equivalent diameter exceeding 700 μm. The substrate orientation has an impact on the size distribution. The number of grains is higher for the substrate with [100] crystal growth direction indicating the presence of more equiaxed (EQ) grains.

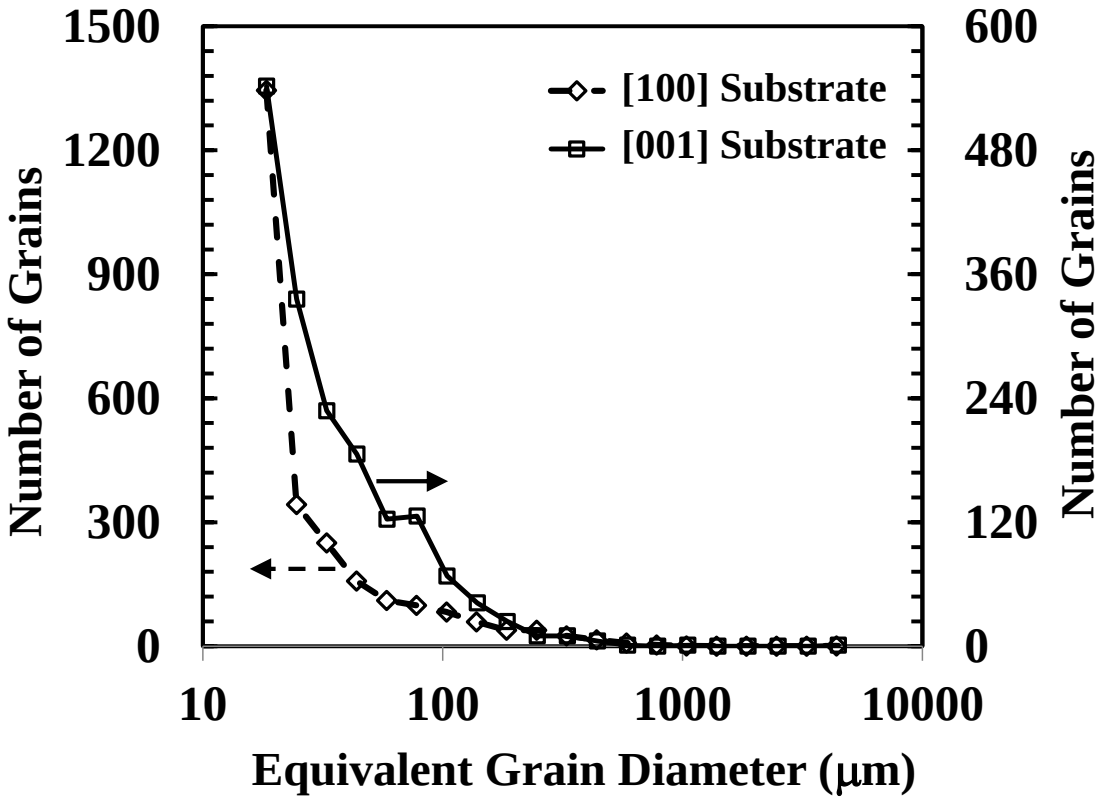

Figure 100. Grain size distribution of the René N5 deposit region for the substrate crystal growth direction [100] and [001].

Figures 101(a) and 101(b) show the pole figures (PF) for the SLE deposited René N5 on René N5 substrates with [100] and [001] substrate crystal growth direction, respectively. No significant differences are observed between Figures 101(a) and 101(b). For both samples, a unidirectional growth is achieved along the [001] directions as illustrated in Figures 101(c)

and 101(d).

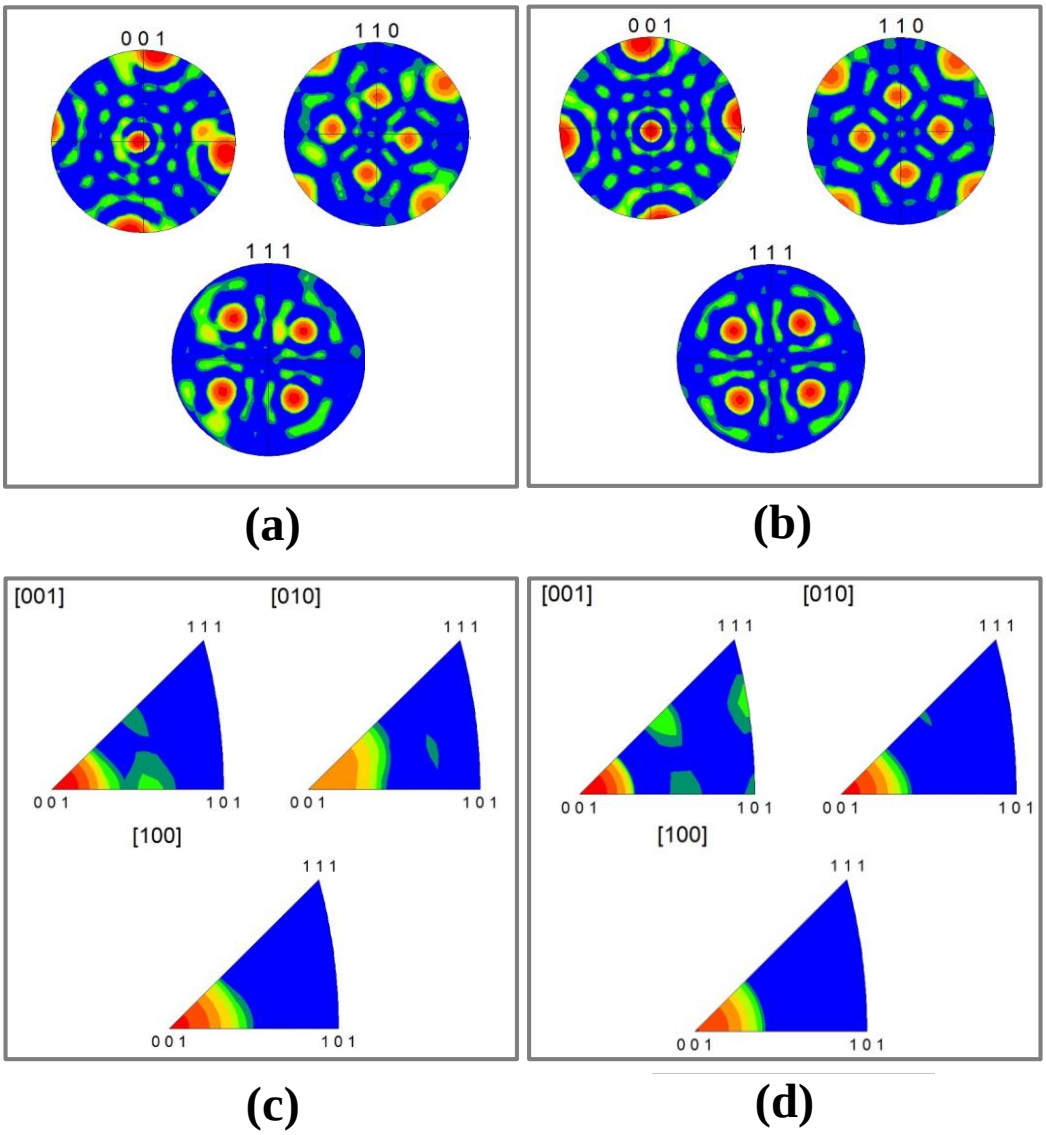

Figure 101. Pole figure (PF) maps obtained by EBSD for René N5 deposit on René N5 substrate with (a) [100] and (b) [001] crystal growth direction. Inverse pole figure (IPF) maps obtained by EBSD for René N5 deposit on René N5 substrate with (a) [100] and (b) [001] crystal growth direction.

6.2.7 Vickers microhardness measurement

Microhardness measurements conducted over the substrate region do not show any significant changes in microhardness due to change in the substrate crystal growth directions.

The average microhardness values for the cast substrate are in the ranges of 400 to 440 HV. However, variations in microhardness are observed in different regions of the deposit. The [001] columnar region consistently shows higher microhardness values ranging from 460 to 500 HV.

The increase in the hardness values may be attributed to the finer γ/γ' microstructure, minor compositional differences or residual stress buildup. The [100] columnar and EQ regions show microhardness values in the range of 420 – 480 HV. The microhardness values are similar for both René N5 samples with [100] and [001] substrate crystal growth direction. Table 14 reports the average hardness values in the deposit, substrate, and interface regions of the as-deposited René N5 sample.

Table 14. Summary of the Vickers microhardness measurements for René N5.

Region	HV_{2000}	St. Dev. in HV_{2000}	HV (GPa)	σ_y (GPa)
Substrate	428.3	21.4	4.2	1.4
Interface	463.8	11.9	4.5	1.5
Deposit ([001])	482.2	19.3	4.7	1.6
Deposit ([100], EQ)	467.3	10.3	4.6	1.5

6.2.8 Conclusions on René N5

In the present study, the single-pass fabrication of René N5 on René N5 substrates is demonstrated using SLE. The process is found to be capable of producing more than 1000 μm thick uniform deposits in a single pass without any sign of cracking and interface fusion defects. SLE is able to deposit unidirectional structures of René N5 on top of René N5

substrates with [100] and [001] crystal growth direction and more than 500 μm of columnar height is obtained. The maximum columnar height is approximately 150 μm higher for the [100] substrate compared to the [001] substrate under identical SLE operating conditions.

Microstructural refinement is observed in the deposit region. The average PDAS is found to be approximately 10 times finer in the deposit region compared to the substrate region. Approximately 15% higher microhardness values are measured in the deposit region due to a finer γ/γ′microstructure in the deposit region relative to the substrate. SEM studies show the presence of primary and secondary γ/γ′ precipitates, carbides, eutectics, and segregated dendritic microstructure in the deposit region. The carbide precipitates are mostly blocky, elongated and Chinese-script shaped and Ta-rich.

The results show strong segregation tendency of heavy elements (Re, W) to the dendrite core. Interdendritic regions mostly consist of the γ′ forming elements (Al, Mo, and Ta) and carbon (C). In the interdendritic region, Ta, Hf, Re, Mo, W, and C show strong segregation tendency to the carbide precipitates. In the final stages of solidification, a highly segregated supersaturated γ′ phase rich in Cr, Co, and Mo form a layer around the eutectic pools. XRD and EBSD results reveal the presence of a unidirectional solidification microstructure and SX growth texture in the SLE-fabricated René N5 samples.

6.3 Summary

This chapter discusses the SLE development for SX deposits. Some of the key conclusions from this study are:

- This is a first-of-its-kind demonstration of deposition of CMSX-4® and René N5

having thickness exceeding 1000 μm, widths exceeding 5000 μm, and lengths exceeding 35,000 μm with more than 500 μm of SX height in a single pass using an LPBF-based AM process.

- Dense deposits are obtained for two high-γ′ nickel-base superalloys such as CMSX-4® and René N5 for a range of operating conditions without preheating the powder bed.

- The SLE process can be accurately controlled in order to achieve thin melt back depth. A shallow melt-back depth ensures that the energy input to the substrate is minimal reducing the thermal stress accumulated within the melt-back region and avoiding any crack formation. The absence of cracks in the current study vouches for the reduced thermal stress accumulation in the SLE-deposited SX samples.

- The deposit region shows finer microstructure compared to the substrate region. The deposit region also shows dendritic segregation. The SLE-deposited microstructures also show finer γ′ features compared to the substrate. Such finer microstructures improve the microhardness in the deposit region by approximately 10% compared to the substrate. The hardness values are unevenly distributed in the deposit region.

- The deposit region shows three different microstructural features such as the γ′ precipitates, the γ matrix, and the eutectics. The γ′ precipitates are polygonal shaped.

- The comparison between the SLE-deposited CMSX-4® and René N5 microstructures reveal the following:

- Dense and crack-free deposits of CMSX-4® with no interface fusion defects can be obtained with E values of 18.75 – 70.30 J/mm^3. For René N5, only a handful of experimental runs are performed. The results show that E values between 29.16 – 32.81 J/mm^3 give deposit formations without interface fusion defects.

- The comparison between the SLE-deposited CMSX-4® and René N5 microstructures reveal that the deposit region shows formation of carbide precipitates in René N5 due to the presence of B and C. Three different types of carbide precipitates are observed namely blocky, elongated, and Chinese-script carbides. The carbide precipitates are mostly Ta-rich, however, trace amount of Re is also found.

- Microhardness of [001] columnar CMSX-4® deposit is in the range of 464 HV while the [001] columnar René N5 region shows hardness values in the range of 482 HV. This suggests that René N5 may have higher yield stress compared to CMSX-4®.

Chapter 7: SLE process development for heterogeneous deposits

This chapter discusses the feasibility of depositing René 142 on EQ René 125 and SX René N5. René 142 is one of the most oxidation resistant superalloys that has been developed. René 142 performs better than "second-generation" SX-cast alloys CMSX-4® and PWA1484 and is demonstrated to exhibit only 25.4 μm (i.e. 1 mil) surface metal loss after 200 hours at 2150 °F compared to 215.9 μm (i.e. 8.5 mil) and 127 μm (i.e. 5 mil) loss for CMSX-4® and PWA1484, respectively [132]. By depositing René 142 on EQ René 125 and SX René N5, a direct assessment is possible between the EQ and DS/SX René 142 microstructures.

René 142 is derived from René 150, a DS alloy that was invented in the seventies [18]. René 150 contains about 3% Re for solid solution strengthening and does not contain any Ti. The alloy has excellent castability and exceptional longitudinal rupture strength: 100 °F greater than conventionally cast René 80, 65 °F over DS René 80H and 35°F greater than DS MM 200 and is equivalent to single-crystal René N4, PWA 1480, and CMSX-3®. René 150 also exhibits excellent transverse rupture strength and ductility. However, René 150 contains about 2.2 wt. % V which even though is a significant γ′ strengthener, causes the alloy's very poor high velocity oxidation resistance.

René 142 was developed with the aim of retaining René 150's excellent rupture strength and castability while significantly improving René 150's oxidation resistance. V was eliminated, and was replaced by Al and Ta which when coupled with higher levels of Cr

improved the alloy's oxidation resistance. To date, only the electron beam melting (EBM) was successful in depositing DS René 142 [139]. However, no results have been reported for René 142 with LPBF-based AM processes.

7.1 Materials

Commercially available René 142 powder produced by the Carpenter Technology Corporation is used. The chemical compositions of the René 142 powder and the René N5 substrate are listed in Table 15. The René 142 powder particles are mostly random shaped. However, a few spherical particles are also found as shown in Figure 102(a). Some particles contain secondary satellites attached to them as shown in Figure 102(a). After polishing the powder, a few particles are observed to contain internal porosity as shown in Figure 102(b).

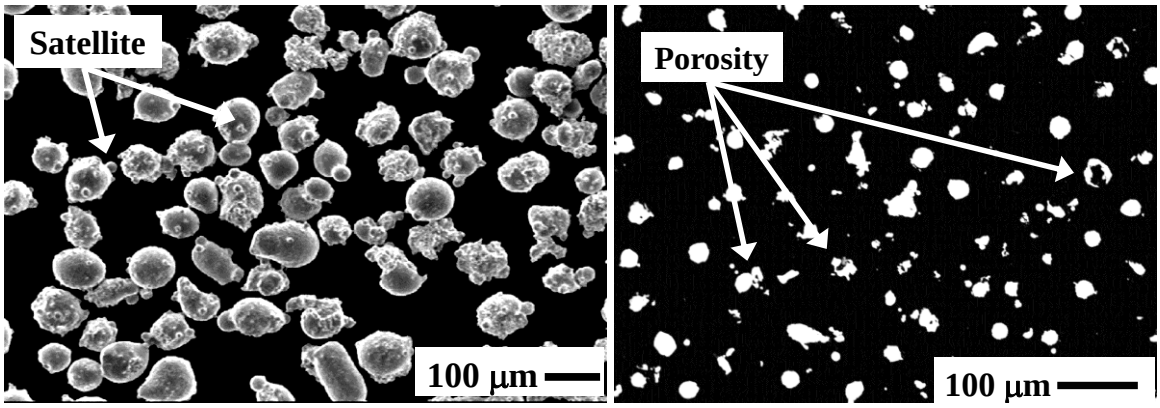

Figure 102. René 142 powder particles showing satellites as revealed by SEM and (b) the René 142 powder cross-section after mirror polishing as revealed by OM.

The SLE process is conducted on rectangular EQ cast René 125 substrates having dimensions of 35.56 mm x 6.86 mm x 2.54 mm. The SX cast René N5 substrate coupons are rectangular in shape having dimensions of 35.56 mm x 6.86 mm x 2.54 mm with [100] and [001] crystal growth direction.

Table 15. Composition of the René 142 powder, the René 125 substrate, and the René N5 substrate (wt. %).

	Cr	Co	Mo	Re	W	Al	Ti	Ta	Hf	B	C	Zr	Ni
René 142	6.8	12.0	1.5	2.8	4.9	6.15	-	6.35	1.5	0.015	0.12	0.02	Bal
René 125	8.9	10.0	2.0	-	7.0	4.8	2.5	3.8	1.5	0.015	0.11	0.05	Bal
René N5	7.1	8.0	2.0	3.0	5.0	6.0	-	7.0	0.15	0.004	0.05	-	Bal

7.2 Results on EQ René 142 deposited on EQ René 125

René 142 is first deposited on René 125 substrates having EQ microstructures. The deposit characteristics are analyzed with OM, SEM, and EDS. The following section discusses some of the key results obtained for this material system.

7.2.1 Deposit characteristics

Figure 103(a) shows the length-wise cross-sectional microstructure of an as-deposited René 142 sample [140]. The average deposit thickness is found to be more than 1000 μm. As can be seen from Figure 103(a), there is an excellent metallurgical bond between the substrate and the deposit region along the entire length of the substrate. The deposit is also demonstrated to be crack-free and dense.

The deposit region shows a finer microstructure compared to the substrate region as illustrated in Figure 103(b). The microstructural refinement might be due to the focused heating and fast cooling from the fast moving laser heat source application. The microstructure of the deposited region reveals dendrite segregation patterns as shown in Figure 103(c). The deposit region shows mostly EQ microstructure. However, discreet locally columnar microstructures are also observed at various locations.

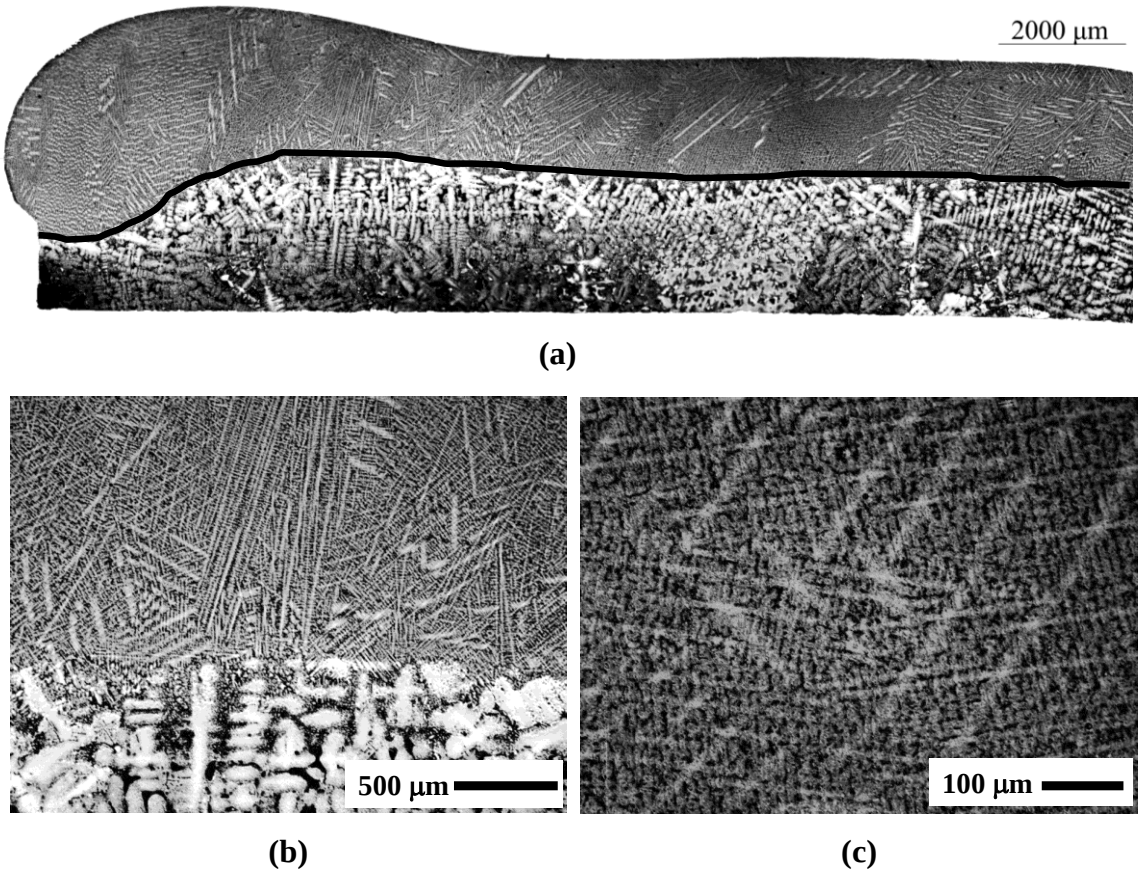

Figure 103. Representative transverse optical micrograph of René 142 deposited on René 125 cast substrate showing (a) crack-free and dense deposit, (b) metallurgical bond between the substrate and the deposit, and (c) dendrite segregation pattern in the deposit region. The black line in (a) represents the substrate-deposit interface.

7.2.2 Microstructures

The major constituents of the microstructure of René 142 are the γ matrix, the γ′ precipitates in the γ matrix, the eutectics and the carbides. Figure 104(a) illustrates an SEM image of the deposit region showing the major constituents. As shown in Figure 104(b), the primary γ′ precipitates show a characteristic dimension in the range of 2 μm in the substrate region whereas in the deposit region, the γ′ precipitates in the range of 100 nm as shown in Figure 104(c). Homogeneously precipitated γ′ is seen to vary in size depending on location.

This size distribution is illustrated in Figure 104(c) with finer γ′ in the range of 50 nm and coarser γ′ in the range of 100 nm. There are γ/γ′ eutectic morphologies with high aspect ratios in the interdendritic regions where the average size of γ′ is of order 150 – 200 nm as illustrated in Figure 104(d).

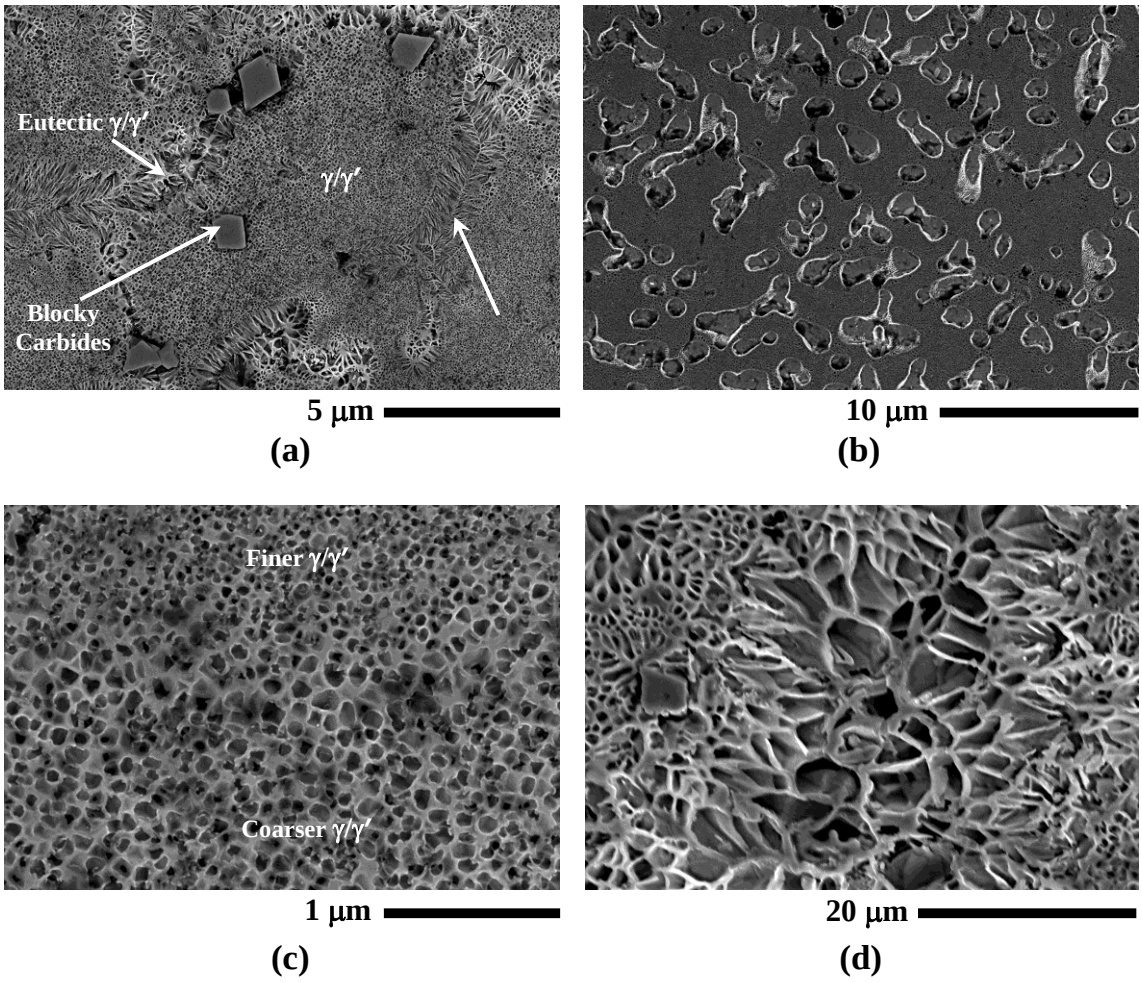

Figure 104. SEM image showing the γ matrix, the γ′ precipitates in the γ matrix, the eutectics and the carbides, (b) γ/γ′ morphology in the substrate region, (c) size variation of the γ/γ′ morphology in the deposit region, (d) the γ/γ′ eutectic morphology in the deposit region.

7.2.3 Elemental segregation

EDS line scan is performed across a typical eutectic region as shown in Figures 105(a)

and 105(b). Figure 105(c) illustrates the carbide morphology in the deposit region. Although, a trace amount of boron is present in the alloy, borides were not observed in the deposit region. EDS analysis is performed to characterize the MC carbides. The carbides are found to be rich in Ta, Ti, Mo, Hf, W, and C in Figure 105(d).

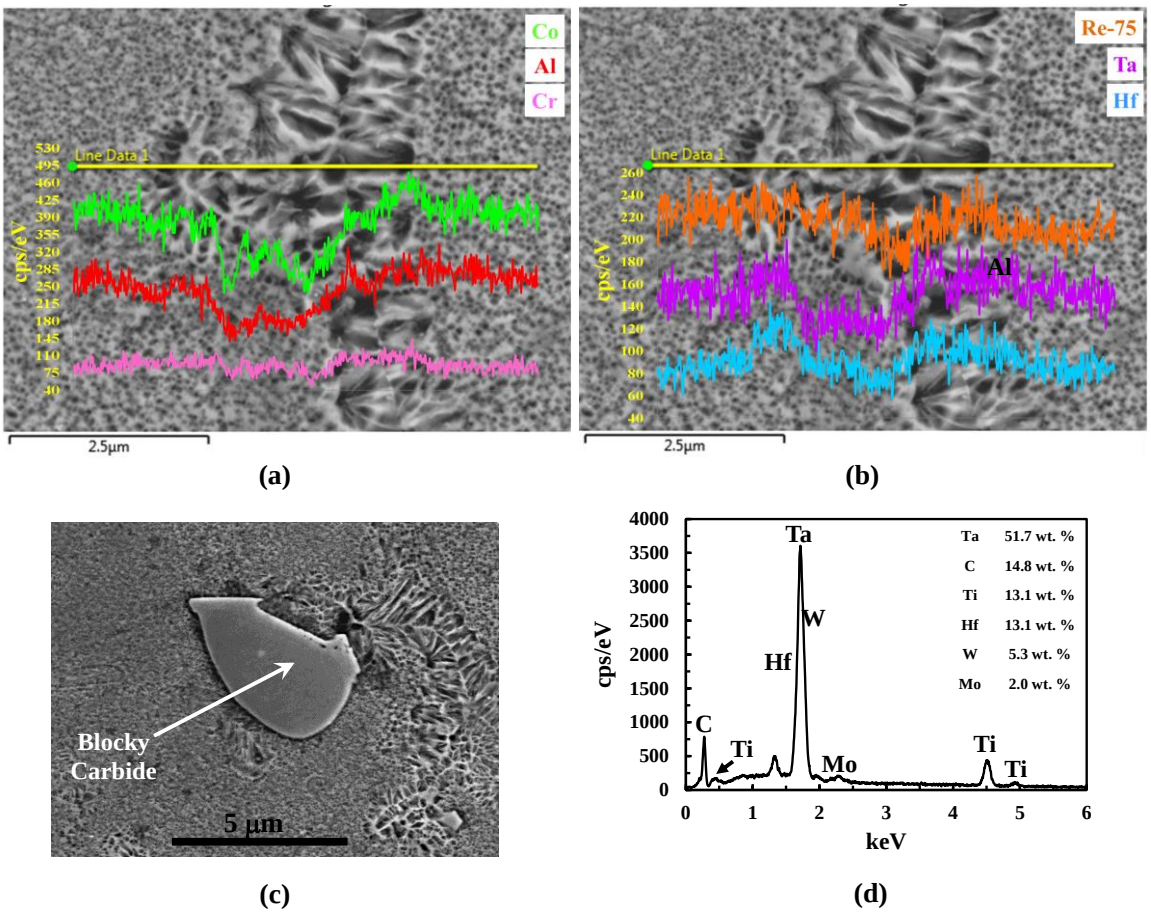

Figure 105. EDS line scan profile across a representative eutectic region for (a) Co, Al and Cr; and (b) Re, Ta, and Hf, (c) representative blocky carbide morphology in the deposit region and (d) SEM-EDS profile of the blocky carbide in (c).

7.2.4 Conclusions on EQ René 142 on EQ René 125

The SLE process is investigated for the deposition of René 142 atop René 125. The process is found to be capable of producing more than 1000 µm of deposit in a single-pass

without any indications of cracking. Microstructural investigations reveal the formation of γ/γ′ morphologies in the deposit region. Fan-shaped eutectic regions are found in the deposit region. Significant variations in elemental composition are observed across the eutectics. SEM/EDS studies show the presence of blocky MC carbides. The carbides are found to be rich in Ta, Ti, Mo, Hf, W, and C.

7.3 Results on SX René 142 deposited on SX René N5

René 142 is deposited on René N5 substrates having SX microstructures. The deposit characteristics are analyzed with OM, SEM, EDS, XRD, EBSD, and hardness measurements. The following section discusses some of the key results obtained for this material system.

7.3.1 Deposit characteristics

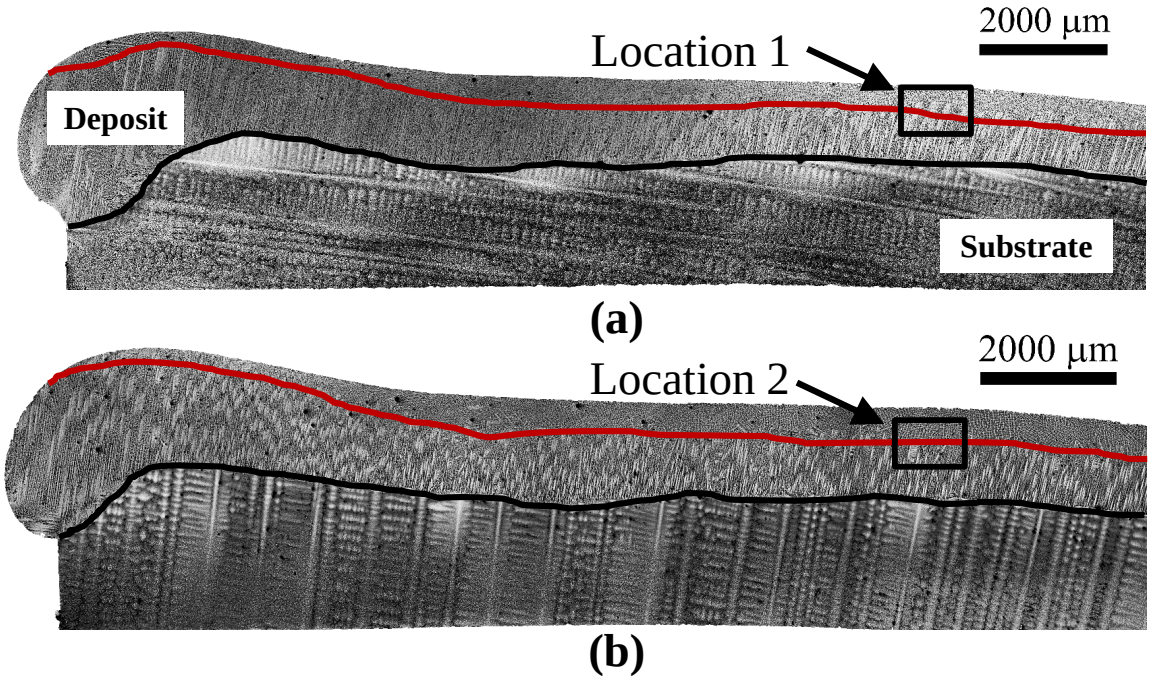

Figure 106. Length-wise cross-section of the SLE deposited René 142 on René N5 substrates with (a) [100] and (b) [001] crystal growth direction. For (a) and (b), the black line and the red line denote the substrate-deposit interface and the columnar region,

respectively.

Figures 106(a) and 106(b) show the longitudinal cross-sections of the as-deposited René 142 samples on René N5 substrates with [100] and [001] crystal growth direction, respectively. As shown in Figures 106(a) and 106(b), the SLE-deposited René 142 thickness is found to be more than 1500 μm. The crack-free and dense deposits show more than 1000 μm of columnar height [141]. A few pores are observed in the deposit region as shown in Figures 106(a) and 106(b). A DoE-based optimization study has previously demonstrated that the number of pores may be decreased by increasing the energy density [42]. With an increase in the energy density, the melt pool expands and overlaps with the solidified region deposited in the previous pass. Thus, the pores formed in the previous pass are re-melted, and thereafter, when re-solidification takes place, there are less chance for the formation of pores again.

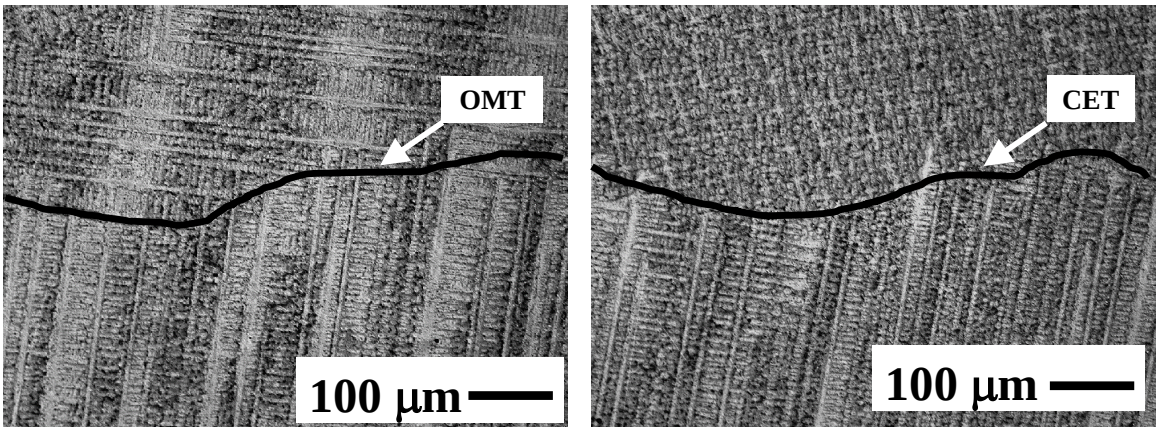

Figure 107. OM image of the René 142 deposit showing the (a) oriented-to-misoriented transition (OMT) [taken at Location 1 of Figure 106(a)] (b) columnar-to-equiaxed transition (CET) [taken at Location 2 of Figure 106(b)]. For (a) and (b), the black line denotes the transition region.

The deposit region shows three distinct types microstructures: a columnar dendritic

region in [001] direction, a columnar dendritic region in the [100] direction, and a fine equiaxed dendritic region. The OMT that represents a flip in the dendrite direction from [001] to [100] is shown in Figure 107(a). Similarly, the CET is illustrated in Figure 107(b). Both OMT and CET are detrimental to the epitaxial deposit formation as they thwart the unidirectional dendritic growth.

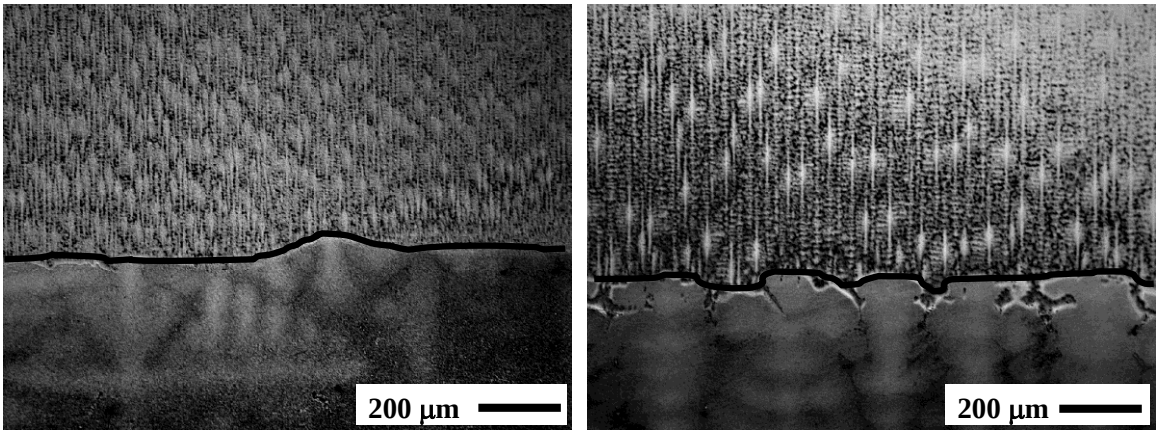

(a) **(b)**

Figure 108. Transverse OM image showing columnar dendritic growth of SLE deposited René 142 on René N5 substrates with (a) [100] and (b) [001] crystal growth direction. For (a) and (b), the black line denotes the substrate-deposit interface.

The substrate dendritic orientation of [100] does not disrupt the columnar growth in the [001] direction in the deposit region as illustrated in Figures 108(a) and 108(b). The columnar dendrites grow epitaxially along the direction of the dominant thermal gradient from the partially re-melted dendrites of the substrate that served as the nuclei for directional crystal growth. The partially melted secondary and primary dendrite trunks give the directionality to the epitaxial deposit of René 142 along the [001] direction for the [100] and [001] substrates (Figures 108(a) and 108(b)). The average PDAS is of order 20 – 30 μm in the deposit region. The substrate region shows an average PDAS of 200 μm. Therefore, the microstructures

obtained by SLE are about 10 times finer than the as-cast structure. The interface between the substrate and the deposit is free from any fusion defects as illustrated in Figures 108(a) and 108(b).

7.3.2 Microstructure

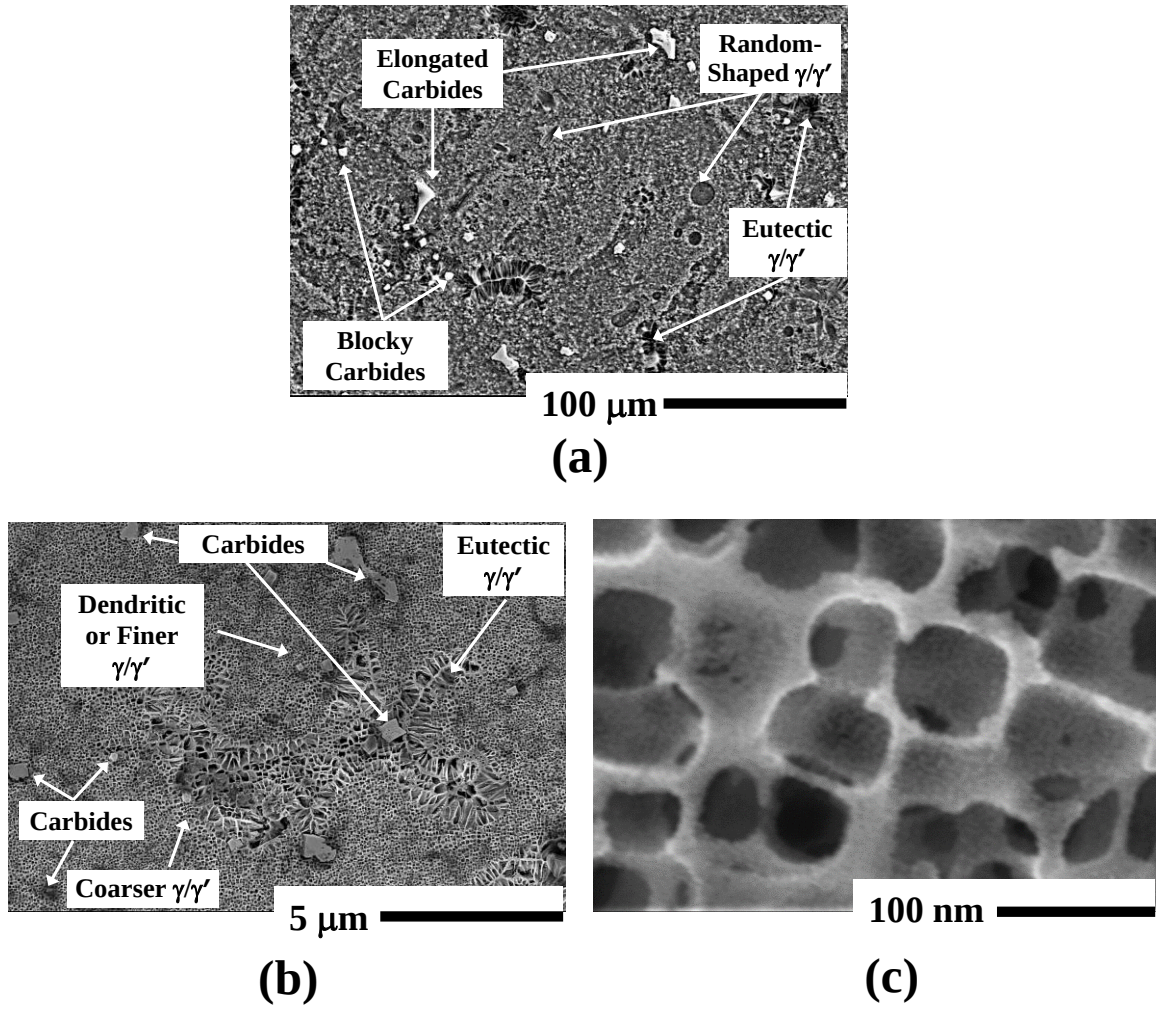

Figure 109. (a) The γ matrix, the γ′ precipitates, the random-shaped γ/γ′ islands, the eutectics and the carbides in the deposit region, (b) finer and coarser γ/γ′ precipitates and the γ/γ′ phases in the eutectic regions, and (c) the γ/γ′ microstructure at the dendrite core.

The SLE-deposited microstructure of René 142 shows five different microstructural features namely the γ matrix, the γ′ precipitates, the isolated random-shaped γ/γ′ islands

(observed in the dendrite core regions), the γ/γ′ eutectics, and the carbide precipitates as shown in Figure 109(a). The carbide and the eutectic phases are seen in the interdendritic region as these phases typically form during the final states of solidification. Figure 109(b) shows that the carbide precipitates are mostly elongated and blocky shaped. The γ′ phases are mostly cuboidal that follow variations in size depending on location as shown in Figure 109(b).

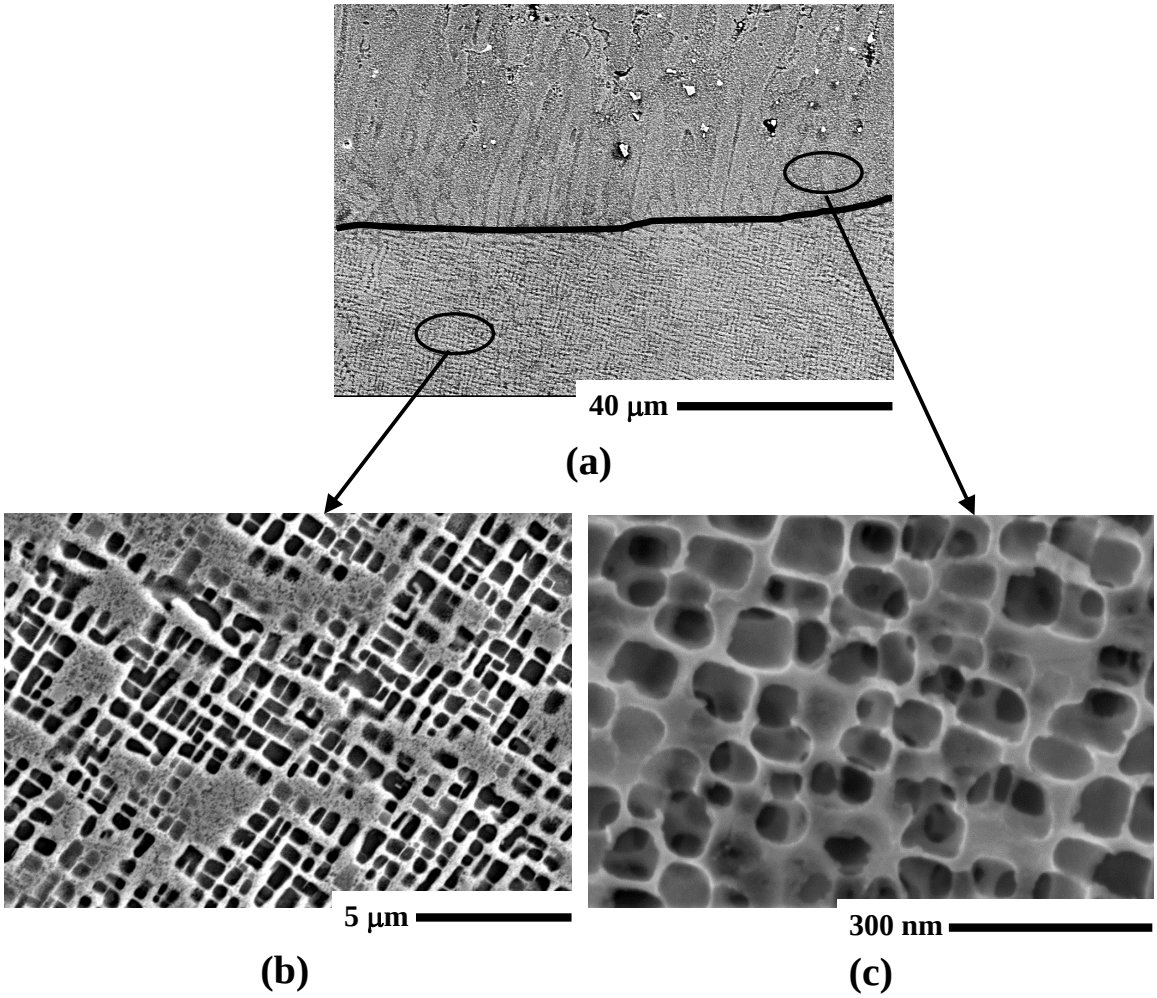

Figure 110. The γ/γ′ microstructure in the (a) interface region (the blackline denotes the substrate-deposit interface), (b) substrate region, and (c) deposit region.

The smaller precipitates are seen to be of order 50 nm while the larger precipitates are of order 100 nm. During the initial phases of solidification, the γ′ phases precipitate coherently

from the γ dendrites when the melt is cooled below the γ′-solvus forming fine homogeneous and fine γ/γ′ microstructures within the dendrite core as shown in Figure 109(c). Figure 109(b) also shows the γ/γ′ microstructure in the eutectic region showing the cubic and the channel shaped γ/γ′ precipitates. The channel length is from 0.5 – 1 μm while the channel width is of order 200 – 400 nm. The cubic γ/γ′ precipitates are of order 50 – 100 nm in the eutectic region as shown in Figure 109(b).

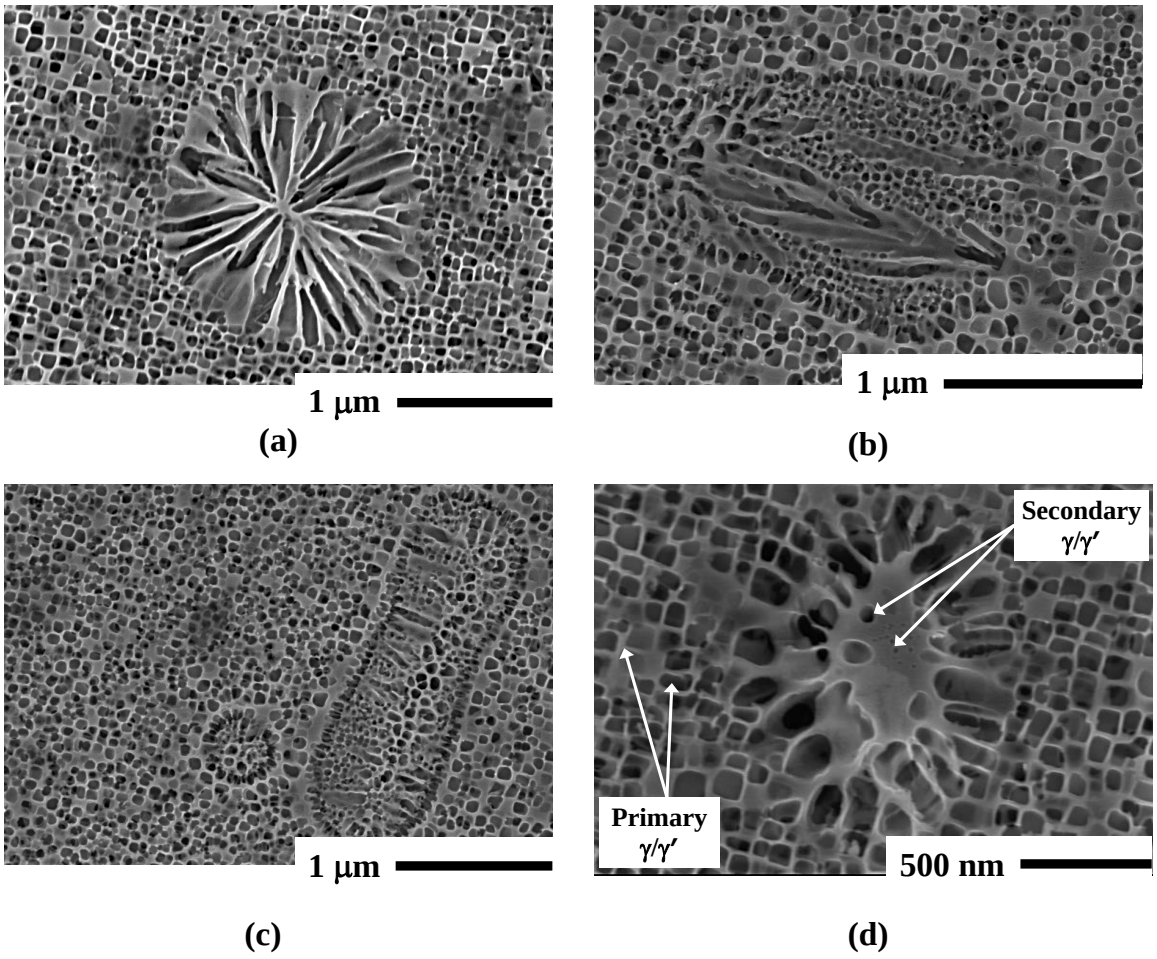

Figure 111. (a-c) The γ/γ′ microstructure in the random-shaped islands. (d) The secondary γ/γ′ microstructure in the random-shaped islands.

Figure 110(a) illustrates the SEM image of the etched γ/γ′ microstructure in the René N5

near the interface region showing columnar dendritic growth along the [001] direction. Figure 110(b) illustrates the SEM images of the γ/γ′ microstructure in the René N5 substrate region. While the primary γ′ shows size in the range of 0.5 – 1 μm in the substrate region, the secondary γ′ shows size in the range of 50 nm (Figure 110(b)). The primary γ′ shows size in the range 50-100 nm in the deposit (Figure 110(c)). The finer γ/γ′ microstructure in the deposit region increases the interface areas between the γ and γ′ structures compared to the cast substrate.

Figures 111(a) through 111(c) show the γ/γ′ microstructure in the random-shaped islands in the dendrite core region. These closed-loop structures are randomly oriented and no correlation is found between their orientation and the dendritic growth direction. Most of the structures are of order 1 – 2 μm in length while the width is of order 500 nm. Some of these structures also show secondary γ′ formation with size ranging from 1– 5 nm as shown in Figure 111(d). The formation of these structures in René 142 suggests the presence of secondary solidification paths in carbon-containing nickel-base superalloys under rapid directional solidification conditions [142].

7.3.3 Crystalline phases and texture

The XRD profile for the René 142 powder shows a prominent (111) peak as shown in Figure 112(a). The diffraction peaks at 2θ = 44°, 51°, 75°, 91°, and 96° indicate the diffraction of (111), (200), (220), (311), and (222) planes of the γ matrix. A significant peak at around 51° indicates a strong (200) growth in the substrate and the deposit regions as shown in Figures 112(b) and 112(c). The (200) peak in the SLE deposited René 142 parallel to the build direction represents a unidirectional solidification texture. The strong (200) growth is present in the SLE deposited René 142 with substrates with [100] and [001] crystal growth direction.

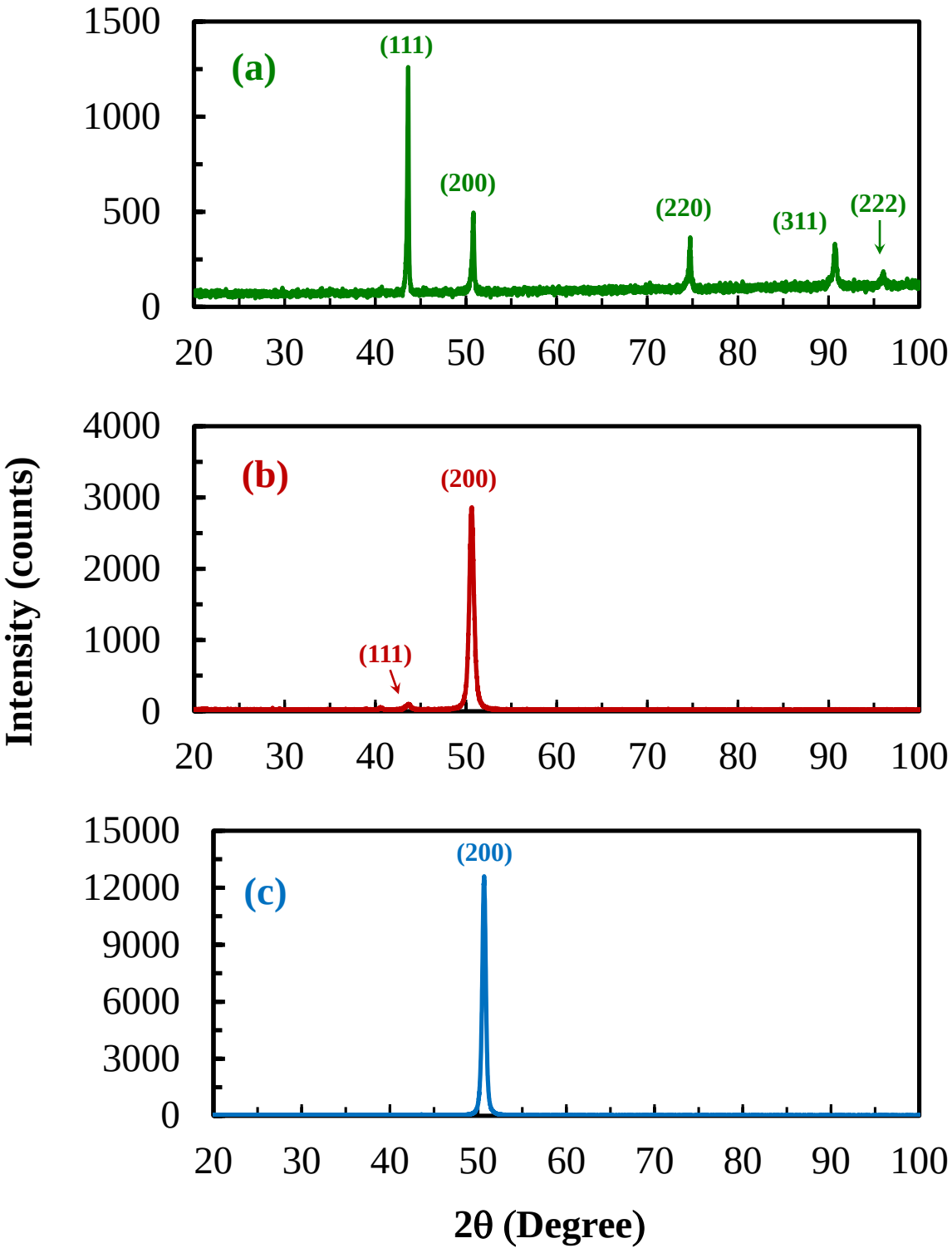

Figure 112. XRD profile of the (a) pre-alloyed René 142 powder, (b) René N5 substrate, and (c) René 142 deposit.

EBSD analysis is carried out to characterize crystallographic texture as well as the grain orientation on two representative René 142 samples deposited on the [100] and [001] René N5 substrates, respectively. As shown in Figures 113(a) and 113(b), apart from a few sporadic stray grains at the leading edge and in the deposit, and an equiaxed region at the top, most of the deposit region appears to be a single grain.

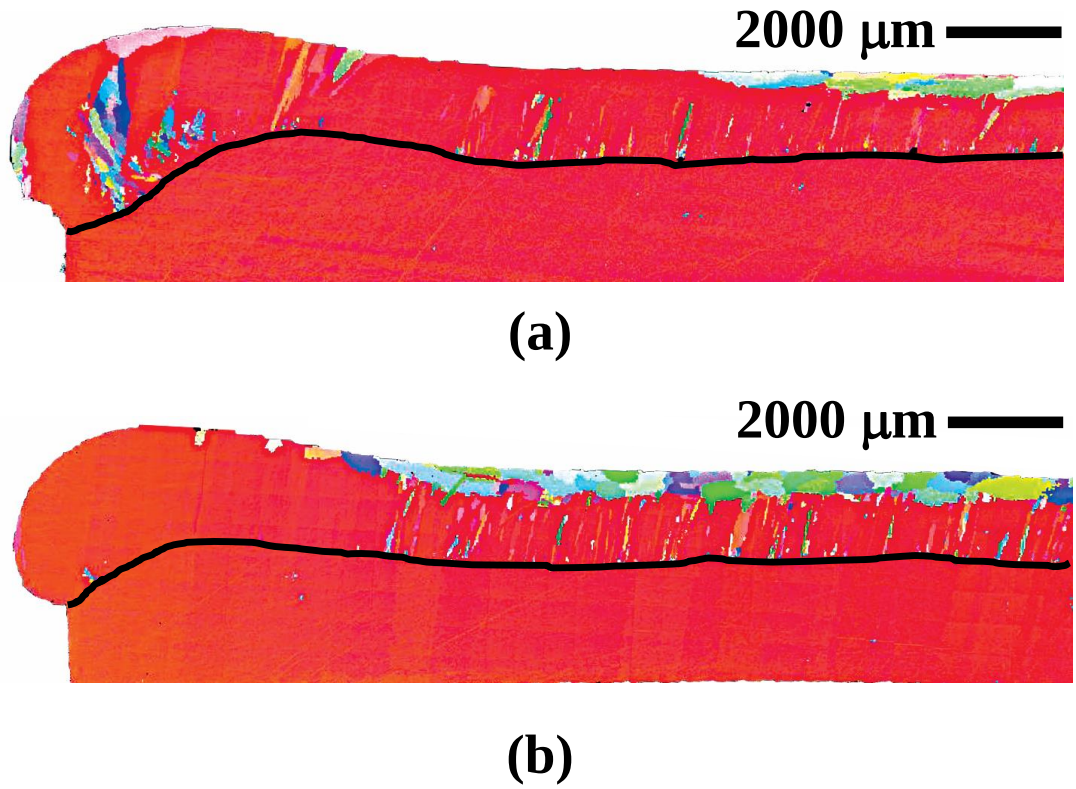

Figure 113. Large area orientation map obtained by EBSD for René 142 deposit on René N5 substrates with (a) [100] and (b) [001] crystal growth direction. The black line denotes the substrate-deposit interface.

Figure 114 shows the grain size distribution as estimated from the EBSD analysis for the entire deposit region (the region indicated above the black line in Figures 114(a) and 114(b)). Most of the deposit region is a single grain with an equivalent diameter exceeding 700 μm. The number of grains is similar for both the cases indicating that the substrate crystal growth

direction does not have any significant effect on the EQ grain formation.

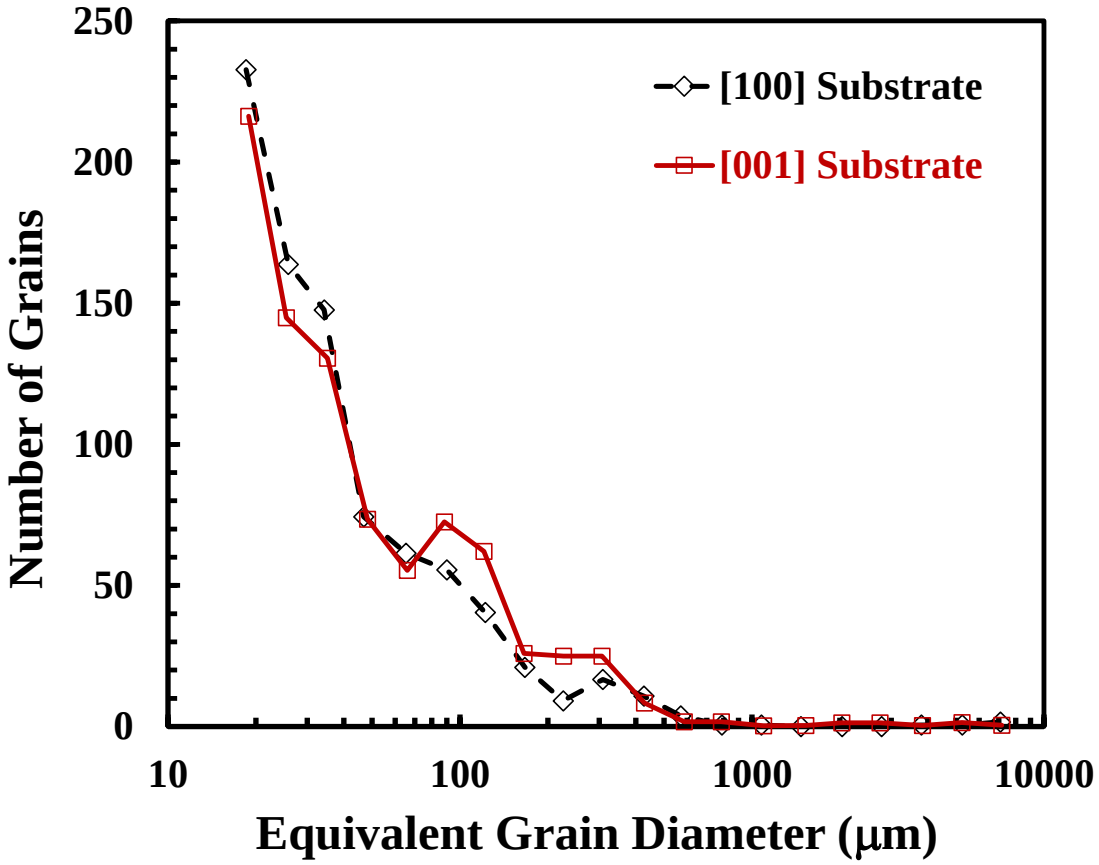

Figure 114. Grain size distribution of the René 142 deposit region for the substrate crystal growth direction in (a) [100] and (b) [001].

7.3.4 Elemental segregation

EDS line scans are performed across representative eutectic regions in the substrate and deposit, respectively (Figures 115(a) and 115(b)). The line profiles of a representative element (Ta) across a eutectic region in the substrate and the deposit are shown in Figures 115(c) and 115(d), respectively. From the elemental line profiles, the maximum and the minimum counts are extracted and a segregation parameter is defined as degree of segregation (k) = maximum cps/minimum cps (where cps denotes counts per second).

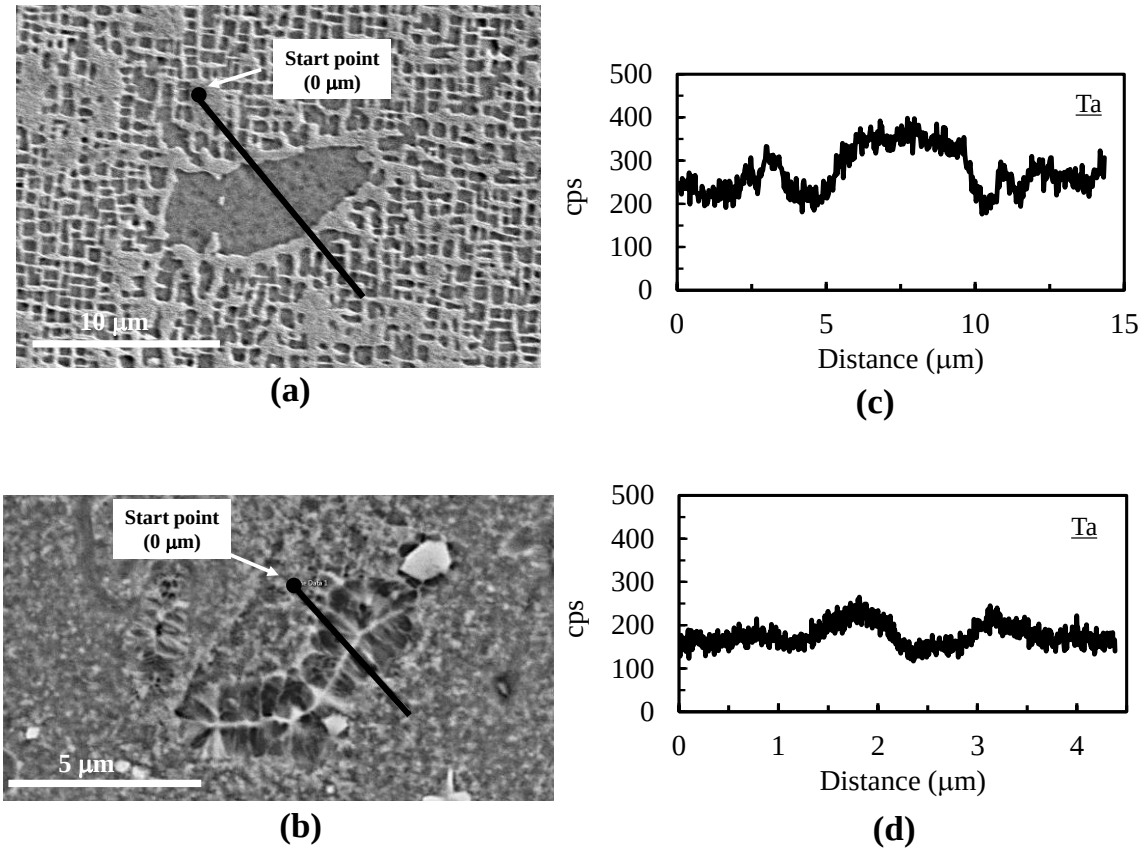

Figure 115. SEM image of a representative line scan domain in the eutectic region of (a) substrate and (b) deposit. EDS line profile of Ta across a representative eutectic region in the (c) substrate and (d) deposit.

The k values for various elements are plotted in Figure 116. In comparison to the bulk alloy composition, the γ/γ′ eutectic phase shows strong elemental segregation in the substrate. In the deposit region, the degree of segregation is considerably lower.

René 142 contains about 0.12 wt. % C and 0.015 wt. % B that along with the refractory elements drive precipitation of carbides in the deposit region. Blocky and elongated carbide precipitates are found in the deposit region (Figure 117(a)). The carbides are found to be rich in refractory elements (Ta, Hf, and W), however trace amounts of Mo, Cr, Co, Re, and Al were also present as shown in Figure 117(b).

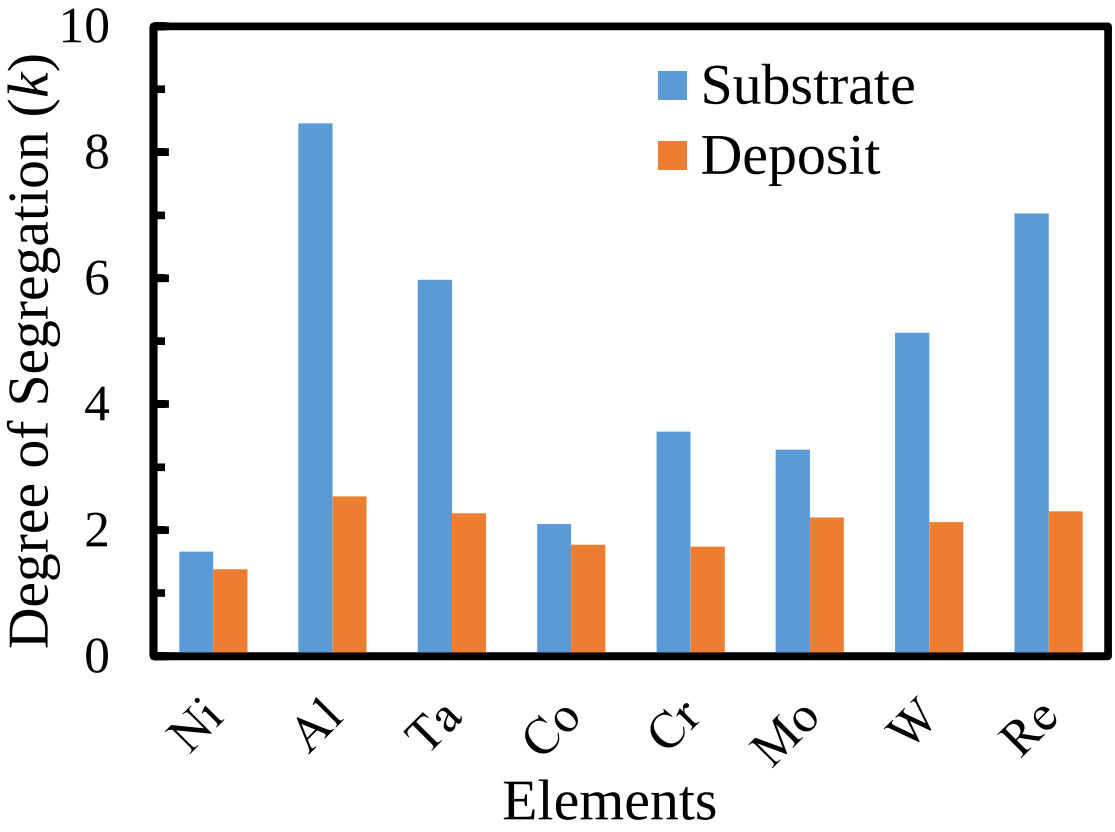

Figure 116. Degree of segregation (k) of various alloying elements across representative eutectic pools in the substrate and the deposit

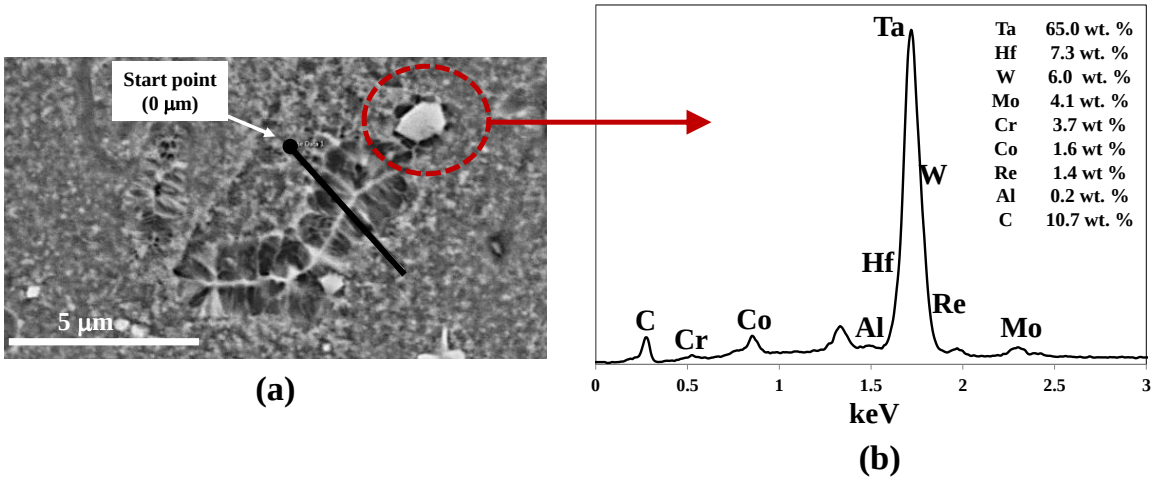

Figure 117. (a) SEM image of a representative carbide precipitate in the deposit region of René 142 and (b) the EDS profile of the carbide precipitate.

7.3.5 Vickers microhardness

Microhardness measurements conducted over the René N5 substrate region do not show any significant change of hardness due to changes in columnar orientation. The average value of the cast substrate hardness ranges from 400 to 420 HV. The [001] columnar region in the deposit region consistently shows higher HV values ranging from 465 to 482. The [100] region shows an HV value of 450. The EQ region displayed a lower hardness of 436. Table 16 summarizes the microhardness and yield stress results obtained at different locations of the SLE deposited René 142.

Table 16. Summary of microhardness results.

Region	HV_{2000}	HV (GPa)	σ_y (GPa)
Substrate	410	4.02	1.34
Deposit [001]	469.6	4.61	1.54
Deposit [100]	449.2	4.41	1.47
Deposit [EQ]	436	4.28	1.43

7.3.6 Conclusions on SX René 142 on SX René N5

Crack-free deposits of René 142 are successfully fabricated on René N5 substrates with [100] and [001] crystal growth direction using the scanning laser epitaxy (SLE) process. The powder used in the present study has internal porosity and secondary satellites. However, SLE is able to deposit near-fully-dense structure with low porosity implying SLE may be able to successfully process non-ideal powder or potentially recycled powder. The superior oxidation resistance and excellent rupture properties of René 142 can potentially improve the performance of the legacy components made of lower oxidation resistance superalloys. Such

AM deposition will thus enable repair of existing hot-section components resulting in a superior cycle life and high-temperature performance. The findings, therefore, can open up the possibility of fabricating superalloy components with a potential multi-material and functionally-graded capability.

The SLE-deposited René 142 demonstrates epitaxial columnar growth in the [001] direction with more than 1000 μm of columnar height in a single pass. Overall, three different types of grain morphologies are observed such as [001] columnar grains, [100] columnar grains, and EQ grains. From SEM investigations, it is found that the deposit region typically consisted of five different type of microstructures including the γ matrix, the γ′ precipitates, the isolated random-shaped γ/γ′ islands in the dendrite core regions, the γ/γ′ eutectics, and the carbide precipitates. Carbide precipitates of different shapes are seen in the interdendritic region.

The deposit region shows approximately 90% reduction in the γ′ precipitate size compared to the substrate. Finer microstructure can impart more strength. Microhardness measurements demonstrated that the deposit region has approximately 10% higher HV values compared to the substrate. The values obtained in the current studies are marginally higher compared to the EBM-processed René 142 by about 5% [139]. Such increase in the hardness values may be attributed to the higher cooling rate in the LPBF processes resulting in a finer microstructure.

7.4 Summary

This chapter discusses the SLE development for René 142 on two different dissimilar chemistry substrates namely EQ René 125 and SX René N5. Crack-free and dense deposits of

René 142 are obtained in both types of substrates for a range of operating conditions. Some of the key conclusions from this study are:

- The SLE process is able to deposit René 142 with thickness exceeding 1000 μm in a single pass for dissimilar powder-substrate combination. Depending on the initial seed orientation or the substrate crystal growth direction, the deposited René 142 can have EQ or SX/DS microstructures.

- The deposit region shows finer microstructure compared to the substrate region. The deposit region also shows dendritic segregation. The SLE-deposited microstructures also show finer γ′ features compared to the substrate. Such finer microstructures improve the microhardness in the deposit region by approximately 10% compared to the substrate.

- The deposit region shows three different microstructural features such as the γ′ precipitates, the γ matrix, the eutectics, and the carbides. The γ′ precipitates are polygonal shaped while the carbides are typically blocky shaped.

- The comparison between the SLE-deposited EQ René 142 and SX René 142 microstructures reveal the following:

    - The SX René 142 shows the typical characteristics of any DS/SX deposits made by AM process. The deposited SX René 142 shows three different microstructures such as the [001] columnar, [100] columnar, and an EQ microstructure. However, EQ René 142 shows locally columnar and EQ microstructures.

    - The carbide precipitates are distributed in the deposit region of the EQ René 142. However, in the deposit of SX René 142, carbide precipitates are found in the

interdendritic region. The deposit of SX René 142 reveals the formation of closed-loop random structures in the dendritic core region implying the existence of secondary solidification paths. However, EQ René 142 does not show the presence of these structures.

- A trace amount of Re is found in the blocky carbides in SX René 142. However, Re is absent in the blocky carbides of EQ René 142 indicating the presence of secondary solidification paths in the unidirectional solidification of Re containing nickel-base superalloys.

Chapter 8: Summary and conclusions

This chapter begins with a description on the unique characteristics of the SLE process. It then summarizes the significant findings followed by key conclusions. Thereafter, the intellectual contribution is discussed and the technical and commercial impacts of this dissertation are outlined. The chapter concludes with suggestions for potential avenues of future research in this area.

8.1 Unique characteristics of SLE

Although metal AM processes are based upon the same principle of layer-wise material consolidation, each is distinct with regard to, e.g., energy source type, processing techniques, operating conditions, usable materials, and metallurgical consolidation mechanisms. These dissimilarities result in a wide range of microstructural properties across the processes. Figure 118 illustrates the classification of various metal AM processes. These processes are first categorized on the basis of the energy source type, and thereafter they are classified according to the consolidation mechanisms [5]. In general, the AM-based processes are divided into two major categories namely the directed energy deposition (DED) process and the powder bed (PB)-based process. The DED processes may be either powder-feed- or wire-feed-based. AM-based processes also differ based on the type of energy sources. There are three main types of energy sources available such as laser, electron beam, and arc.

The key differences between SLE and the powder-feed-based DED processes such as laser engineered net shaping (LENS®) [45, 69, 143] are twofold. In SLE, the powder bed is stationary, while in LENS®, the powder is fed via a deposition head. This powder feeding

causes additional turbulence and unwanted convection in the melt pool, thus disrupting the partially solidified dendrites in the mushy zone and inhibiting DS/SX growth. Another difference is related to the speed of the substrate's mechanical movement in the LENS® process. Here, the scan speed is limited by the speed of the powder feed assembly, and hence, for "non-weldable" superalloys, the combination of lower scan speed and high scan power results in parts that have lower quality in terms of crack propensity and fatigue strength.

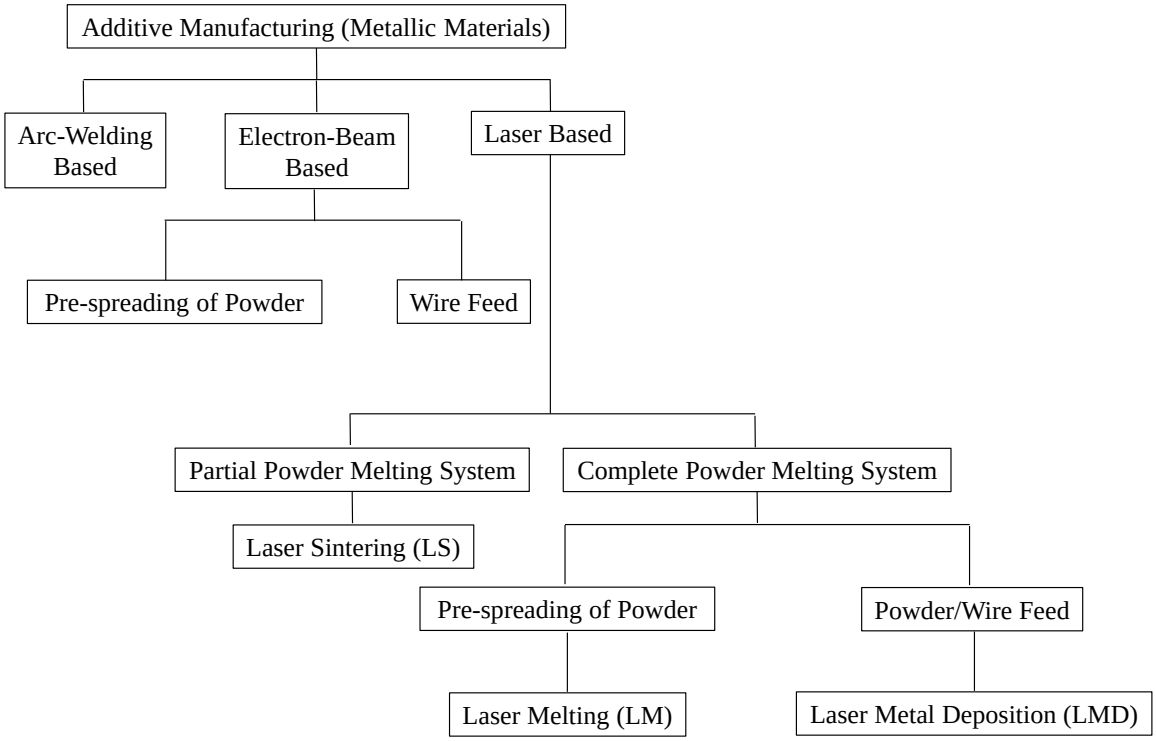

Figure 118. Classification of AM processes [5].

In SLE, the galvanometer-driven movement of the laser beam allows precise motion and faster scan speed, thus potentially improving the quality of the fabricated component. In the DED processes, the speed of the energy source is limited by the speed of mechanical powder feed assembly. Such restrictions do not apply to the SLE process, and hence, SLE is capable of operating at a significantly higher scan velocity compared to the DED processes. Thus, it

offers more flexibility on the scan speed and has the potential to reduce the crack formation due to low scan speed [144].

Powder bed laser-based AM processes such as selective laser melting (SLM) are not capable of creating structures with defined microstructure, and often have issues with warping and porosity in underlying layers [5]. Direct metal laser sintering (DMLS) has issues with regulating the melt depth of each layer. Powder bed EBM-based AM processes such as SEBM suffer from a major pitfall related to maintaining high level of vacuum during processing. Under high vacuum, the vaporization temperature of the alloying elements may drop below their melting temperature resulting in direct sublimation. This leads to a significant change in alloy composition in the deposited part. In SEBM, the powder bed also needs to be heated up before processing adding a significant amount of complexity. Processes such as SLM, DMLS, and LENS® operate using open-loop control schemes and under improper atmospheric conditions, limiting the quality of the produced deposits. In contrast, for SLE, feedback control is attempted and is found to consistently produce dense, uniform deposits for both EQ superalloys [4].

Any additive processing technique involving superalloys involves melting of the component and the addition of material to obtain a proper metallurgical bond and to maintain epitaxy between the deposit and the substrate, unless filler material is used for a brazing like procedure and epitaxy is not desired. The wide solidification range of superalloys promotes solidification cracking; the local dissolution of different phases causes liquation cracking, and the incorporated gas results in porosity within the deposit region. The high-resolution scan spacing used in the SLE process causes each subsequent raster scan to overlap a portion of both the prior and the subsequent raster scans, resulting in a pre-heat and post-heat treatment

during the scanning operation, reducing in the possibility of hot tearing as seen in other processes.

The high-resolution scan spacing also results in the development of considerably finer grain structures in the deposits made via SLE as compared to investment casting and cladding limiting the stresses that would otherwise cause liquation cracking [37, 144]. The melt pool size is of order 2500 μm in width. The controlled heat input through a finely focused Gaussian beam of diameter 40 microns and fast movement of the laser beam enable successful fabrication of superalloy deposits atop like-chemistry substrates without the need of filler materials that may have significantly different composition relative to the substrate. The use of a very finely focused and localized heat source, capable of delivering immense energy density (of order 10^{10} J/m^3) potentially makes this process suitable for repairing and manufacturing complex blade contours in gas turbines.

The SLE process integrates several different key components such as laser, scanner, scanner controller, video camera, and thermal imaging camera facilitating complete control over the process parameters such as laser power, scan speed, scan spacing, scan geometry, and powder layer thickness. SLE can be conducted in an extremely pure environment reducing the possibilities of oxide formation. Oxide layers are detrimental to the deposit as during subsequent melting, the layer gets broken into small pieces and those inclusions are trapped inside the deposit that may act as crack initiation sites. AM-fabricated deposits typically have structure, properties, and performance that are significantly different from their cast and wrought counterparts due to very high cooling rates. The SLE process is designed to advance the field of alloy design for AM through high throughput experimentation. The substrate

coupon setup, carrier plate design, and the conveyor belt assembly inside the customized build chamber is geared towards developing new alloys through experimentation in short time.

8.2 Dissertation summary

This dissertation is aimed at achieving a fundamental understanding of the AM-based processing of high-γ′ nickel-base superalloys through SLE. The results of this research are able to:

- Identify key processing regimes that can result at creating crack-free structures in nickel-base superalloys through SLE with as desired microstructure and properties.

- Develop a comprehensive framework (as shown in Figure 119) involving both experimental and computational techniques to gain insights into the melting, solidification, and microstructure evolution during SLE.

- Establish process-structure-property relationships for a range of nickel-base superalloys processed through SLE.

- Contribute to the science of multi-material structures enabling alloy design for AM-based processing.

Chapter 2 of this dissertation describes the evolution of nickel-base superalloys, their processing difficulties, and the state-of-the-art repair efforts carried out on these material systems. Chapter 3 describes the development of scanning laser epitaxy (SLE), a laser powder bed fusion (LPBF)-based AM process. This chapter also documents the advanced materials characterization techniques that are implemented to characterize the SLE-deposited microstructures. Chapter 4 highlights the development of a coupled flow-thermal model in

order to predict the flow-thermal-microstructural evolution in SLE. The flow-thermal model is extended to a number of different superalloys such as IN100, René 80, CMSX-4®, and René N5.

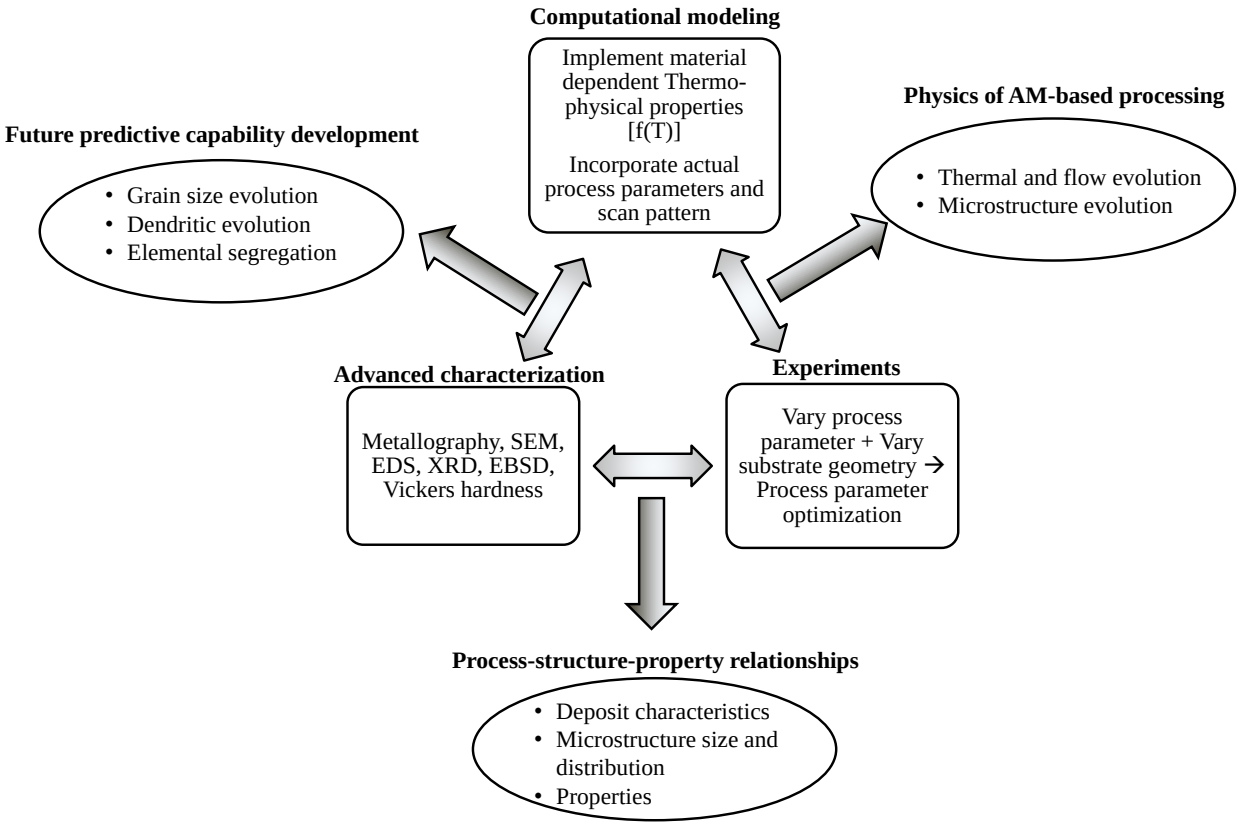

Figure 119. Schematic presentation of the integrated experimental and modeling approach towards advanced materials and structures processed through SLE.

Chapter 5 describes the successful fabrication of crack-free EQ deposits through SLE. Two high-γ′ alloys namely IN100 and MAR-M247 are investigated. Chapter 6 focuses on the successful fabrication of SX deposits through SLE. Two high-γ′ alloys namely CMSX-4® and René N5 are investigated. Chapter 7 highlights the successful deposition of heterogeneous structures through SLE. The depositions of high-γ′ René 142 on SX René N5 and EQ René 125 are carried out.

8.3 Key conclusions

The following conclusions in the areas of the process development, multi-physics modeling, experimental optimization, and materials characterization are obtained from the dissertation research.

8.3.1 Process development

The SLE process development reveals a number of significant capabilities. These are listed below:

- A number of different high-γ′ nickel-base superalloys are investigated. Table 17 shows the composition of the alloy powders used in this dissertation. Table 17 also shows the minimum and maximum wt. % of the individual elements. However, SLE is able to fabricate dense deposits from these powders establishing SLE's versatile capability in AM of high-γ′ nickel-base superalloy powders.

- Some of the powders used in the present research have porosity, non-spherical particles, and secondary satellites. The powder particle size varies between 20 μm to 150 μm. However, SLE is able to fabricate deposits with very low porosities implying that SLE may be able to successfully process non-ideal powders or potentially recycled powders.

- A range of powder layer thicknesses is also explored in this present research. Table 18 shows the powder layer thickness that is used in this dissertation. It is shown that SLE is able to fabricate dense deposits for a range of powder layer thicknesses implying that it may be feasible to change powder layer thickness along the build direction in order to strike a balance between faster build-rate and resolution for finer features.

Table 17. Chemical composition and the γ′ volume fraction of superalloy powders used in this dissertation (wt. %).

	IN100	MAR-M247	CMSX-4®	René N5	René 142	Max	Min
Cr	10	8	6.5	7.1	6.8	10	6.5
Co	15	10	9.7	8	12	15	8
Mo	3	0.7	0.4	2	1.5	3	0.4
Re	-	-	3	3	2.8	3	0
W	-	10	6.4	5	4.9	10	0
Al	4.7	6	5.6	6	6.15	6.15	4.7
Ti	5.5	1	1	-	-	5.5	0
Ta	-	3	6.5	7	6.35	7	0
Hf	-	1	-	0.15	1.5	1.5	0
B	0.014	0.015	-	0.004	0.015	0.015	0
C	0.18	0.15	-	0.05	0.12	0.18	0
Zr	0.06	0.05	-	-	0.02	0.06	0
Ni	61.546	60.085	60.900	61.696	57.845	61.696	57.845
γ′ volume fraction	60 [145]	62 [107]	70 [146]	> 65 [147]	59 [139]	70	59

Table 18. Powder layer thickness for different superalloys.

Material system	Powder Thickness (mm)
IN100 on IN100	1.4
MAR-M247 on MAR-M247	1.7
CMSX-4® on CMSX-4® Substrate 1	1.4
CMSX-4® on CMSX-4® Substrate 2	1.7
René N5 on René N5	1.2
René 142 on René 125	1.4
René 142 on René N5	1.4

- The SLE process is able to fabricate crack-free deposits of high-γ′ superalloys on a range of substrate sizes for different superalloys. The substrate sizes are listed in Table 19. The substrates also have different crystal growth directions. The results set the stage for SLE to process complex geometries having non-uniform cross-sections.

Table 19. Substrate size for different superalloys.

Material system	Substrate Size (mm x mm mm)
IN100 on IN100	35.56 x 6.86 x 2.54
MAR-M247 on MAR-M247	31.50 x 5.84 x 2.54
CMSX-4® on CMSX-4® Substrate 1	35.56 x 6.86 x 2.54
CMSX-4® on CMSX-4® Substrate 2	38.10 x 11.85 x 2.54
René N5 on René N5	35.56 x 6.86 x 2.54
René 142 on René 125	35.56 x 6.86 x 2.54
René 142 on René N5	35.56 x 6.86 x 2.54

8.3.2 Multiphysics modeling

A 2D CFD model is developed in order to simulate flow-thermal-microstructure evolution in SLE. The key conclusions are:

- For all the superalloys investigated, the determination of emissivity is done systematically to ensure calibration of the thermal imaging camera and accurate estimation of temperature during the SLE process. A novel method developed previously [4] is implemented to compute the emissivity of nickel-base superalloys by observing the change of slope in the temperature curve at solidus and liquidus temperature.

- The temperature field data gathered from the thermal imaging camera enables validation of the model developed. Reasonable agreement is obtained for melt pool size and the average melt pool temperature. The model is also validated using the melt depth profile as obtained from actual micrographs. Again, reasonable agreement is achieved.

- The empirical microstructural model enables qualitative prediction of microstructural transitions such as OMT and CET. The microstructure model is also able to predict the CET/OMT transitions across a broad range of processing parameters.

- The simulation method is coupled with experimental optimization to improve the turnaround time for process development. The results from the simulation provide an initial guess on the process parameters to be explored for experimental trials. Performing manual calculations of the deposit characteristics are error-prone. A previously developed automated digital metallography technique is successfully used to calculate the deposit characteristics automatically from the metallographic images [82].

8.3.3 Experimental optimization

Design of experiments-based studies are conducted on CMSX-4® to understand the effect of process parameters on the deposit characteristics.

- E and Q are two key parameters which control the SLE process. The repeat scan energy plays a critical role in establishing stable melt pool while the scan energy density determines the overall quality of the deposit as the scan progresses.

- Higher values of E increase the melt pool area and cause a smoother flow of powder, thus increasing the deposit uniformity. The higher energy density also draws more powder from the surrounding powder region and increases the average deposit height.

- Higher E decreases the surface tension and causes a smoother flow of powder decreasing the number of SGs. However, the expanded melt pool results in a reduced vertical temperature gradient and consequently lowers SX height.

- A tradeoff exists between the number of SGs and the SX height. SX ratios exceeding 0.5 and number of stray grains of less than 8 could thus be obtained simultaneously with E in the 35 to 50 J/mm^3 range and Q in the 400 to 500 J/mm range.

8.3.4 Materials characterization

A detailed investigation is carried out in this dissertation to accurately characterize the quality of the SLE-fabricated deposits. The key findings are:

- OM investigations reveal that the SLE process is capable of depositing crack-free, dense deposits for a range of popular high-γ′ hot-section superalloys such as CMSX-4®, René N5, René 142, IN100, and MAR-M247.

- OM investigations reveal that the SLE-deposited microstructure has finer PDAS compared to the cast substrates. For example, in the case of CMSX-4®, the PDAS in the deposit region is of order 10 μm while in the substrate region it is of order 500 μm. Therefore, the SLE-deposited microstructure is about 50x finer compared to cast microstructure.

- SEM investigations reveal that the SLE-deposited microstructure is considerably finer compared to the cast substrates. The precipitates are more uniformly distributed in the deposit region. For example, in the case of CMSX-4®, the γ′ size in the deposit region is of order 50 nm while in the substrate region it is of order 2 μm. Therefore, the γ′ precipitates in the SLE-deposited microstructure are about 40x finer compared to those in the cast substrate. Hence, PDAS and γ′ show similar reductions in sizes in the deposit compared to the substrate for CMSX-4®.

- EDS investigations reveal that the deposit region shows a reduced degree of elemental segregation compared to the substrate region. For example, the degree of segregation for one of the heaviest element, Re, in the CMSX-4® deposit region is 3 while in the substrate it is 6. So, with SLE, a reduction of 50% in the degree of elemental segregation for heavy

elements is obtained.

- XRD results reveal that the deposit region shows considerable texture due to a strong thermal gradient in the [001] direction. The results illustrate that for CMSX-4®, René N5, and René 142, the deposit region has SX microstructure.

- EBSD analysis shows that SLE is capable of producing SX deposits in nickel-base superalloys. The deposit region appears to be a single grain with a thin EQ region at the top of the deposit.

- Microhardness results show that the deposit region has approximately 10% higher hardness values compared to the substrate across the different superalloys investigated. Such an increase may be due to the finer microstructure.

- Heat treatment reduces the microstructural non-uniformity in the deposit region. The volume fraction of the eutectic decreases by approximately 80% and the hardness increases by approximately 3.7% because of improvement in microstructural uniformity.

8.4 Intellectual contribution

The following subsections summarizes the key results obtained in the areas of process development, experimental optimization, multi-physics modeling, and materials characterization from the dissertation research.

8.4.1 Process development

A custom-made LPBF-based AM process is used in this dissertation research.

- The challenges associated with the processing of high-γ′ nickel-base superalloys

are well established. The existing AM-based processes such as SEBM, DMLS, SLM, and LENS® have shown capabilities in processing only a handful of high-γ′ nickel-base superalloys. For example, SEBM has shown capabilities with CMSX-4® and René 142 after preheating the powder bed. SLM has shown success with MAR-M247 once the powder bed is heated to 1200 ^{o}C. In contrast, this dissertation research extends the previous works of Acharya [22] and Bansal [4] on CMSX-4®, René 80, and IN100, and demonstrates successful fabrication of several high-γ′ nickel-base superalloys such as MAR-M247, René N5, and René 142 having a wide range of alloy composition and thermo-physical-rheological properties.

- The dissertation research demonstrates the successful fabrication of EQ or SX deposit of the same material i.e. René 142 by changing the seed material i.e. the substrate. René 142 is typically cast with a DS microstructure. However, in this dissertation, it is shown that this alloy can be deposited with an SX microstructure if the seed is SX. The SX substrate may have different crystal growth directions. However, if the primary or the secondary dendritic arms in the substrate are aligned with the direction of dominant thermal gradient i.e. [001], the deposit region shows dendrite growth in the [001] direction.

8.4.2 Experimental optimization

Experimental optimization is carried out to obtain as-desired microstructure in SLE.

- It is well known that shallow melt depth of less than 100 μm lowers the probability of residual stress accumulation in the melt-back region, and therefore, crack formation. This dissertation research shows that a precise control over the operating parameters can be achieved resulting in a shallow melt back depth of less than 100 μm along the entire length and width of a sample across a range of superalloys without any interface fusion defects.

- It is demonstrated through the current research, that the defects such as SGs and CET/OMT in the LPBF-based AM-fabricated SX deposits may be inversely correlated. For example, the higher energy density is helpful in reducing SGs. However, at higher energy density, CET occurs at a lower deposit height. Hence, just by optimizing the process parameters, SG-free and CET-free microstructures may not be obtained and further development on feedback or feedforward control is necessary.

8.4.3 Multiphysics modeling

A fundamental understanding of the AM-based processing of nickel-base superalloys is obtained through the 2D simulation.

- A single 2D computational platform incorporating flow-thermal-microstructure simulation enables greater traceability with significantly lower computational time. This model incorporates the raster scanning laser beam and temperature dependent properties as opposed to existing 2D models based on single bead scan on top of constant property materials. If the thermo-physical properties are readily available, the model can predict the melt depth profile within 12% error.

- The asymmetrical melt pool consists of two rotational vortices that draw the loose powder and expand the melt pool along the transverse and vertical directions. A range of velocities is observed inside the melt pool with higher velocity appearing near the top surface. The rotational vortices at the leading edge control the powder flow characteristics. Hence, the thermal gradient at the leading edge is critical in controlling the surface rippling. However, since, the trailing edge of the melt pool does not undergo further melting, it is solely responsible for the final solidification microstructure. The vortices and the velocities inside the

melt pool are strong functions of the alloy composition. Depending on the thermo-physical properties of the alloy, these vortices may be fully-developed or under-developed resulting in a wide range of deposit characteristics under identical operating conditions.

8.4.4 Materials characterization

A series of advanced materials characterization techniques are implemented to accurately analyze the quality of the SLE-fabricated deposits.

- SLE shows unparalleled performance in the deposition of SX microstructure. For CMSX-4®, René N5, and René 142, single pass depositions of more than 700 μm of columnar growth is obtained on substrates having different size and crystal growth direction. For MAR-M247 and IN100, SLE shows more than 1000 μm of total deposit height in a single pass. These deposit thicknesses exceed the desired thickness for repair or restoration operations of damaged hot-section components.

- Existing research on the AM-based processing of nickel-base superalloys typically establishes the relationship between PDAS and flow-thermal conditions such as temperature gradient (G) and solidification velocity (V) inside the melt pool. However, in this dissertation, a direct correlation between PDAS and processing parameters is obtained leading to better controllability of microstructure by changing the processing conditions.

- For EQ microstructure, an isotropic deposit is generally desired. However, AM-based processing typically shows a significant amount of variation in the microstructure and properties within a single part having EQ microstructure. This dissertation research assesses the variation of microhardness in the EQ deposit region in great detail and demonstrates that

though the processing parameters may have a significant impact on the macroscale deposit quality such as deposit height, melt back depth etc., the microhardness is within $\pm 2\sigma$ level in the entire deposit region for a range of different processing conditions.

- The dissertation research investigates the quality of the SLE-deposited microstructure in great detail across a range of superalloys. The results show that the SLE-deposited microstructure has finer length scale, superior microstructural uniformity, and significantly lower level of elemental segregation which may require less amount of heat treatment time in homogenizing the microstructure facilitating faster turn-around and part qualification.

8.5 Technical impacts

The SLE process demonstrates the fabrication of fully dense, crack-free, and low porosity of conventionally "non-weldable" superalloys while maintaining the desired microstructure. The potential technological impacts of SLE are as follows:

- Due to tighter thermal control and no mechanical tool movement, SLE can easily be extended to complex geometry, allowing repair of turbine blades, vanes, and shrouds.

- As a repair process, SLE is capable of depositing more than 1000 μm SX deposit in a single pass. SLE can easily be extended to a multi-layer process, allowing complete 3D fabrication of superalloy components.

- This comprehensive physics-based model developed in this dissertation can be used to both develop predictions of what microstructure is produced under certain operating parameters, and what operating parameters are required to create particular desired

microstructures. This predictive capability can be powerful in developing real-time control schemes to obtain as-desired microstructure.

8.6 Commercial impacts

The potential commercial impacts of SLE are as follows:

- Enables AM of high-temperature and high-strength superalloys through SLE, currently experiencing high demand by industry, by providing systematic process maps for achieving targeted performance and properties.

- Enables new technologies in a wide range of areas including automotive and aerospace industry, and energy sectors that require high-performance multifunctional materials.

- The processing methodology investigated in this dissertation facilitates AM-based processing of next-generation functionally graded materials and structures (FGMs) that incorporate deliberately designed transitions in materials composition, structure, and properties within a component in preferred directions to enhance and optimize the functional value of that component.

8.7 Suggestions for future work

There is ample scope for further development of the SLE process. Some of those areas are listed below:

8.7.1 Process improvement

The SLE process needs to be studied and optimized for shallow melt pool generation and

for complex geometries where wide and uniform melt pools cannot be maintained. The single-pass deposition also needs to be extended to layer-by-layer manufacturing facilitating fabrication of hot-section components from scratch.

8.7.2 Assessment of solidification path

The current research shows that under rapid solidification conditions, the superalloys show distinct microstructural features that are not present in conventionally fabricated superalloy parts. An assessment of the solidification path is therefore necessary to understand and control the process to obtain as-desired microstructures and properties in AM-fabricated parts.

8.7.3 Design of heat treatment cycles

The AM-fabricated parts show significantly lower elemental segregation compared to their cast counterparts. A lower degree of elemental segregation may require less amount of time to homogenize the microstructure through heat treatment. Design of heat treatment cycles is therefore necessary to optimize the microstructure of the AM-fabricated parts.

8.7.4 Evaluation of mechanical properties

The quality of the deposit needs to be verified from mechanical tests. For this purpose, microindentation hardness is used in this research. To further evaluate the mechanical properties of the deposit under severe conditions, elevated temperature tensile and shear tests need to be performed to understand the benefit of microstructural refinement during SLE.

8.7.5 Advanced characterization of the deposits

The SLE-deposited microstructure can be further assessed using several different

advanced materials characterization methods such as transmission electron microscopy (TEM), scanning transmission electron microscopy with energy dispersive x-ray spectroscopy (STEM-EDS), atom-probe tomography (APT), and x-ray computed tomography (CT). While TEM can characterize the precipitates accurately, STEM-EDS and APT can provide elemental segregation at nanometer levels. CT can provide critical information on the defect distribution such as porosities and micro-cracks in the deposit region.

8.7.6 Prediction of residual stresses, grain structure, and dendritic morphology

The CFD model can be extended to obtain flow-thermal-microstructure evolution in complex arbitrary 2D cross-section and 3D parts. The transient thermal data can be used as a thermal load for thermal stress simulation using FEM. The condition that the stress is zero in the weld pool means that the pool walls become distorted by the compression ahead of the weld. This produces a region of tensile transverse stress adjacent to the weld pool and in turn a region of compressive transverse stress directly behind it. A regeneration model with negligible stiffness inside the melt pool is a viable way to solve for the deformation and stress near the melt pool and the mushy zone. However, this requires accurate mechanical property databases for the superalloys.

The CFD model can further be coupled with Cellular Automata (CA) model to simulate the solidification grain structure. This requires careful consideration of nucleation and grain growth models and significant computational cost due to the requirement of finer mesh in the CA domain. The CFD model can also be coupled with phase field models to predict the dendritic morphology in nickel-base superalloys.

References

[1] M.J. Donachie, S.J. Donachie, Superalloys: a technical guide, ASM international, 2002.

[2] J.K. Tien, Superalloys, Supercomposites and Superceramics, Elsevier, 2012.

[3] T.M. Pollock, S. Tin, Nickel-based superalloys for advanced turbine engines: chemistry, microstructure and properties, Journal of propulsion and power, 22 (2006) 361-374.

[4] R. Bansal, Analysis and feedback control of the scanning laser epitaxy process applied to nickel-base superalloys, Ph.D. Thesis, Georgia Institute of Technology, Atlanta, Georgia, USA (2013).

[5] A. Basak, S. Das, Epitaxy and microstructure evolution in metal additive manufacturing, Annual Review of Materials Research, 46 (2016) 125-149.

[6] B.B. Seth, Superalloys--the utility gas turbine perspective, Minerals, Metals and Materials Society/AIME, Superalloys 2000(USA), (2000) 3-16.

[7] P. Spittle, Gas turbine technology, Physics education, 38 (2003) 504.

[8] L.S. Langston, Gems of turbine efficiency, Mechanical Engineering, 136 (2014) 76.

[9] M. Yoo, On the theory of anomalous yield behavior of Ni_3Al—Effect of elastic anisotropy, Scripta metallurgica, 20 (1986) 915-920.

[10] R. Decker, J. Mihalisin, Coherency strains in gamma prime hardened nickel alloys, ASM Trans. Quart., 62 (1969) 481-489.

[11] A. Gregori, A survey of welding and repairing of nickel superalloys for gas turbines, TWI Core Research Programme, 774 (2003) 2003.

[12] S. Mokadem, Epitaxial laser treatment of single crystal nickel-base superalloys, Ph.D. Thesis, EPFL Lausanne (2004).

[13] Y. Xu, L. Zhang, J. Li, X. Xiao, X. Cao, G. Jia, Z. Shen, Relationship between Ti/Al ratio and stress-rupture properties in nickel-based superalloy, Materials Science and Engineering: A, 544 (2012) 48-53.

[14] R.C. Reed, The superalloys: fundamentals and applications, Cambridge university press, 2008.

[15] W. Betteridge, S. Shaw, Development of superalloys, Materials science and technology, 3 (1987) 682-694.

[16] V. Swaminathan, N. Cheruvu, Advanced materials and coatings for combustion turbines: proceedings of ASM 1993 Materials Congress Materials Week '93, October 17-21, 1993, Pittsburgh, Pennsylvania, Asm Intl, 1994.

[17] G. Erickson, K. Harris, DS and SX superalloys for industrial gas turbines, Proceedings Materials for Advanced Power Engineering, Kluwer Academic Publishers, Belgium, Liege, (1994) 1055-1074.

[18] E.W. Ross, K.S. O'hara, René 142 - A high strength, oxidation resistant DS turbine, Superalloys 1992, (1992) 257-265.

[19] P. Schilke, A. Foster, J. Pepe, Advanced gas turbine materials and coatings, General Electric

Company, 1991.

[20] A. Scholz, Y. Wang, S. Linn, C. Berger, R. Znajda, Modeling of mechanical properties of alloy CMSX-4, Materials Science and Engineering: A, 510 (2009) 278-283.

[21] W. Kurz, D. Fisher, Fundamentals of solidification, 1986, Trans Tech Publications, Switzerland.

[22] R. Acharya, Multiphysics modeling and statistical process optimization of the scanning laser epitaxy process applied to additive manufacturing of turbine engine hot-section superalloy components, Ph.D. Thesis, Georgia Institute of Technology, Atlanta, Georgia, USA (2014).

[23] Y. Yang, J. Yu, X. Sun, T. Jin, H. Guan, Z. Hu, Investigation of impact toughness of a Ni-based superalloy at elevated temperature, Materials & Design (1980-2015), 36 (2012) 699-704.

[24] F.R. Larson, A time temperature relationship for rupture and creep stress, Trans. ASME, (1952) 765-775.

[25] F. Garofalo, Fundamentals of Creep and Creep-Rupture in Metals, translated by M, Adachi, Maruzen, Tokyo, 139 (1968).

[26] T. Egly, K.-H. Lang, D. Löhe, Influence of phase shift and strain path on the thermomechanical fatigue behavior of CMSX-4 specimens, International Journal of Fatigue, 30 (2008) 249-256.

[27] X. Guo, Fundamentals of solidification, Trans Tech, Switzerland, (1986).

[28] M. Haafkens, J. Matthey, A new approach to the weldability of nickel-base As-cast and power metallurgy superalloys, Weld. J.(Miami);(United States), 61 (1982).

[29] M. Henderson, D. Arrell, R. Larsson, M. Heobel, G. Marchant, Nickel based superalloy welding practices for industrial gas turbine applications, Science and Technology of Welding and Joining, 9 (2004) 13-21.

[30] O. Ojo, M. Chaturvedi, On the role of liquated γ′ precipitates in weld heat affected zone microfissuring of a nickel-based superalloy, Materials Science and Engineering: A, 403 (2005) 77-86.

[31] S. Babu, S. David, J. Park, J. Vitek, Joining of nickel base superalloy single crystals, Science and technology of welding and joining, 9 (2004) 1-12.

[32] R.J. Stueber, T. Milidantri, M. Tadayon, Welding high-strength nickel base superalloys, US Patent No. 5,374,319 (1994).

[33] J.J. Marcin Jr, J.A. Neutra, D.H. Abbott, J.P. Aduskevich, D.M. Shah, D.N. Carraway, R.P. Langevin, M.R. Sauerhoefer, R.A. Stone, Method of repairing metallic articles by energy beam deposition with reduced power density, US Patent No. 5,914,059 (1999).

[34] R. Mah, Directed light fabrication, Advanced Materials and Processes, 151 (1997).

[35] Y. Kathuria, Laser surface cladding: a unique application to the turbine industry, in: Proceedings of the Laser Assisted Net Shape Engineering, 1997, pp. 23-26.

[36] E. Kreutz, Pulsed laser deposition of ceramics–fundamentals and applications, Applied surface science, 127 (1998) 606-613.

[37] M.T. Rush, P.A. Colegrove, Z. Zhang, B. Courtot, An investigation into cracking in nickel-base superalloy repair welds, in: Advanced Materials Research, Trans Tech Publ, 2010, pp. 467-

472.

[38] J.C. Lippold, S.D. Kiser, J.N. DuPont, Welding metallurgy and weldability of nickel-base alloys, John Wiley & Sons, 2011.

[39] T. Anderson, J. DuPont, T. DebRoy, Stray grain formation in welds of single-crystal Ni-base superalloy CMSX-4, Metallurgical and Materials Transactions A, 41 (2010) 181.

[40] A. Jacot, C.-A. Gandin, Formation of Microstructures, Grain Textures, and Defects during Solidification, ASM Handbook, Volume 22B: Metals Process Simulation, (2010) Pages 214-227.

[41] M. Asta, C. Beckermann, A. Karma, W. Kurz, R. Napolitano, M. Plapp, G. Purdy, M. Rappaz, R. Trivedi, Solidification microstructures and solid-state parallels: Recent developments, future directions, Acta Materialia, 57 (2009) 941-971.

[42] R. Acharya, S. Das, Additive Manufacturing of IN100 Superalloy Through Scanning Laser Epitaxy for Turbine Engine Hot-Section Component Repair: Process Development, Modeling, Microstructural Characterization, and Process Control, Metallurgical and Materials Transactions A, (2015) 1-12.

[43] M. Lamm, R. Singer, The effect of casting conditions on the high-cycle fatigue properties of the single-crystal nickel-base superalloy PWA 1483, Metallurgical and Materials Transactions A, 38 (2007) 1177-1183.

[44] M. Gäumann, C. Bezencon, P. Canalis, W. Kurz, Single-crystal laser deposition of superalloys: processing–microstructure maps, Acta Materialia, 49 (2001) 1051-1062.

[45] S. Mokadem, C. Bezençon, A. Hauert, A. Jacot, W. Kurz, Laser repair of superalloy single

crystals with varying substrate orientations, Metallurgical and Materials Transactions A, 38 (2007) 1500-1510.

[46] A. Gregori, D. Bertaso, Welding and Deposition of Nickel Superalloys 718, Waspaloy and Single Crystal Alloy CMSX-10, Welding in the World, 51 (2003) 34-47.

[47] D. Rosenthal, The Theory of Moving Sources of Heat and Its Application of Metal Treatments, Transactions of ASME, 68 (1946) 849-866.

[48] N. Christensen, V.d.L. Davies, K. Gjermundsen, Distribution of temperatures in arc welding, British Welding Journal, 12 (1965) 54-75.

[49] J. Goldak, A. Chakravarti, M. Bibby, A new finite element model for welding heat sources, Metallurgical and Materials Transactions B, 15 (1984) 299-305.

[50] W. Liu, J. DuPont, Effects of melt-pool geometry on crystal growth and microstructure development in laser surface-melted superalloy single crystals: Mathematical modeling of single-crystal growth in a melt pool (part I), Acta materialia, 52 (2004) 4833-4847.

[51] T. Anderson, J. DuPont, T. DebRoy, Origin of stray grain formation in single-crystal superalloy weld pools from heat transfer and fluid flow modeling, Acta Materialia, 58 (2010) 1441-1454.

[52] T. Childs, A. Tontowi, Selective laser sintering of a crystalline and a glass-filled crystalline polymer: experiments and simulations, Proceedings of the Institution of Mechanical Engineers, Part B: Journal of Engineering Manufacture, 215 (2001) 1481-1495.

[53] T. Childs, C. Hauser, M. Badrossamay, Mapping and modelling single scan track formation

in direct metal selective laser melting, CIRP Annals-Manufacturing Technology, 53 (2004) 191-194.

[54] T. Childs, C. Hauser, Raster scan selective laser melting of the surface layer of a tool steel powder bed, Proceedings of the Institution of Mechanical Engineers, Part B: Journal of Engineering Manufacture, 219 (2005) 379-384.

[55] K. Mundra, T. DebRoy, K. Kelkar, Numerical prediction of fluid flow and heat transfer in welding with a moving heat source, Numerical Heat Transfer, Part A Applications, 29 (1996) 115-129.

[56] W. Zhang, C.-H. Kim, T. DebRoy, Heat and fluid flow in complex joints during gas metal arc welding—Part II: Application to fillet welding of mild steel, Journal of Applied Physics, 95 (2004) 5220-5229.

[57] W. Zhang, C.-H. Kim, T. DebRoy, Heat and fluid flow in complex joints during gas metal arc welding—Part I: Numerical model of fillet welding, Journal of applied physics, 95 (2004) 5210-5219.

[58] R. Houldcroft, Dilution and uniformity in aluminum alloy weld beads, British Welding Journal, 1 (1954) 468-472.

[59] R. Acharya, R. Bansal, J.J. Gambone, S. Das, A Coupled Thermal, Fluid Flow, and Solidification Model for the Processing of Single-Crystal Alloy CMSX-4 Through Scanning Laser Epitaxy for Turbine Engine Hot-Section Component Repair (Part I), Metallurgical and Materials Transactions B, 45 (2014) 2247-2261.

[60] R. Acharya, R. Bansal, J.J. Gambone, S. Das, A Microstructure Evolution Model for the Processing of Single-Crystal Alloy CMSX-4 Through Scanning Laser Epitaxy for Turbine Engine Hot-Section Component Repair (Part II), Metallurgical and Materials Transactions B, 45 (2014) 2279-2290.

[61] C. Chan, J. Mazumder, M. Chen, Effect of surface tension gradient driven convection in a laser melt pool: Three-dimensional perturbation model, Journal of Applied Physics, 64 (1988) 6166-6174.

[62] T. Chande, J. Mazumder, Two-dimensional, transient model for mass transport in laser surface alloying, Journal of applied physics, 57 (1985) 2226-2232.

[63] H. Cline, T. Anthony, Heat treating and melting material with a scanning laser or electron beam, Journal of Applied Physics, 48 (1977) 3895-3900.

[64] G. Oreper, T. Eagar, J. Szekely, Convection in arc weld pools, Welding journal, 62 (1983) 307-312.

[65] J. Mazumder, Overview of melt dynamics in laser processing, Optical engineering, 30 (1991) 1208-1219.

[66] A. Paul, T. DebRoy, Free surface flow and heat transfer in conduction mode laser welding, Metallurgical and Materials Transactions B, 19 (1988) 851-858.

[67] D. Bedenko, O. Kovalev, Modelling of heat and mass transfer in the laser cladding during direct metal deposition, Thermophysics and Aeromechanics, 20 (2013) 251-261.

[68] Z. Liu, H. Qi, Numerical simulation of transport phenomena for a double-layer laser powder

deposition of single-crystal superalloy, Metallurgical and Materials Transactions A, 45 (2014) 1903-1915.

[69] M. Gäumann, Epitaxial laser metal forming of a single crystal superalloy, Ph.D. Thesis, EPFL, Lausanne (1999).

[70] R. Trivedi, Interdendritic spacing: Part II. A comparison of theory and experiment, Metallurgical Transactions A, 15 (1984) 977-982.

[71] H. Esaka, W. Kurz, R. Trivedi, Evolution of Primary Dendrite Spacing in Succinonitrile Acetone Alloys, Solidification Processing 1987, (1987) 198-201.

[72] J. Hunt, Steady state columnar and equiaxed growth of dendrites and eutectic, Materials science and engineering, 65 (1984) 75-83.

[73] M. Rappaz, S. David, J. Vitek, L. Boatner, Development of microstructures in Fe− 15Ni− 15Cr single crystal electron beam welds, Metallurgical and Materials Transactions A, 20 (1989) 1125-1138.

[74] M. Gäumann, R. Trivedi, W. Kurz, Nucleation ahead of the advancing interface in directional solidification, Materials Science and Engineering: A, 226 (1997) 763-769.

[75] M. Rappaz, C.-A. Gandin, Probabilistic modelling of microstructure formation in solidification processes, Acta metallurgica et materialia, 41 (1993) 345-360.

[76] J. Vitek, The effect of welding conditions on stray grain formation in single crystal welds–theoretical analysis, Acta materialia, 53 (2005) 53-67.

[77] M. Rappaz, S. David, J. Vitek, L. Boatner, Analysis of solidification microstructures in Fe-

Ni-Cr single-crystal welds, Metallurgical Transactions A, 21 (1990) 1767-1782.

[78] S. Das, Direct selective laser sintering of high performance metals: Machine design, process development and process control, Ph.D. Thesis, University of Texas, Austin, USA (1998).

[79] A. Ghaemi, Freezing-point-blackbody radiation sources for the 29.78–1084.62° C temperature range, Applied optics, 35 (1996) 2211-2215.

[80] K.C. Mills, Y.M. Youssef, Z. Li, Y. Su, Calculation of thermophysical properties of Ni-based superalloys, ISIJ international, 46 (2006) 623-632.

[81] G.F. Vander Voort, E.P. Manilova, G.M. Lucas, Metallographic Techniques for Superalloys, Microscopy and Microanalysis, 10 (2004) 690-691.

[82] J.J. Gambone, Quantitative metallography tracking and analysis for the scanning laser epitaxy process applied to CMSX-4 and Rene-80 nickel-based superalloys, MS Thesis, Georgia Institute of Technology, Atlanta, Georgia, USA (2012).

[83] A. Basak, R. Acharya, R. Bansal, S. Das, Scanning Laser Epitaxy – A Novel Metal Additive Manufacturing Process Developed for Gas Turbine Hot-Section Alloys, in: In Proceedings of Materials Science and Technology Conference, 2015, pp. 1697 - 1706.

[84] A. Basak, R. Acharya, S. Das, Computational Modeling and Experimental Validation of Melting and Solidification in Equiaxed Superalloys Processed through Scanning Laser Epitaxy, in: In Proceedings of the 26th Annual International Solid Freeform Fabrication Symposium, 2015, pp. 1264 - 1274.

[85] A. Basak, R. Acharya, S. Das, Modeling and Characterization of Microstructure Evolution in

Single-Crystal Superalloys Processed through Scanning Laser Epitaxy, in: In Proceedings of the 26th Annual International Solid Freeform Fabrication Symposium, 2015, pp. 1237-1247.

[86] I. Hamill, Implementation of a Solidification Model in CFX-5, in, Technical Report, CFX Ltd., Oxfordshire, United Kingdom, 2003.

[87] W.L. McCabe, J.C. Smith, P. Harriott, Unit Operations of Chemical Engineering, McGraw-Hill New York, 1993.

[88] M. Zieliñska, M. Yavorska, M. Porêba, J. Sieniawski, Thermal properties of cast nickel based superalloys, Archives of Materials Science and Engineering, 44 (2010) 35-38.

[89] P. Quested, R. Brooks, L. Chapman, R. Morrell, Y. Youssef, K. Mills, Measurement and estimation of thermophysical properties of nickel based superalloys, Materials Science and Technology, 25 (2009) 154-162.

[90] T. Matsushita, H.-J.r. Fecht, R.K. Wunderlich, I. Egry, S. Seetharaman, Studies of the Thermophysical Properties of Commercial CMSX-4 Alloy†, Journal of Chemical & Engineering Data, 54 (2009) 2584-2592.

[91] A. Sengupta, S. Putatunda, L. Bartosiewicz, J. Hangas, P. Nailos, M. Peputapeck, F. Alberts, Tensile behavior of a new single-crystal nickel-based superalloy (CMSX-4) at room and elevated temperatures, Journal of Materials Engineering and Performance, 3 (1994) 73-81.

[92] Y. Lee, M. Nordin, S. Babu, D. Farson, Influence of Fluid Convection on Weld Pool Formation in Laser Cladding, Welding Journal, 93 (2014) 292-300.

[93] Engineering Properties of IN-100 Alloy

(https://www.nickelinstitute.org/~/media/Files/TechnicalLiterature/IN_100AlloyEngineeringProperties_483_.ashx), Nickel Institute.

[94] G. Bi, C.-N. Sun, H.-c. Chen, F.L. Ng, C.C.K. Ma, Microstructure and tensile properties of superalloy IN100 fabricated by micro-laser aided additive manufacturing, Materials & Design, 60 (2014) 401-408.

[95] A. Basak, S. Das, Additive Manufacturing of Nickel-Base Superalloy IN100 through Scanning Laser Epitaxy (SLE), JOM, DOI: 10.1007/s11837-017-2638-6.

[96] K. Harris, G. Erickson, R. Schwer, MAR M 247 Derivations - CM 247 LC DS Alloy, CMSX® Single Crystal Alloys, Properties and Performance, Superalloys 1984, (1984) 221-230.

[97] M. Kaufman, Properties of Cast Mar-M-247 for Turbine Blisk Applications, Superalloys 1984, (1984) 43-52.

[98] J. Kattus, Mar-M247 (Code 4218), Aerospace Structural Metals Handbook, Purdue Research Foundation, West Lafayette, Indiana, (1999).

[99] H. Lee, S. Lee, The morphology and formation of gamma prime in nickel-base superalloy, Journal of Materials Science Letters, 9 (1990) 516-517.

[100] K. Zeisler-Mashl, B. Pletka, Segregation during solidification in the MAR-M 247 system(of nickel-base superalloys), Superalloys 1992, (1992) 175-184.

[101] S. Das, T.P. Fuesting, G. Danyo, L.E. Brown, J.J. Beaman, D.L. Bourell, K. Sargent, Direct laser fabrication of gas turbine engine component - microstructure and properties - Part I and II, in: Proceedings of Solid Freeform Fabrication (SFF) Symposium, 1998, pp. 1-18.

[102] J.A. Ramos, J. Murphy, K. Lappo, K. Wood, D.L. Bourell, J.J. Beaman, Single-layer Deposits of Nickel Base Superalloy by means of Selective Laser Melting, Solid Freeform Fabrication Proceedings, (2002) 211-223.

[103] Y. Hagedorn, J. Risse, W. Meiners, N. Pirch, K. Wissenbach, R. Poprawe, Processing of nickel based superalloy MAR M-247 by means of High Temperature–Selective Laser Melting (HT-SLM), in: High Value Manufacturing: Advanced Research in Virtual and Rapid Prototyping: Proceedings of the 6th International Conference on Advanced Research in Virtual and Rapid Prototyping, Leiria, Portugal, 1-5 October, 2013, CRC Press, 2013, pp. 291.

[104] L.N. Carter, M.M. Attallah, R.C. Reed, Laser powder bed fabrication of nickel-base superalloys: influence of parameters; characterisation, quantification and mitigation of cracking, in: Proceeding of Superalloys, 2012, pp. 577-586.

[105] V. Divya, R. Muñoz-Moreno, O. Messé, J. Barnard, S. Baker, T. Illston, H. Stone, Microstructure of selective laser melted CM247LC nickel-based superalloy and its evolution through heat treatment, Mater. Charact. 114 (2016) 62-74.

[106] A. Basak, S. Das, Microstructural Characterization of MAR-M247 Fabricated Through Scanning Laser Epitaxy, in: The 27th Annual International Solid Freeform Fabrication Symposium – An Additive Manufacturing Conference, 2016, pp. 448 - 459.

[107] A. Basak, S. Das, Microstructure of nickel-base superalloy MAR-M247 additively manufactured through scanning laser epitaxy (SLE), Journal of Alloys and Compounds, 705 (2017) 806-816.

[108] A. Basak, S. Das, Characterization of MAR-M247 Deposits Fabricated through Scanning

Laser Epitaxy (SLE), in: The 28th International Solid Freeform Fabrication Symposium, Austin, Texas, 2017.

[109] A. Basak, S. Das, Effect of Heat Treatment on the Microstructure of MAR-M247 Processed Through Scanning Laser Epitaxy, in: In Proceedings of Materials Science and Technology Conference, 2016, pp. 59 - 66.

[110] F. Liu, X. Lin, G. Yang, M. Song, J. Chen, W. Huang, Microstructure and residual stress of laser rapid formed Inconel 718 nickel-base superalloy, Opt. Laser Technol. 43 (2011) 208-213.

[111] R. Freere, E. Weibel, Stereologic techniques in microscopy, J. R. Microsc. Soc. 87 (1964) 25-34.

[112] C. Sims, N. Stoloff, W.C. Hagel, Superalloys II: high temperature materials for aerospace and industrial power. 1987, NY: John Wiley & Sons.

[113] I.M. Lifshitz, V.V. Slyozov, The kinetics of precipitation from supersaturated solid solutions, J. Phys. Chem. Solids 19 (1961) 35-50.

[114] C. Wagner, Theory of the aging of precipitates by dissolution-reprecipitation (Ostwald ripening), Z. Elektrochem 65 (1961) 581-591.

[115] A. Basak, S. Das, Carbide Formation in Additive Manufacturing of Equiaxed Superalloy MAR-M247 Processed through Scanning Laser Epitaxy, in: The 27th Annual International Solid Freeform Fabrication Symposium – An Additive Manufacturing Conference, 460 - 468, 2016.

[116] X. Xie, G. Wang, J. Dong, C. Xu, W.-D. Cao, R. Kennedy, Structure stability study on a newly developed nickel-base superalloy-Allvac® 718Plus™, in: Proceedings of Sixth

International Special Emphasis Symposium on Superalloys 718, 625, 706 and Derivatives, 2005, pp. 179-191.

[117] M. Fitzpatrick, A. Fry, P. Holdway, F. Kandil, J. Shackleton, L. Suominen, Determination of residual stresses by X-ray diffraction, (2005).

[118] K.P. Fullagar, R.W. Broomfield, M. Hulands, K. Harris, G.L. Erickson, S.L. Sikkenga, Aero Engine Test Experience With CMSX-4® Alloy Single Crystal Turbine Blades, in: ASME 1994 International Gas Turbine and Aeroengine Congress and Exposition, American Society of Mechanical Engineers, 1994, pp. V002T002A003-V002T002A003.

[119] K. Harris, G. Erickson, S. Sikkenga, W. Brentnall, J. Aurrecoechea, K. Kubarych, Development of the rhenium containing superalloys CMSX-4® & CM 186 LC® for single crystal blade and directionally solidified Vane applications in advanced turbine engines, Superalloys 1992, 297 (1992).

[120] D. Frasier, J. Whetstone, K. Harris, G. Erickson, R. Schwer, Process and alloy optimization for CMSX-4 superalloy single crystal airfoils, High Temperature Materials for Power Engineering, (1990) 1281-1300.

[121] A. Giamei, D. Pearson, D. Anton, γ/γ′: The Key to Superalloy Behavior, in: MRS Proceedings, Cambridge Univ Press, 1984, pp. 293-308.

[122] M. Ramsperger, R.F. Singer, C. Körner, Microstructure of the Nickel-Base Superalloy CMSX-4 Fabricated by Selective Electron Beam Melting, Metallurgical and Materials Transactions A, 47 (2016) 1469-1480.

[123] A. Basak, R. Acharya, S. Das, Additive Manufacturing of Single-Crystal Superalloy CMSX-4 Through Scanning Laser Epitaxy: Computational Modeling, Experimental Process Development, and Process Parameter Optimization, Metallurgical and Materials Transactions A, 47 (2016) 3845-3859.

[124] A. Basak, S. H R, S. Das, Microstructures and Microhardness Properties of CMSX-4® Additively Fabricated through Scanning Laser Epitaxy (SLE), Journal of Materials Engineering and Performance, DOI: https://doi.org/10.1007/s11665-017-3008-9.

[125] A. Basak, K. Kalaitzidou, S. Das, Effects of Processing Parameters on the Mechanical Properties of CMSX-4® Additively Fabricated through Scanning Laser Epitaxy (SLE), in: The 28th Annual International Solid Freeform Fabrication Symposium – An Additive Manufacturing Conference, Austin, Texas, 2017.

[126] M. Gäumann, S. Henry, F. Cleton, J.-D. Wagniere, W. Kurz, Epitaxial laser metal forming: analysis of microstructure formation, Materials Science and Engineering: A, 271 (1999) 232-241.

[127] Y.-J. Liang, H.-M. Wang, Origin of stray-grain formation and epitaxy loss at substrate during laser surface remelting of single-crystal nickel-base superalloys, Materials & Design, 102 (2016) 297-302.

[128] A. Basak, S. Das, Effect of Heat Treatment on the Microstructures of CMSX-4® Processed through Scanning Laser Epitaxy (SLE), in: The 28th Annual International Solid Freeform Fabrication Symposium – An Additive Manufacturing Conference, Austin, Texas, 2017.

[129] M. Ramsperger, L. Mújica Roncery, I. Lopez-Galilea, R.F. Singer, W. Theisen, C. Körner, Solution Heat Treatment of the Single Crystal Nickel-Base Superalloy CMSX-4 Fabricated by

Selective Electron Beam Melting, Advanced Engineering Materials, 17 (2015) 1486-1493.

[130] R. Aluru, W. Gale, S. Chitti, N. Sofyan, R. Love, J. Fergus, Transient liquid phase bonding of dissimilar nickel base superalloys - wettability, microstructure and mechanical properties, Materials Science and Technology, 24 (2008) 517-528.

[131] J. Lapin, T. Pelachová, O. Bajana, The effect of microstructure on mechanical properties of single crystal CMSX-4 superalloy, in: Metal, 2003, pp. 1277-1282.

[132] A. Basak, S. Das, Additive Manufacturing of Nickel-Base Superalloy René N5 through Scanning Laser Epitaxy (SLE)− Material Processing, Microstructures, and Microhardness Properties, Advanced Engineering Materials, 19 (2017) 1 - 10 (1600690).

[133] A. Basak, S. Das, A Study on the Effects of Substrate Crystallographic Orientation on Microstructural Characteristics of René N5 Processed through Scanning Laser Epitaxy, in: Superalloys 2016: Proceedings of the 13th Intenational Symposium of Superalloys, John Wiley & Sons, Inc., 2016, pp. 1041-1049.

[134] K. Ravindran, S. Brown, J. Spittle, Prediction of the effective thermal conductivity of three-dimensional dendritic regions by the finite element method, Materials Science and Engineering: A, 269 (1999) 90-97.

[135] A. Basak, S. Das, Carbide Formation in Additive Manufacturing of Single-Crystal Superalloy René N5 Processed Through Scanning Laser Epitaxy, in: Materials Science and Technology Conference, Salt Lake City, Utah, 2016, pp. 51-58.

[136] A. Wasson, G. Fuchs, The effect of carbide morphologies on elevated temperature tensile

and fatigue behavior of a modified single crystal Ni-base superalloy, Superalloys 2008, (2008) 489-497.

[137] G. Soto, H. Tiznado, J. Diaz, E. Samano, A. Reyes-Serrato, Evaluation of rhenium carbide as a prospective material for hard coating, Thin Solid Films, 519 (2011) 3236-3241.

[138] A. Basak, S. Das, An Investigation of Dendritic Segregation in Single-Crystal René N5 Fabricated through Scanning Laser Epitaxy, in: The 27th Annual International Solid Freeform Fabrication Symposium – An Additive Manufacturing Conference, 2016, pp. 487 – 498.

[139] L. Murr, E. Martinez, X. Pan, S. Gaytan, J. Castro, C. Terrazas, F. Medina, R. Wicker, D. Abbott, Microstructures of Rene 142 nickel-based superalloy fabricated by electron beam melting, Acta Materialia, 61 (2013) 4289-4296.

[140] A. Basak, S. Das, A Study on the Microstructural Characterization of René 142 Deposited atop René 125 Processed through Scanning Laser Epitaxy, Materials Science Forum, 879 (2017) 187-192.

[141] A. Basak, R. Acharya, S. Das, Epitaxial Deposition of Nickel-Base Superalloy René 142 through Scanning Laser Epitaxy (SLE), Submitted to Additive Manufacturing.

[142] Y.-J. Liang, J. Li, A. Li, X.-T. Pang, H.-M. Wang, Solidification path of single-crystal nickel-base superalloys with minor carbon additions under laser rapid directional solidification conditions, Scripta Materialia, 127 (2017) 58-62.

[143] M.G. Glavicic, K. Sargent, P. Kobryn, S. Semiatin, The repair of single crystal nickel superalloy turbine blades using laser engineered net shape (lens) technology, in, DTIC Document,

2003.

[144] O. Hunziker, D. Dye, S. Roberts, R. Reed, A coupled approach for the prediction of solidification cracking during the welding of superalloys, in: Fifth International Seminar on the Numerical Analysis of Weldability, 1999, pp. 299-319.

[145] A. Szczotok, Study of casting from IN100 nickel-based superalloy using quantitative metallography and analytical electron miroscopy, Materialwissenschaft und Werkstofftechnik, 46 (2015) 320-329.

[146] TMS, Compositions of Typical Cast Superalloys, in, http://www.tms.org/Communities/FTAttachments/superalloystable_castcomp.pdf.

[147] N. Ratel, Investigation of the strain induced rafting of the gamma prime precipitates in single crystal nickel based superalloys, in, Université Joseph-Fourier-Grenoble I, 2007.

Vita

Before starting graduate studies at Georgia Tech in 01/2012, Amrita Basak was a Lead Engineer at General Electric (Aviation) Bangalore, Karnataka, India for six years (07/2005 – 12/2011). Even before that, she was a Masters student in Chemical Engineering (05/2003 – 05/2005) at the Indian Institute of Technology, Kanpur, India. Back in a magical decade, she was born in a small town named Coochbehar in West Bengal, India. She spent her wonder-years at various parts of West Bengal, India till she graduated with a B.E. in Chemical Engineering (05/1999 – 05/2003) from Jadavpur University, Kolkata, India.

During graduate school at Georgia Tech, she joined the Direct Digital Manufacturing Lab and worked on the development of a laser powder bed fusion (LPBF)-based additive manufacturing process, scanning laser epitaxy (SLE) under the direction of Dr. Suman Das. She completed her Masters of Science in Aerospace Engineering in 2015 and received her Doctor of Philosophy in Mechanical Engineering in 2017 for her dissertation titled *Advanced Powder Bed Fusion-Based Additive Manufacturing with Turbine Engine Hot-Section Superalloys through Scanning Laser Epitaxy*. She spent the summer of 2014 at Robert Bosch, Palo Alto doing internship. She was also a student member of the Industrial Assessment Center at Georgia Tech.